Fluid Mechanics of Ingress in a 1.5-Stage Gas Turbine Experimental Facility

Patinios, Mario

Award date:
2017

Awarding institution:
University of Bath

Fluid Mechanics of Ingress in a 1.5-Stage Gas Turbine Experimental Facility

Patinios, Mario

Award date:
2017

Awarding institution:
University of Bath

Fluid Mechanics of Ingress in a 1.5-Stage Gas Turbine Experimental Facility

Marios Patinios

A thesis submitted for the degree of Doctor of Philosophy

University of Bath
Department of Mechanical Engineering
November 2016

Abstract

The gas turbine engine is undoubtedly one of the most versatile engines, with applications ranging from aircraft, maritime and locomotive propulsion to electricity generation. Increasing fuel costs and strict environmental legislation demand increasingly efficient engines. Engine efficiency can be improved by operating at a turbine entry temperature (TET) beyond the melting point of the turbine components. To enable this, compressor flow is diverted to the turbine for cooling and sealing the cavities (or wheel-spaces) formed between adjacent stator and rotor discs. Insufficient sealing flow reduces component operating life and superfluous use reduces the benefits of increased TET.

Rim-seals, fitted at the periphery of the rotor discs, are used to minimise the ingress of hot gas and therefore reduce the amount of sealing flow required. These rim-seals are designed using computational fluid dynamics (CFD) software which require experimental validation in facilities operating at engine-simulated conditions as well as experimental rigs operating at low Reynolds number.

This thesis presents: (*i*) the design, assembly and commissioning of a new 1.5-stage turbine experimental facility, (*ii*) measurements of ingress through generic seals in an upstream and downstream wheel-space and (*iii*) parametric studies of the performance of eight Siemens proprietary seals.

The new 1.5-stage test facility is designed to investigate ingress into the wheel-spaces upstream and downstream of a rotor disc. The flow structure inside the wheel-spaces is representative of the one found in engines with the rig operating at incompressible flow conditions, far removed from the harsh environment of the engine which is not conducive to experimental measurements. The test facility features interchangeable rim-seal components, offering significant flexibility and expediency in terms of data collection over a wide range of sealing-flow rates. The rig was specifically designed to enable an efficient method of ranking and quantifying the performance of generic and engine-specific seal geometries.

The radial variation of concentration effectiveness based on CO_2 gas concentration, pressure and swirl is measured to explore, for the first time, the flow structure in both the upstream and downstream wheel-spaces. For both single and double radial-clearance seals, the measurements show that the concentration effectiveness in the core is equal to that on the stator and that both distributions are virtually invariant with radius. These measurements confirm that mixing between ingress and egress is essentially complete immediately after the ingested fluid enters the wheel-space, and that the fluid from the boundary-layer on the stator

is the source of that in the core. The swirl in the core is shown to determine the radial distribution of pressure in the wheel-space.

The variation of concentration effectiveness with sealing flow rate in the upstream and the downstream wheel-spaces is obtained and found to be independent of rotational Reynolds number for a common flow coefficient in the mainstream annulus. A simple theoretical orifice model was fitted to the experimental data showing good agreement between theory and experiment for all cases. This observation is of great significance as it demonstrates that the orifice model can accurately capture the variation of effectiveness with sealing flow rate in both wheel-spaces.

The driving mechanism for ingress in the downstream wheel-space is identified using concentration effectiveness measurements taken in a rotationally-induced (RI) ingress experiment. The measurements of the RI test were found to be equal to those of the externally-induced (EI) ingress test, showing that RI ingress dominates in the downstream wheel-space.

Three parametric studies including eight Siemens proprietary seals were performed in the downstream wheel-space using measurements of CO_2 concentration, swirl ratio and pressure. In the first study it was proven that the inter-blade gaps in engines have a negative effect on the performance of the seals. In the second study it was shown that a significant decrease in ingress can be achieved by using a compound angel-wing/radial-clearance seal as opposed to a simple angel-wing seal. In the third study the negative effect of the introduction of a buffer cavity in the design of seals for the downstream wheel-space was revealed. In all cases, the majority of the wheel-space was dominated by the expected flow structure and good agreement between the theoretical orifice model and experiments was observed despite the complex geometry of the seals.

This is dedicated to my late mother who I hope I make proud by completing this and to my grandmother for taking her place after her death to raise me to be the person that I am today.

Acknowledgements

First and foremost, I would like to thank and express my gratitude to my lead supervisor Dr. Carl Sangan and secondary supervisor Prof. Gary Lock for their friendly approach, supervision, advice and constant support over the past three years.

Special thanks to my colleague and friend Dr. James Scobie who has given me, since day one, invaluable help throughout my studies and who shared with me his knowledge and experiences around the subject of ingress in gas turbines.

I would also like to thank Emeritus Prof. Michael Owen, for being actively involved in my research by providing advice and sharing his many years of knowledge and experience.

Many thanks also to my colleagues and friends Dr. GeonHwan Cho and Hui Tang for being an absolute pleasure working with and incredible people.

I would also like to express many thanks to the technicians Andrew Langly and Steve Thomas whose technical skills and experience are some of the primary reasons for the success of the research program.

The work presented in this thesis was funded by the EPSRC and Siemens AG.

Contents

List of Figures

List of Tables

Nomenclature

Symbols

b	characteristic radius of seal
c	concentration; blade chord length
C	vane exit velocity
$C_{d,e}$	egress discharge coefficient
$C_{d,i}$	ingress discharge coefficient
C_F	flow coefficient $[= W/\Omega b]$
C_p	pressure coefficient $[= (p_2 - \overline{p_2})/(0.5\rho\Omega^2 b^2)]$
C_w	vane exit tangential velocity; non-dimensional flow rate $[= \dot{m}/\mu b]$
$C_{w,0}$	non-dimensional flow rate of sealing flow
$C_{w,min}$	minimum value of $C_{w,0}$ to prevent ingress
d	diameter
F	force
G	gap ratio $[= S/b]$
G_c	seal-clearance ratio $[= s_c/b]$
h_{buffer}	depth of buffer cavity
k_a	empirical constant
L_e	entrance length
m	mass
$\dot{m}$	mass flow rate
M	Mach number
p	absolute static pressure
p_0	total pressure

q	heat
r	radius
Re_w	axial Reynolds number [$= \rho W b/\mu$]
Re_Φ	rotational Reynolds number [$= \rho \Omega b^2/\mu$]
s	entropy
s_c	seal clearance
$s_{overlap}$	axial overlap of radial clearance seal
S	axial clearance between rotor and stator; wheel-space gap
T	temperature
T_s	torque generated by stage
U	bulk-mean velocity through rim seal clearance [$= \dot{m}/2\pi\rho b s_c$]
v	volume
V	blade exit velocity
V_r	radial component of velocity
V_z	axial component of velocity
V_Φ	tangential component of velocity
W	axial velocity in annulus
W_s	work generated by stage
z	axial co-ordinate in wheel space
α	vane inlet/exit angle
β	blade inlet/exit angle; swirl ratio in wheel-space [$= V_\Phi/\Omega r$]
Γ_c	ratio of discharge coefficients [$= C_{d,i}/C_{d,e}$]
$\Gamma_{\Delta p}$	external pressure parameter [$= \Delta C_p/C_{\beta,1}$]
δ	radial growth of rotor disc
ΔC_p	non-dimensional pressure difference [$= \Delta p/(0.5\rho\Omega^2 b^2$]
Δp	peak-to-trough pressure difference in annulus
ε	sealing effectiveness [$C_{w,0}/C_{w,e} = \Phi_0/\Phi_e$]
ε_c	concentration effectiveness [$= (c_s - c_a)/(c_0 - c_a)$]
θ	angular co-ordinate, non-dimensional vane pitch
θ_{slot}	slot pitch
λ_T	turbulent flow parameter [$= c_{w,0} Re_\Phi^{-0.8}$]
μ	dynamic viscosity
ρ	density
σ	standard deviation
Φ	non-dimensional sealing parameter [$= U/\Omega b$]
Φ_{min}	value of Φ when $C_w = C_{w,min}$

Φ_{min}'	value of Φ when $\varepsilon = 0.95$
Φ_0	value of Φ when $C_w = C_{w,0}$
ψ	blade loading coefficient
ω	angular velocity of rotating core in wheel-space
Ω	angular velocity of rotating disc

Subscripts

a	annulus
ax	axial
c	concentration
DWS	downstream wheel-space
e	egress
EI	externally-induced ingress
i	ingress
in	inner
max	maximum
min	minimum
out	outer
rad	radial
ref	reference
RI	rotationally-induced ingress
s	stator
UWS	upstream wheel-space
w	axial coordinate
Φ	angular coordinate
0	superposed flow
1, 2	locations in wheel-space and annulus
∞	core

Superscripts

–	average value
*	new definitions

Chapter 1: Introduction

1.1 The Gas Turbine Engine through History

The gas turbine engine is undoubtedly one of the most versatile engines with applications ranging from aircraft, maritime and locomotive propulsion to electricity generation. What enabled the use of gas turbine engines in all these applications is their high power-to-weight ratio, fuel flexibility and reliability.

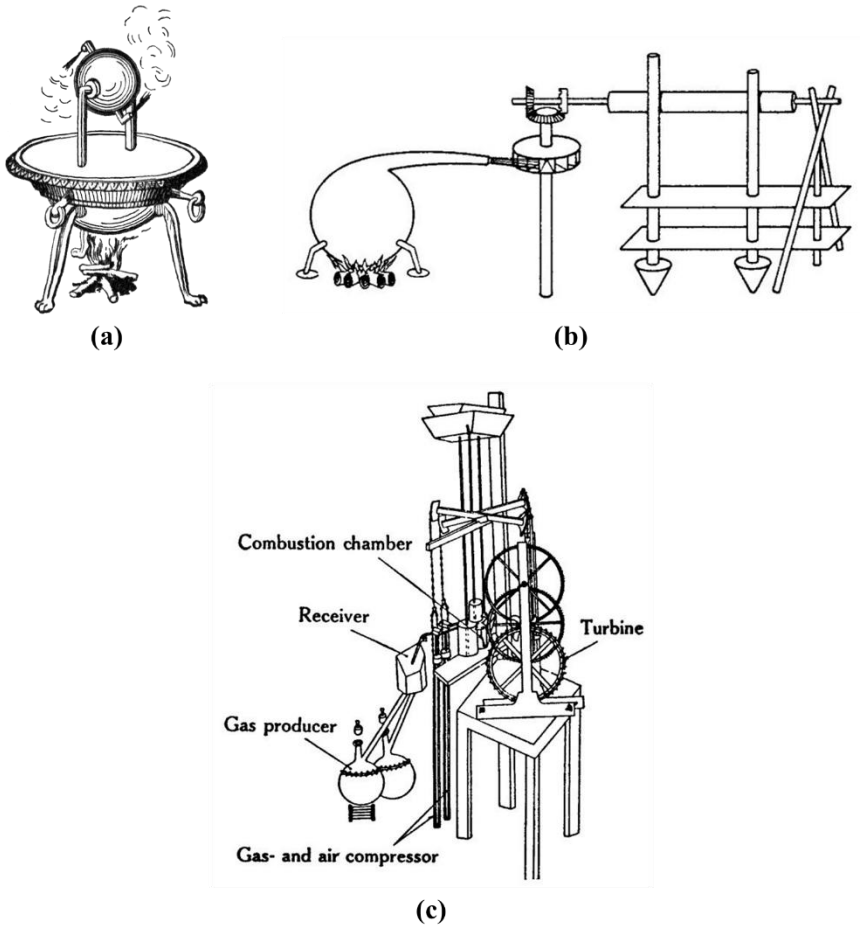

Figure 1.1: The early turbine engines – (a) Hero's engine, the Aeolipile; (b) Giovanni Branca's turbine driven stamping mill; (c) John Barber's patent drawing (from Meher-Homji (2000))

The working principles of gas turbine engines involve the extraction of energy from a heated gas and the conversion of this energy into usually rotational motion. The first time that this principle was realised was around 100 *BC* where a Greek mathematician and engineer named Hero designed the "Aeolipile" (Figure 1.1 (a)), a sphere capable of rotating by taking advantage of the momentum of steam emerging from two opposite facing nozzles. Hero's engine can be seen in Figure 1.1 (a). In 1629 Giovanni Branca, an Italian engineer, designed a stamping mill powered by a steam driven impulse turbine as shown in Figure 1.1 (b). In 1791

John Barber, a British engineer, filed a patent for a machine operating using compressed air from a reciprocating combustor that was mixed with charcoal gas prior to being ignited to produce a hot gas that was then fed to a reaction turbine. Barber's machine, even though never built, is considered to be the first machine conceived to operate using the thermodynamic cycle of modern gas turbine engines.

The modern gas turbine engine was first developed as an industrial and aerospace engine, almost simultaneously, during the first half of the 1900s. After a series of patents and trials on experimental gas turbines between 1900 and 1937, the first industrial gas turbine capable of successfully generating electricity was introduced by Dr. Adolf Meyer, the director of BBC Brown Boveri, in 1939 at Neuchatel, Switzerland. The Neuchatel engine operated at a turbine entry temperature of 550 ^{o}C, had a power output of 4 MW and an efficiency if 17.4%.

The idea of an aerospace variant of the gas turbine engine started with two patents, one by Sir Frank Whittle in 1930, in England and one by Dr. Hans von Ohain in 1935, in Germany. In 1939, just before the beginning of World War 2, an engine designed by von Ohain but built by Ernst Heinkel, the HeS 3B, became the first gas turbine engine to successfully power an aircraft. In 1942, the first mass production engine, the Junkers Jumo 004B turbojet, entered service on the Messerschmitt Me-262 fighter aircraft. The Jumo 004B could provide a thrust of 8.22 kN and had a life time of only 25 hours. By the end of the war 6000 of these engines were manufactured. Seven years after the end of World War 2, in 1952, the de Havilland Ghost 50 Mk1, became the first aero engine to power a civil aircraft.

In the following years a huge amount of effort and resources was invested in further development of the gas turbine engine. As a result modern gas turbines are capable of producing huge amounts of power by consuming relatively small amounts of fuel while demonstrating high efficiencies. An example of a modern industrial gas turbine engine is the Siemens SGT5-8000H. This heavy-duty industrial gas turbine can produce 400 MW of power with an efficiency of 80% when operating in a combined cycle; 100 times more powerful and almost 5 times more efficient than its predecessor the Neuchatel engine. An example of a modern aero engine is the Rolls-Royce Trent 7000. This engine is capable of delivering 320 kN of thrust with an efficiency greater than 90%. The development of the industrial and aero gas turbine engines, since the 1940s, is illustrated in the timeline provided in Figure 1.2 through the products of various American and European manufacturers.

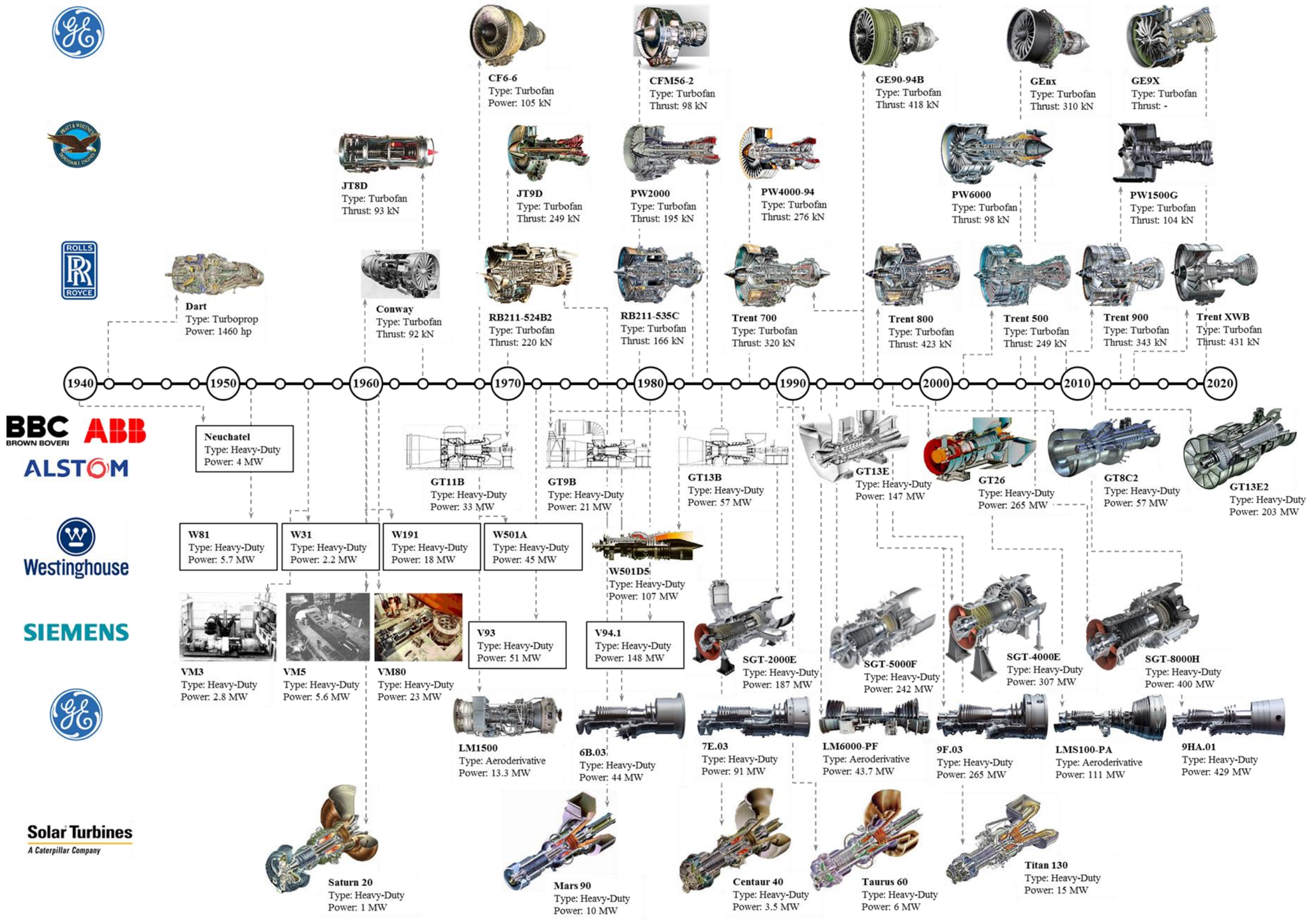

Figure 1.2: Timeline of the evolution of the aero and industrial gas turbine engine through the products of the major European and American manufacturers

1.2 The Brayton Cycle and Engine Efficiency

A gas turbine engine consists of three main components: the compressor, the combustor and the turbine. These components form the core of the engine and, as illustrated in Figure 1.3, are a common feature of all of the engine's variants. The air first passes through the compressor where it compresses and its pressure raises. The high-pressure air is then fed to the combustor (or combustion chamber) where it mixes with fuel and ignited. Lastly, the now high-pressure, high-temperature gas expands through the turbine where energy is extracted to drive the compressor and the load. In the examples shown in Figure 1.3 the load is the fan in the case of the turbofan engine (c) and an electric alternator in the case of the power generation engine (b).

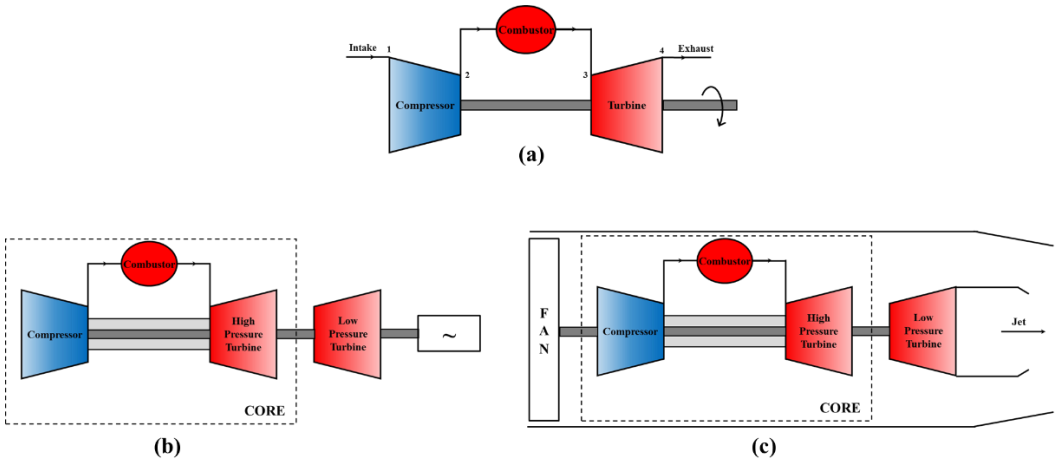

Figure 1.3: Variations of a gas turbine - (a) simple cycle gas turbine; (b) gas turbine driving an alternator; (c) turbofan gas turbine

The gas turbine engine operates based on an open thermodynamic cycle with the compressor always drawing fresh atmospheric air at ambient pressure and temperature and the turbine exhausting gas to the atmosphere at a temperature higher than ambient. The Brayton cycle is often used to describe the operating principles of the core of the engine. A diagram of the Brayton cycle is shown in Figure 1.4. In an ideal case, where no losses exist, the compression and expansion processes are isentropic and are represented by the solid lines connecting points 1 to 2' and 3 to 4' respectively. In practise, losses result in an increase in entropy S and therefore non-isentropic compression and expansion. The realistic processes are represented by the dashed lines connecting points 1 to 2 and 3 to 4. At entry to the compressor the temperature T_1 and the pressure p_1 are both atmospheric (here p_a refers to atmospheric pressure so that $p_1 = p_a$). At the outlet of the compressor and inlet to the combustor the pressure is p_2 so that $p_2 > p_1$. During combustion, the temperature increases by adding energy to the flow in the form of heat (q_{in}). In the case of the ideal cycle, combustion is considered to have

taken place at a constant pressure so that p_3, the pressure at the outlet of the combustor, is equal to p_2; in reality there is a pressure drop during the combustion process so that $p_3 < p_2$. The flow leaves the combustor and enters the turbine with a temperature T_3. In the turbine the flow expands to a lower pressure and temperature, p_4 and T_4 respectively. The flow exhausts to atmosphere so that $p_4 = p_a$ but with T_4 being higher than atmospheric. The processes described above are repeated when the compressor draws in fresh atmospheric air.

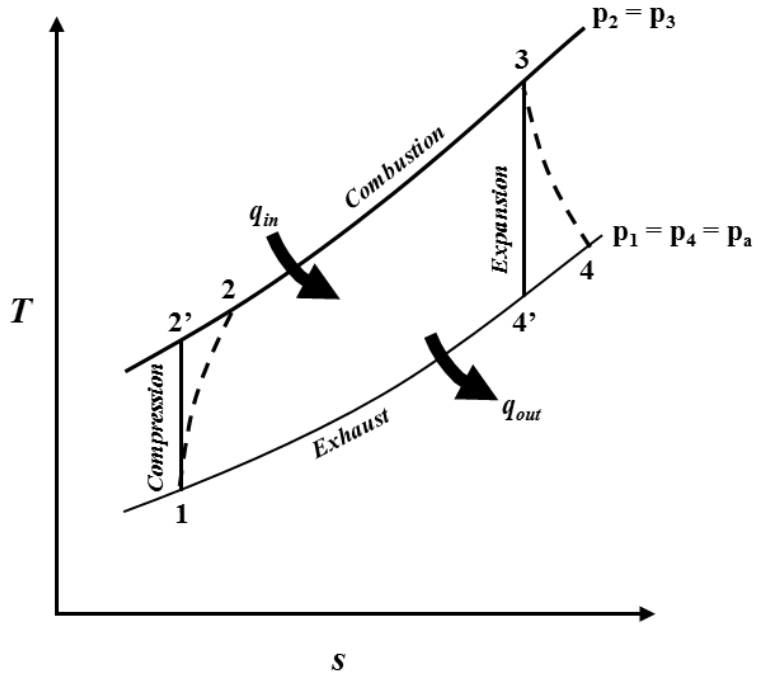

Figure 1.4: Brayton cycle temperature-entropy (T-s) diagram

The performance of the core of a gas turbine engine is usually evaluated based on the specific work output and the thermodynamic efficiency. The specific work output, W depends on both the pressure ratio, r ($=p_2/p_1 = p_3/p_4$) and the temperature ratio, t ($= T_3/T_1$). Figure 1.5 shows the effect of the temperature ratio on the variation of specific work output with pressure ratio for a real gas turbine engine with losses where the efficiency of the compressor, η_c is equal to the efficiency of the turbine, η_t and equal to 90%. As it can be seen, there is an optimum pressure ratio at which the specific work output reaches a maximum. For any pressure ratio the higher the temperature ratio the higher the work output. The thermodynamic efficiency is given by the ratio of the net work output to the heat supplied to the system. In the ideal case where the compression and expansion processes are isentropic, the efficiency depends only on the pressure ratio. In the real case where losses exist the efficiency also depends on the temperature ratio. Figure 1.6 shows the effect of the temperature ratio on the variation of efficiency with pressure ratio for a gas turbine engine operating on a real cycle

with losses. For a given pressure ratio, the higher the temperature ratio the higher the thermodynamic efficiency of the engine.

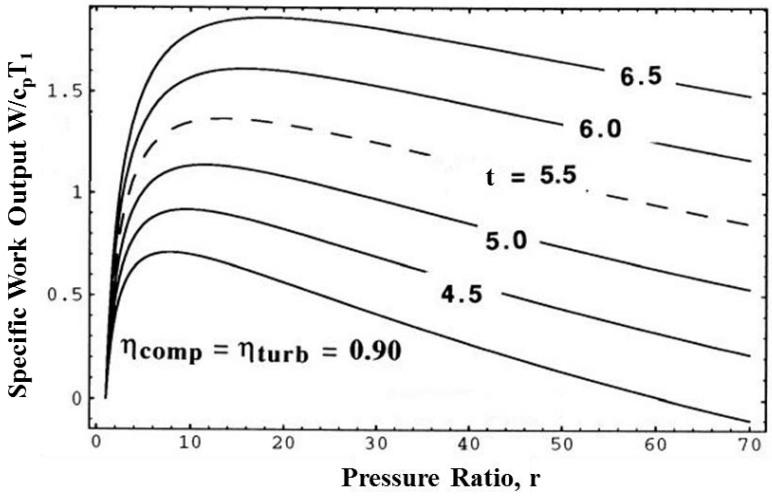

Figure 1.5: The effect of temperature ratio on the variation of specific work output with pressure ratio for a real gas turbine engine with losses (adapted from Cumpsty (2003))

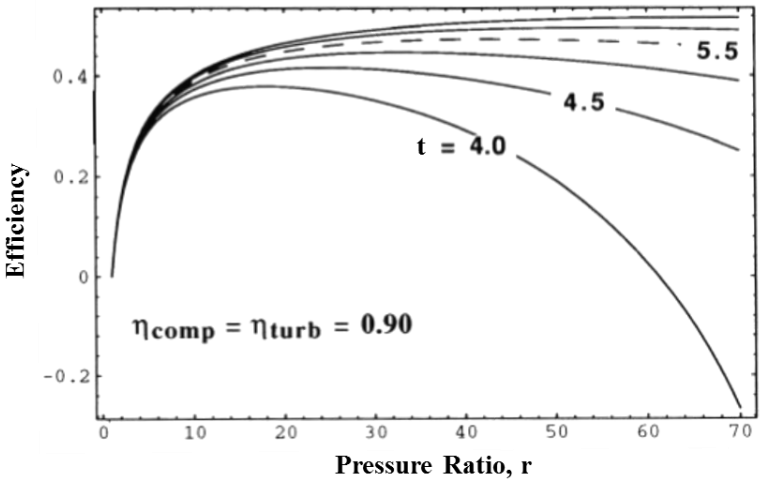

Figure 1.6: The effect of temperature ratio on the variation of efficiency with pressure ratio for a real gas turbine engine with losses (adapted from Cumpsty (2003))

Increasing the pressure and temperature ratios has always been important to engine designers. As shown in Figures 1.7 (a) and (b) and Figure 1.8, there has been a steady increase in the pressure ratio and temperature ratio of the aerospace and industrial engines through the years, which is reflected in the products of all major engine manufacturers. Due to lack of available information the equivalent of Figure 1.8 for the aerospace engine could not be produced, but similar trends apply.

The limit to which the pressure ratio can be increased depends on compressor design limitations including rotor speed, flow axial velocity and fluid deflection angles in the rotor blades. These are beyond the scope of this thesis and therefore no further reference will be made to the pressure ratio.

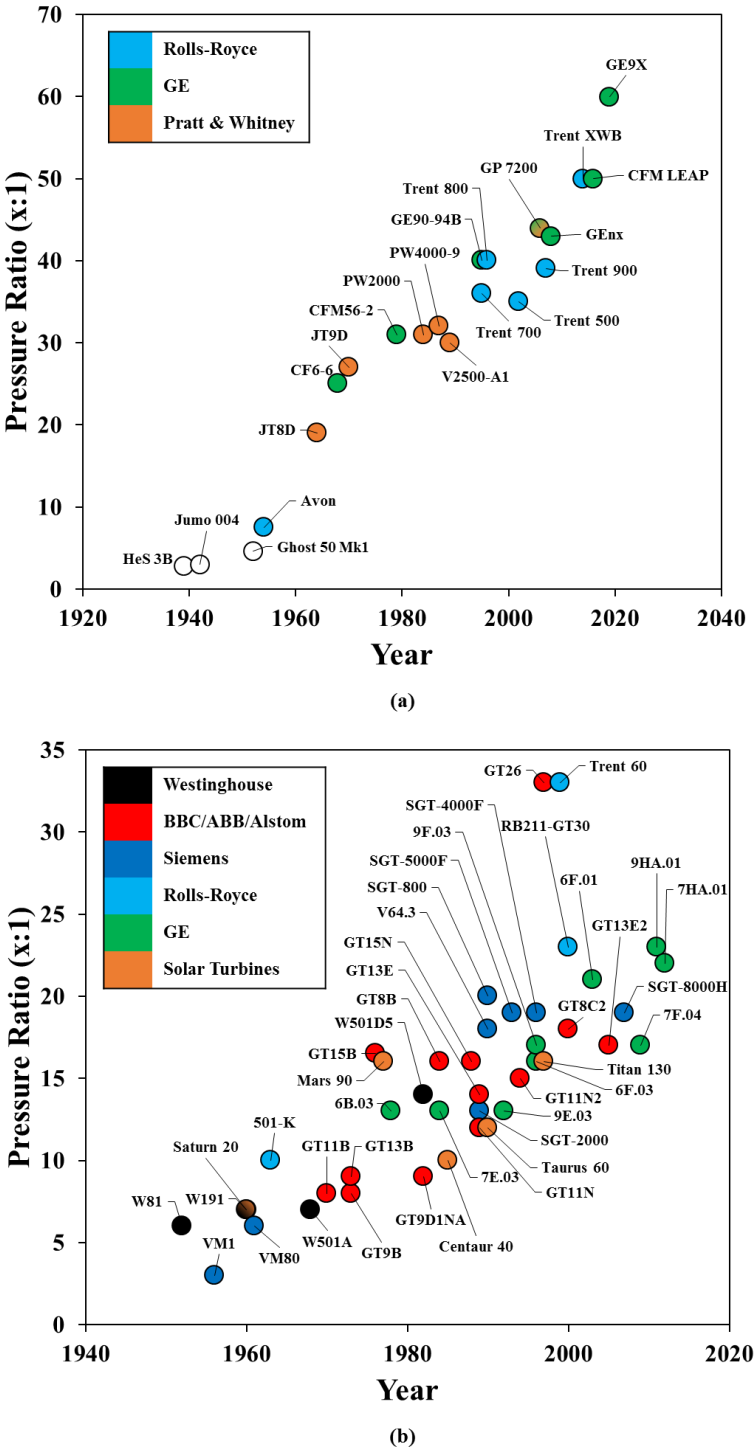

Figure 1.7: Increase of compressor pressure ratio through the years for (a) aerospace and (b) industrial gas turbine engines

The limit to which the temperature ratio can be increased depends on the metallurgical limit of the components that make up the turbine. An increase in the temperature ratio can only be achieved by increasing $T_{3,}$ the turbine entry temperature (TET); T_1, the temperature of the air entering the compressor, is controlled by the environment and cannot be altered. Modern gas turbine engines operate at a TET above the melting point of their components, with air from the compressor supplied to cool the turbine.

The use of compressor air for cooling comes with a performance penalty for the engine. It is therefore crucial to avoid superfluous cooling flow.

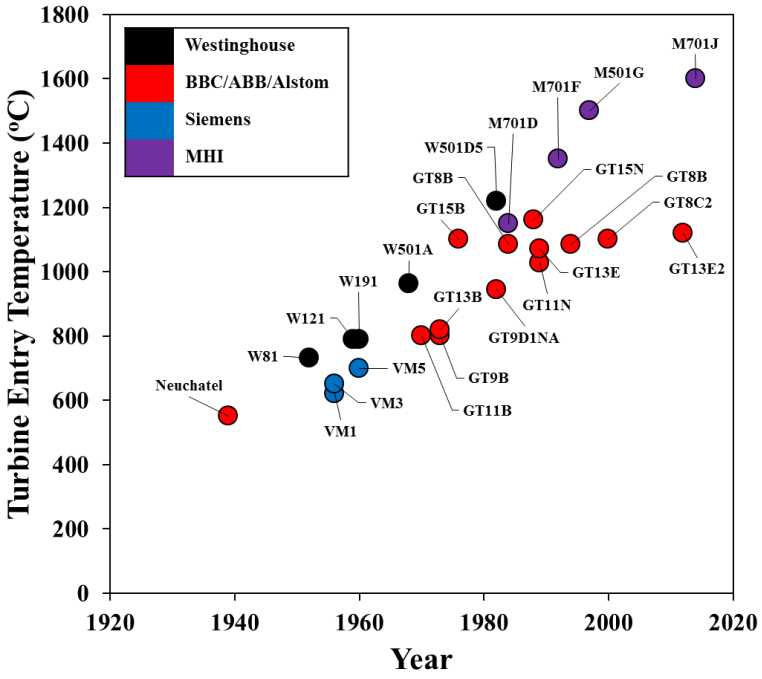

Figure 1.8: Increase of turbine entry temperature (TET) of industrial gas turbine engines

1.3 Secondary Air System and Hot Gas Ingress

The supply of cooling flow from the compressor to the components of the turbine is achieved through the secondary air system (SAS). Figure 1.9 shows the flow of cooling air through a typical turbine SAS. Cooling flow is directed not only to the vanes and blades but also to the cavities (also referred to as wheel-spaces) formed between stationary and rotating discs. Hot gas from the mainstream flow-path (referred to as the annulus) can be ingested into the wheel-space as a result of differences between the pressure in the annulus and that in the wheel-space.

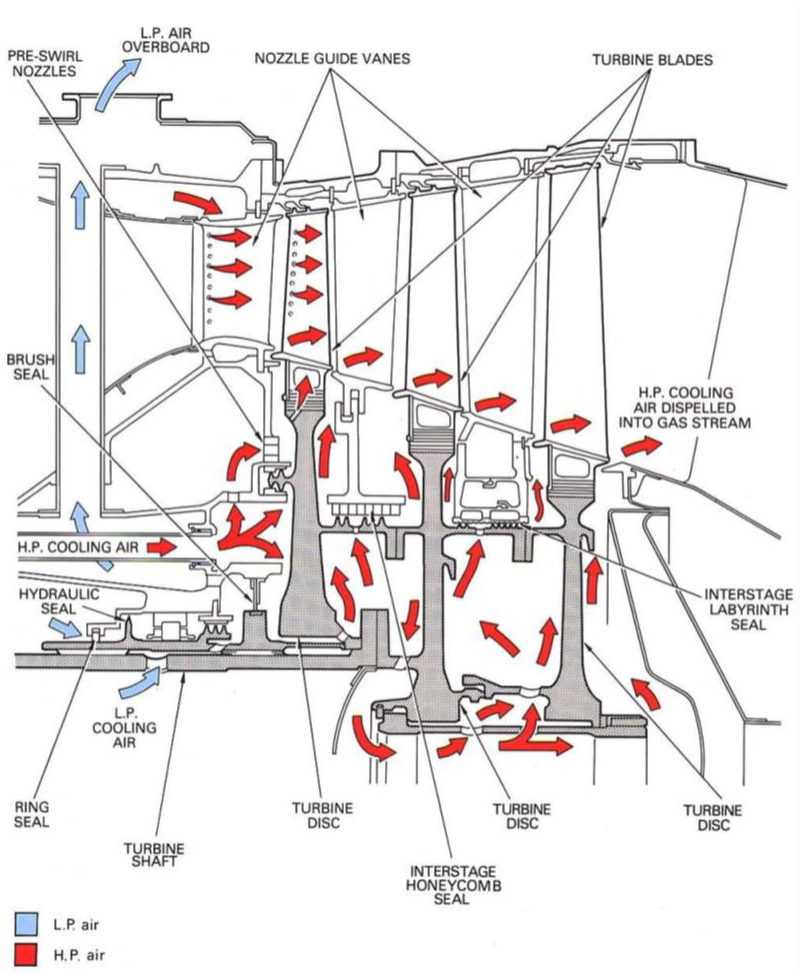

Figure 1.9: A typical turbine cooling system, also called the secondary air system (SAS), and its intricate cooling air passages (from Rolls-Royce (1996))

As shown in Figure 1.10, the stationary vanes and rotating blades create a circumferential distribution of pressure radially outward of the wheel-space shroud, upstream and downstream of the rotor. The steady circumferential distribution of pressure created by the vanes is known to be the cause of ingress into the upstream wheel-space; ingress occurs where the pressure in the annulus is higher than that in the wheel-space and egress occurs where it is lower. This type of ingress is called *externally-induced (EI) ingress* and under typical engine operating conditions its effects dominate the ones of the other types of ingress.

In the absence of any external circumferential pressure variation ingress can still occur due to rotational effects. This mechanism is *called rotationally-induced (RI) ingress*. The rotating fluid in the wheel-space creates a radial pressure gradient which can cause the pressure to drop below that of the mainstream flow in the annulus. This causes the egress of fluid near the rotating disc, where the centrifugal effects are the greatest; this is often referred to as the *disc-*

pumping effect. Ingress of external fluid through the rim-seal occurs near the stator disc in order to conserve radial mass flow.

Some speculate that ingress into the downstream wheel-space is caused by the unsteady pressure variation created by the rotating blades. Others speculate that the steady pressure variation created by the downstream vane bow-wave could also have a strong influence on ingress. In Chapter 4 of this thesis experimental evidence are provided showing that the downstream wheel-space of the rig used is dominated by *rotationally-induced (RI) ingress*.

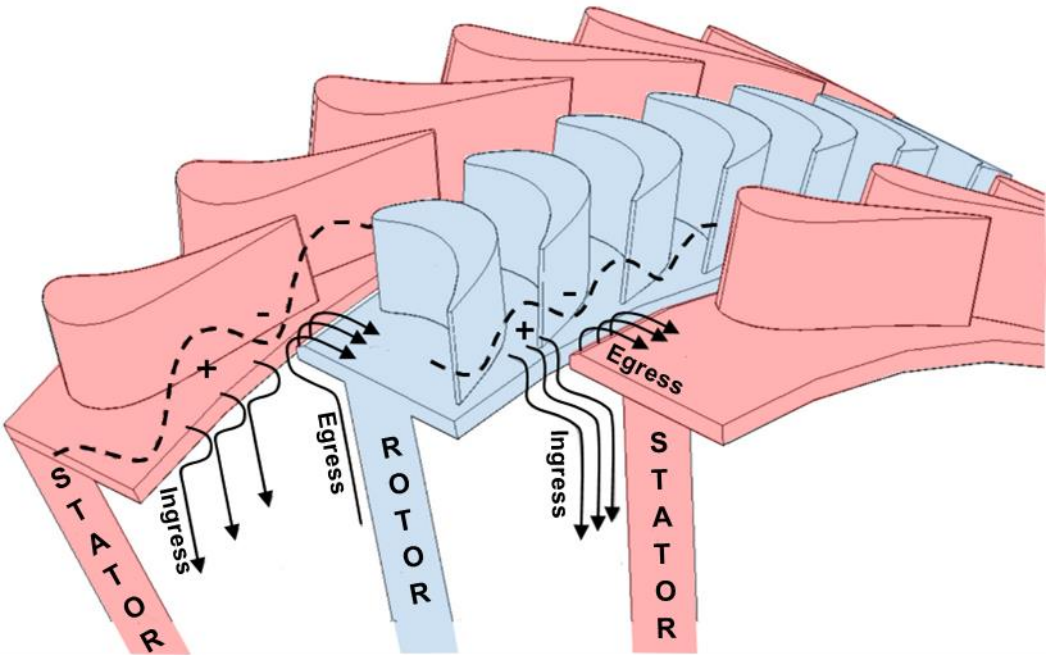

Figure 1.10: Circumferential variation of static pressure in the annulus of turbines indicating regions of ingress and egress - red highlight: stationary components; blue highlight: rotating components

1.3.1 Rim-Seals

Rim-seals are fitted to the periphery of the stators and rotors, as shown in Figure 1.11, to minimise ingress and therefore reduce the amount of cooling flow (most commonly referred to as sealing or purge flow) required to seal the wheel-space and cool the discs. Rim-seal designs vary depending on the engine; older engines usually feature single and double radial-clearance seals whereas modern engines featuring more advance angel-wing seals (see Figure 1.12).

There is a growing trend within industry to design rim-seals using advanced computational fluid dynamics (CFD). However, simulations of the complex, three-dimensional flows in the

annulus and wheel-spaces are computationally expensive, time consuming, and require significant insight into rotating flow and experimental validation. To improve rim seal designs and the efficient use of sealing flow, test rigs operating at near-engine as well as more benign conditions are required. Experimental facilities simulating engine conditions offer a realistic testing environment, while rigs operating at lower rotational speeds have the advantages of improved instrumentation-density, accuracy, flexibility and expedience, and lower cost and risk.

Chapter 3 discusses the design of the University of Bath facility used to fundamentally investigate ingress into the wheel-spaces upstream and downstream of a rotor disc. Despite the rig operating at lower than engine conditions ($Re_{\Phi} \sim 10^6$, annulus Mach number ~ 0.4), the flow structure in the wheel-spaces is set in such a way (see Chapter 3, Section 3.1.1) that is representative of the flow structure expected in an engine. The experimental data from the rig, in conjunction with theoretical modelling methods and CFD, not only allow for a better understanding of the fluid mechanics of ingress but also enable an efficient method of ranking and quantifying the performance of various rim-seal geometries for the engine designer.

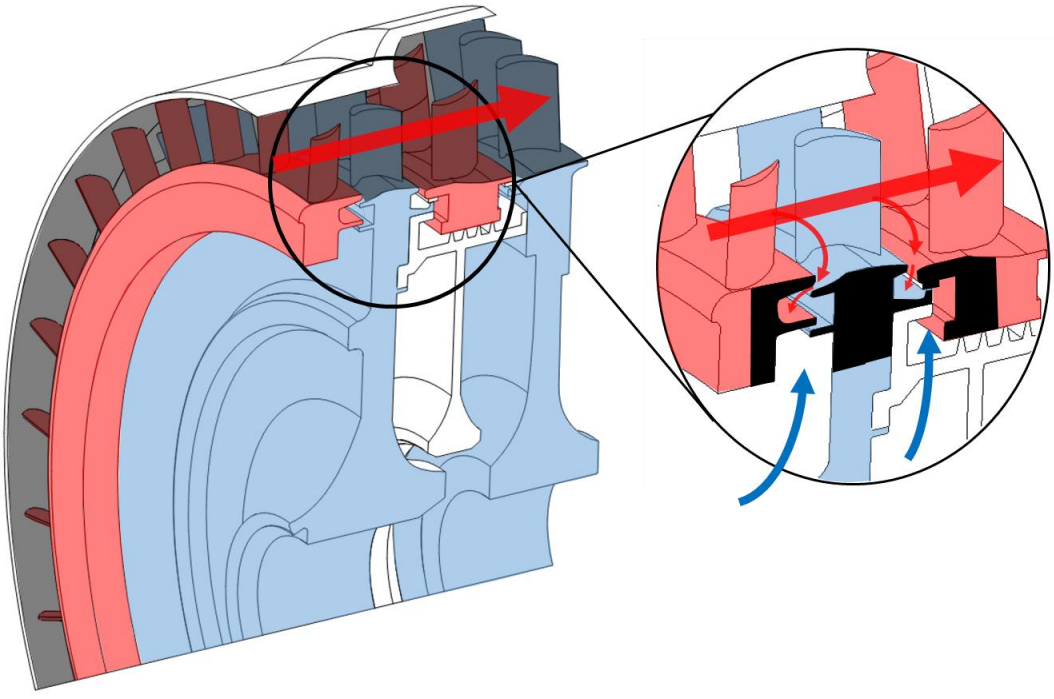

Figure 1.11: Rim-seals fitted in the upstream and downstream wheel-spaces of a 2-stage turbine – red highlight: stationary components; blue highlight: rotating components: red arrows: mainstream flow; blue arrows: sealing flow

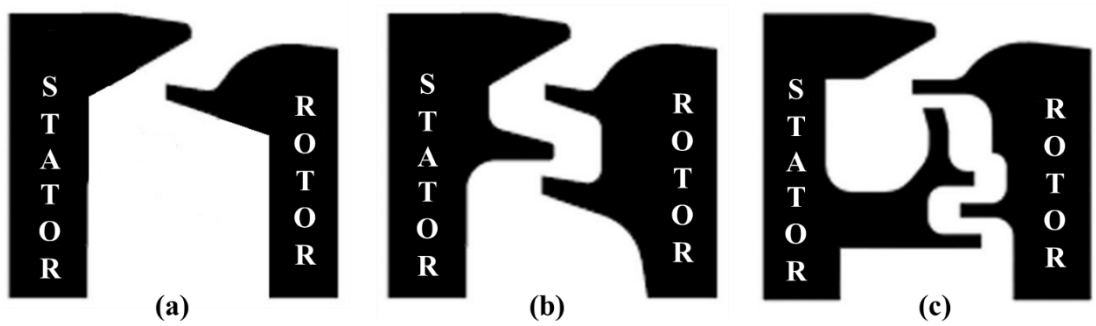

Figure 1.12: Realistic rim-seal geometries - (a) single radial-clearance seal; (b) double radial-clearance seal; (c) angel-wing seal (adapted from Scobie *et al.* (2015))

1.4 Thesis Aim and Objectives

The aim of this thesis is to investigate the fundamental fluid mechanics of ingress through generic and advanced rim-seal geometries in an upstream and downstream wheel-space.

This is to be realised through a series of objectives listed below:

i. **To design, build and commission a new, highly-instrumented, 1.5-stage experimental facility. The new facility is to operate at lower than engine conditions to allow for instrumentation access, low cost and risk whilst simulating the flow structure expected to be found in the wheel-space of an engine.**
ii. **To measure pressure in the annulus at various locations on the hub and shroud in order for the driving mechanism for ingress into the upstream and downstream wheel-spaces to be identified. These measurements are to be taken for a range of rig operating conditions.**
iii. **To measure CO_2[1] concentration on the stator wall and rotating core so that the flow structure in the two wheel-spaces can be identified. These measurements are to be taken for a range of sealing flow rates.**
iv. **To measure static and total pressure in both wheel-spaces in order for the radial variation of the swirl ratio and pressure to be established and the flow structure to be further investigated. These measurements are to be taken for a range of sealing flow rates.**
v. **To measure CO_2 concentration in both wheel-spaces in order to evaluate the performance of generic as well as Siemens proprietary rim-seal geometries.**

[1] CO_2 is used as a tracer gas for the purpose of seeding the sealing flow in an experiment where the annulus flow remains unseeded and the amount of ingress is evaluated by measuring the dilution between the two flows at various locations in the wheel-spaces.

vi. **To compare experimental measurements with theoretical predictions.**

vii. **To rank the performance of Siemens proprietary seals.**

1.5 The Contribution to Knowledge

The work described in this thesis contributes to the knowledge in the subject of hot gas ingestion into gas turbine engine rotor-stator systems by:

i. **Presenting the design of a new, highly instrumented and versatile 1.5-stage gas turbine test facility that has the capability of simulating the flow structure found in the wheel-spaces of gas turbine engines whilst operating at lower Mach numbers and rotational Reynolds numbers than the engine. These design characteristics make the rig ideal for fundamental studies of ingress in an upstream and a downstream wheel-space and for performance studies of advanced rim-seals designed in industry.**

ii. **Providing unprecedented experimental measurements of CO_2 concentration in the rotating core in addition to CO_2 concentration, pressure and swirl ratio measurements on the stator surface that confirm the expected flow structure in the upstream wheel-space and, for the first time, show that the flow structure in the downstream wheel-space is identical to the one in the upstream.**

iii. **Investigating for the first the driving mechanism for ingress in the downstream wheel-space and through measurements of CO_2 concentration showing that rotationally-induced (RI) ingress occurs.**

iv. **Demonstrating that a simple theoretical orifice model can successfully and with great accuracy describe the variation of ingress with sealing flow rate in the upstream and downstream wheel-spaces of an engine fitted with both generic and complex rim-seals.**

v. **Informing the design of future, more advanced rim-seals by experimentally identifying through measurements of CO_2 concentration, pressure and swirl ratio the effect of key geometric features on ingress into the downstream wheel-space.**

1.6 Thesis Outline

Chapter 1 gives an introduction to the development of the gas turbine engine. The operating cycle of the core components of the engine is described and the problem of hot gas ingress and how this affects engine performance is introduced. The significance of using rim-seals to minimise ingress and therefore maximise performance is discussed and the importance of experimental studies in turbine test facilities in designing more efficient seals is explained. Finally, the aim and objectives and the contribution to the knowledge of ingress of the work included in this thesis along with a list of publications are provided.

Chapter 2 presents a literature review related to ingress in rotor-stator systems of gas turbine engines. The early ingress research is discussed followed by specific research regarding the flow structure in the wheel-space and the driving mechanisms for ingress. A theoretical model for ingress as well as CFD research are also discussed. The literature review chapter concludes with a review of some modern, current experimental facilities and with the advantage of the research conducted at the University of Bath.

Chapter 3 provides the design features and operating capabilities of a new 1.5-stage experimental facility. Special reference is made to the instrumentation versatile capabilities of the new facility. An uncertainty analysis of the experimental results is provided along with important commissioning measurements.

Chapter 4 discusses the flow structure in the upstream and downstream wheel-spaces and its effect on the concentration measurements. The flow structure is investigated using measurements of concentration effectiveness, swirl and pressure taken in both the upstream and downstream wheel-spaces for the case of single and double radial-clearance seals. The experimental results are compared with predictions obtained from a theoretical orifice model and good agreement is observed. Comparisons between the measurements in both wheel-spaces for the same rim seal geometry are presented and used to enable a first indication of the driving mechanism for ingress in the downstream wheel-space. This is further investigated by conducting an experiment under conditions of rotationally-induced ingress. The results of this test show that for the blade and vane geometry featured in the rig the downstream wheel-space is dominated by rotationally-induced ingress.

Chapter 5 presents three parametric studies examining the effect of various geometrical changes on the performance of a range of Siemens-proprietary rim-seals in the downstream wheel-space. The first study examines the effect of two different sized cut-outs on the performance of single radial-clearance seals. The second study investigates the potential performance increase of single angel-wing seals by the addition of a second winglet and an

inner radial-clearance seal. The last study explores the effect of a buffer cavity on the performance of angel-wing seals. The chapter concludes with the ranking of the various rim-seals tested based on performance.

Chapter 6 summarises the conclusions of this thesis and provides recommendations for future experimental investigations.

1.7 Publications

The work included in this thesis has resulted in a paper that was both presented at the 2016 ASME IGTI conference and accepted for journal publication. The author has also conducted experiments which will form the basis of four papers that are to be submitted for conference and journal publication in autumn 2016 and beginning of 2017.

Publications:

- **Patinios, M.**, Scobie, J. A., Sangan, C. M., Owen, J. M., Lock, G. D., 2016, *"Measurements and Modelling of Ingress in a New 1.5-Stage Turbine Research Facility"*, ASME Paper No. GT2016-57163, Journal of Engineering for Gas Turbines and Power, 139(1), 012603-012603.

Future publications:

- **Patinios, M.**, Scobie, J. A., Sangan, C. M., Lock, G. D., *"Measurements of Ingress in Upstream and Downstream Turbine Wheel-Spaces"*.
  European Turbomachinery Conference in Stockholm, 3-7 April 2017.

- Tang H., Cho, G., **Patinios, M.** Scobie, J. A., Sangan, C. M., Owen, J. M., Lock, G. D., *"Effect of Ingress on Rotor Temperature in a 1.5-Stage Gas Turbine Rig"* .
  To be submitted to the ASME Journal of Turbomachinery, January 2017.

- Scobie, J. A., Hualca, P. F., **Patinios, M.**, Sangan, C. M., Owen, J. M., Lock, G. D., *"Re-Ingestion of Upstream Egress in a 1.5-Stage Gas Turbine Rig"*, ASME Paper No. GT2017-64620
  Submitted to the ASME 2017 Turbo Expo.

- **Patinios, M.**, Scobie, J. A., Sangan, C. M., Owen, J. M., Lock, G. D., *"Driver for Ingress in the Downstream Wheel-Space of a Gas Turbine"*.
  In progress.

Chapter 2: Literature Review

2.1 Rotating Disc in Initially Stationary Fluid (Free Disc)

The first case of rotating flow investigated is the free disc. This involves a disc of radius b spinning in free air with a uniform angular velocity Ω as shown in Figure 2.1. In order for the no-slip condition on the surface of the disc to be satisfied, the fluid gains a tangential component of velocity u_Φ which varies with distance from the disc surface from $V_\Phi = \Omega r$ at $z = 0$ on the surface of the disc to $V_\Phi = 0$ in the free stream outside the boundary layer. Shear between the fluid and the rotating disc generates centrifugal forces which pump the flow radially outwards resulting in a radial component of velocity V_r with $V_r = 0$ at both $z = 0$ and outside of the boundary layer in the free stream. This radial outflow of fluid is most commonly known as the free disc "pumping effect". The radial outflow necessitates an axial entrainment of fluid so that conservation of mass is satisfied, giving rise to an axial component of velocity, V_z.

The flow inside the boundary layer can be either laminar or turbulent depending on whether the local Reynolds number Re_Φ has reached a critical value. A study performed by Gregory *et al.* (1955) identified this critical value as $Re_{\Phi,\,critical} \approx 2 \times 10^5$. Usually near the axis of rotation the flow is laminar with turbulent flow occupying the higher radii.

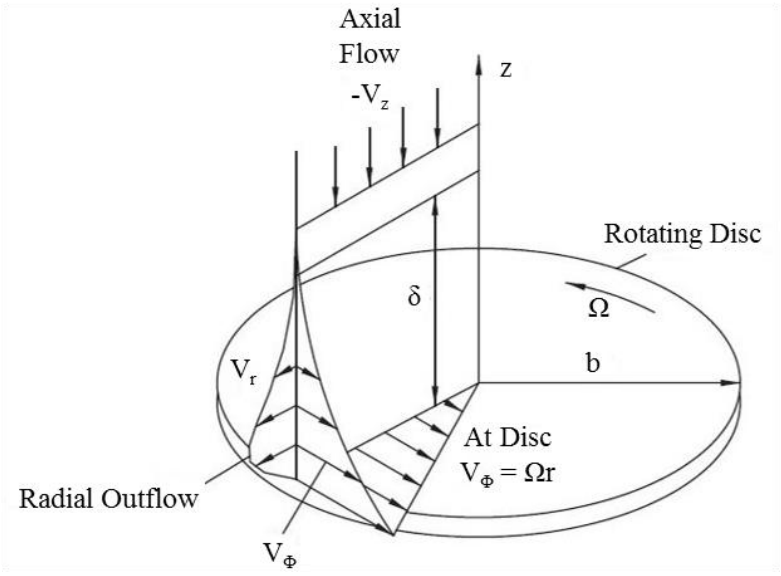

Figure 2.1: The profiles of the tangential (V_Φ), radial (V_r) and axial (V_z) components of velocity in the case of a free disc rotating in an initially stationary fluid (adapted from Childs (2011))

2.2 Stationary Disc Adjacent to Rotating Fluid

The flow structure associated with the case of a stationary disc positioned adjacent to a rotating fluid is shown in Figure 2.2. The flow rotating outside the boundary layer is in equilibrium under the influence of the centrifugal force which is balanced by a radial pressure gradient. The tangential velocity of the fluid V_Φ decreases near the disc surface resulting into a corresponding decrease in the local centrifugal force. The radial pressure gradient, being independent of axial distance away from the disc surface, causes a radial inflow near the disc surface towards the axis of rotation with a radial component of velocity, V_r. In order for conservation of mass, to be satisfied this radial inflow necessitates an axial flow away from the disc surface with an axial component of velocity V_z.

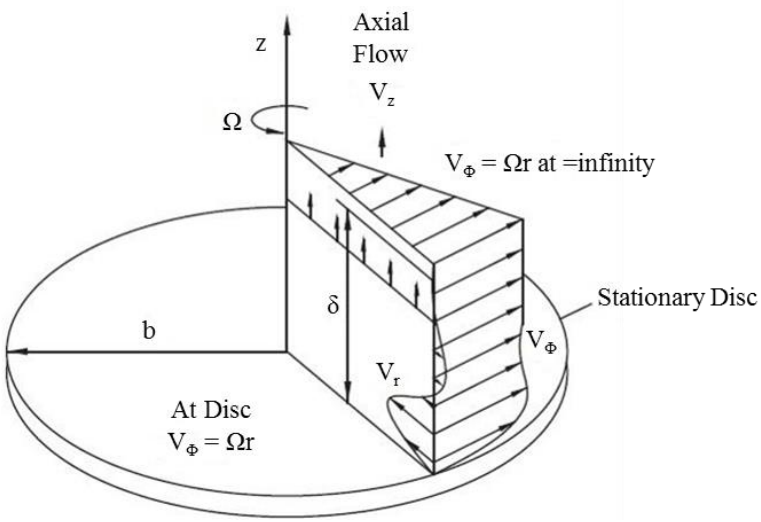

Figure 2.2: The profiles of the tangential (V_Φ), radial (V_r) and axial (V_z) components of velocity in the case of a stationary disc adjacent to a rotating fluid (adapted from Childs (2011))

2.3 Rotor - Stator Systems

Figure 2.3 shows a rotor-stator system most commonly found in gas turbine engines consisting of a shrouded stationary disc (or stator) and a shrouded rotating disc (or rotor) with radius *b*, separated by an axial clearance *S*, to form a cavity known as the wheel-space. Despite the rotor-stator system being a combination of the simple cases of the free disc and the stationary disc mentioned in the two preceding sections, the fluid mechanics occurring in the wheel-space are much more complicated than the ones of the simple cases.

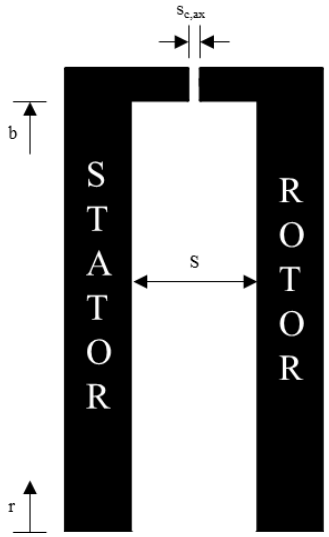

Figure 2.3: A schematic of a rotor – stator system including important geometrical dimensions

The first to discuss the flow structure in the wheel-space of a rotor-stator system was Batchelor (1951). Batchelor's work suggested that boundary layers are formed on the surface of the rotor and stator discs. A core of inviscid fluid, which rotates at a fraction of the rotor disc speed, exists between the two boundary layers. Fluid moves radially outward in the rotor boundary layer and inwards in the stator boundary layer. Over much of the wheel-space, fluid moves axially across the rotating core, from the stator boundary to the one on the rotor, so that conservation of mass is satisfied. The velocity profiles corresponding to the Batchelor flow in a rotor-stator system are shown in Figure 2.4 (a) to (c).

Contrasting the proposition of Batchelor, Stewartson (1953) suggested that the flow in a rotor-stator system is similar to that of a free disc. More specifically Stewardson concluded that the tangential velocity component of the flow in the rotor boundary layer varies with axial distance away from the rotor disc surface from $V_\Phi = \Omega r$ on the surface of the disc to $V_\Phi = 0$ in the free stream outside of the boundary layer. A rotating core does not exist neither does a stator boundary layer. The velocity profiles corresponding to the Stewardson type of flow in a rotor-stator system can be seen in Figure 2.4 (d) to (f).

The Batchelor-Stewardson paradox remained unresolved for more than a decade until initially numerical studies and later experiments finally provided an explanation. The general conclusion was that both types of flow can exist depending on the flow conditions. In the absence of any superposed flow, the flow structure in the wheel-space resembles that proposed by Batchelor. When the superposed flow becomes greater than the free disc entrainment rate, the flow structure in the wheel-space resembles the one proposed by Stewardson.

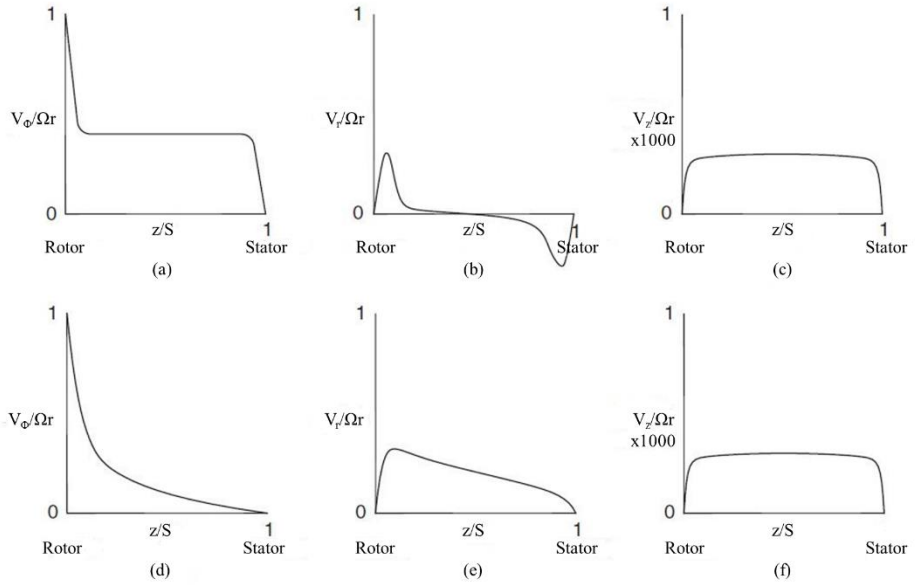

Figure 2.4: Velocity profiles for Batchelor (a to c) and Stewardson (d to f) flow in a rotor-stator system: (a and d) tangential velocity profile, (b and e) radial velocity profile, (c and f) axial velocity profile (adapted from Childs (2011))

The flow structure in rotor-stator systems can change depending on the geometry of the wheel-space and rotational speed of rotor disc. An important study addressing the effect of these parameters is Daily and Nece (1960). This study categorises the flow in the wheel-space into four distinct regimes which are a function of the gap ratio G (= S/b) and the rotational Reynolds number Re_Φ, as shown Figure 2.5. These regimes are the following:

- **Regime 1**: This regime is characterised by a small stator-rotor clearance, laminar flow and merged boundary layers.
- **Regime 2**: This regime is characterised by a large stator-rotor clearance, laminar flow and separated boundary layers. A rotating core of inviscid fluid between the stator and rotor boundary layers exists in this regime.
- **Regime 3**: This regime is characterised by a small stator-rotor clearance, turbulent flow and merged boundary layers.
- **Regime 4**: This regime is characterised by a large stator-rotor clearance, turbulent flow and separated boundary layers with a rotating core of inviscid fluid in between. Gas turbine engines operate in this regime. The new 1.5-stage turbine test facility described in Chapter 3 was also designed to operate within this regime so that the flow structure inside its upstream and downstream wheel-spaces is representative of that found in an engine.

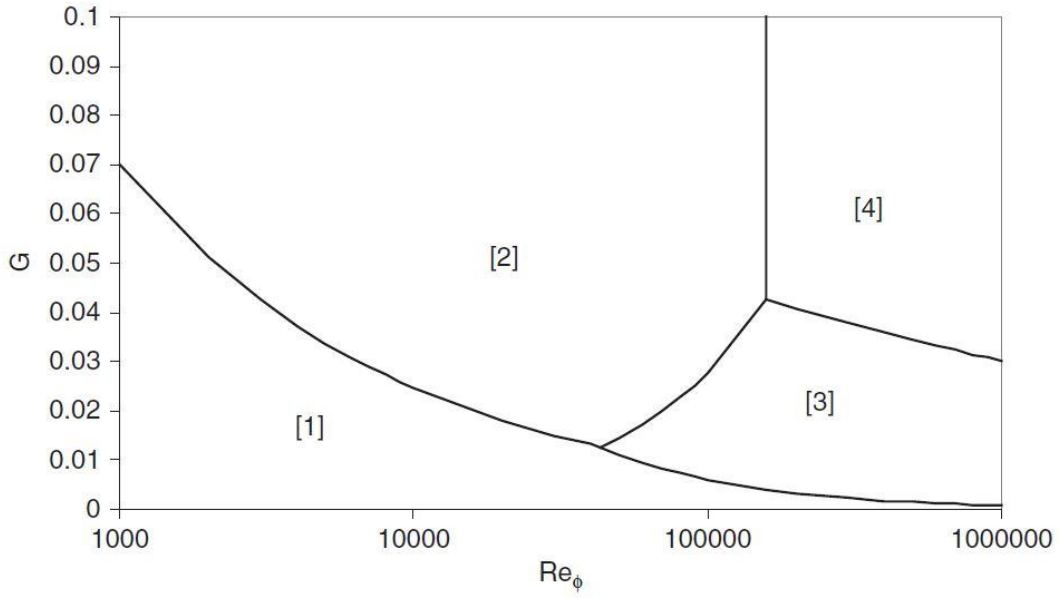

Figure 2.5: Categorisation of flow in the wheel-space of rotor – stator systems based on the gap ratio *G* and the rotational Reynolds number Re_Φ, as proposed by Daily and Nece (1960) (from Childs (2011))

2.4 Flow Structure in Rotor-Stator Systems with Ingress

Figure 2.6 shows the flow structure in the wheel-spaces upstream and downstream of the rotor for the case where there is a superposed radial flow, with swirl, together with ingress through the rim seal. The gap ratio *G*, is large enough to ensure separate boundary layers on the two discs, both of which start at $r = a$. Fluid moves radially outward in the boundary layer on the rotor and inward in the boundary layer on the stator. Over much of the wheel-space, fluid moves axially across the rotating inviscid core from the boundary layer on the stator to that on the rotor. According to the Taylor-Proudman theorem (Childs (2011)) there can be no axial gradients of the tangential and axial components of velocity in an axisymmetric inviscid rotating core, and the radial component must be zero. Importantly, all radial flow is confined to the boundary layers on the rotor and stator.

The superposed flow enters the system through an inner region which extends to $r = r_{in}$, by which point all the available flow has been entrained by the boundary layer on the rotor. In the outer region, some fluid flows from the rotor to the stator and the remainder (with a flow rate equal to that of the superposed flow) leaves the system through the rim-seal. The inner and outer regions are the sources for the flow in the boundary layers on the rotor and stator respectively, and in the radii between these regions the axial flow is from the stator to the rotor.

A complete exploration of the flow structure in the upstream and downstream wheel-spaces is shown for the first time in this thesis.

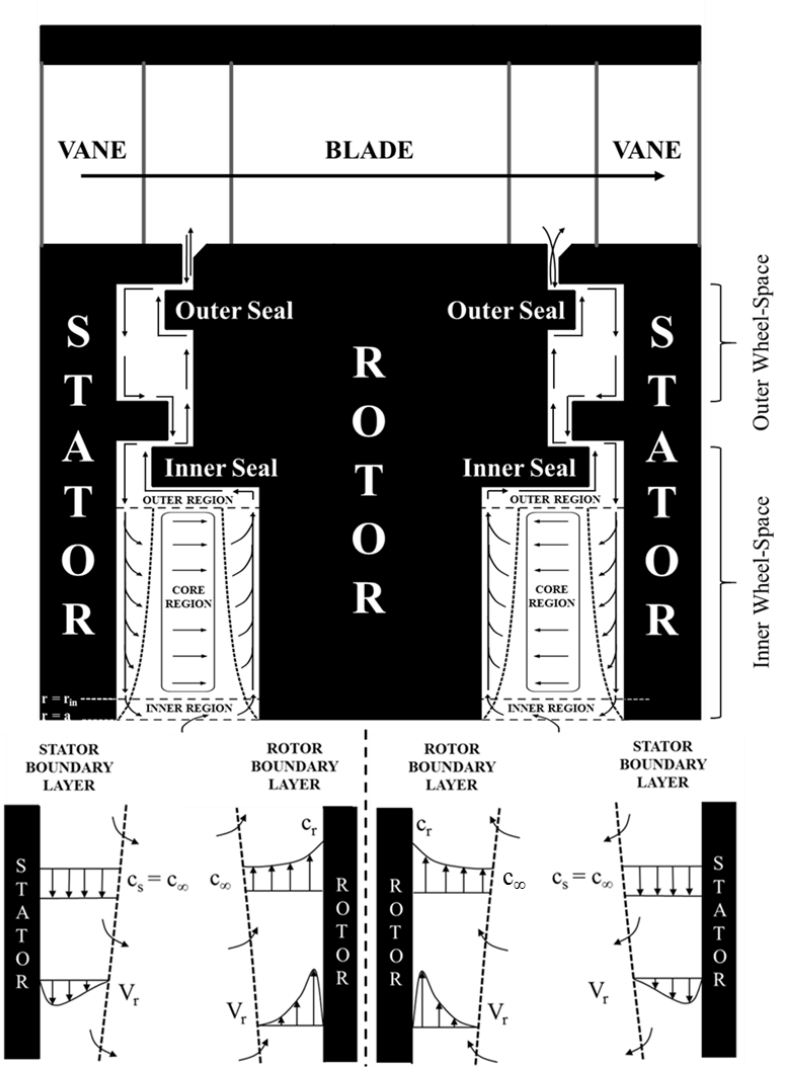

Figure 2.6: Simplified diagram of the flow structure in an upstream and downstream wheel-space with ingress and egress showing concentration and velocity boundary layers on the stator and rotor surfaces

The flow structure in the downstream wheel-space is almost a mirror image of that in the upstream wheel-space. The biggest difference is that in the downstream case the egress from the rotor side creates an axisymmetric jet (or fluid 'barrier') that the ingress stream tubes in the mainstream flow must cross before fluid is ingested into the wheel-space. The mass flow rate of the egress will be greater, and - as shown by Cho *et al.* (2015) and Mear *et al.* (2015) - the concentration of the CO_2 tracer-gas in the egress will also be greater, than that in the ingress. The subsequent exchange of angular momentum and chemical species (that is, CO_2) between the ingress and egress at the entrance to the seal will therefore result in two effects: (*i*) a reduction in the unsteady non-axisymmetric distribution of pressure immediately outside the seal clearance; and (*ii*) an increase in the level of CO_2 concentration of the ingested fluid. Relative to the upstream case, both these effects will create an increase in the measured sealing effectiveness in the downstream wheel-space. As the sealing flow rate is increased and the

ingress is consequently reduced, these effects will result in an improved effectiveness for the downstream seal. By attenuating the pressure asymmetry in the flow near the seal clearance will tend to create combined ingress (see Section 1.5.3) and, in the limit, rotationally-induced ingress (see Section 1.5.2).

2.5 Governing Non-Dimensional Parameters for Ingress

The ingress of fluid through the rim-seal is an inertial phenomenon driven by differences in pressure, whereas the flow inside the wheel-space is a viscous phenomenon controlled by the boundary-layers on the rotor and stator. In this section the most important non-dimensional parameters used in literature to describe ingress in rotor-stator systems are provided.

The rotational Reynolds number, Re_Φ is the ratio of the inertial to the viscous effects of the flow in the wheel-space and is defined as

$$\boldsymbol{Re_\Phi = \frac{\rho \Omega b^2}{\mu}} \qquad \textbf{(Eq. 2.1)}$$

where Ω the rotational speed of the rotor disc and b the radius of the rim-seal.

The non-dimensional sealing flow rate supplied to the wheel-space has been traditionally defined as

$$\boldsymbol{C_{w,0} = \frac{\dot{m}_0}{\mu b}} \qquad \textbf{(Eq. 2.2)}$$

where $\dot{m}_0$ the mass flow rate of the sealing flow.

The geometric clearance of the various rim-seals is non-dimensionalised using the seal clearance ratio, G_c defined as

$$\boldsymbol{G_c = \frac{s_{c,ax}}{b}} \qquad \textbf{(Eq. 2.3)}$$

where $s_{c,ax}$ the axial clearance of the rim-seal.

The sealing flow parameter Φ_0 combines the effects of $C_{w,o}$, G_c and Re_Φ into a single variable:

$$\boldsymbol{\Phi_0 = \frac{C_{w,0}}{2\pi G_c Re_\Phi} = \frac{U}{\Omega b}} \qquad \textbf{(Eq. 2.4)}$$

where U is the bulk mean radial velocity of sealing air through the seal clearance. Both Re_Φ and $C_{w,0}$ include viscous terms which cancel, and it is important to understand that Φ_0 is therefore an inviscid parameter depending only on inertial effects. In the subsequent chapters

of this thesis, Φ_0 will be used instead of $C_{w,0}$ to describe the amount of sealing flow supplied to the wheel-space.

The swirl ratio of the fluid in the inviscid core between the boundary layers in the wheel-space is defined as

$$\boldsymbol{\beta = \frac{V_{\Phi,\infty}}{\Omega r}} \qquad \textbf{(Eq. 2.5)}$$

All radial flow occurs inside the boundary layers, and the value of β adjusts to satisfy the continuity of the flow rate in the boundary layers.

The structure of the flow in the wheel-space is determined by the turbulent flow parameter (governing a viscous phenomenon), which is defined as

$$\boldsymbol{\lambda_T = C_{w,0} Re_{\Phi}^{-0.8}} \qquad \textbf{(Eq. 2.6)}$$

For the free disc, where there is no stator, the entrained flow rate is characterised by $\lambda_T \approx 0.22$. It follows from Eq. 2.4 and Eq. 2.6 that

$$\boldsymbol{\lambda_T = 2\pi G_c Re_{\Phi}^{0.2} \Phi_0} \qquad \textbf{(Eq. 2.7)}$$

In the subsequent chapters of this thesis and whenever measurements related to the flow structure in the wheel-space are presented (i.e. pressure and swirl ratio measurements) λ_T will be used instead of Φ_0 to describe the amount of sealing flow supplied to the wheel-space.

2.6 Driving Mechanisms for Ingress

2.6.1 Externally-induced (EI) ingress

Externally-induced ingress (Owen (2010b)) occurs due to a circumferential pressure asymmetry in the annulus caused by the flow passing over the vanes and blades. *Ingress* occurs at the locations where the external pressure in the annulus is greater than that in the wheel-space and *egress* occurs where it is lower. EI ingress is the dominant mechanism for ingress in gas turbine engines.

EI ingress has been extensively studied since the late 1980s at various institutions such as the *University of Sussex*, *Aachen University*, *Arizona State University*, *University of Surrey*, *Ohio State University* and the *University of Bath*. A thorough review of computational, theoretical and experimental modelling of EI ingress (and ingress driven by the other two mechanisms mentioned in the following sections) is provided by Scobie *et al.* (2016). Only a selection of seminal studies will be discussed here.

Chew *et al.* (1994) investigated the effect of axial Reynolds number Re_w and vane axial position relative to the seal clearance on ingress into the wheel-space of a single-stage test facility. The rig featured a stator disc with 18 vanes and a bladeless rotor. Measurements of pressure on the vane platform in the annulus showed that the amplitude of the peak-to-trough difference of the pressure asymmetry in the annulus increased with Re_w but decreased with distance from the vane trailing edge. Measurements of N_2O[2] concentration in the wheel-space taken for different Re_w and Re_Φ values and at various vane axial positions showed that ingress is predominantly driven by the circumferential pressure variation in the annulus with the disc pumping effect becoming significant only at very small values of Re_w.

Bohn *et al.* (2000) examined the effect of rotating blades on ingress for various axial and rotational Reynolds number conditions and sealing flow rates. Pressure measurements taken in the annulus showed that the presence of the blades significantly increased the peak-to-trough magnitude of the circumferential pressure downstream of the stator vanes. However, no solid conclusion could be drawn on the effect of the blades on the concentration effectiveness in the wheel-space; for one rim-seal configuration effectiveness deteriorated with blades and for the other improved. In order to shed more light on the effect of blades on ingress an unsteady 3D CFD simulation was performed for the rim-seal geometry that showed an increase in effectiveness when blades were present. The results of the simulations indicated an increase in static pressure, above the seal clearance, upstream of the blades, which had the effect of reducing the amount of egress from the wheel-space. This reduction of egress caused a subsequent reduction of ingress.

The effect of the vane-blade interactions on the annulus pressure field and hence ingress was further investigated by Hills *et al.* (2002) using a 3D unsteady CFD simulation performed on a segment of the test rig described by Chew *et al.* (1994). In the CFD model the vanes resembled the ones used in the rig but the blades were simulated using pegs. The simulation results showed that the unsteadiness due to the rotor pegs had a considerable and adverse effect on ingestion despite generating a smaller circumferential pressure asymmetry than the one generated by the stator vanes.

Bohn and Wolff (2003) examined the effect of sealing flow rate on the effectiveness of four different rim-seal geometries under the influence of various external flow circumferential pressure asymmetries, using CO_2 concentration measurements. The results of the measurements showed that effectiveness increased as the sealing flow rate increased and that

[2] N_2O is used as a tracer gas for the purpose of seeding the sealing flow in an experiment where the annulus flow remains unseeded and the amount of ingress is evaluated by measuring the dilution between the two flows at various locations in the wheel-spaces.

for the same sealing flow rate, the effectiveness reduced as the magnitude of the peak-to-trough difference of the pressure asymmetry in the annulus ΔC_p increased. The variation of the minimum amount of sealing flow rate required to prevent ingress $C_{w,min}$ was shown to increase linearly with ΔC_p for all rim seal geometries tested and be dependent on G_c, ΔC_p, Re_{c1}[3] and an empirical constant. The empirical constant can only be determined through experiments, will be different for each rim-seal geometry and will depend on the position at which the external flow circumferential pressure asymmetry is evaluated.

Roy *et al.* (2005) conducted an experimental study of ingress in the wheel-space of a test facility featuring a stator disc with 22 vanes and a rotor disc with 28 blades. The experiments involved measurements of steady and unsteady static pressure and CO_2 concentration. The results of the unsteady pressure measurements showed that the annulus pressure field contained an unsteady, blade-related component which near the rim-seal was greatly affected by the amount of egress. A spectral analysis of the unsteady measurements taken in the rim-seal revealed spikes at lower than the blade passing frequency which the authors attributed to large scale structures similar to the ones reported by Jakoby *et al.* (2004) (for details see Section 1.8).

Zhou *et al.* (2010) used measurements of pressure, CO_2 concentration and velocity (using PIV) in order to investigate ingress through three different rim-seal geometries shown in Figure 2.7. The measurements were taken in the test facility described by Roy *et al.* (2005). Figure 2.8 shows the radial distribution of effectiveness in the wheel-space for the three seal geometries tested. For the same amount of sealing flow rate an increase in effectiveness is observed when using a double seal (configurations 2 and 3). For these seals ingress was also shown to be confined in the part of the wheel-space between the outer and inner seals. The results of the PIV measurements revealed that ingress and egress took place at various distinct circumferential regions within the axial clearance of the three seals.

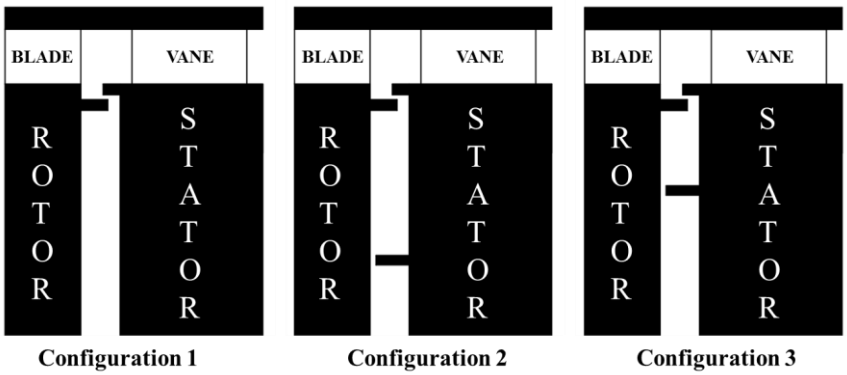

Figure 2.7: Rim seal configurations tested by Zhou *et al.* (2010)

[3] External flow Mach number based on vane exit velocity and flow conditions.

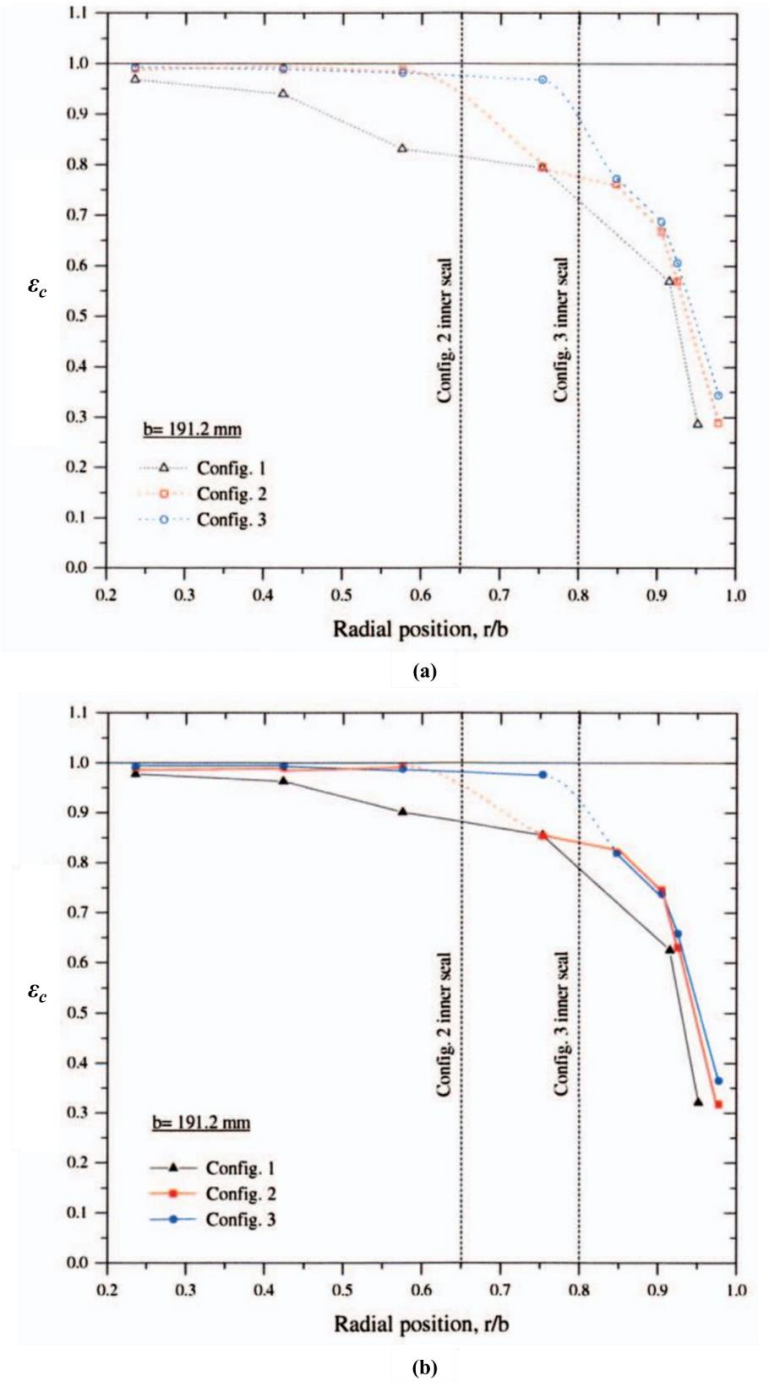

Figure 2.8: Radial distribution of effectiveness for three rim-seal configurations
(a): $Re_w = 1.12 \times 10^5$; $Re_\Phi = 5.86 \times 10^5$; $C_w = 1574$
(b): $Re_w = 9.27 \times 10^4$; $Re_\Phi = 4.63 \times 10^5$; $C_w = 1574$
(adapted from Zhou *et al.* (2010))

Sangan *et al.* (2012a) conducted an extensive study of ingress using measurements of pressure and CO_2 concentration in a single-stage test facility featuring a stator disc with 32 vanes and a rotor disc with 41 symmetrical blades. The experiments were performed at three operating conditions corresponding to 2000, 3000 and 3500 rpm; these generated a maximum

rotational Reynolds number, $Re_\Phi = 9.68 \times 10^5$. Experiments were run at a $C_F = 0.538$ resulting in a maximum axial Reynolds number, $Re_w = 5.21 \times 10^5$ and a Mach number $M = 0.398$. Measurements of the circumferential pressure variation in the annulus taken at various axial and radial locations were provided by the authors. For the same axial location downstream of the vane trailing edge the peak-to-trough non-dimensional pressure difference, ΔC_p in the annulus was found to increase from the vane platform to the outer dimeter of the annulus due to a radial pressure gradient as a result of the swirling motion of the mainstream flow. For both vane platform and outer radius measurements, ΔC_p decreased with axial distance. The effect of the sealing flow rate on the pressure asymmetry was also investigated with the results indicating a decrease in ΔC_p with increase in Φ_0 for the measurements taken in the vane platform. This effect was referred to as the "*spoiling effect*". Using CO_2 concentration measurements the performance of two rim-seal geometries, an axial seal and a single radial-clearance seal was also evaluated, as shown in Figure 2.9 . For both seals the concentration effectiveness, ε_c increased as the sealing flow rate, Φ_0 increased and the wheel-space was pressurised. Using Φ_0 to represent the amount of sealing flow rate supplied to the wheel-space instead of $C_{w,min}$ used in previous studies, the data were collapsed onto single curves showing the EI ingress is independent of Re_Φ. For the same sealing flow rate the performance of the single-radial seal was found to be superior to that of the axial seal.

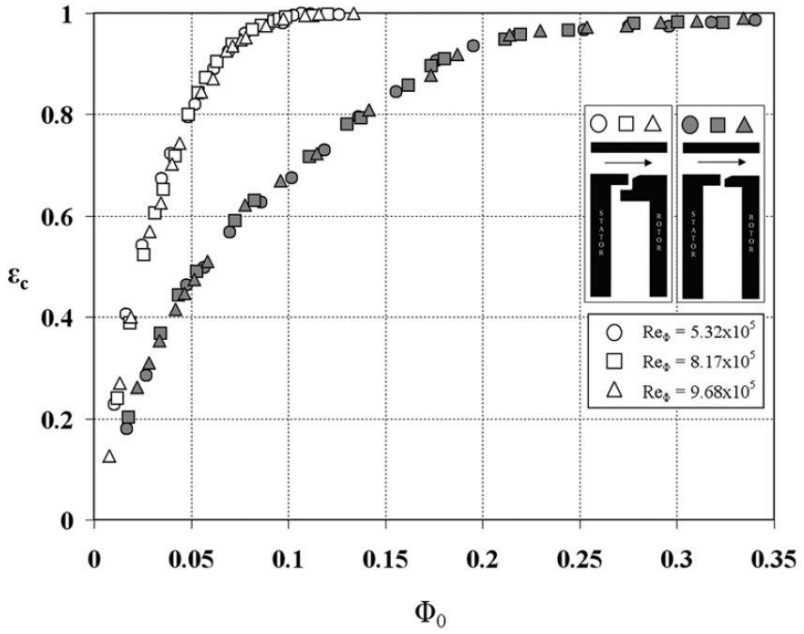

Figure 2.9: Variation of ε_c with Φ_0 for an axial and a single radial clearance seal (from Sangan *et al.* (2012a))

Sangan *et al.* (2013) expanded their previous work by investigating ingress through six different generic rim-seal geometries, shown in Figure 2.10. Comparison of the measurements of the variation of concentration effectiveness with sealing flow rate for all six seals showed that the most effective geometry is the double radial-clearance seal D2. As revealed by the measurements of the radial variation of effectiveness in the wheel-space the superior performance of D2 in the inner wheel-space when compared to S2c (see Figure 2.11) is due to the effect of the buffer cavity to attenuate the pressure asymmetry in the ingested flow and thus constrain ingress predominantly within the outer wheel-space.

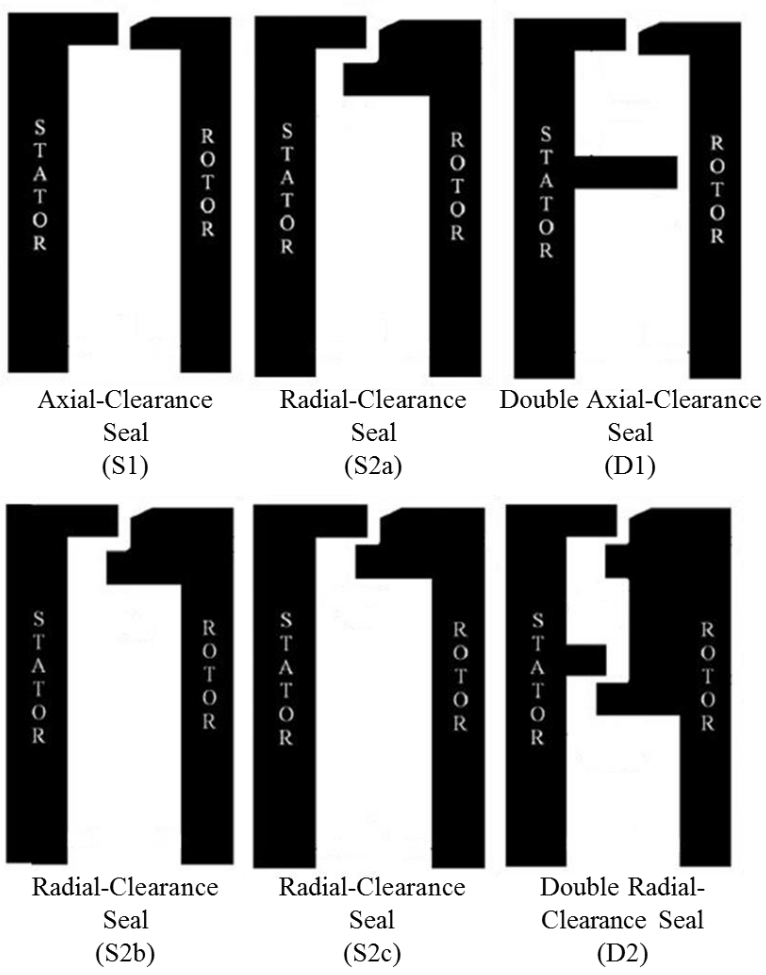

Figure 2.10: Rim seal geometries tested by Sangan *et al.* (2013)

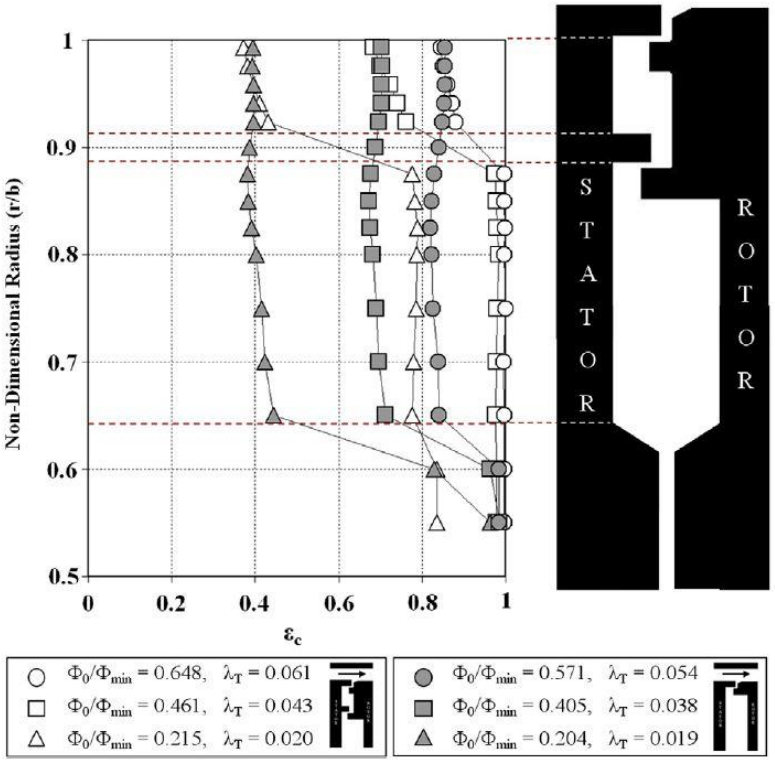

Figure 2.11: Effect of sealing flow rate on radial variation of effectiveness on the stator wall for single and double radial-clearance seals, S2c and D2 respectively. Open symbols correspond to D2; solid symbols correspond to S2c. (from Sangan *et al.* (2013))

The studies mentioned above focus on ingress in the *upstream* wheel-space of a gas turbine; far fewer investigators have conducted detailed studies downstream of the rotor. One of these studies is the one of Balasubramanian *et al.* (2016). The experiments were conducted in a 1.5-stage turbine test facility including a 40-vane upstream and 48-vane downstream stator and a 52-blade rotor. All aerofoil geometries were partial-height, full-length. The upstream wheels-space of this rig was fitted with a double radial-clearance seal whereas the downstream wheel-space was fitted with a double axial-clearance seal as shown in Figure 2.12. The experimental conditions were the following: Re_Φ = 7.35 × 10^5; 8.18 × 10^5; and 9.01 × 10^5 and Re_w = 5.07 × 10^4; 5.64 × 10^4; 6.21 × 10^4. Measurements of the circumferential variation of static pressure at various axial locations in the annulus shroud upstream and downstream of the rotor were presented. The results indicated that for all axial positions a smaller peak-to-trough circumferential pressure variation existed downstream of the rotor than upstream. A significant influence of the downstream vane bow-wave was also shown as the magnitude of the peak-to-trough circumferential pressure variation was found to increase closer to the vanes.

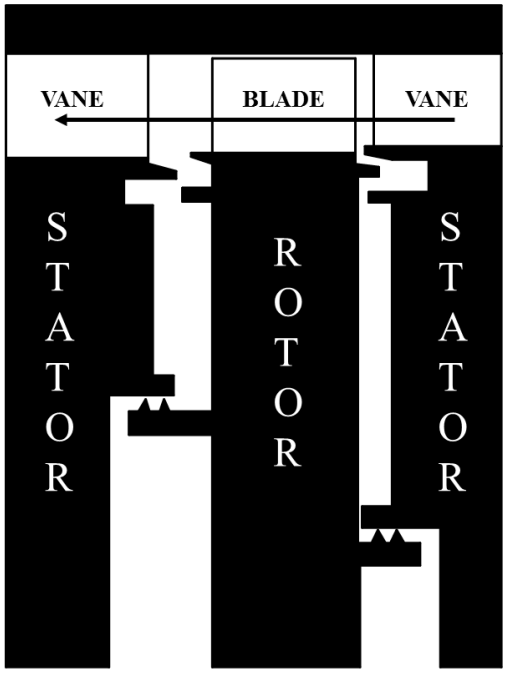

Figure 2.12: The upstream and downstream rim-seal geometries of the ASU 1.5-stage turbine test rig

2.6.2 Rotationally-induced (RI) ingress

In the absence of any external circumferential pressure variation ingress can still occur due to rotational effects. This mechanism is called rotationally-induced ingress (Owen (2010a)). The rotating fluid in the wheel-space creates a radial pressure gradient which can cause the pressure to drop below that of the mainstream flow in the annulus. This causes the egress of fluid near the rotating disc, where the centrifugal effects are greatest; this is often referred to as the *disc-pumping* effect. Ingress of external fluid through the rim-seal occurs near the stator disc in order to conserve radial mass flow.

One of the earliest experimental studies regarding ingress of mainstream flow into rotor-stator systems under RI conditions was conducted by Bayley and Owen (1970) at the University of Sussex. The description of RI ingress provided in the previous paragraph is derived from the results of their measurements.

A more recent study of RI ingress is the one by Sangan *et al.* (2012b). In this study measurements of CO_2 concentration were taken in the wheel-space of the single-stage rig described by Sangan *et al.* (2012a) in order for the performance of an axial and radial clearance seals to be evaluated. The results of these measurements showed that for the same amount of sealing flow rate a higher effectiveness can be achieved using a radial-clearance seal than an axial seal. A clear effect of rotational speed on the performance of the seals was observed with

the effectiveness reducing as Re_{Φ} was increased. Using Φ_0 instead of C_w the results of the variation of sealing effectiveness with sealing flow collapsed onto a single curve independent of Re_{Φ}.

For an extensive review of RI ingress studies the reader is referred to Scobie *et al.* (2016).

2.6.3 Combined (CI) ingress

Combine ingress (CI) is the mechanism for ingress where EI and RI ingress are both significant (Owen (2010b)). An example of this mechanism would be ingress through the outer and inner seals of a double radial-clearance seal (see Figure 2.10). If the annular space between the outer and inner seals is large enough to attenuate the circumferential pressure asymmetry in the ingested flow, then EI ingress can occur through the outer seal and CI ingress through the inner seal. Another example is when an engine operates at over-speed or low-C_F conditions.

Phadke and Owen (1988) were the first to investigate CI ingress. Their experimental measurements showed that for small values of C_F, the minimum amount of sealing flow rate required to prevent ingress ($C_{w,min}$) decreased as Re_w increased but for large values of C_F the effect of rotation was small and $C_{w,min}$ was proportional to Re_w, as shown in Figure 2.13.

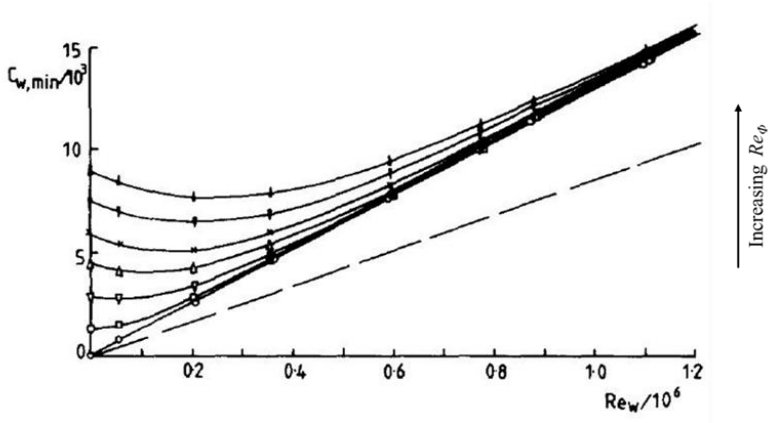

Figure 2.13: Effect of rotation on the variation of $C_{w,min}$ with Re_w – symbols denote experimental data; dashed line denotes quasi-axisymmetric case (adapted from Phadke and Owen (1988))

A more recent study investigating the effect of operating at off-design conditions on ingress is the one presented by Scobie *et al.* (2013). The experiments were conducted in the single-stage rig described by Sangan *et al.* (2012a) using an axial, single radial and double radial clearance seals. Of particular interest are the results of the concentration measurements taken

in the outer and inner wheel-spaces of the double radial clearance seal. Figure 2.14 shows the variation of the non-dimensional sealing flow rate required for an effectiveness of 95%, Φ_{min}' with C_F. The values of Φ_{min}' corresponding to the inner seal are much smaller than the ones corresponding to the outer seal indicating that the ingress through the inner seal was CI dominated.

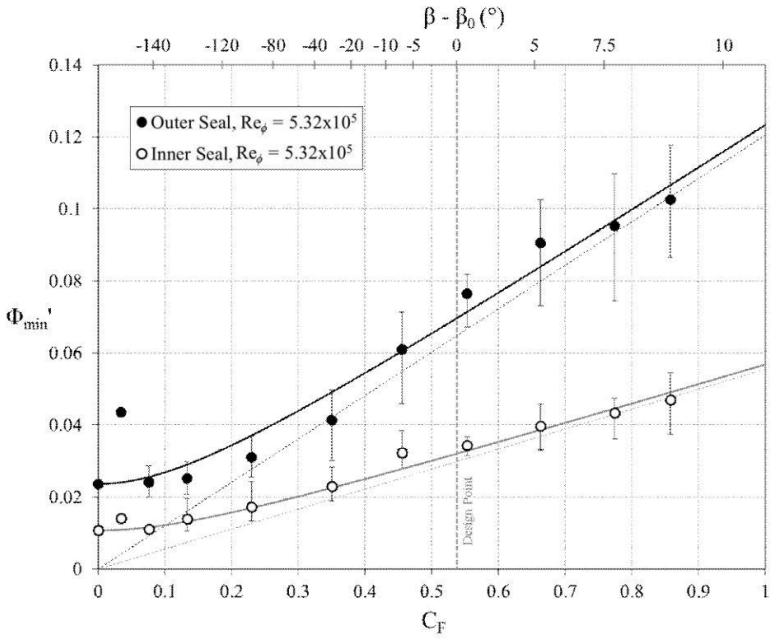

Figure 2.14: Variation of Φmin' with flow coefficient for a double radial-clearance seal; symbols denote experimental measurement, solid lines denote CI fits of model developed by Owen (2010b), broken lines are EI asymptotes (from Scobie *et al.* (2013))

2.7 Orifice Model

Owen (2010a, b) developed a simple mathematical model capable of capturing the variation of sealing effectiveness with sealing flow rate for various seals under RI, EI and CI ingress conditions. The model makes use of the orifice equations by treating the axial gap between stationary and rotating discs as an orifice ring as shown in Figure 2.15. Egress and ingress occur simultaneously with the flow passing through distinct elemental areas, δA_e and δA_i respectively. The sum of these two areas is equal to the seal clearance area, A_c. Two discharge coefficients were introduced to account for viscous losses, $C_{d,e}$ for egress and $C_{d,i}$ for ingress. These are theoretically indeterminate and they have to be treated as empirical constants for each seal.

The sealing effectiveness ε is defined as

$$\boldsymbol{\varepsilon = \frac{\dot{m}_0}{\dot{m}_\iota + \dot{m}_0}} \qquad \textbf{(Eq. 2.8)}$$

where subscripts *i* and *0* refer to ingress and sealing flow respectively and $\dot{m}$ the mass flow rate given by

$$\boldsymbol{\dot{m} = 2\pi\rho b s_c U} \qquad \textbf{(Eq. 2.9)}$$

and U the mean bulk velocity through the seal clearance and s_c the effective clearance of the rim-seal. From Eq.2.8 it follows that $\varepsilon = 1$ when ingress is zero and $\varepsilon = 0$ when the sealing flow rate is zero and maximum ingress occurs. The orifice equations also showed that effectiveness was invariant with rotational speed and so Eq.2.8 can also be expressed as shown below in terms of the non-dimensional sealing flow parameter, Φ given in Eq.2.4.

$$\boldsymbol{\varepsilon = \frac{\Phi_0}{\Phi_\iota + \Phi_0}} \qquad \textbf{(Eq. 2.10)}$$

Although the orifice model was first developed in terms of pressures, it is convenient for use with concentration measurements to express the equations in terms of the sealing flow parameter, Φ. The resulting equations are called the *effectiveness equations* and their derivation for the case of RI and EI ingress is provided by Sangan *et al.* (2012a, b).

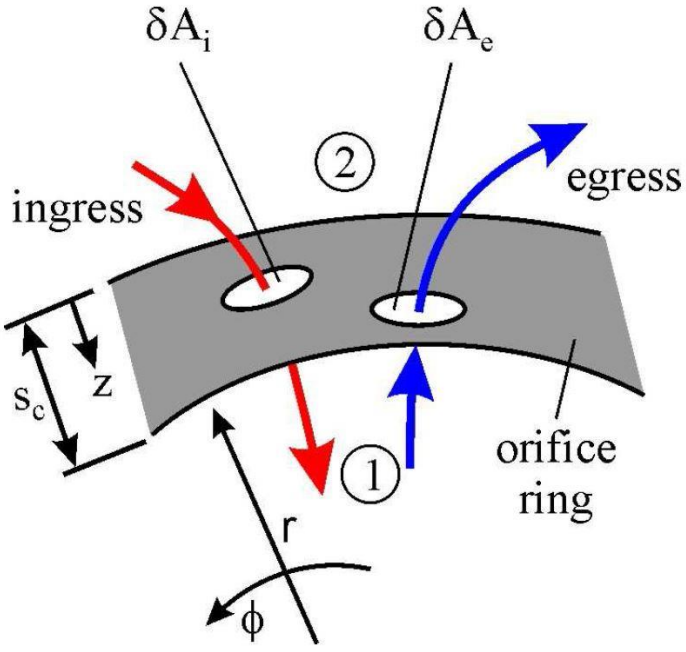

Figure 2.15: Physical illustration of the orifice model. The region labelled as 1 is the wheel-space and the one labelled as 2 is the annulus (from Owen (2010a))

The effectiveness equation for *RI ingress* is

$$\frac{\boldsymbol{\Phi_0}}{\boldsymbol{\Phi_{min,RI}}} = \frac{\boldsymbol{\varepsilon}}{[\mathbf{1}+(\mathbf{1}-\boldsymbol{\varepsilon})^{1/2}]\left[\mathbf{1}+\boldsymbol{\Gamma_c^{-2}}(\mathbf{1}-\boldsymbol{\varepsilon})\right]^{1/2}} \qquad \textbf{(Eq. 2.11)}$$

where Φ_{min} the minimum value of Φ_0 required to prevent ingress and Γ_c the ratio of discharge coefficient (= $C_{d,i}/C_{d,e}$).

From the orifice equations it was shown that $\Phi_{min,RI}$ was related to β_1, the swirl ratio in the wheel-space, such that

$$\boldsymbol{\Phi_{min,RI}} = \boldsymbol{C_{d,e}C_{\beta_1}^{1/2}} \qquad \textbf{(Eq. 2.12)}$$

where $C_{\beta 1}$ the modified internal swirl ratio, defined as

$$\boldsymbol{C_{\beta_1}} = \boldsymbol{\beta_1^2}\left(\mathbf{1}-\left(\frac{\boldsymbol{r_1}}{\boldsymbol{r_2}}\right)^2\right) \qquad \textbf{(Eq. 2.13)}$$

The effectiveness equation for *EI ingress* is

$$\frac{\boldsymbol{\Phi_0}}{\boldsymbol{\Phi_{min,EI}}} = \frac{\boldsymbol{\varepsilon}}{\left[\mathbf{1}+\boldsymbol{\Gamma_c^{-2/3}}(\mathbf{1}-\boldsymbol{\varepsilon})^{2/3}\right]^{3/2}} \qquad \textbf{(Eq. 2.14)}$$

From the orifice equation it was shown that $\Phi_{min,EI}$ was related to Δ_p, the peak-to-trough difference of the circumferential pressure variation in the annulus, such that

$$\boldsymbol{\Phi_{min,EI}} = \frac{\mathbf{2}}{\mathbf{3}}\boldsymbol{C_{d,e}}\left(\boldsymbol{\Delta C_p}\right)^{1/2} \qquad \textbf{(Eq. 2.15)}$$

where ΔC_p the non-dimensional pressure difference, defined as

$$\boldsymbol{\Delta C_p} = \frac{\boldsymbol{\Delta p}}{\mathbf{1/2}\boldsymbol{\rho\Omega^2 b^2}} \qquad \textbf{(Eq. 2.16)}$$

For CI, Owen (2010b) showed that $\Phi_{min,CI}$, the minimum amount of Φ_0 required to prevent ingress under CI conditions can be obtained from

$$\frac{\boldsymbol{\Phi_{min,CI}}}{\boldsymbol{\Phi_{min,RI}}} = \frac{\mathbf{2}}{\mathbf{3}}\frac{\left[\mathbf{1}+\boldsymbol{k_c C_F^{\,2}}\right]^{3/2}-\mathbf{1}}{\boldsymbol{k_c C_F^{\,2}}} \qquad \textbf{(Eq. 2.17)}$$

where k_c an empirical constant and C_F the flow coefficient given defined in the nomenclature.

In the above equations Φ_{min} and Γ_c are empirical constants that can only be obtained by fitting the effectiveness equations to experimental measurements of the variation of concentration effectiveness, ε_c with non-dimensional sealing flow rate, Φ_0. In most

experiments ε_c is obtained by measuring the concentration of a tracer gas, usually CO_2, in the sealing flow in the wheel-space. The concentration effectiveness is defined as

$$\boldsymbol{\varepsilon_c = \frac{c_s - c_a}{c_0 - c_a}} \qquad \textbf{(Eq. 2.18)}$$

where c_s, c_a and c_0 the concentration on the stator wall in the wheel-space, in the annulus and of the sealing flow respectively.

To fit the effectiveness equations to experimental data Zhou *et al.* (2012) used a maximum likelihood estimation (MLE) method whereby the true value of the unknown parameters (in this case Φ_{min} and Γ_c) is the one that maximises the probability of data according to the *likelihood function*. This method was initially validated using simulated noisy data generated from the effectiveness equations. It was then successfully used by researchers at the University of Bath in studies involving ingress through various rim-seal geometries under both RI and EI conditions such as the ones of Sangan *et al.* (2012b), Sangan *et al.* (2013), Sangan *et al.* (2014) and Scobie *et al.* (2015). The orifice equations were also fitted to experimental measurements obtained by other research groups by Scobie *et al.* (2016) as shown in Figures 2.16 and 2.17. In all cases excellent agreement between the orifice model and experimental measurements was observed.

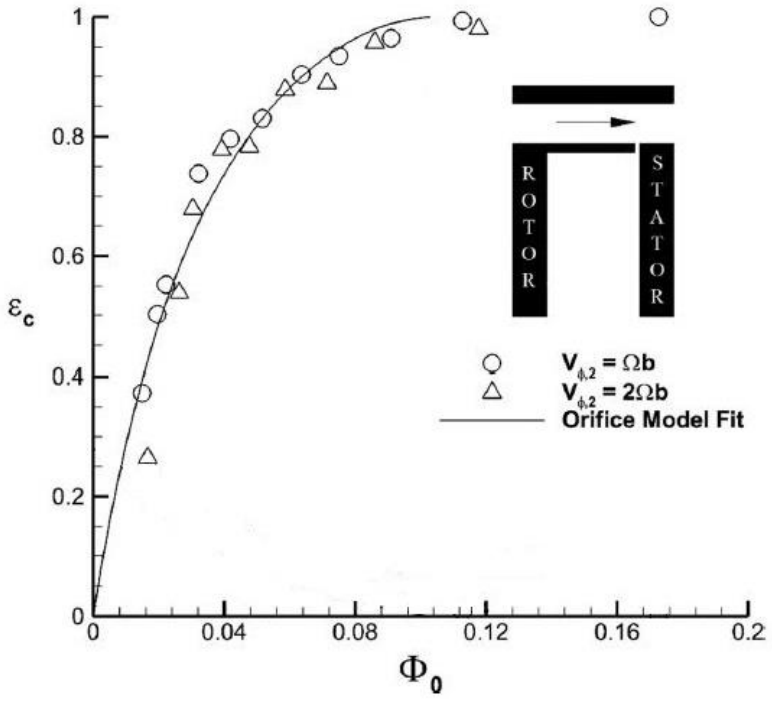

Figure 2.16: Fit of the effectiveness equations to RI ingress experimental measurements conducted by Graber *et al.* (1987) (adapted from Scobie *et al.* (2016))

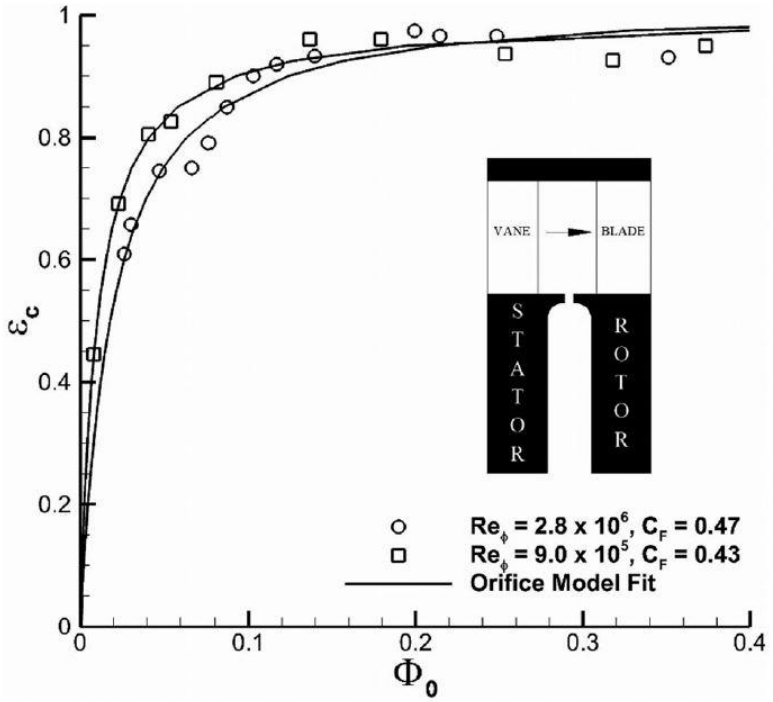

Figure 2.17: Fit of the effectiveness equations to EI ingress experimental measurements conducted by Gentilhomme *et al.* (2003) (adapted from Scobie *et al.* (2016))

2.8 Computational Fluid Dynamics (CFD)

An alternative to experimental studies of ingress is computational fluid dynamics (CFD). The benefit of CFD simulations is that they provide visualisation of the flow phenomena occurring in the seal clearance and wheel-space and that they allow for results to be collected on both stationary and rotating surfaces. These benefits make CFD ideal for investigating unsteady flow phenomena, an effect which is difficult to capture in experimental rigs. Unsteady phenomena include large scale structures (LSS) in the wheel-space that rotate at a speed close to the rotor speed, creating regions of low pressure and low concentration. Two important CFD studies detailing LSS are described below.

Jakoby *et al.* (2004) performed an unsteady CFD simulation of a 360° sector in an attempt to explain spikes in the unsteady pressure measurements taken in the 1.5-stage test facility of Bohn *et al.* (2003). In their simulation the interaction between the vanes and blades was neglected. The results indicated three large scale structures that rotated at a speed of about 80% of that of the rotor. The area occupied by these structures was an area of low pressure (Figure 2.18 (a)) and therefore an area of increased ingestion (Figure 2.18 (b)). Although the 360° model was able to capture the increase of ingress due to the LSS it still under-predicted the experimentally obtained data.

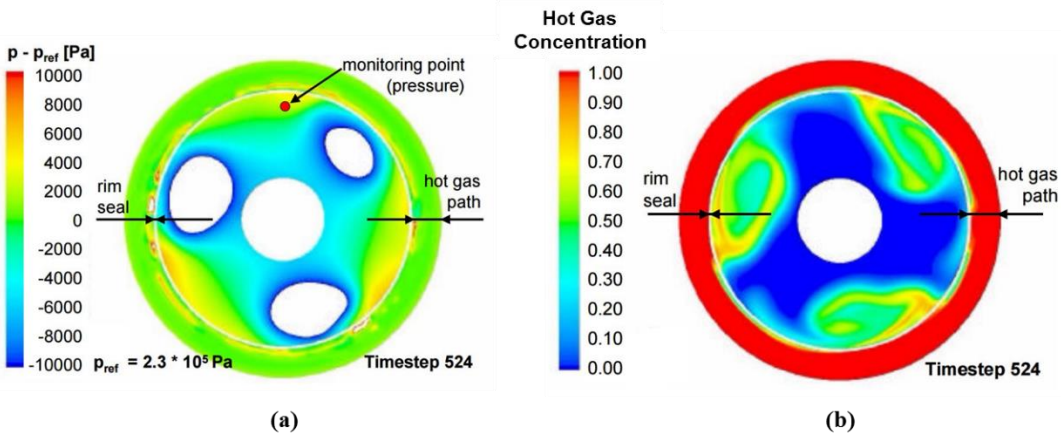

Figure 2.18: Contours of (a) static pressure and (b) hot gas concentration in the wheel-space (Re_Φ = 2.4 × 10^6, C_F = 0.46, G_c = 0.03, Φ_0 = 0.015) (from Jakoby *et al.* (2004))

Wang *et al.* (2013) performed an unsteady, 3-dimensional CFD simulation on a 360° sector model of the single turbine stage featured in the test rig of Zhou *et al.* (2010). The rim-seal configuration used in the simulation is the one labelled as configuration 1 in Figure 2.7. The results of the simulations of the annulus pressure field showed that the vane trailing edge wake and the blade leading edge bow-wave interacted in such a way that irregular pressure patterns were formed in the annulus immediately outboard of the seal clearance as shown in Figure 2.19. These interactions were described as the cause for ingress in the upstream wheel-space. The results of the simulations of the flow inside the wheel-space indicated 12 LSS that rotated at a speed of about 86% of the speed of the rotor disc and were more profound at intermediate values of sealing flow rate. The LSS were found to cause an increase in ingress and therefore a decrease in sealing effectiveness as shown Figure 2.20. Comparisons of the simulations with experimental measurements showed that the simulations over-predicted ingestion when a small amount of sealing flow was supplied to the wheel-space with the agreement improving at higher sealing flow rates.

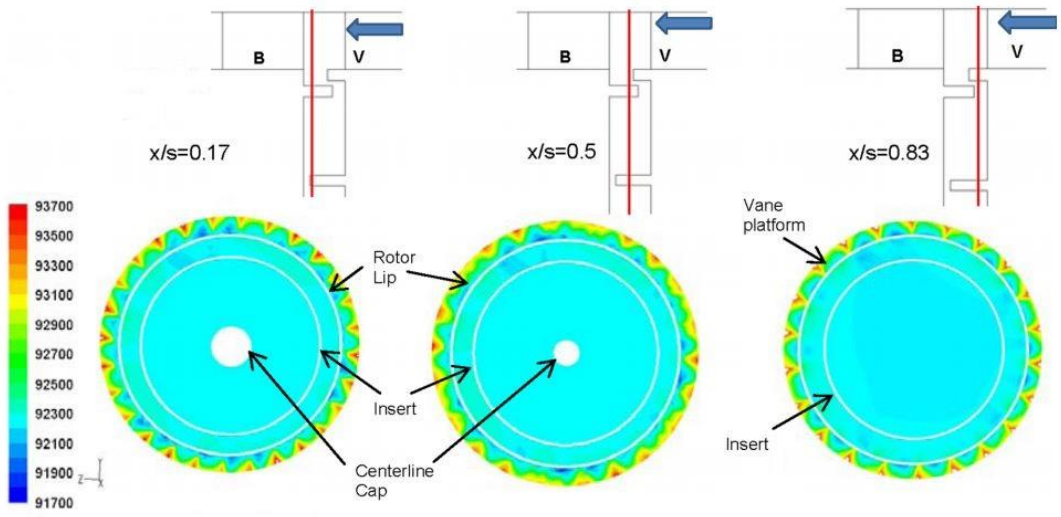

Figure 2.19: Vane-blade pressure field interactions for three different axial locations (from Wang *et al.* (2013))

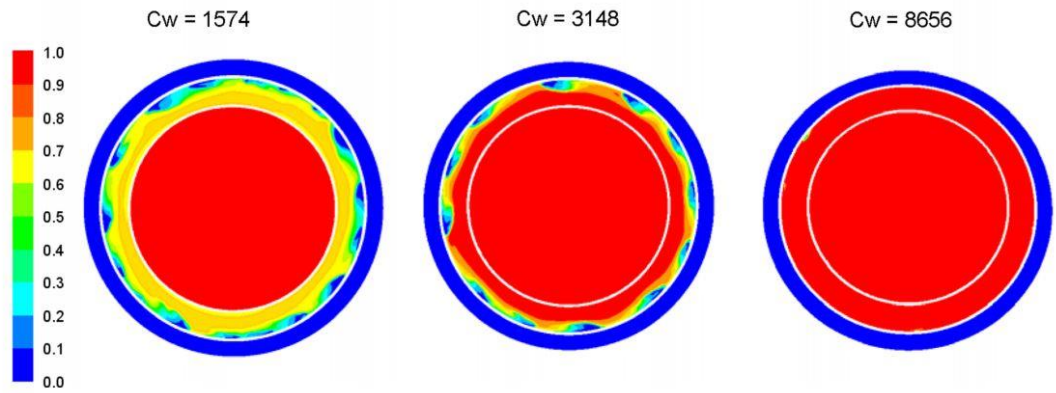

Figure 2.20: Sealing effectiveness contours for three different sealing flow rates (from Wang *et al.* (2013))

2.9 Test Facilities

There is a growing trend in industry to design rim-seals using advanced computational fluid dynamics (CFD). CFD simulations are time consuming and require experimental validation. Test facilities that operate at near-engine and at more benign conditions provide important validation data. Experimental facilities simulating engine conditions offer a realistic testing environment, while rigs operating at lower rotational speeds have the advantages of high instrumentation-density, accuracy, flexibility and expedience, and lower cost and risk. There are numerous test facilities described in the open literature. A brief overview of a selected few of these facilities is provided by Barringer *et al.* (2014). This section makes reference to modern and currently-active test facilities.

GE Global Research Centre

Palafox *et al.* (2013) presented a 1.5-stage turbine facility that was built at the General Electric (GE) Global Research Centre for the investigation of ingress into an upstream and downstream wheel-space (see Figure 2.21). The upstream and downstream stator discs included 48 vanes each and a rotor disc with 96 blades. The operating speed of the rotor was 7600 rpm resulting in a rotational Reynolds number, $Re_{\Phi} = 6 \times 10^6$. Several secondary air flow paths were incorporated in the design of the GE facility including upstream and downstream wheel-space sealing air, chordal hinge leakage and shank leakage. In contrast to most of the experimental facilities investigating ingress, the mainstream flow of the GE facility was supplied hot at a nominal temperature of 204 ^{o}C. The mainstream flow rate was 6.5 kg/s generating an axial Reynolds number, $Re_w = 1 \times 10^7$. A variety of experimental measurements can be made in the GE facility including total pressure, steady and unsteady static pressure, total temperature and CO_2 concentration. The measurements can be taken at various axial, radial and circumferential locations in both the upstream and downstream wheel-spaces on the surface of the stator and rotor (via slip rings) and in the annulus. Palafox *et al.* (2013) presented only some basic commissioning results.

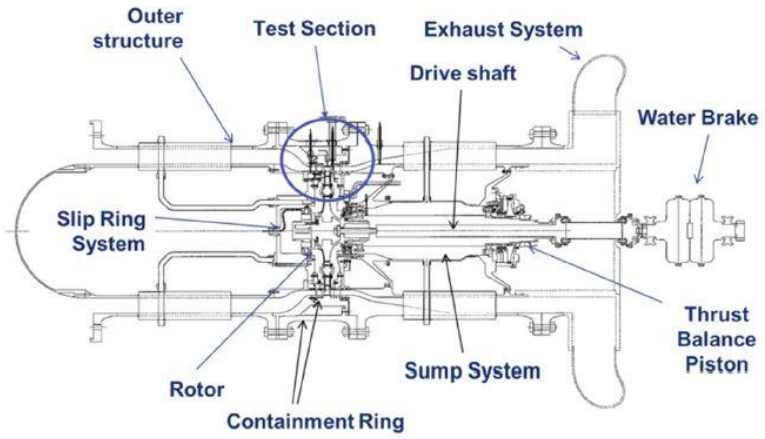

Figure 2.21: Cross-section of the GE Global Research Centre 1.5-stage gas turbine rig indicating the main auxiliary components (from Palafox *et al.* (2013))

Pennsylvania State University

Barringer *et al.* (2014) described the design of a 1.5-stage turbine test facility that was built at the Pennsylvania State University for the study of ingress and aerofoil heat transfer. A true scale, half span aerofoil geometry was used for both vanes and blades. The annulus flow and the sealing flow were supplied by a 1.1MW compressor discharging air at temperatures of 395 K, pressures of 4.8 bar and flow rates of up to 5.7 kg/s. Out of this flow 4.56 kg/s were diverted

directly to the annulus and the remaining 1.14 kg/s were diverted to the leakage air system through a thermal conditioning unit which reduced the temperature to 275 K. This created a coolant-to-mainstream density ratio of 1.3. The rotor was supported by magnetic bearings and could be rotated at speeds of up to 13000 rpm, resulting in a rotational Reynolds number, $Re_\Phi = 1 \times 10^7$. The axial Reynolds number of the rig at the blade inlet was 3×10^5. Measurements of steady and unsteady static pressure, concentration and temperature could be made on both the stationary and the rotating surfaces. These measurements could be taken at various positions in the upstream and downstream wheel-spaces and in the annulus. Static pressure taps were also incorporated in some of the aerofoil profiles on both the pressure and the suction surfaces, stretching along the whole of the chord length. The seals incorporated in the design were single and double radial seals.

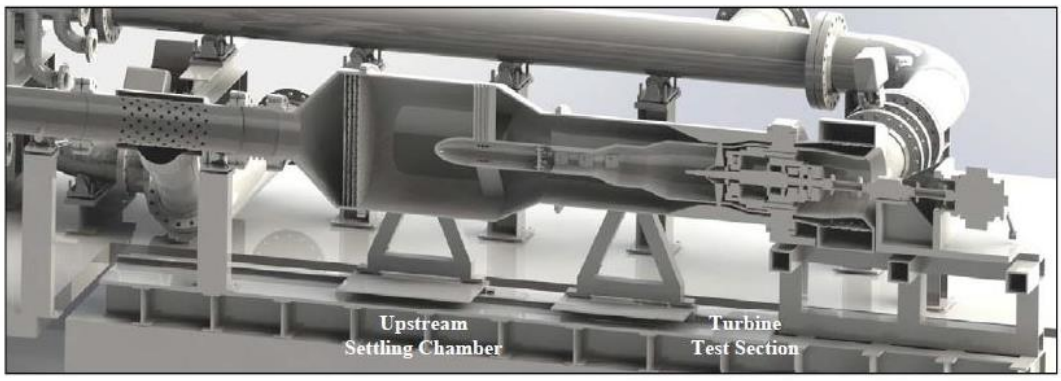

Figure 2.22: Cross-section of the Pennsylvania State University 1.5-stage turbine test facility (from Barringer *et al.* (2014))

University of Oxford

The first experimental ingress work at the University of Oxford was presented by Beard *et al.* (2016) and involved the investigation of unsteady flow phenomena in the wheel-space of a single-stage turbine rig. The stage featured a bladeless stator and rotor fitted with a chute seal with clearance, s_c of either 1 mm or 1.65 mm. The rotor could be spun up to 9000 rpm generating a maximum rotational Reynolds number of $Re_\Phi = 3 \times 10^6$. Measurements of unsteady pressure in the wheel-space were made in the absence of any annulus flow using Kulite™ unsteady pressure transducers placed at various radial and circumferential locations. The output of the transducers was passed through bespoke heat transfer amplifier electronics for amplification and conditioning. AC coupling and anti-aliasing filtering was also applied to the signal. Analysis of the spectra of the unsteady measurements revealed a "spike" at a frequency of 22 times the rotating frequency of the rotor for all radial locations. The "spike"

magnitude decreased as the radius increased or the rotational speed decreased with the effect of the sealing flow rate being small but noticeable especially in the seal-clearance. Phase analysis of the circumferential unsteady pressure signals at a radius of r/b = 0.96 revealed the existence of 26 to 29 structures, depending on Re_Φ and C_w conditions, rotating at about 80% of the speed of the rotor. These findings were in good agreement with the findings of the CFD studies mentioned in Section 1.8.

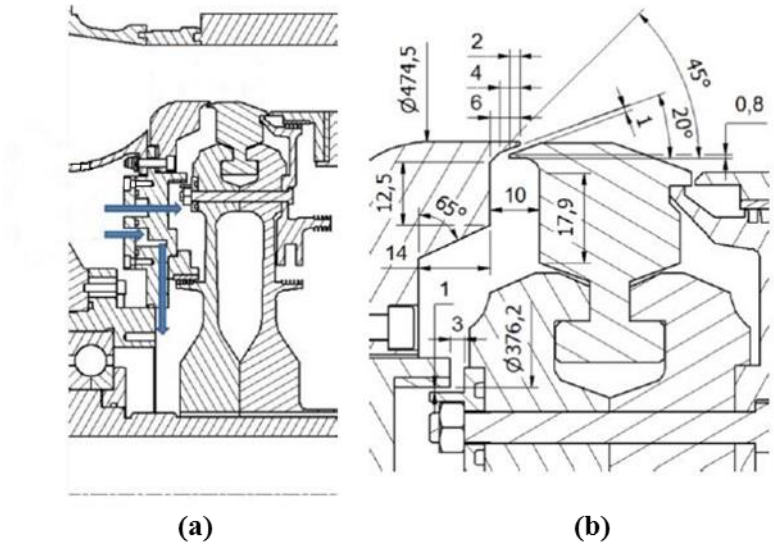

Figure 2.23: The single-stage turbine rig at the University of Oxford - (a) cross-section of the turbine; (b) rim-seal geometry and dimensions (adapted from Beard *et al.* (2016))

University of Cambridge

Savov *et al.* (2016) presented a single-stage turbine test facility that was built at the University of Cambridge. The stator disc featured 40 vanes and on the rotor disc 96 removable, tear-drop shaped blockage elements (referred to below as blades). The wheel-space was fitted with either a single or a double lip seal shown in the inserts of Figure 2.24. CO_2 concentration measurements were taken in the wheel-space for both rim seal geometries, with and without blades and for a range of Re_Φ and Mach number, M conditions. As shown in Figure 2.24, effectiveness increased with sealing flow rate for both seals, with the double lip seal geometry demonstrating better performance. As far as the effect of the blades and Re_Φ was concerned, an inconsistency between the two seal geometries was observed; the double lip seal effectiveness was independent of the existence of the blades and Re_Φ whereas the single lip seal showed some dependency.

Measurements of concentration at various circumferential and two radial locations were also conducted for both seal geometries and in the absence of blades. A significant variation of effectiveness with circumferential position was observed for the case of the single lip seal. For the same amount of sealing flow rate this variation was higher at the higher radii than at the lower ones and diminishes as the sealing flow rate increases. The authors attributed this circumferential variation of effectiveness to eccentricity in the stator which resulted in regions of high and low effectiveness around the circumference of the disc. Measurements of the radial distribution of effectiveness on the stator wall also indicated some variation. Considering these findings an ingress flow path was proposed as shown in Figure 2.25. According to this path ingress moved both circumferentially and radially along the surface of the stator disc. Unsteady pressure measurements at low and high radii in the wheel-space were also made using the bladed and bladeless rotor configurations at various sealing flow rates and flow coefficients. The results indicated large scale structures that rotated at speeds of 25-35 times the speed of the rotor that were only observed in the case where no blades were fitted. The effect of the large scale structures on ingress was found to be stronger at off-design conditions.

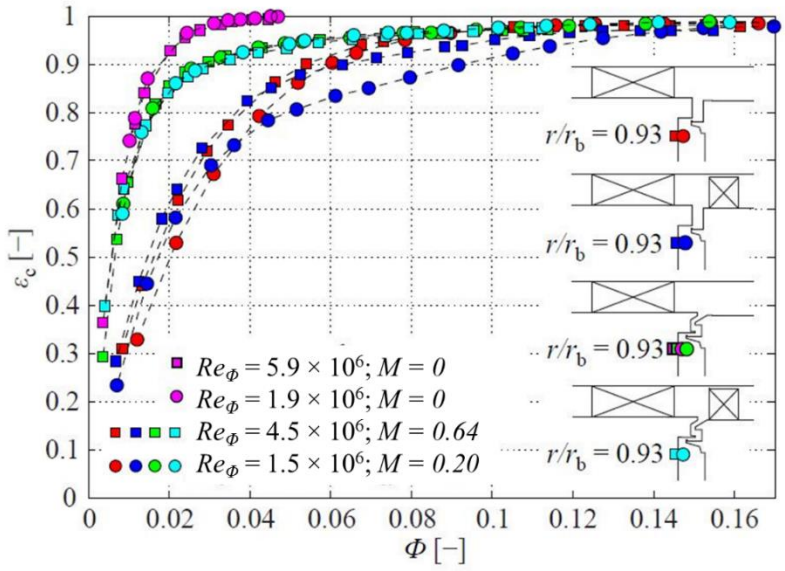

Figure 2.24: Variation of effectiveness with sealing flow rate at different Re_Φ and M conditions (adapted from Savov *et al.* (2016))

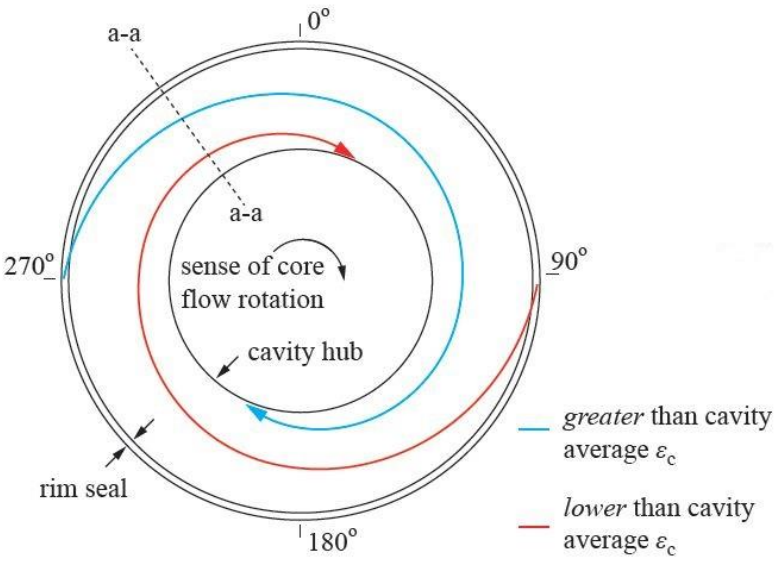

Figure 2.25: Hypothesised flow path in stator boundary layer (from Savov *et al.* (2016))

2.10 Bath Advantage

Figure 2.26 shows the operating capabilities in terms of rotational and axial Reynolds number, Re_Φ and Re_w respectively, for selected test facilities appearing in the open literature. A typical engine operates at $Re_\Phi = 2 - 3 \times 10^7$ (Childs (2011)). The majority of the test rig facilities operate at lower-than-engine rotational speeds. This is because there are many advantages to low-speed experimental modelling: principally greater accuracy, lower cost and lower risk. Fluid-dynamic scaling of the size and speed of engine conditions permits detailed, expedient and accurate measurements. Instrumentation can be accommodated in locations and conditions that would otherwise be prohibitive. Lower rotational speeds result in lower stresses, and therefore reduced hardware and testing costs. Finally, low-speed (incompressible) testing provides an opportunity to test designs and configurations without risking the disruption of a major engine programme.

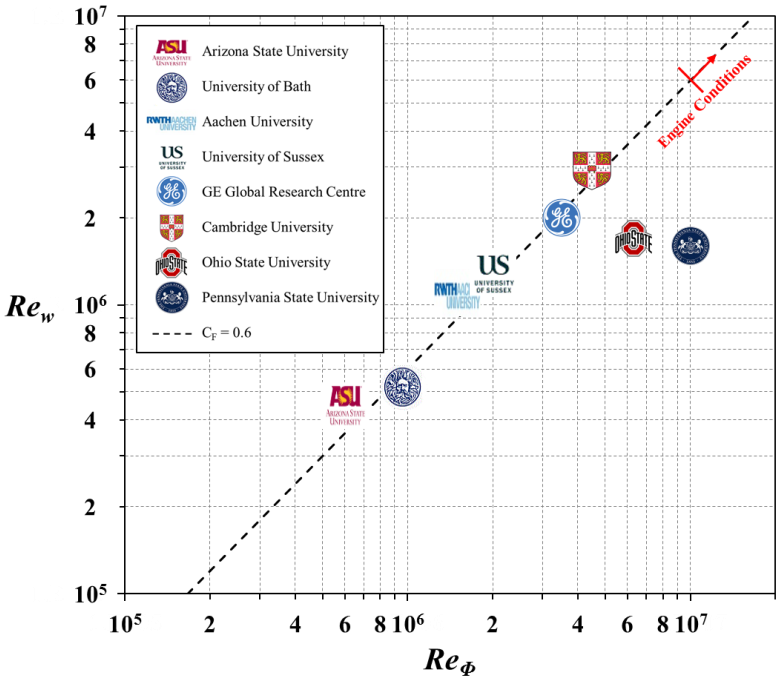

Figure 2.26: Operating capabilities of a selected few of the numerous ingress test facilities appearing in literature

A new 1.5-stage turbine test facility was designed at the University of Bath. The facility operates at low rotational speeds ($Re_\Phi \sim 10^6$) and incompressible conditions (annulus Mach number ~ 0.4) thus benefiting from the advantages of low-speed testing mentioned above. More specifically, the test facility offers flexibility and expediency in terms of data collection over a wide range of sealing flow rates. This enables an efficient method of ranking and quantifying the performance of a wide range of generic and engine-specific seals that are developed in industry using CFD simulations. The experiments are thus used to inform the design criteria that can be scaled to engine operating conditions through the use of the orifice model (see Section 1.7) and CFD. Details of the design of the 1.5-stage turbine facility and experimental measurements conducted in both its upstream and downstream wheel-spaces are provided in the subsequent chapters.

Chapter 3: The 1.5-Stage Gas Turbine Test Facility

This chapter presents the design features and operating capabilities of a new, versatile and highly instrumented, 1.5-stage turbine test facility. The new facility was designed and built at the University of Bath with the purpose of extending the ingress research to include a downstream wheel-space using an engine representative turbine geometry. The author of this thesis was provided with the preliminary design of the rig but had taken sole responsibility of all the other phases of the project that led to the existence of the facility including the detailed design, drafting of technical drawings for manufacture, liaising for and overseeing all manufacturing processes, set-up and installation of instrumentation and acquisition system and commissioning. In the following sections, special reference is made to the design of the turbine assembly, the design of the mainstream and sealing flow supply assemblies and to the experimental measurement capabilities and instrumentation of the new facility. The measurements conducted as part of the commissioning phase of the new facility are presented and their significance in the successful operation of the rig is discussed.

3.1 Facility Overview

Following the completion of a successful three-year (2008 – 2011) research collaboration with Siemens for the investigation of ingress through turbine rim-seals in a simplistic turbine rig (see Sangan *et al.* (2012a)), a new collaboration was formed in 2013. The aim of the new collaboration was to extend the research of ingress through company proprietary rim-seals in a downstream wheel-space of a test facility featuring engine representative blade and vane geometries. To achieve this aim a new 1.5-stage turbine test facility had to be designed and built. A unique opportunity arose for research with not only industrial impact but also with academic significance as the rig could be used for fundamental studies of ingress in the *upstream*, but most importantly, in a *downstream* wheel-space where research efforts have been limited.

Figure 3.1 shows the new 1.5-stage turbine test facility that was designed and built at the University of Bath. The facility consists of hundreds of parts that make-up three major assemblies: the turbine assembly, the flow supply assembly (mainstream and sealing flow) and the drivetrain assembly. The first two assemblies have been entirely designed at the University of Bath whereas the drivetrain assembly was subcontracted to an external specialist. For this reason no detailed description of this is provided in this chapter. Detailed descriptions of the turbine and flow assemblies are given in Sections 3.2 and 3.3. An overview of the test facility is provided below.

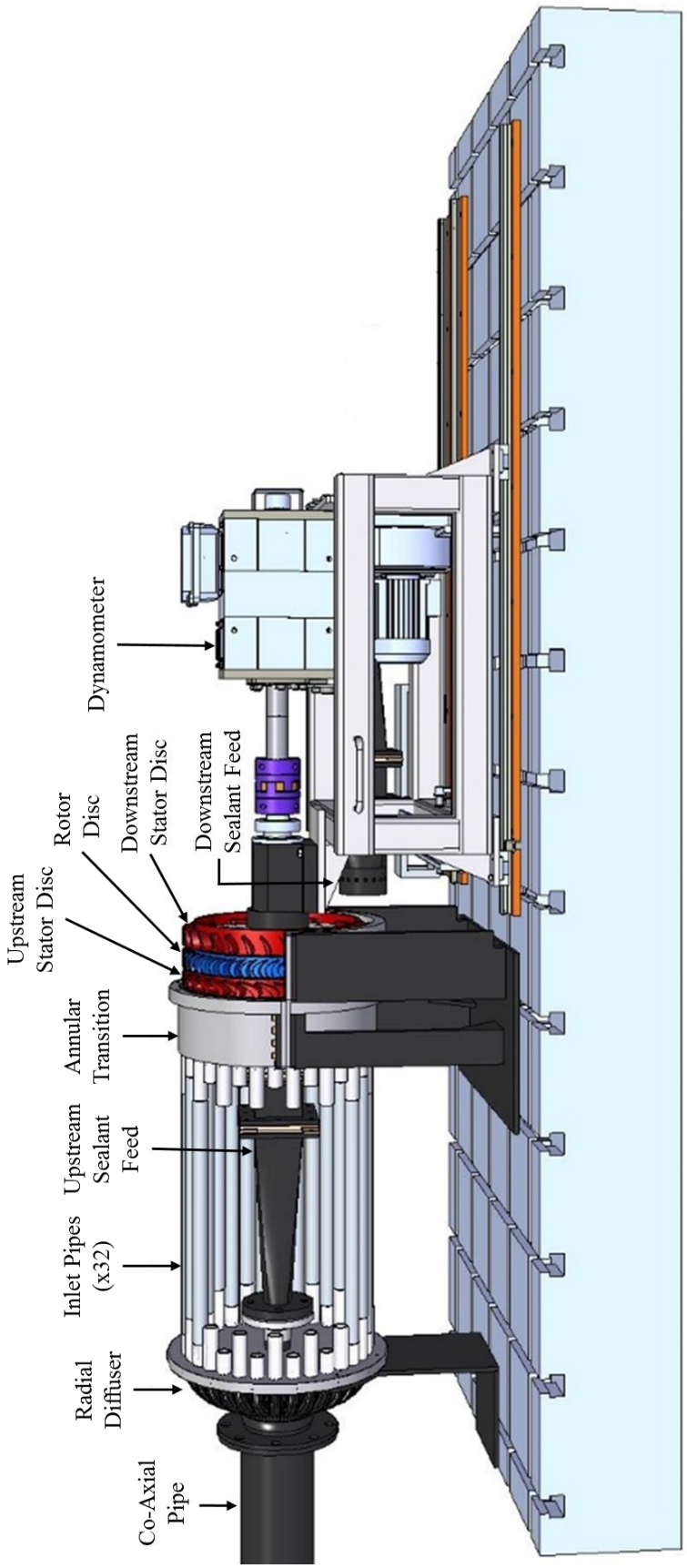

Figure 3.1: The 1.5-stage turbine test facility (stators are marked in red and rotor in blue). The top half of the turbine casing, and some of the mainstream flow supply tubes are removed so that the turbine and sealing flow feed are exposed.

The turbine assembly consists of an upstream and a downstream stator and a rotor disc. Both stator discs feature 32 vanes that are integrated into 180° split rings, also referred to as blings. The split construction of the blings makes the 1.5-stage facility ideal for rim-seal performance studies as both radially and axially assembled seals can be rapidly installed and tested. The rotor features 48 turned blades that are integral to the disc to form a blisc. A 34kW dynamometer is used to absorb the power generated by the turbine and also to drive the rotor to the required speed. The dynamometer assembly was supplied by an external supplier along with the control and data acquisition system. The blings and blisc are made of titanium which ensures component integrity under operating loads and also provides the low thermal conductivity surfaces required for heat transfer experiments. Further details about individual components of the turbine assembly are provided in Section 3.2.

Mainstream flow is supplied to the annulus of the turbine through a radial diffuser and 32 (one per vane) inlet pipes which connect to a split casing made of two 180° segments. Inside this casing carbon fibre inserts are employed to transition the flow from the circular cross-section of the inlet pipes to the annular cross-section of the mainstream flow path. The amount of flow supplied to the annulus is measured and controlled using a thermal mass flow meter and controller. Further details about the annulus flow supply assembly are provided in Section 3.3.

Sealing flow to the upstream and downstream wheel-spaces is supplied via sealant feeds which are primarily used for conditioning the flow prior to its entry into the wheel-space. These feeds comprise of two mesh heaters which are only used during heat transfer experiments to raise the temperature of the sealing flow up to 60°C. The amount of sealing flow supplied to the wheel-spaces is measured and adjusted using thermal mass flow meters and controllers. Further details about the sealing flow supply assemblies are provided in Section 3.3.

Measurements of CO_2 concentration, steady and unsteady static pressure, total pressure and temperature can be taken at various locations in the annulus and in the upstream and downstream wheel-spaces. Figure 3.2 shows a cut-out through the turbine section of the rig revealing some of the instrumentation locations in the upstream wheel-space. The majority of the measurements in the wheel-spaces are taken on the stator walls. The sole measurements made on the surface of the rotor are of temperature using infrared (IR) sensors. The IR sensors can be seen in Figure 3.2 at the back of the downstream stator. Detailed discussion about the measurement capabilities of the 1.5-stage rig is provided in Section 3.4.

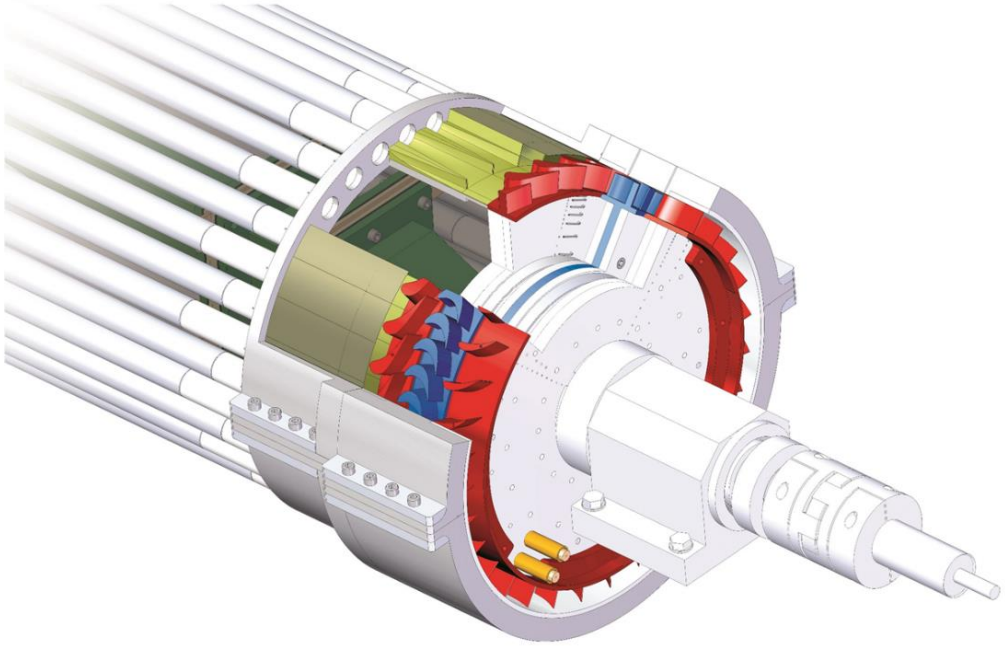

Figure 3.2: A cut-out through the turbine section of the 1.5-stage turbine test facility (stators are marked in red, rotor in blue and components of the flow supply assembly in green)

3.1.1 Operating Conditions

Table 3.1 shows the operating conditions of the 1.5-stage turbine test facility. Experiments are performed at two rotor disc speeds of 3000 and 4000 rpm corresponding to rotational Reynolds numbers, $Re_\Phi = 7.2 \times 10^5$ and 1.0×10^6 respectively. Despite the maximum Re_Φ being an order of magnitude smaller than that typically found in engines, the flow structure in rotor-stator systems is principally governed by the turbulent flow parameter λ_T and depends only weakly on Re_Φ (Owen and Rogers (1989)). In modern engines λ_T is typically much less than 0.22; $\lambda_T << 0.22$ in all experiments presented in this thesis.

The amount of flow supplied to the annulus of the turbine can be controlled so that a wide range of flow coefficients C_F can be created, allowing for the test rig to be operated at off-design conditions. The operating flow coefficient for the experiments was $C_F = 0.34$. At the maximum operating speed this resulted in a maximum axial Reynolds Number, $Re_w = 3.4 \times 10^5$. At these conditions the Mach number at the exit of the upstream vanes was $M = 0.37$.

Figure 3.3 is a modified version of Figure 2.26 showing a comparison of the operating capabilities of the 1.5-stage rig with other facilities around the world. As it can be seen, the 1.5-stage rig operates at relatively low rotational and axial Reynolds numbers in comparison to the majority of the other facilities. This was a deliberate design feature which, as discussed in Section 2.10, offered amongst many other advantages, flexibility and expediency in terms

of data collection; an advantage that goes hand-to-hand with the experimental requirements of the collaboration with Siemens and with the research philosophy at the University of Bath. The operating C_F of the rig is also lower than the one of the majority of the other facilities. A higher flow coefficient was not possible due to limitations in the flow rate that could be supplied by the compressor providing the annulus flow.

Parameters	**Disc Speed (RPM)**	
	3000	**4000**
Rotational Reynolds Number, $\boldsymbol{Re_\Phi}$	7.2×10^5	1.0×10^6
Axial Reynolds Number, $\boldsymbol{Re_w}$	2.4×10^5	3.4×10^5
Flow Coefficient, $\boldsymbol{C_F}$	0.34	
Vane exit Mach Number, $\boldsymbol{M}$	0.28	0.37

Table 3.1: Operating conditions of the 1.5-stage turbine test facility

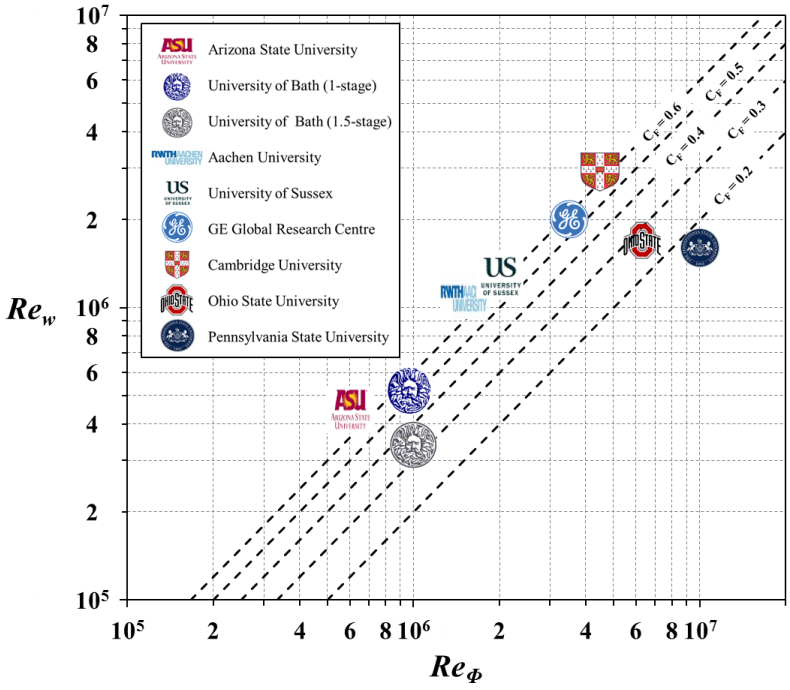

Figure 3.3: Comparison of the operating capabilities of the 1.5-stage turbine experimental facility with other facilities around the world

3.2 The 1.5-Stage Turbine

3.2.1 Vane and Blade Geometries

The profiles of the stator vanes and rotor blades of the 1.5-stage turbine are based on Siemens' SGT-8000H engine. There are 32 vanes on each stator and 48 turned, untwisted blades on the rotor. Figure 3.4 shows the velocity triangles for the 1.5-stage turbine with the corresponding parameters provided in Table 3.2.

Flow enters the turbine with an axial velocity component W, at a purely axial direction, resulting in a vane inlet angle $\alpha_1 = 0^o$. It then exits the upstream vanes with an exit velocity in the stationary frame of reference C_2, at an exit angle $\alpha_2 = 77.5^o$. The flow then enters the rotor blades with a blade inlet velocity in the rotating frame of reference V_2, at an angle $\beta_2 = 57.9^o$ and exits with a blade exit velocity V_3, at an angle $\beta_3 = 66.7^o$. Finally, the flow enters the downstream vanes with a vane inlet velocity in the stationary frame of reference C_3, at an inlet angle $\alpha_3 = 30.8^o$ and exits with a vane exit velocity C_4, at an exit angle $\alpha_4 = 46.3^o$.

Table 3.3 includes the performance parameters of the 1.5-stage turbine, calculated based on the velocity triangle parameters discussed above. Two non-dimensional parameters are included. The first is the *degree of reaction* Λ given by

$$\boldsymbol{\Lambda = \frac{C_F}{2}(\tan\beta_3 - \tan\beta_2)} \qquad \textbf{(Eq. 3.1)}$$

where C_F the flow coefficient defined in the nomenclature. The second parameter is the *blade loading coefficient* Ψ, given by

$$\boldsymbol{\Psi = 2C_F(\tan\beta_2 + \tan\beta_3)} \qquad \textbf{(Eq. 3.2)}$$

The power and torque generated by the stage, W_s and T_s respectively were also calculated using the velocity triangle parameters and the following equations

$$\boldsymbol{W_s = \Omega b\,(C_{w2} - C_{w3})} \qquad \textbf{(Eq. 3.3)}$$

$$\boldsymbol{T_s = \frac{W_s}{\Omega}} \qquad \textbf{(Eq. 3.4)}$$

where $(C_{w2} + C_{w3})$ is the change in whirl and Ω the angular velocity of the rotor. The maximum work output and torque produced by the stage are $W_s = 8.5$ kW and $T_s = 20.3$ Nm respectively.

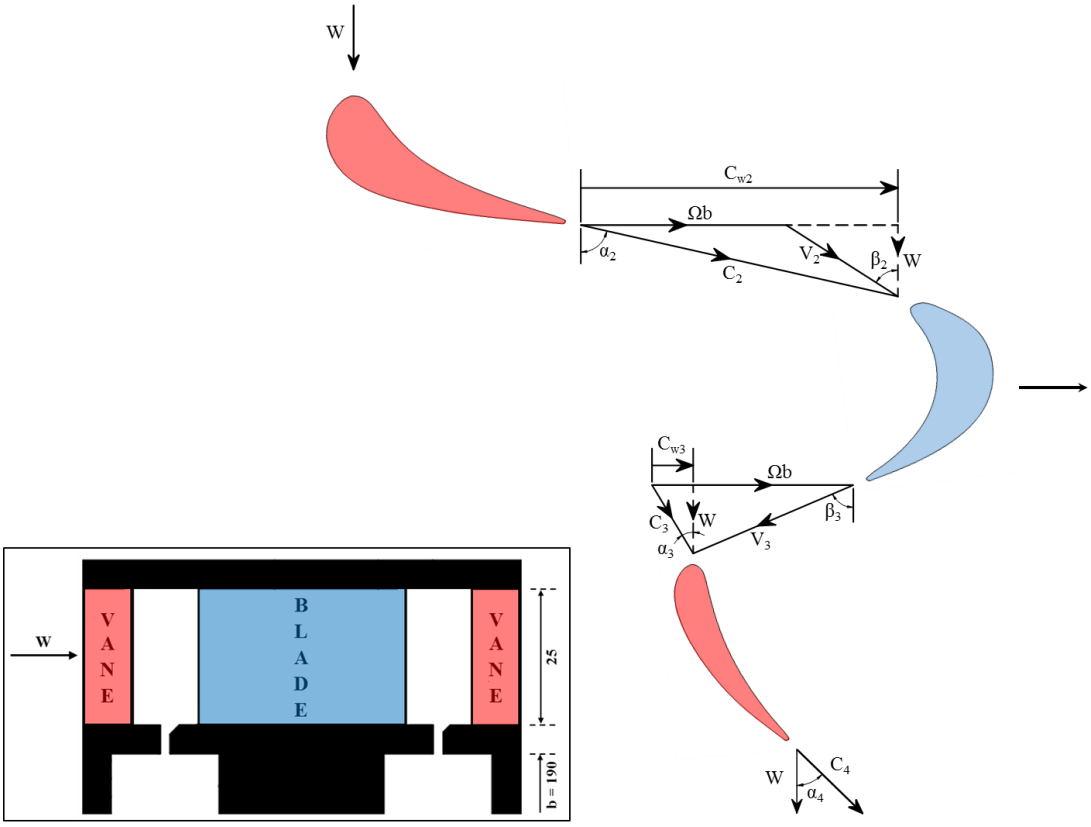

Figure 3.4: Velocity triangles for 1.5-stage turbine

Velocity Triangle Parameters	Disc Speed (RPM)	
	3000	4000
Upstream Vane Inlet Angle, α_1	0^o	
Usptream Vane Exit Angle, α_2	77.5^o	
Blade Inlet Angle, β_2	57.9^o	
Blade Exit Angle, β_3	66.7^o	
Downsream Vane Inlet Angle, α_3	30.8^o	
Downstream Vane Exit Angle, α_4	46.3^o	
Rotational Velocity, Ωb (m/s)	59.7	79.6
Axial Velocity, W (m/s)	20.5	27.3
Upstream Vane Exit Velocity, C_2 (m/s)	94.5	126.1
Blade Inlet Velocity, V_2 (m/s)	38.5	51.4
Blade Exit Velocity, V_3 (m/s)	51.7	69
Downstream Vane Inlet Velocity, C_3 (m/s)	23.8	31.8
Downstream Exit Velocity, C_4 (m/s)	29.7	39.5
Change in Whirl, $(C_{w2} - C_{w3})$ (m/s)	80.2	106.9

Table 3.2: Velocity triangle parameters of the 1.5-stage turbine

Stage Performance Parameters	Disc Speed (RPM)	
	3000	4000
Degree of Reaction, Λ	12.5%	
Blade Loading Coefficient, ψ	2.7	
Power Generated by Stage, W_s (kW)	4.8	8.5
Torque Generated by Stage, T_s (Nm)	15.3	20.3

Table 3.3: Performance parameters of the 1.5-stage turbine

3.2.2 Turbine Design

Figure 3.5 shows a colour-coded cross-section of the turbine assembly based on the materials used for the manufacture of its various components. Exploded views of the subassemblies of the upstream and downstream stators and rotor are also included along with some important dimensions.

Consider first the rotor subassembly. The rotor disc consists of 48 turned, untwisted blades manufactured integrated to the disc to form a blisc (**bl**aded d**isc)**. The blisc was made of titanium, a material that offers high specific strength (a requirement for structural rigidity under operating loads and for operation within the deflection limitations of the drive-shaft) and low thermal conductivity (a requirement of heat transfer experiments). Removable cover plates made of either aluminium or Rohacell®[4]/polycarbonate composite are fitted on both sides of the blisc. These can be of different thicknesses allowing for the axial gap of both the upstream and downstream wheel-spaces to be altered. The aluminium cover plates are used for experiments involving pressure and CO_2 concentration measurements whereas the composite cover plates are used for heat transfer experiments where near adiabatic surfaces are required. Inlet seals are also fitted on either side of the blisc at low radius. The purpose of the inlet seals is to condition the sealing flow prior to its entry to the main wheel-space. The material of choice for these parts was constrained solely by the adiabatic surface requirement of the heat transfer experiments. For this reason the inlet seals were made of Rohacell® foam.

Consider now the upstream and downstream stator subassemblies. Each of these consist of two 180º split rings that are manufactured integrated to a total of 32 vanes to form blings (**bl**aded r**ings**). Similarly to the blisc, the blings are also made of titanium. The split construction of the blings allows for both axially and radially assembled rim-seals to be tested making the test facility ideal for rim-seal performance studies. The blings are mounted at the

[4] Rohacell® is a closed cell, low density, machinable foam with a very small thermal conductivity (around 0.0257 W/mK).

periphery of aluminium stator discs. These discs accommodate the majority of the instrumentation used for measurements in the upstream and downstream wheel-spaces. As it was the case for the rotor, the stators are fitted with aluminium cover plates used for varying the axial gap of the wheel-space and Rohacell® inlet seals used for the conditioning of the sealing flow.

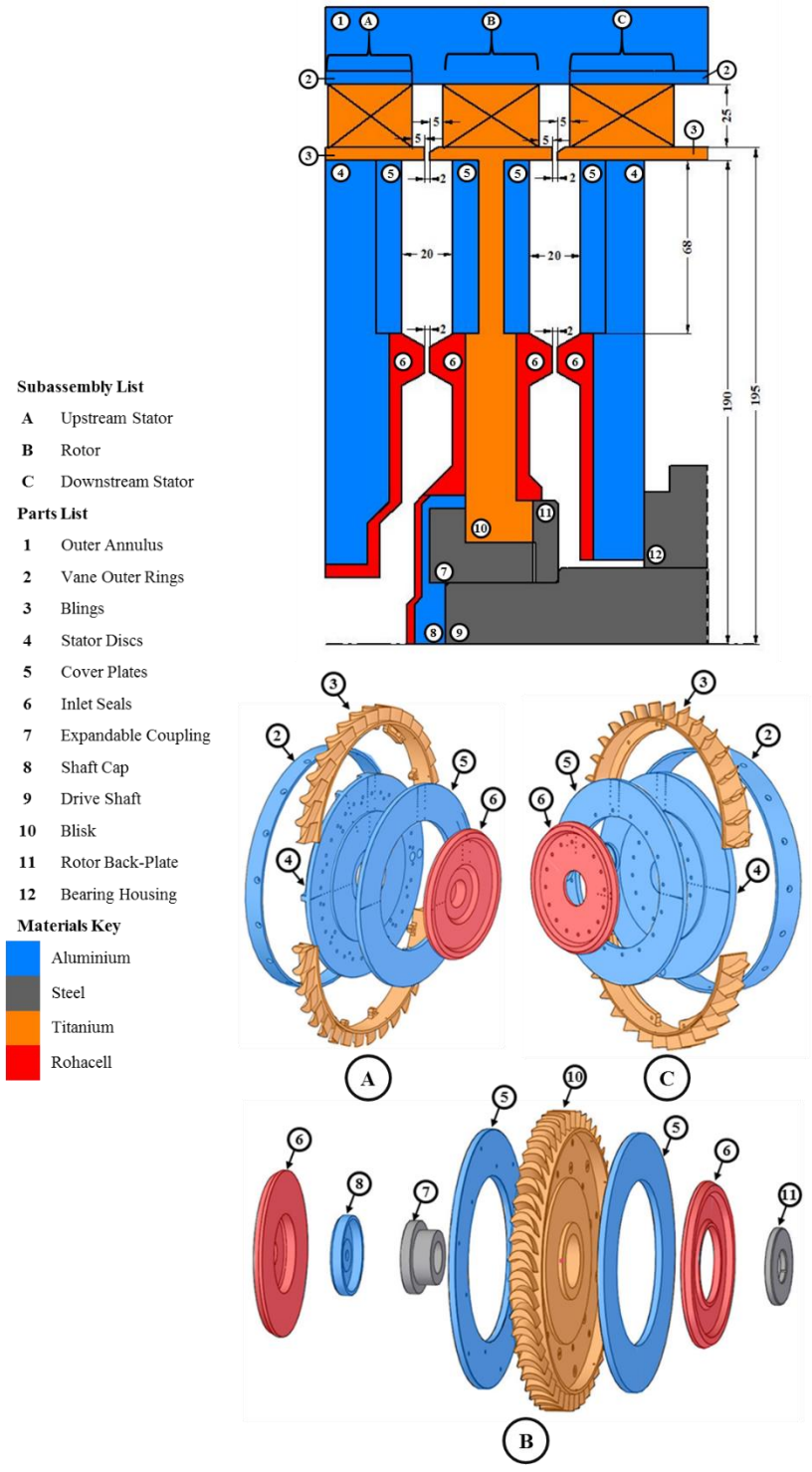

Figure 3.5 Colour-coded cross-section of turbine assembly based on material selection with exploded view of the upstream and downstream stator (A and C) and rotor (B) subassemblies.

3.3 Annulus and Sealing Flow Supply Assemblies

Figure 3.6 shows an exploded view of the mainstream and upstream sealing flow supply assemblies. A cross-section view focusing on materials selection and important dimensions is shown in Figure 3.7.

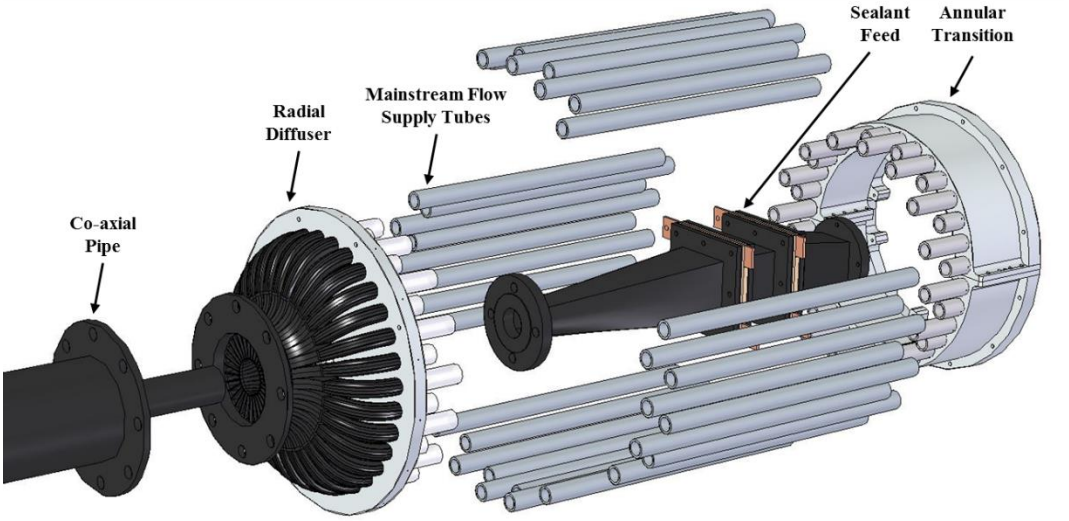

Figure 3.6: Explode view of mainstream and downstream sealing flow supply assemblies

Mainstream flow is supplied to the turbine by a 160 kW Atlas Copco compressor capable of delivering up to 1.6 kg/s of flow at a pressure of 1.2 bar and ambient temperature. The flow travels through a 6-inch co-axial pipe before it is fed through a radial diffuser. The radial diffuser consists of 32 carbon fibre composite flow-guides which are used to guide the mainstream flow from the outlet of the 6-inch pipe to 32 aluminium tubes (one per vane) leading to the turbine inlet. The flow guides are designed with an increasing cross-section in the direction of flow, reducing the velocity of the mainstream flow and thus regaining some of the pressure lost in the in the piping system. The transition from the circular cross-section of the supply tubes to the annular cross section of the turbine is achieved in the annular transition. In line with the general split design approach adopted for the 1.5-stage turbine facility, the annular transition is manufactured as two 180^{o} split rings, allowing for improved access to the instrumentation at the rear of the upstream stator disc. The distance between the inlet of the supply tubes and turbine entry is set so that fully developed flow is supplied to the turbine. To calculate the minimum length required for fully developed flow the following equation was used

$$L_e = 1.6dRe_d^{0.25} \quad \textbf{(Eq. 3.5)}$$

where L_e the length required for fully developed flow, d the diameter of the supply tubes (= 26.25 mm) and Re_d the Reynolds number based on the diameter d. The required length for fully developed flow is found to be L_e = 805 mm. Allowing for an error margin of about 5% the distance between the inlet of the supply tubes and turbine entry was set to 846 mm.

Sealing flow is supplied to the upstream wheel-space through the bore of the upstream stator disc via a 2-inch pipe and a sealant feed system. The feed system is made of carbon fibre composite and includes two 4 kW mesh heaters capable of raising the temperature of the sealing flow up to 60 ºC. A Rohacell® foam inner lining was included to minimise the amount of heat transfer from the flow to the walls of the feed system. For the purpose of the experiments described in the subsequent Chapters, no power is supplied to the mesh heaters and therefore the sealing flow is supplied at ambient temperature. The only case where the mesh heaters are used is during heat transfer experiments where a temperature difference between the sealing and annulus flow is required in order for uncertainties in experimental data to be minimised.

Figure 3.8 shows an exploded view of the downstream sealing flow supply assembly. A cross-section view focusing on materials selection is shown in Figure 3.9. Sealing flow is supplied to the downstream wheel-space via 12 flexible tubes connected to a sealant feed system featuring a manifold outlet. In terms of construction the downstream feed system is identical to the upstream one with carbon fibre composite used for the construction of the outer shell and Rohacell® foam for the inner lining. Mesh heaters are also included in the downstream feed system which are only used in heat transfer experiments.

Figure 3.10 shows the primary and alternative paths of the sealing flow in the upstream and downstream wheel-spaces. The path of the mainstream flow is also shown for completeness. Sealing flow can be supplied to the upstream wheel-space at low radius through the bore of the upstream stator disc (primary path) or at a higher radius through 16, equally spaced holes of 6 mm in diameter (alternative path). The primary path was used for supplying the sealing flow in the experiments in the upstream wheel-space described in Chapter 4. The alternative path is intended to be used in future experiments involving the effect of leakage flow from the vane carrier ring gap on ingress. Sealing flow to the downstream wheel-space can also be supplied through a primary and an alternative flow path. The downstream primary path involves the supply of the flow through 16 circumferentially spaced holes of 6 mm in diameter placed at low radius below the inlet seal; because of the rotor drive shaft passing through the bore of the downstream stator, bore supply was not possible in this case. The downstream alternative path is identical to that of the upstream, in both construction and purpose, and is

only intended to be used in future experiments. For the experiments described in Chapters 4 and 5, the sealing flow to the downstream wheel-space was introduced only through the primary path.

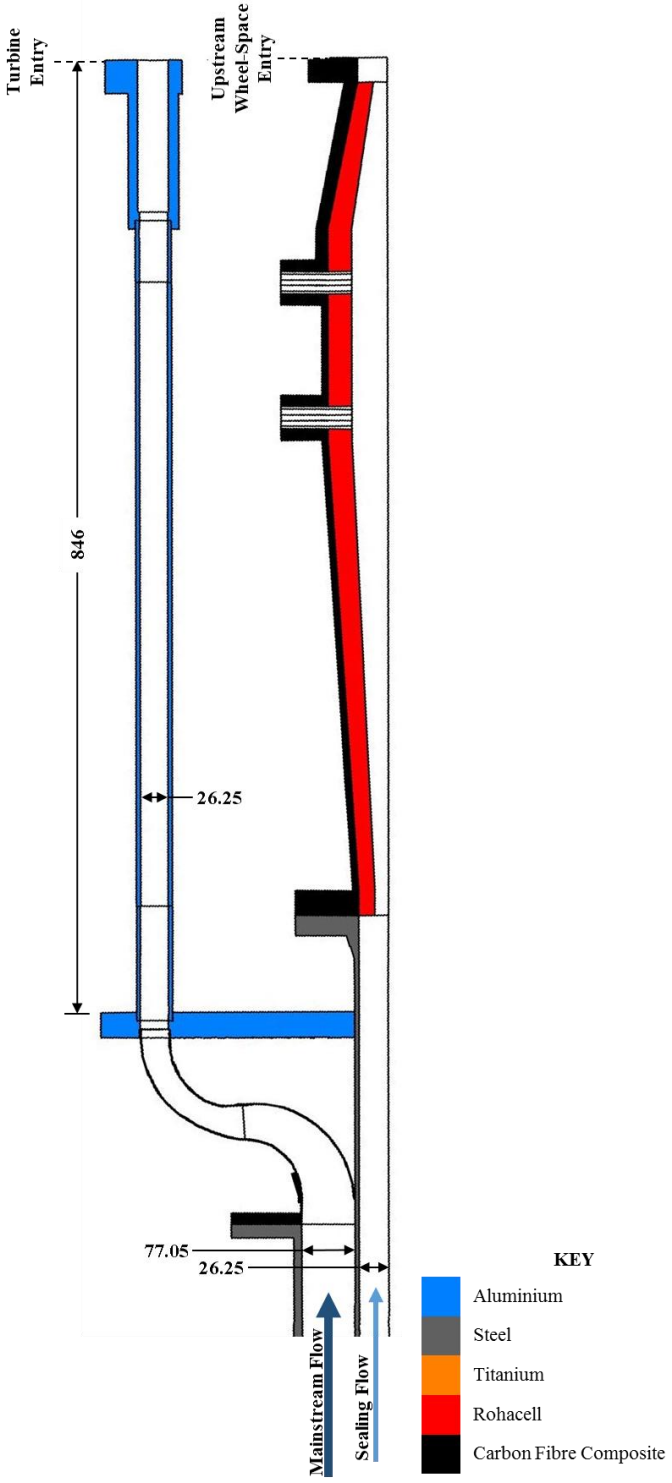

Figure 3.7: Cross-section of mainstream and upstream sealing flow supply assemblies indicating the materials used and important dimensions (all dimensions in mm)

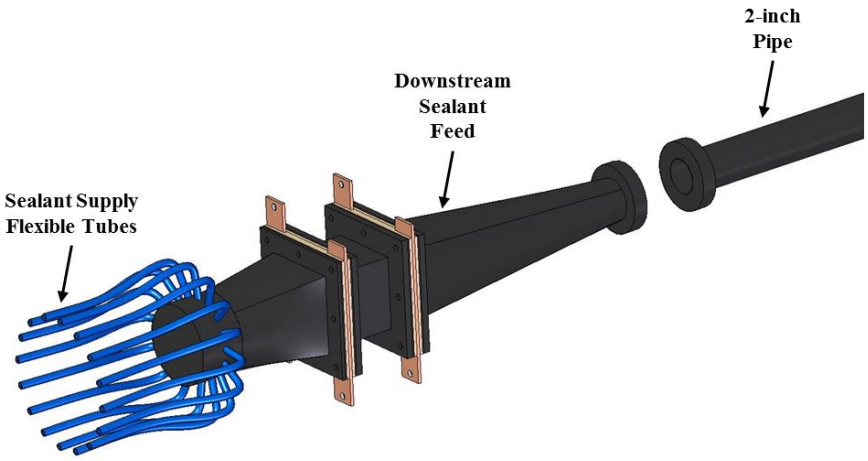

Figure 3.8: Exploded view of downstream sealing flow supply assembly

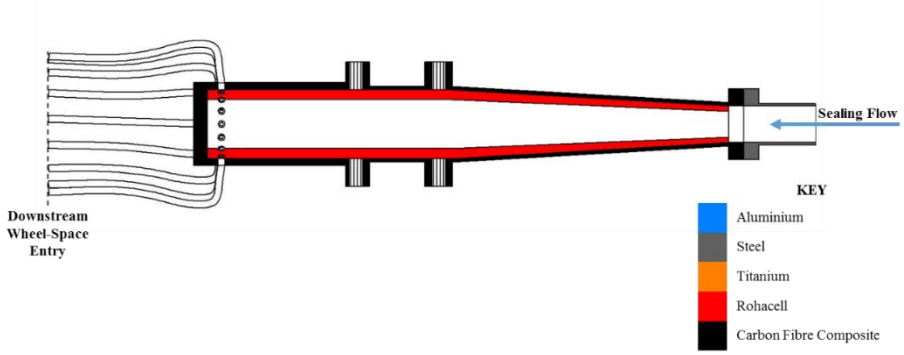

Figure 3.9: Cross-section of downstream sealing flow supply assembly indicating the materials used

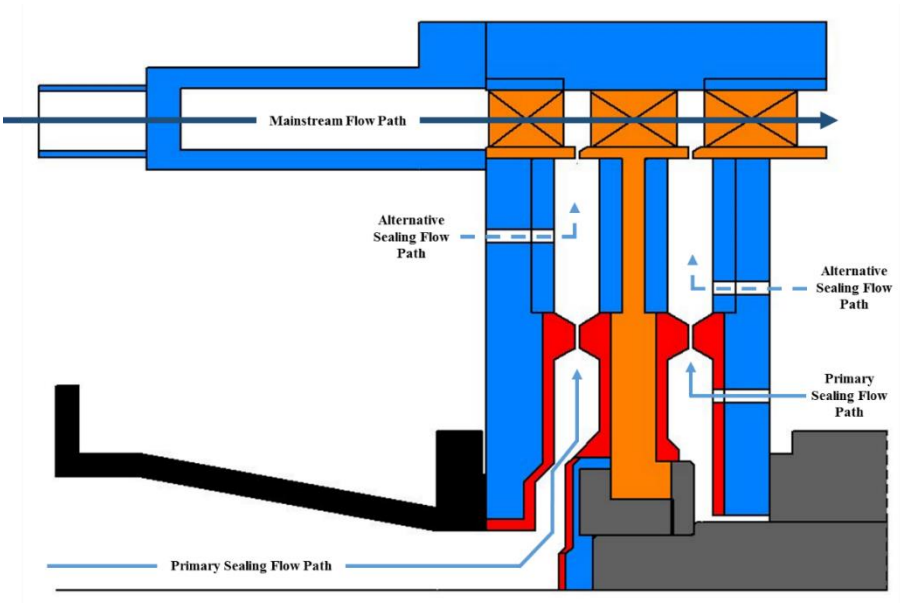

Figure 3.10: Turbine cross-section showing the mainstream and sealing flow paths (colours correspond to different materials as per Figure 3.5)

3.4 Experimental Capability

3.4.1 Measurement Locations

The design specifications of the 1.5-stage rig require a detailed investigation of the performance of various rim-seal geometries and the fundamental study of ingress. These demanded high instrumentation density in both the upstream and downstream wheel-spaces and in the annulus of the turbine.

Figure 3.11 and 3.12 show the locations at which static and total pressure, CO_2 concentration, temperature and rotor disc displacement measurements are taken in the 1.5-stage turbine facility. Figure 3.11 shows a cross-section of the turbine and Figure 3.12 a cut-out through the downstream stator and rotor discs exposing the upstream wheel-space stator wall.

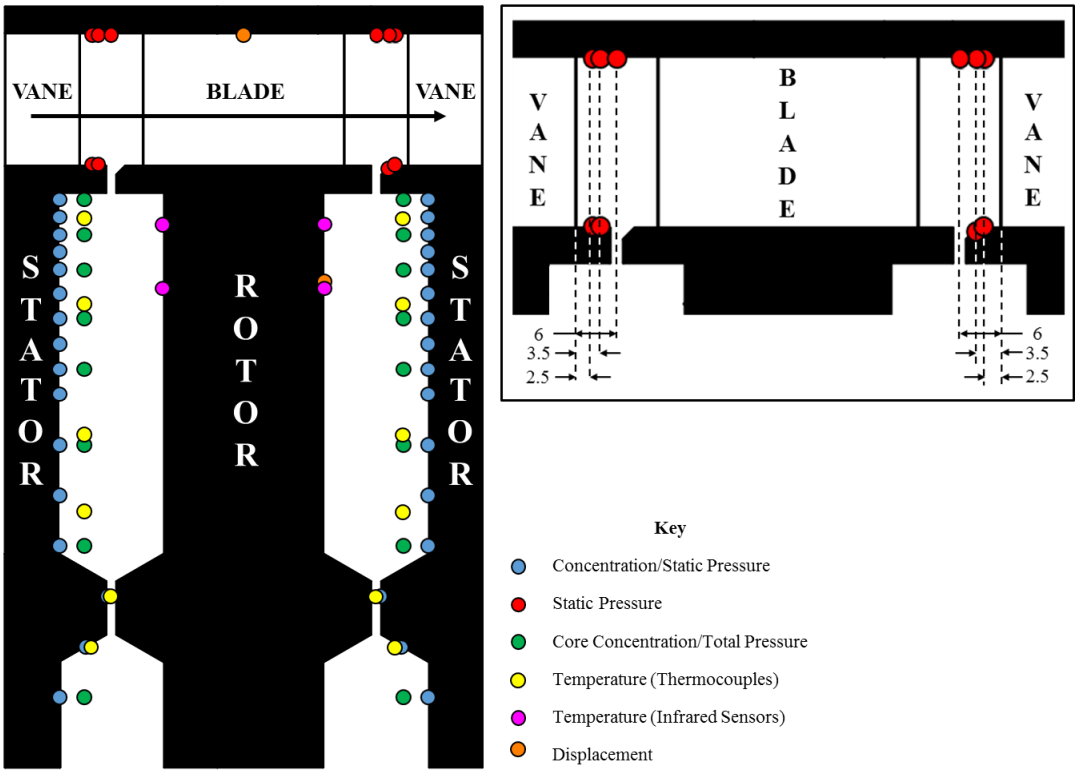

Figure 3.11: A cross-section of the 1.5-stage turbine showing the axial and radial locations for experimental measurements

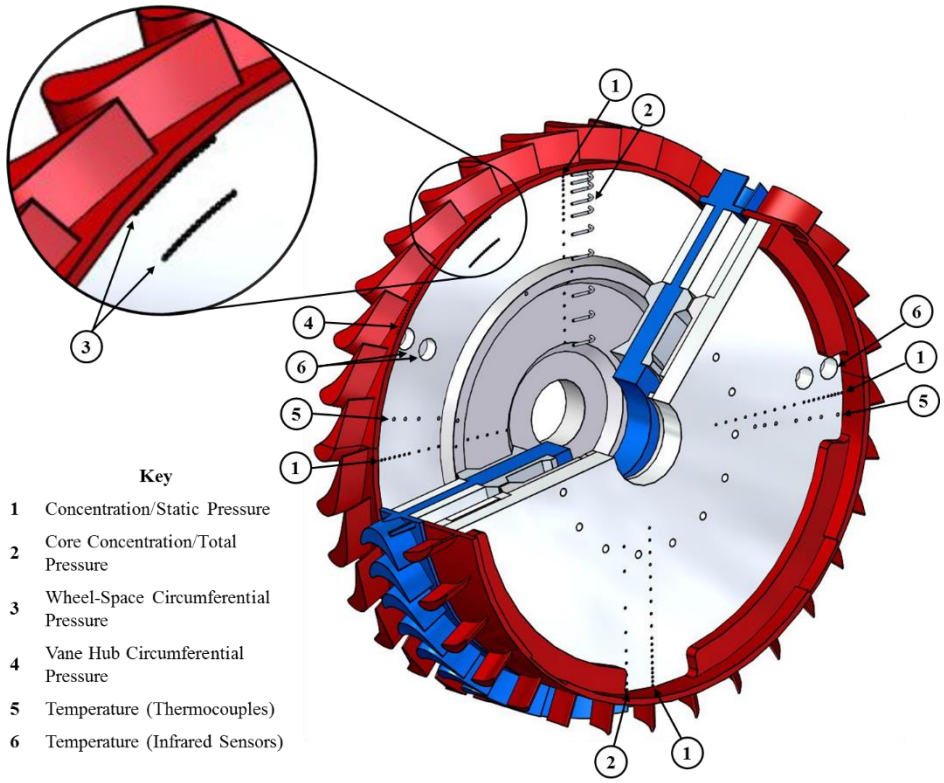

Figure 3.12: A cut-out through the upstream stator and rotor of the 1.5-stage experimental facility exposing the radial and circumferential locations for experimental measurements

Pressure measurements in the annulus can be taken at two radial locations at the shroud (outer radius) and at the hub (inner radius). At the shroud there are 12 sets of 15 pressure taps, each covering one vane pitch (11.25^o), and positioned at six axial locations (three upstream and three downstream of the blades) and two circumferential locations, 180^o apart. The axial positioning of the sets is 2.5 mm, 3.5 mm and 6 mm downstream of the upstream stator vanes and 2.5 mm, 3.5 mm and 6 mm upstream of the downstream stator vanes, as shown in the inset of Figure 3.11. At the hub there are eight sets of 15 pressure taps each covering one vane pitch and located at four axial locations and two circumferential locations, 180^o apart. The axial positioning of the hub sets is 2.5 mm, 3.5 mm downstream of the upstream stator vanes and 2.5 mm and 3.5 mm upstream of the downstream stator vanes.

Static pressure and CO_2 concentration can be measured in the upstream and downstream wheel-spaces at 20 radial locations on the surface of the stator discs and at two circumferential locations, 90^o apart. The circumferential variation of pressure and CO_2 concentration can be measured at three radial locations (r/b = 0.993; 0.958; 0.85) using three sets of 15 taps, covering one vane pitch. Total pressure measurements and core concentration measurements are taken at 10 radial locations using pitot-tubes positioned 5 mm away from the surface of the stator discs inside the rotating core. Measurements of rotating core temperature can be

taken in both the upstream and downstream wheel-space at six radial locations. The temperature on the rotor surface can be measured at two radial locations corresponding to *r/b* = 0.937 and 0.81, using infrared (IR) probes. Table 3.4 includes the radii of the locations at which static pressure/ stator-wall concentration, total pressure/core concentration and core temperature can be measured.

Non-Dimensional Radius (*r/b*)	Static Pressure/ Stator-Wall Concentration	Total Pressure/ Core Concentration	Core Temperature
0.993	•	•	–
0.976	•	–	–
0.974	–	–	•
0.958	•	•	–
0.941	•	–	–
0.924	•	•	–
0.900	•	–	–
0.889	–	–	•
0.875	•	•	–
0.850	•	–	–
0.831	–	–	•
0.825	•	•	–
0.800	•	–	–
0.750	•	•	–
0.740	–	–	•
0.700	•	–	–
0.658	–	–	•
0.650	•	•	–
0.600	•	–	•
0.550	•	•	•
0.500	•	–	–
0.450	•	–	–
0.400	•	•	–
0.350	•	–	–
0.300	•	•	–

Table 3.4: Radial locations at which static pressure/ stator-wall concentration, total pressure/core concentration and core temperature can be measured

3.4.2 Instrumentation and Definitions

The specifications of the instrumentation described below are summarised in Table 3.5.

Four Scani-Valves connected to differential pressure transducers supplied by ESI Technology are used for the measurement of steady static and total pressure. Each of the Scani-Valves consists of 48 channels allowing for measurements of pressure from 48 different sampling locations to be made using a single transducer. This allows for direct comparison of all the measurements taken using the same Scani-Valve as the same bias error applies. Differential transducers are also used for measuring the mainstream and sealing flow pressures. The accuracy of the differential transducers is provided by the manufacturer as ±0.3% of the measurement range. The measurements of static and total pressure are used for the calculation of the following non-dimensional parameters:

i. **Annulus pressure coefficient, $C_{p,a}$** given by

$$C_{p,a} = \frac{p_a - \overline{p_a}}{1/2\rho\Omega^2 b^2} \qquad \textbf{(Eq. 3.6)}$$

where p_a the annulus pressure at any of the 15 sampling locations in the annulus and $\overline{p_a}$ the average pressure across a vane pitch.

ii. **Wheel-space pressure coefficient, C_p** given by

$$C_p = \frac{p - p_{ref}}{1/2\rho\Omega^2 b^2} \qquad \textbf{(Eq. 3.7)}$$

where p the wheel-space pressure at any of the 20 sampling locations in the annulus and p_{ref} the pressure at $r/b = 0.6$.

iii. **Swirl ratio, β** given by Eq. 2.5 but also provided here for completeness

$$\beta = \frac{V_{\Phi,\infty}}{\Omega b} \qquad \textbf{(Eq. 3.8)}$$

where $V_{\Phi,\infty}$ the tangential component of velocity in the wheel-space calculated using Bernoulli's equation.

Ingress is quantified using measurements of CO_2 concentration which allows for both the mainstream and sealing flows to be at ambient temperature. Experiments using this method involve the seeding of the sealing flow with around 1% of CO_2 while the mainstream flow in the annulus is kept unseeded. The performance of rim-seals can be evaluated by considering the dilution, and therefore decrease of CO_2 concentration in the sealing flow, as a result of mixing with the ingested mainstream flow. The concentration of CO_2 in the upstream and downstream wheel-spaces can be measured using a 2-channel Signal Group gas analyser and two 20-channel multiplexers. The multiplexers are essentially an assembly of solenoid valves which can be automatically triggered so that flow samples from various locations in the wheel-spaces can be directed to the analyser. The gas analyser uses an infrared optical filter to determine the concentration of CO_2 in the sample which directly displays on two small screens and also transmits to the acquisition system. The gas analyser has an accuracy and repeatability of ±0.5% of its range and a linearity of ±0.5% of its range. The measurements of CO_2 concentration are used for determining the concentration effectiveness, ε_c which is given by Eq. 2.18 but also provided below for completeness

$$\boldsymbol{\varepsilon_c = \frac{c_s - c_a}{c_0 - c_a}} \qquad \textbf{(Eq. 3.9)}$$

where c_s the concentration on the stator wall evaluated at any radial position in the upstream downstream wheel-space, c_a the concentration in the annulus evaluated upstream of the turbine entry and c_0 the concentration in the sealing flow at entry to the wheel-space. When no sealing flow is provide to the wheel-spaces, the maximum amount of ingress occurs with $c_s = c_a$ and $\varepsilon_c = 0$. When adequate sealing flow is provided to the wheel-space so that no ingress occurs, $c_s = c_0$ and $\varepsilon_c = 1$.

The amount of mainstream flow supplied to the annulus and sealing flow supplied to the upstream and downstream wheel-spaces is measured and controlled using thermal mass flow meters and controllers (TMFMs). The accuracy of these TMFMs is provided by the manufacturer as ±0.5% of the measured value plus an additional ±0.1% of the full scale. The measurements of sealing flow rate are used for determining the non-dimensional sealing parameter Φ_0 defined in Eq. 2.4 but also provided below for completeness

$$\boldsymbol{\Phi_0 = \frac{C_{w,0}}{2\pi G_c Re_\Phi} = \frac{U}{\Omega b}} \qquad \textbf{(Eq. 3.10)}$$

where $C_{w,0}$, the non-dimensional axial flow rate defined in Eq. 2.2, $\dot{m}$, the mass flow rate of the sealing flow, G_c, the sealing clearance ratio, Re_Φ, the rotational Reynolds number and U the bulk mean radial velocity of sealing flow through the seal.

Measurements of temperature in the rotating core and rotor surface in the upstream and downstream wheel-spaces are primarily restricted to heat transfer experiments which the author did not conduct. For completeness, the instrumentation required to measure the aforementioned temperatures is also discussed here. Fast response K-Type thermocouples, manufactured at the University of Bath, are used for measuring the core temperature. These thermocouples have a frequency response of 160 Hz and measurement accuracy of ±0.2 ^{o}C. The temperature on the rotor surface is measured using infrared (IR) probes mounted on the stator discs. The frequency response of the IR probes is 10 Hz with an accuracy of ±0.2 ^{o}C and a target size of 6 mm. The temperature of the annulus and sealing flow is measured using standard K-type thermocouples with an accuracy of ±0.5 ^{o}C.

When sealing flow is supplied to either wheel-space, the pressure difference between the upstream and downstream sides of the rotor exerts a force which causes the blisc to deflect in the axial direction. Additionally, centrifugal forces cause a radial growth of the blisc. Considering that the seal clearance in the rig is 2 mm and that the blade tip clearance is 0.5 mm it is necessary to monitor the movements of the blisc. This is achieved using two capacitance sensors provided by Micro-Epsilon. The sensor monitoring the radial growth of the blisc is mounted on the outer casing and the sensor monitoring the axial displacement is mounted on the downstream stator disc. The resolution of the radial growth and axial displacement sensors is 0.0025 mm and 0.1 mm respectively. For the case of the radial growth sensor the resolution is 4% of the maximum radial growth of the disc (see Section 3.5.1) and for the case of the axial displacement sensor the resolution is 10% of the maximum allowable axial displacement of the rotor. The frequency response of both sensors is 5 kHz with a linearity of ±0.025% of the measurement range.

For the acquisition of experimental data and the control of the rig the Sierra-CP CADET system is used. CADET is a powerful, reliable and configurable data acquisition and test control system, most commonly used by the automotive industry for testing internal combustion (IC) engines. The adaptation of CADET to the needs of the 1.5-stage rig was made possible due to the similarity of IC engine and gas turbine engine test requirements. Figure 3.13 shows a schematic of the interaction between the instrumentation of the 1.5-stage test facility and CADET. There are 58 analogue input channels and four analogue output channels capable of receiving and transmitting a wide range of voltage and current signals. The instrumentation connected to the analogue input channels includes the displacement sensors,

thermocouples, pressure transducers, thermal mass flow meters and gas analyser. The instrumentation connected to the analogue output channels includes the thermal mass flow meter controllers, mainstream flow supply compressor and control valve. There are also 48 digital input and 24 digital output channels; these were solely used for controlling the two multiplexers and the Scani-Valves.

All of the results presented in the following chapters are derived from averaging the raw measurements of CO_2 concentration and pressure. The sampling period was 10 seconds at the the maximum acquisition frequency of CADET of 160 Hz.

Description	Manufacturer	Model	Range	Response	Accuracy
Differential Pressure Transducers	ESI Technology	PR3202	0 – 80 mbar	-	±0.3% of range
			-40 – 40 mbar		
			-20 – 20 mbar		
CO_2 Gas Analyser	Signal Group	9000MGA	1%	15s	±0.5% of range Linearity: ±0.5% of range
			5%		
			10%		
Thermal Mass Flow Meters and Controllers	Bronkhorst	F-106EI	1.42 kg/s	-	± (0.5% of reading + 0.1% of range)
		F206-AI	0.048 kg/s		
			0.02 kg/s		
		F-202AI	0.003 kg/s		
Thermocouples (fast response)	Custom Made	K-Type	10 – 70 °C	160 Hz	±0.2 °C
Thermocouples	TC Direct	K-Type	0 – 100 °C	-	±0.5 °C
Infrared Probes	Custom Made	N.A	10 – 70 °C	10 Hz	±0.2 °C
Displacement Sensors	Micro-Epsilon	capaNCDT 6220	0 – 0.5 mm	5 kHz	Linearity: ±0.025%
			0 – 20 mm		

Table 3.5: Instrumentation specifications for 1.5-stage turbine test facility

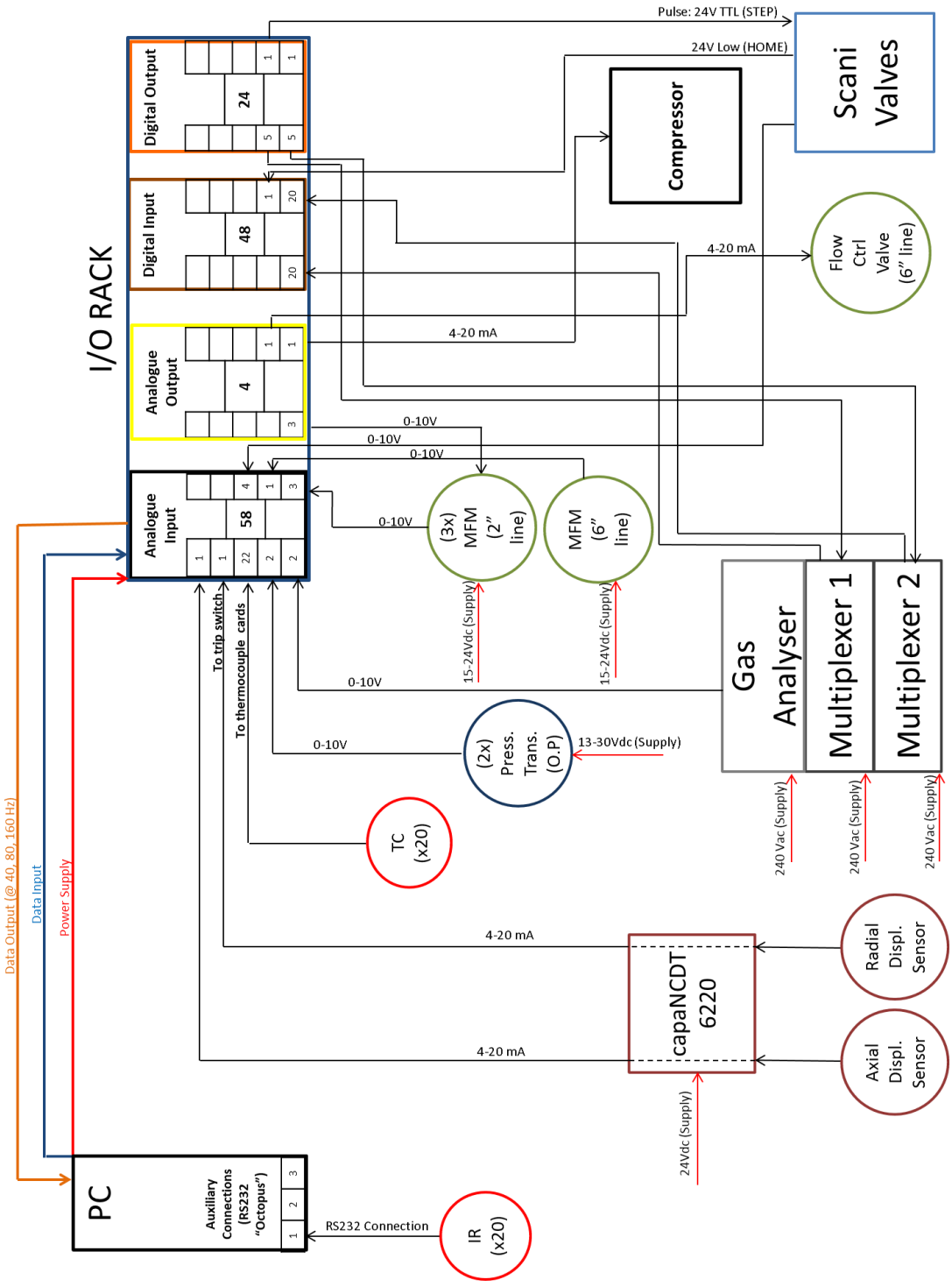

Figure 3.13: A schematic showing the interaction of the 1.5-stage turbine test facility with CADET, the control and acquisition system

3.4.3 Uncertainty in Measurements

The definition of sealing effectiveness (ε_c denoted here for simplicity as ε) is given in Eq. 3.2. Let δ_ε, δ_s, δ_0, δ_a be uncertainties in ε, c_s, c_0, c_a respectively so that

$$\begin{aligned}\boldsymbol{\varepsilon \pm \delta_\varepsilon} &= \frac{\boldsymbol{c_s \pm \delta_s - (c_a \pm \delta_a)}}{\boldsymbol{c_o \pm \delta_0 - (c_a \pm \delta_a)}} \\ &= \frac{\boldsymbol{(c_s - c_a)[1 + (\pm\delta_s \pm \delta_a)/(c_s - c_a)]}}{\boldsymbol{(c_0 - c_a)[1 + (\pm\delta_0 \pm \delta_a)/(c_0 - c_a)]}} \\ &= \boldsymbol{\varepsilon}\frac{\boldsymbol{[1 + (\pm\delta_s \pm \delta_a)/(c_s - c_a)]}}{\boldsymbol{[1 + (\pm\delta_0 \pm \delta_a)/(c_0 - c_a)]}}\end{aligned} \qquad \textbf{(Eq. 3.11)}$$

If $(\pm \delta_0 \pm \delta_a) / (c_0 - c_a) << 1$ then

$$\boldsymbol{\varepsilon + |\delta_\varepsilon| \le \varepsilon\left\{1 + \frac{|\delta_s| + |\delta_a|}{c_s - c_a} + \frac{|\delta_0| + |\delta_a|}{c_0 - c_a}\right\}} \qquad \textbf{(Eq. 3.12)}$$

Hence,

$$\boldsymbol{\frac{|\delta_\varepsilon|}{\varepsilon} \le \left\{\frac{|\delta_s| + |\delta_a|}{c_s - c_a} + \frac{|\delta_0| + |\delta_a|}{c_0 - c_a}\right\}} \qquad \textbf{(Eq. 3.13)}$$

If the uncertainty is a percentage of the full-scale range, which was the case in the experiments, then $\delta_s = \delta_0 = \delta_a = \delta$, say, and Eq. 3.13 simplifies to

$$\boldsymbol{\frac{|\delta_\varepsilon|}{\varepsilon} \le 2\delta\frac{1 + \varepsilon^{-1}}{c_0 - c_a}} \qquad \textbf{(Eq. 3.14)}$$

or

$$\boldsymbol{|\delta_\varepsilon| \le 2\delta\frac{1 + \varepsilon}{c_0 - c_a}} \qquad \textbf{(Eq. 3.15)}$$

The average standard deviation, σ, in the range $0 < \varepsilon < 1$ can be calculated from Eq. 3.15 by

$$\boldsymbol{\sigma = \frac{2\delta}{c_0 - c_a}\sqrt{\int_0^1 (1 + \varepsilon)^2 d\varepsilon} = 3.06\frac{\delta}{c_0 - c_a}} \qquad \textbf{(Eq. 3.16)}$$

The CO_2 gas analyser had an overall uncertainty of 0.015% of each of its ranges. In the tests, where the 1% range was used, the concentration of gas in the sealing flow was close to the 1% range maximum. Hence $\delta / (c_0 - c_a) \approx 0.015$, and from Eq. 3.16 it follows that $\sigma \approx 0.046$. This value, which is an upper bound, exceeds the standard deviation found from the fitted $\Phi_0 - \varepsilon$ curves.

3.5 Commissioning Measurements

3.5.1 Blisc Radial Growth

One of the most important commissioning tests is the experimental determination of the radial growth of the blisc under operating conditions. The results of this test are used to determine whether an adequate blade tip clearance is provided and also to determine the dynamic clearances of rim-seals. To measure the radial growth, the rig was set to the disengaged position where the rotor and downstream stator are pulled back outside of the outer casing. This allows for displacement measurements at three locations: the tip of the blades, and the top and bottom sides of the shroud. A capacitance sensor was used for the measurement of the radial growth with a range of 0 to 0.5 mm and a target area requirement of 6 mm. High accuracy was required because of the significance of the test and therefore it was not only important to meet the target area requirements but also to have a continuous surface at which the sensor is pointed. A rim-seal was installed at the underside of the blisc hub to achieve both requirements, as shown in Figure 3.14.

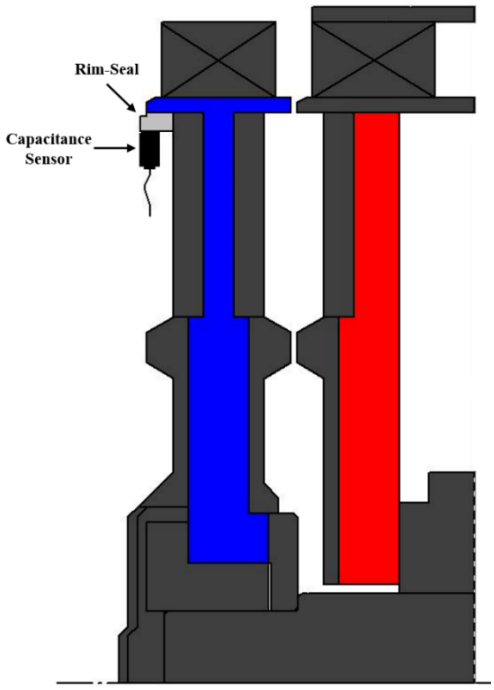

Figure 3.14: Arrangement of radial growth test (blue: blisc; red: downstream stator disc)

The radial growth of a rotating disc is due to the centrifugal force defined as

$$F = m\Omega^2 r \qquad \textbf{(Eq. 3.17)}$$

where F is the centrifugal force, m the mass of the disc, Ω the disc rotational speed in rad/s and r the radius of the disc.

Figure 3.15 shows the variation of radial growth of the blisc δ with the square of rotational speed Ω^2. As expected δ increases linearly with Ω^2. The deflection of the disc at the two operating speeds, 3000 and 4000 rpm, is 0.0325 mm and 0.0587 mm. The latter is an order of magnitude less than the blade tip clearance (0.5 mm) ensuring safe operation of the rig. A straight line passing through (0, 0) was fitted to the experimental results. This can be used for calculating the dynamic radial clearance of the seals at any operating speed. The equation of the fitted line is given by

$$\delta = 0.003\Omega^2 \qquad \textbf{(Eq. 3.18)}$$

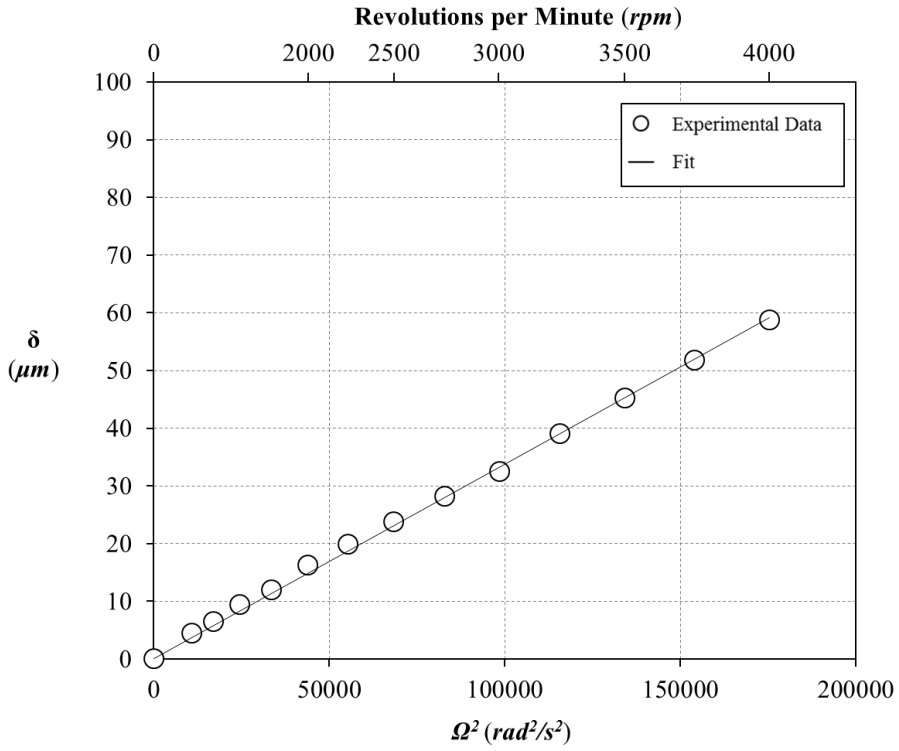

Figure 3.15: Variation of radial growth of rotor disc with rotational speed

3.5.2 Axisymmetry of Mainstream Flow Supply

It is important to have axisymmetric flow to the inlet of the turbine as non-axisymmetric supply can result in circumferential differences in the level of ingress into the wheel-space. Figure 3.16 shows the variation of static pressure with circumferential position measured at 32 locations (one per vane) just upstream of the turbine inlet. A straight line indicating the average pressure value is also included. The maximum variation in supply pressure is found to be 1.8 mbar which results in an asymmetry of 3%.

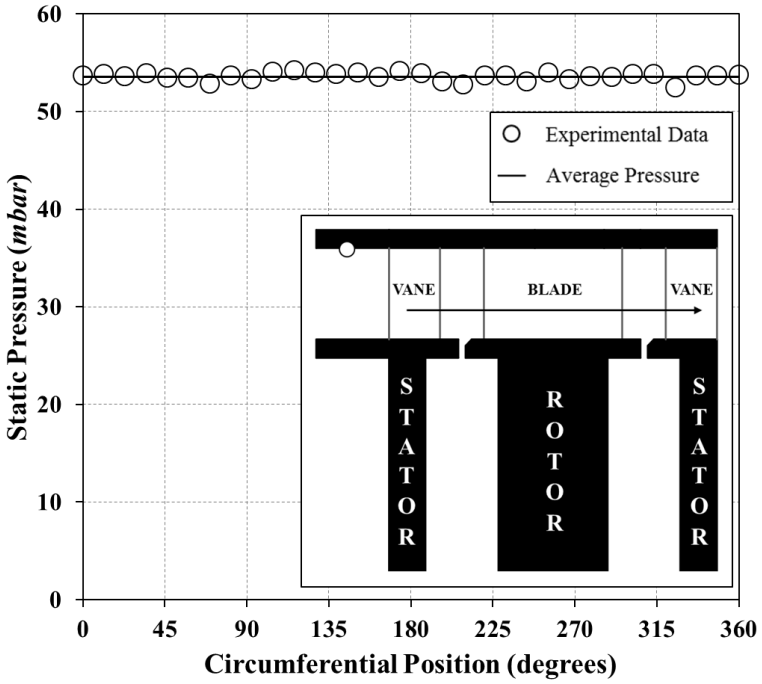

Figure 3.16: Static pressure variation in mainstream flow supply tubes ($Re_w = 2.4\times10^5$)

3.5.3 Annulus Pressure Variation

The circumferential pressure variation in the annulus is the cause for externally-induced (EI) ingress. Figure 3.17 shows the variation of non-dimensional pressure $C_{p,a}$ with non-dimensional vane pitch θ in the annulus, at four locations on the hub (A1 to A4) and six locations on the shroud (B1 to B6) upstream of the rotor blades. The measurements were made for the case of no sealing flow, i.e. at $\Phi_0 = 0$. The asymmetry in the upstream pressure locations (A1, A2 and B1 to B3) is caused by the potential field of the upstream vane. In contrast, the downstream measurements (A3, A4 and B4 to B6) demonstrate the influence of the bow-wave that propagates forward from the downstream vane leading edge.

Figure 3.18 shows how $\Delta C_{p,a}$ varies in the annulus at all of the measurement locations. Upstream of the rotating blades at both the vane platform (A locations) and outer shroud (B locations), $\Delta C_{p,a}$ decreases with axial distance x. The difference in peak-to-trough pressure decays with axial distance from the upstream vane trailing edge. The downstream measurements show that $\Delta C_{p,a}$ increases as the vane leading edge is approached and the effect of the bow-wave is intensified. For both the upstream and downstream measurements a difference in $\Delta C_{p,a}$ can be observed when comparing the results taken at the same axial location on the vane platform and outer shroud, e.g. A1 with B1 and A3 with B5. Swirl in the annulus causes a radial pressure gradient which results in larger $\Delta C_{p,a}$ values at the outer locations. Figure 3.18 highlights that $\Delta C_{p,a}$ depends on where in the annulus it is measured and that the non-dimensional peak-to-trough pressure difference, $\Delta C_{p,a}$ is greater upstream than that downstream.

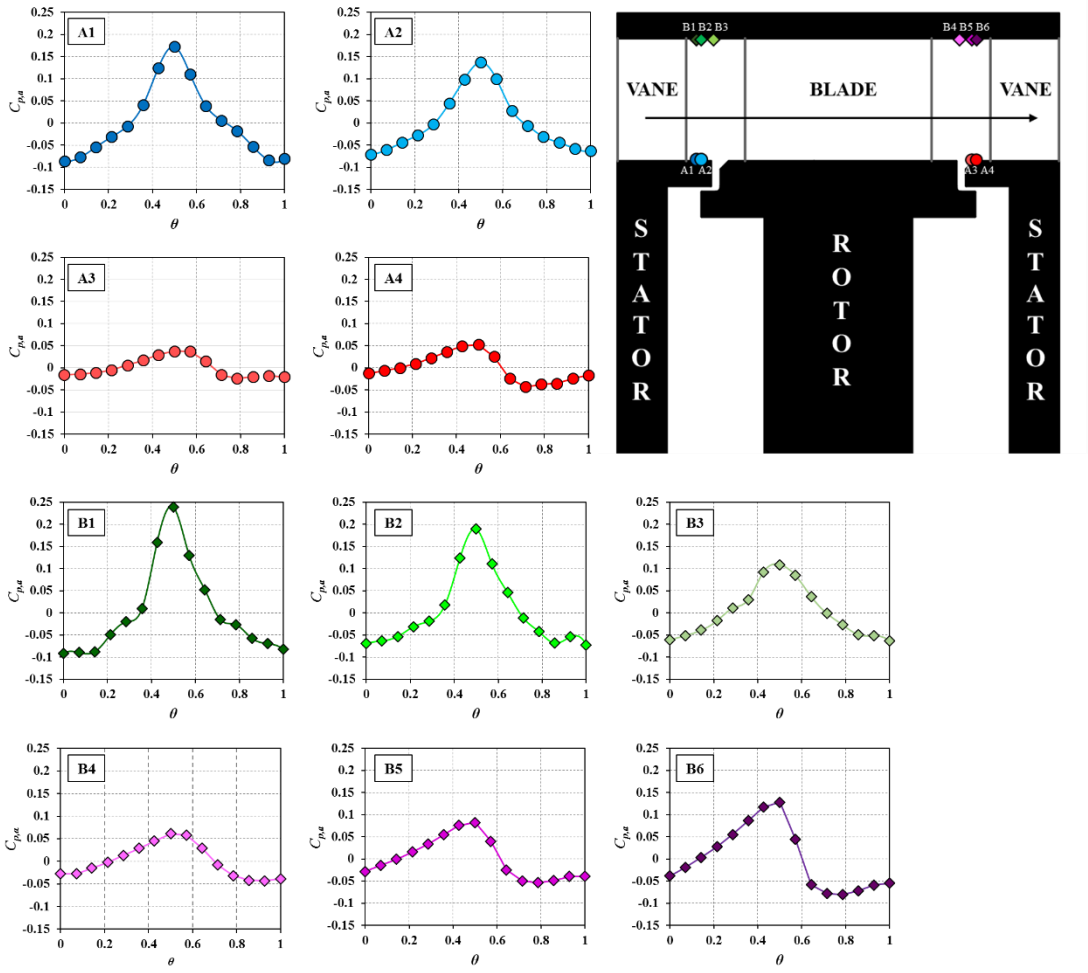

Figure 3.17: Circumferential pressure variation in the annulus at locations A1 to A4 and B1 to B6 (C_F = 0.34, Re_Φ = 7.2 × 10^5, Φ_0 = 0)

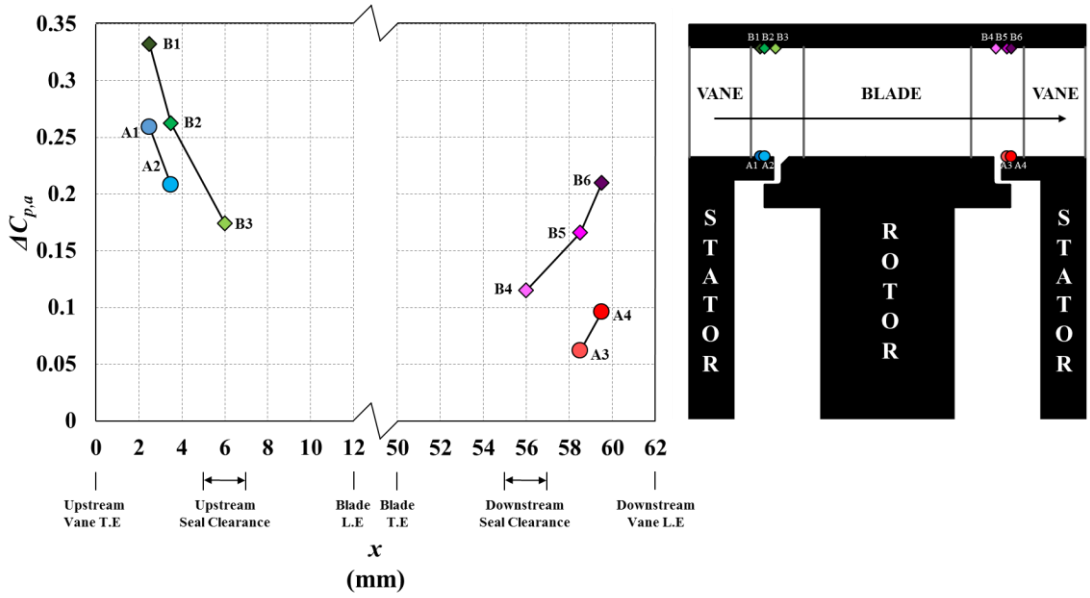

Figure 3.18: Variation of annulus peak-to-trough pressure difference (C_F = 0.34, Re_Φ = 7.2 × 10^5, Φ_0 = 0)

Figure 3.19 shows the variation of $\Delta C_{p,a}^{1/2}$ with flow coefficient, C_F in the annulus upstream of the rotating blades at locations A1, A2, B1, B2 and B3. For all measurement locations $\Delta C_{p,a}^{1/2}$ increases linearly with C_F. The amount of ingestion of mainstream flow in the upstream wheel-space is therefore expected to increase as C_F increases. The variation of $\Delta C_{p,a}^{1/2}$with C_F was correlated by

$$\Delta C_p^{1/2} = k_a C_F \qquad \textbf{(Eq. 3.19)}$$

where k_a an empirical constant representing the gradient of the straight lines. The values of k_a at the various measurement locations are provided in the table within the figure.

Figure 3.20 shows the variation of $\Delta C_{p,a}^{1/2}$ with C_F in the annulus downstream of the rotating blades, at locations A3, A4, B4, B5 and B6; unlike the upstream variation the relationship is clearly not linear. For all locations $\Delta C_{p,a}^{1/2}$ reaches a minimum at a flow coefficient close to the operating point, where the flow velocity triangles are aligned with the inlet angle of the downstream vane. Either side of this, the blockage increases as the flow impinges on the vane causing an increase in pressure. The outer shroud locations will also be affected by the blade tip clearance and the corresponding leakage flow.

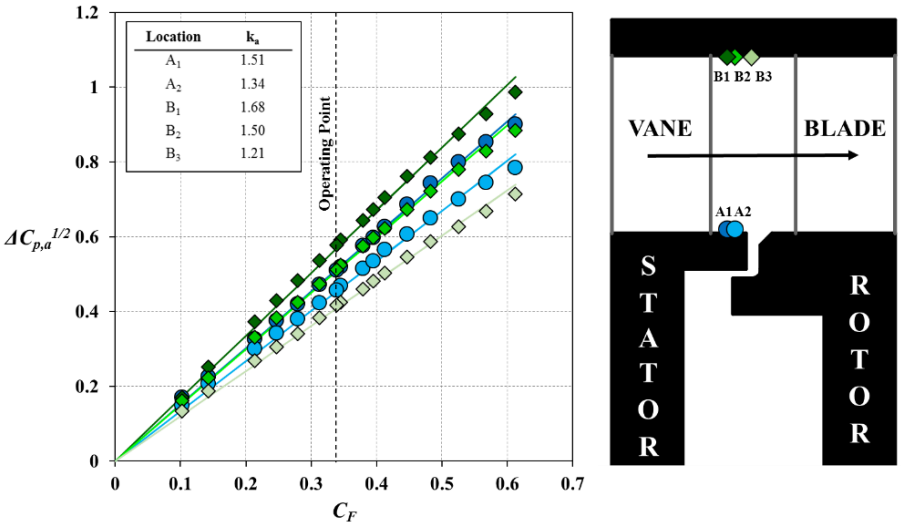

Figure 3.19: Variation of $\Delta C_{p,a}^{1/2}$ with flow coefficient C_F in the annulus upstream of the rotor blades ($Re_\Phi = 7.2 \times 10^5$, $\Phi_0 = 0$)

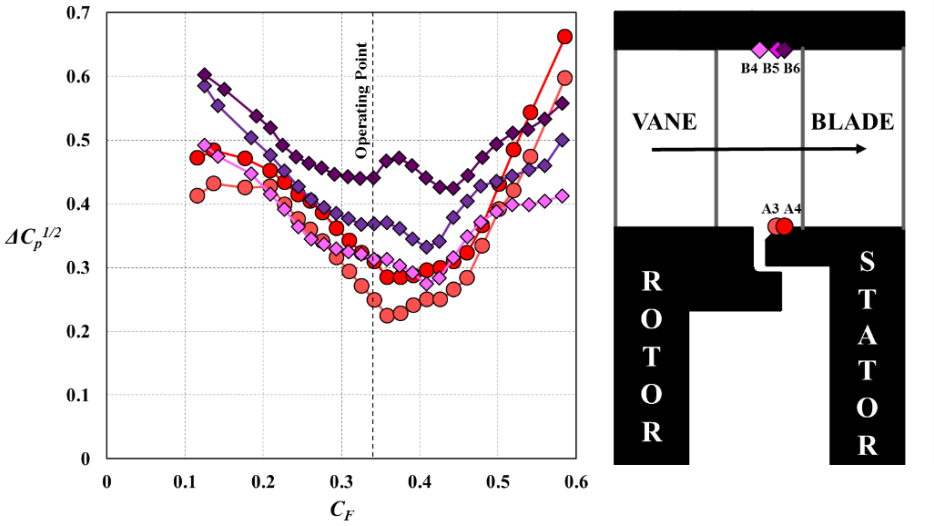

Figure 3.20: Variation of $\Delta C_{p,a}^{1/2}$ with flow coefficient C_F in the annulus downstream of the rotor blades ($Re_\Phi = 7.2 \times 10^5$, $\Phi_0 = 0$)

3.6 Summary

In this chapter a detailed overview of the design features, operating capabilities, employed instrumentation and commissioning of the new 1.5-stage turbine experimental facility was presented.

The turbine assembly of the new facility consists of an upstream and downstream stator featuring 32 vanes and a rotor with 48 turned blades. The geometry of the vanes and blades was provided by Siemens and is a scaled-down version of the vane-blade geometry of the Siemens SGT-8000H engine. Both sets of vanes were manufactured in two integrated 180^o split rings which are mounted to the periphery of the stator discs to form blings. The split design of the blings allows for virtually any rim seal geometry, axially or radially assembled, to be installed and tested. The blades and rotor disc are also manufactured as a single component to form a blisc. The blisc can be rotated to speeds of up to 4000 rpm by the means of a 34 kW dynamometer. The dynamometer is also used to absorb the power generated by the stage.

Experiments can be performed at two rotational speeds, 3000 rpm and 4000 rpm. At the higher operating speed the rotational Reynolds number is, $Re_\Phi = 1 \times 10^6$. The operating flow coefficient is $C_F = 0.34$ which created an axial Reynolds number, $Re_w = 3.4\times 10^5$. The vane exit Mach number achieved at this condition is $M = 0.37$.

Measurements of static and total pressure, temperature and CO_2 concentration can be taken at various axial, radial and circumferential locations in both the upstream and downstream wheel-spaces and annulus. Four, 48-channel Scani-Valves connected to differential pressure transducers are used to measure pressure. Fast response thermocouples and infrared sensors are used to measure the temperature in the rotating core and on the rotor surface respectively. A two-channel infrared gas analyser connected to two, 20-channel multiplexers is used for measuring CO_2 concentration on the stator wall and in the rotating core in both wheel-spaces.

Measurements of the radial growth of the rotor disc, pressure at the turbine inlet and pressure in the annulus upstream and downstream of the rotor blades were taken as part of the commissioning of the rig. At the maximum operating speed of 4000 rpm the rotor disc was found to have grown by almost 0.06 mm. This is an order of magnitude smaller than the blade tip clearance (0.5 mm). The pressure measurements at the turbine inlet upstream of the stator vanes showed a maximum variation of 1.8 mbar resulting in an asymmetry of 3%. This value is very small and therefore the supply of mainstream flow to the turbine was considered axisymmetric. The pressure in the annulus upstream and downstream of the rotor blades was found to have the expected circumferential variation, as a result of the flow passing through

the stator vanes. In general the peak-to-trough difference $\Delta C_{p,a}$ upstream of the rotor blades was found to be greater than that downstream. $\Delta C_{p,a}$ was shown to decay with axial distance away from the upstream vane trailing edge and increase as the downstream vane leading edge was approached and as the influence of the bow-wave was intensified. The variation of $\Delta C_{p,a}^{1/2}$ in the annulus upstream of the rotor blades varied linearly with flow coefficient C_F whereas downstream reached a minimum at a C_F close to the operating point.

Chapter 4: Ingress through Generic Seals in the Upstream and Downstream Wheel-Spaces

This chapter examines ingress through a generic single and a generic double radial-clearance seal in the upstream and downstream wheel-spaces of the 1.5-stage rig. The expected flow structure in the two wheel-spaces is discussed first in terms of concentration measurements. Measurements of the radial distribution of concentration effectiveness, swirl ratio and pressure in the upstream and downstream wheel-spaces are then provided and used as evidence to support the expected flow structures. The variation of concentration effectiveness with sealing flow rate in the upstream and downstream wheel-spaces for the two seals is also presented. A simple theoretical model is fitted to the experimental results indicating good agreement between experiment and theory in all cases. A comparison of the concentration measurements taken using the same seal in the upstream and downstream wheel-spaces is provided. This indicates a weaker driver for ingress in the downstream wheel-space. The driver for ingress in the downstream wheel-space is further investigated using concentration measurements. The results show that rotationally-induced (RI) ingress occurs in the downstream wheel-space.

4.1 Background

4.1.1 Flow Structure and Concentration Measurements

Figure 4.1 shows a simplified version of the flow structure in the upstream and downstream wheel-spaces of gas turbine engines. Detailed discussion of its characteristics is provided in Chapter 2, Section 2.4. The purpose of this section is to relate these characteristics to the CO_2 concentration, and hence effectiveness measurements expected to be seen in the experiments.

In a typical experiment ingress through rim-seals is evaluated using the concentration technique whereby CO_2 is injected to the sealing flow so that its concentration $c_0 = 1\%$ whilst the annulus flow is kept unseeded so that $c_a = 0\%$. Upon its entry to the wheel-space, the sealing flow is entrained into the rotor boundary layer where it moves radially outwards towards the shroud of the wheel-space and into the outer region. In the outer region it mixes with the ingested flow before being entrained into the stator boundary layer where radial inflow occurs. In the stator boundary layer no further mixing occurs and therefore the concentration on the stator wall c_s is expected to be invariant with radius. A rotating core of inviscid fluid exists between the stator and the rotor boundary layers. Flow from the stator boundary layer migrates towards the rotor boundary layer through this core. The concentration of the core c_∞ is therefore expected to be equal to that of the stator wall so that $c_s = c_\infty$.

As explained in Section 2.4, the flow structure in the downstream wheel-space is expected to be a mirror-image of that in the upstream. Considering this, the above discussion also applies to the downstream wheel-space and therefore the concentration measurements taken in the two are expected to be qualitatively similar.

The biggest difference between the upstream and downstream wheel-spaces is that in the downstream case the egress from the rotor side creates an axisymmetric jet (or fluid 'barrier') that the ingress stream tubes in the mainstream flow must cross before fluid is ingested into the wheel-space. The mass flow rate and CO_2 concentration of egress will be greater than that of the ingress. The subsequent exchange of angular momentum and chemical species (that is, CO_2) between the ingress and egress at the entrance to the seal will therefore result in two effects: (*i*) a reduction in the unsteady non-axisymmetric distribution of pressure immediately outside the seal clearance; and (*ii*) an increase in the level of CO_2 concentration of the ingested fluid. Relative to the upstream case, both these effects will create an increase in the measured sealing effectiveness in the downstream wheel-space. As the sealing flow rate is increased and the ingress is consequently reduced, these effects will result in an improved effectiveness for the downstream seal. Attenuation of the pressure asymmetry in the flow near the seal clearance will tend to create combined ingress (see Section 1.5.3) and, in the limit, rotationally-induced ingress (see Section 1.5.2).

Sangan *et al.* (2013) provided experimental evidence of the flow structure in the wheel-space of a single-stage rig by showing that the concentration effectiveness ε_c was invariant with radius for a number of different generic rim-seals. In the following sections of this chapter, the flow structure will be explained in more detail using unprecedented measurements of CO_2 concertation in the rotating core taken in both the upstream and downstream wheel-spaces. The new measurements along with traditional measurements of the radial variation of ε_c on the stator will be used as evidence to support the expected flow structure in the upstream and, for the first time, in the downstream wheel-space. Measurements of the variation of effectiveness with sealing flow rate (ε_c vs. Φ_0) will be used to examine, also for the first time, the effect of the egress 'barrier' on ingress and to provide insights on the driving mechanism for ingress into the downstream wheel-space.

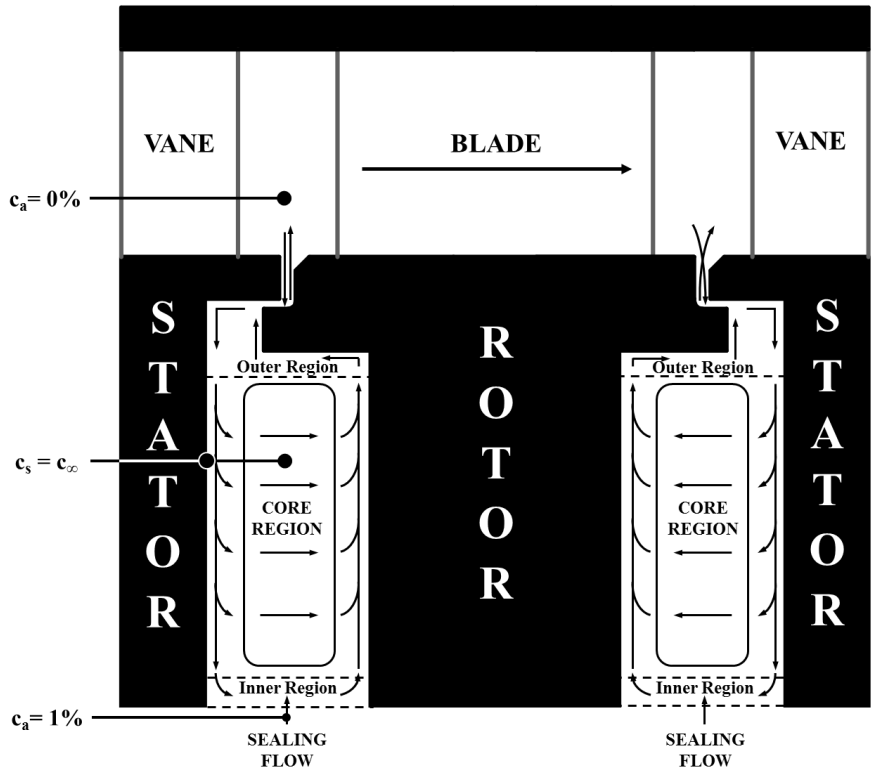

Figure 4.1: Simplified flow structure in the upstream and downstream wheel-spaces with expected concentration values.

4.1.2 Generic Rim-Seal Geometries

Figures 4.2 and 4.3 show the geometric configurations of the single and double radial-clearance seals used for the investigation of the flow structure in the upstream and downstream wheel-spaces. The most important dimensional parameters of the seals are also included in these figures and their dimensions can be found in Table 4.1.

The single radial-clearance seal (also referred to as *single seal*) consists of a rotor-side lip that is mounted into the underside of the rotor-disc shroud. This lip forms a single radial-clearance $s_{c,rad}$ with the stator-disc shroud of 1.28 mm. The double radial-clearance seal (also referred to as *double seal*) consists of both stator- and a rotor-side pieces that are also mounted in the underside of the shroud of their corresponding discs. The rotor-side piece features two lips that, along with the stator-disc shroud and the stator-side lips, form an outer and an inner seal, both having a radial clearance $s_{c,rad}$ = 1.28 mm. An outer wheel-space is formed between the outer and inner seals. The outer wheel-space is most commonly referred to as the buffer cavity and its height h_{buffer} = 16.5 mm. An inner wheel-space is formed below the inner seal extending all the way to an inlet seal (not shown in figures), through which the sealing flow is supplied. The reader is referred to Chapter 3, Section 3.3 for more information regarding the

supply of sealing flow to the wheel-spaces. All stator- and rotor-side features of both seals have a common axial distance, $s_{c,ax}$ = 2 mm with a common upstream and downstream wheel-space axial width, S = 20 mm. These two dimensions provide a gap ratio, G = 0.1 which should provide separated boundary layers in the wheel-spaces (see Daily and Nece (1960)). The two seals also share the same axial overlap $s_{overlap}$ = 1.86 mm, between their stator- and rotor-side features.

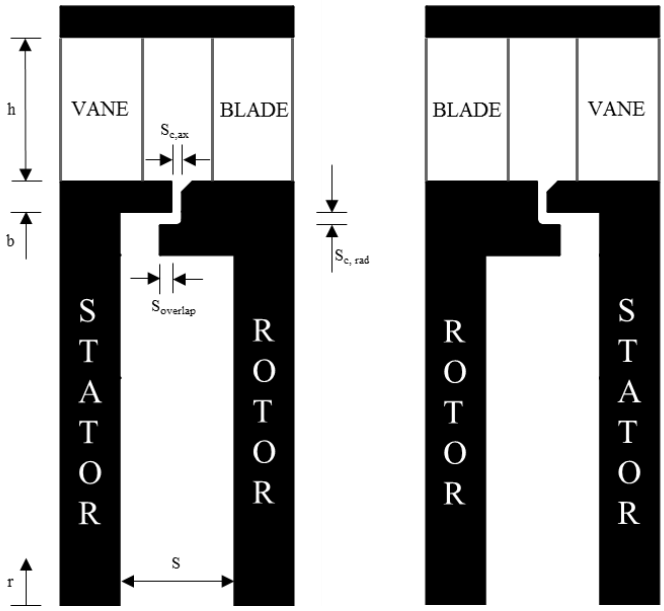

Figure 4.2: Single radial-clearance seal configuration in the upstream and downstream wheel-spaces

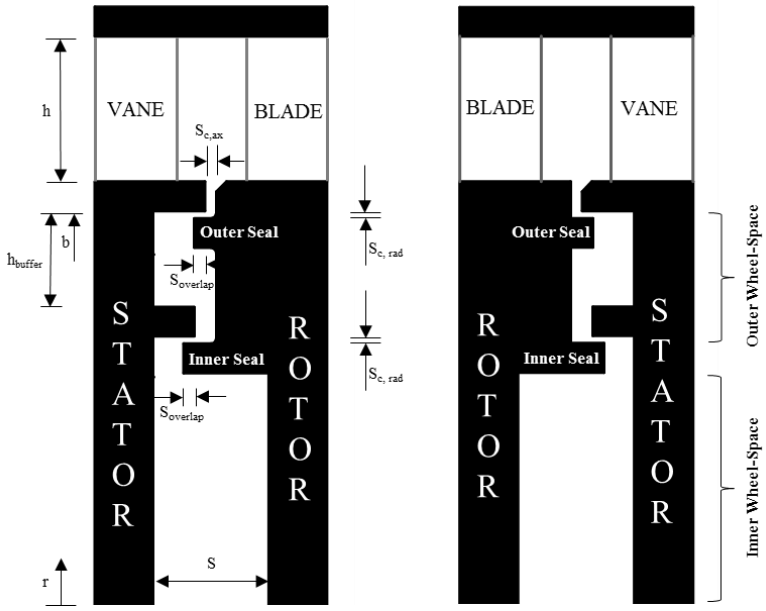

Figure 4.3: Double radial-clearance seal configuration in the upstream and downstream wheel-spaces

Dimensional Parameter	Dimensions (mm)	
	Single Radial-Clearance Seal	Double Radial-Clearance Seal
h	25	
b	190	
S	20	
$s_{c,ax}$	2	
$s_{c,rad}$	1.28	
$s_{overlap}$	1.86	
h_{buffer}	-	16.5

Table 4.1: Dimensions of single and double radial-clearance seals

4.1.3 Experiment Conditions

Table 4.2 lists the operating conditions for the experiments presented in the subsequent sections. Measurements have been taken at two rotor disc speeds of 3000 and 4000 rpm resulting in rotational Reynolds numbers, Re_Φ = 7.2 × 10^5 and 1.0 × 10^6 respectively. According to Owen and Rogers (1989) the flow structure in rotor-stator systems is controlled by the turbulent flow parameter λ_T (given by Eq. 2.6) and it is marginally affected by Re_Φ. The turbulent flow parameter controls the swirl ratio β in the wheel-space and therefore the amount of fluid entrained into the rotor boundary layer. A value of $\lambda_T \approx 0.22$ corresponds to the case of the free-disc entrainment. In modern engines $\lambda_T << 0.22$. Although the 1.5-stage rig cannot achieve the high Reynolds numbers experienced in engines (where $Re_\Phi > 10^7$), the flow rates are chosen to match typical engine-values of λ_T, ensuring representative flow structures. The mass flow rate entering the turbine annulus is controlled in order to set a flow coefficient C_F = 0.34. This corresponds to an axial Reynolds number Re_w = 2.4 × 10^5 and 3.4 × 10^5 and an upstream vane exit Mach number M = 0.28 and 0.34 for 3000 rpm and 4000 rpm respectively.

Parameters	Disc Speed (rpm)	
	3000	4000
Rotational Reynolds Number, $\boldsymbol{Re_\Phi}$	7.2×10^5	1.0×10^6
Axial Reynolds Number, $\boldsymbol{Re_w}$	2.4×10^5	3.4×10^5
Flow Coefficient, $\boldsymbol{C_F}$	0.34	
Vane exit Mach Number, $\boldsymbol{M}$	0.28	0.37

Table 4.2: Operating conditions of experiments

4.2 Ingress in the Upstream Wheel-Space

This section presents experimental measurements of concentration effectiveness ε_c, swirl ratio β and pressure coefficient C_p in the upstream wheel-space. For these experiments the single and double radial-clearance seals described in Section 4.1.2 were used. The results support the expected flow structure in the upstream wheel-space and show that ingress can be accurately predicted using a simple orifice model.

4.2.1 Radial Distributions of Effectiveness

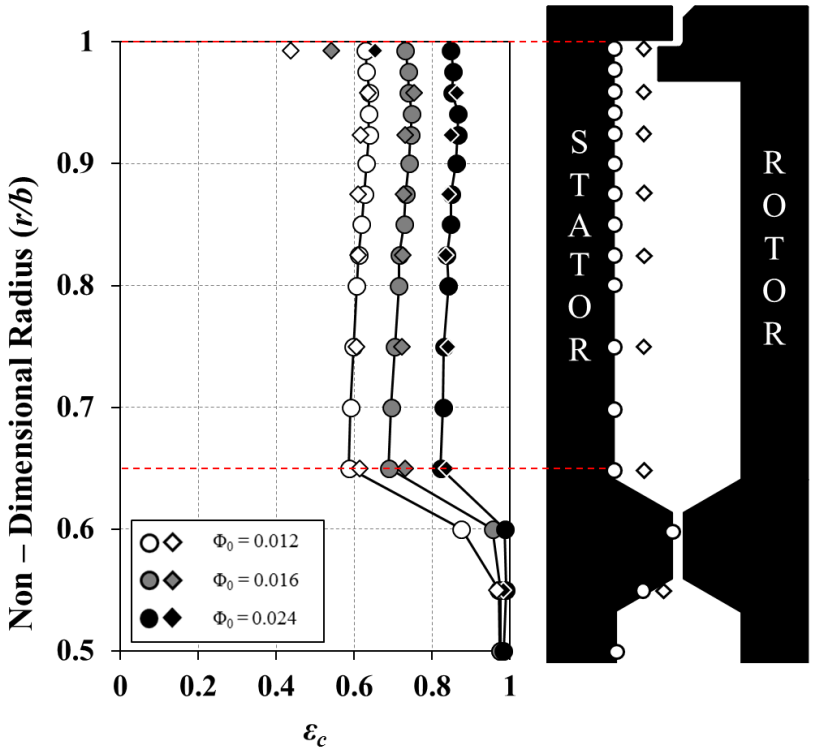

Figure 4.4: Effect of sealing flow rate on radial distribution of effectiveness for single radial-clearance seal in the upstream wheel-space (Re_Φ = 7.2 × 10^5, C_F = 0.34) (circles denote stator-wall; diamonds denote rotating-core)

Figures 4.4 and 4.5 show the radial variation of ε_c in the upstream wheel-space for the single and double radial-clearance seals respectively. The measurements were taken on the stator (circles) and in the rotating-core (diamonds) at z/S = 0.25 using sampling probes. The experiments were conducted at Re_Φ = 7.2 × 10^5 and C_F = 0.34 for several values of Φ_0 and hence λ_T; in all cases ingress occurred. For both seals ε_c on the stator and in the core increases as Φ_0 increases and the sealing flow raises the pressure in the wheel-space relative to the annulus. The rapid increase in ε_c at the smaller radii in all cases is caused by the presence of the inlet seal where the sealing flow is introduced.

For the case of the single radial-clearance seal Figure 4.4 shows that, for all sealant flow rates there is an abrupt increase in concentration effectiveness across the seal from $\varepsilon_c = 0$ in the annulus. The concentration in the core is seen to be equal to that on the stator wall and that both distributions are invariant with radius for $r/b \geq 0.65$. These observations suggest that the stator boundary layer is the source of flow to the rotating core and that near-complete mixing between ingress and egress has occurred in a region very close to the periphery of the wheel-space. At $r/b = 0.993$ the concentration in the core is higher than that measured on the stator. This location is in a region characterised by intense mixing of angular momentum and concentration. The egress will be pumped up through the rotor boundary layer (with high ε_c) and the ingress will enter the wheel-space on the stator side (with low ε_c). The sampling probe in the rotating core at this high radius is in the path of the ingress flow as it enters the wheel-space and therefore affected by its low concentration. The mirrored juxtaposition of the stator and rotor in the downstream wheel-space is expected to have the opposite effect.

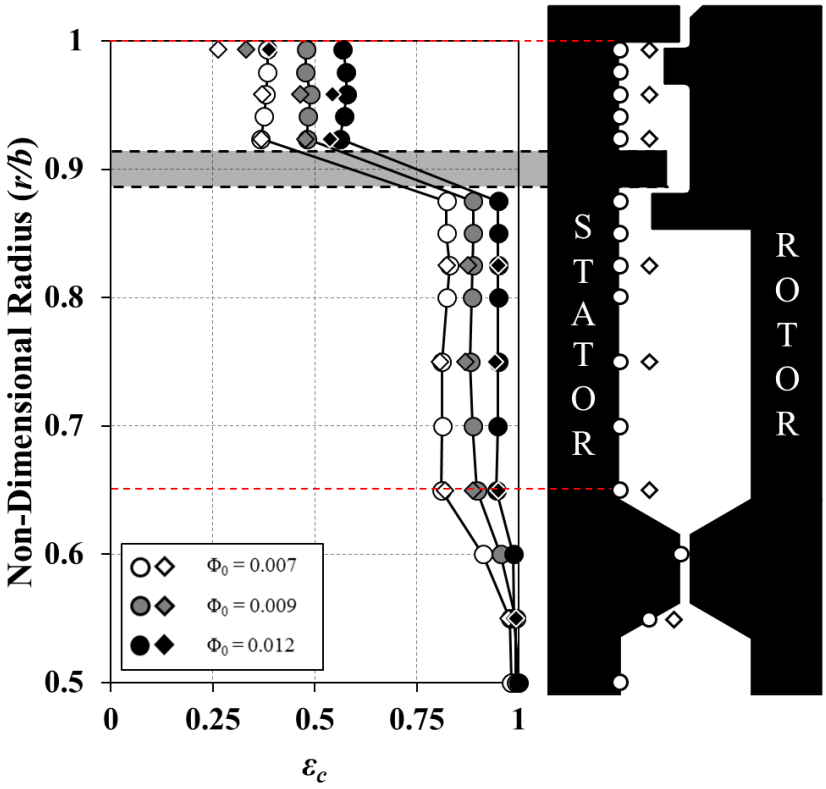

Figure 4.5: Effect of sealing flow rate on radial distribution of effectiveness for double radial-clearance seal in the upstream wheel-space ($Re_\Phi = 7.2 \times 10^5$, $C_F = 0.34$) (circles denote stator-wall; diamonds denote rotating-core)

Figure 4.5 shows that the radial variation of ε_c in the outer ($r/b \geq 0.924$) and inner ($0.875 \geq r/b \geq 0.65$) wheel-spaces of the double radial-clearance seal is similar to that discussed above for the single seal. The only difference is the existence of two mixing regions: one at the periphery of the outer wheel-space and one at the periphery of the inner wheel-space. An additional abrupt increase in effectiveness across the inner seal is observed. This shows the importance of the buffer cavity which attenuates any pressure asymmetries that might exist in the ingested flow constraining ingress to the outer wheel-space.

With reference to the flow structure expected to be found in the upstream wheel-space, the significance of the results presented in this section is twofold. Firstly, the experimental results confirmed that complete mixing between the ingested annulus flow and the sealing flow occurs in a region very close to the periphery of the wheel-space. Secondly, the equivalence of concentration effectiveness on the stator and in the rotating core provided for the first time strong experimental evidence that the stator boundary layer is the source of fluid to the rotating core.

4.2.2 Circumferential Distribution of Effectiveness

Figures 4.6 and 4.7 show the circumferential variation of concentration effectiveness ε_c with non-dimensional vane pitch θ in the upstream wheel-space for the single and double radial-clearance seals respectively. A silhouette of the seal geometries tested is also set alongside these figures, indicating the three radial locations at which the measurements were taken. The results for the single radial-clearance seal were conducted at $\Phi_0 = 0.017$ ($\Phi_0/\Phi_{min} = 28\%$) and the ones for the double seal at $\Phi_0 = 0.012$ ($\Phi_0/\Phi_{min,\ outer} = 23\%$; $\Phi_0/\Phi_{min,\ inner} = 55\%$).

First consider Figure 4.6 and the single radial seal. There is an abrupt increase in sealing effectiveness across the seal, from $\varepsilon_c = 0$ in the annulus to $\varepsilon_c \sim 0.6$, which is invariant with radius. These findings are consistent with the results of the radial distributions of ε_c that were discussed in the previous section and therefore provide additional evidence that support the flow structure discussed in Section 4.1.1. The effectiveness is seen to be invariant with circumferential position despite the large circumferential variation of pressure in the annulus driving ingress. This suggests that the flow in the wheel-space is axisymmetric and any time-averaged influence of the vane position is not communicated to the wheel-space.

Now consider Figure 4.7 and the double radial seal. The discussion provided above for the case of the single radial seal also applies to the measurements taken in the inner and outer wheel-spaces of the double radial seal. In the case of the double seal there is a further increase in effectiveness across the inner seal, with the inner wheel-space nearly sealed, with $\varepsilon_c \sim 0.9$

at r/b = 0.85. Once again this observation is consistent with the measurements of the radial variation of ε_c for this seal, indicating that ingress is constrained within the outer wheel-space.

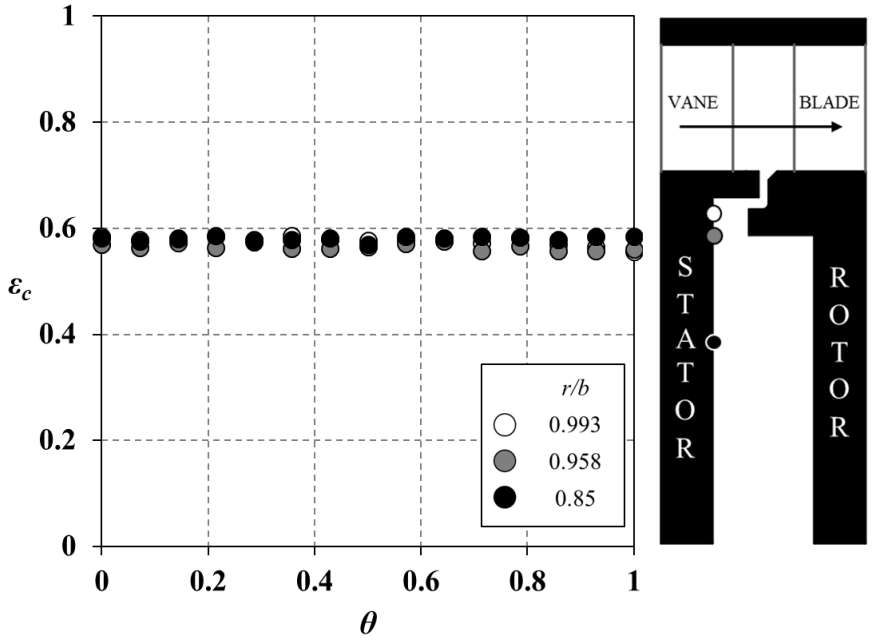

Figure 4.6: Circumferential variation of concentration effectiveness with non-dimensional vane pitch for the single radial-clearance seal in the upstream wheel-space and for three radial locations (Re_Φ = 7.2 × 10^5, C_F = 0.34 and Φ_0 = 0.017)

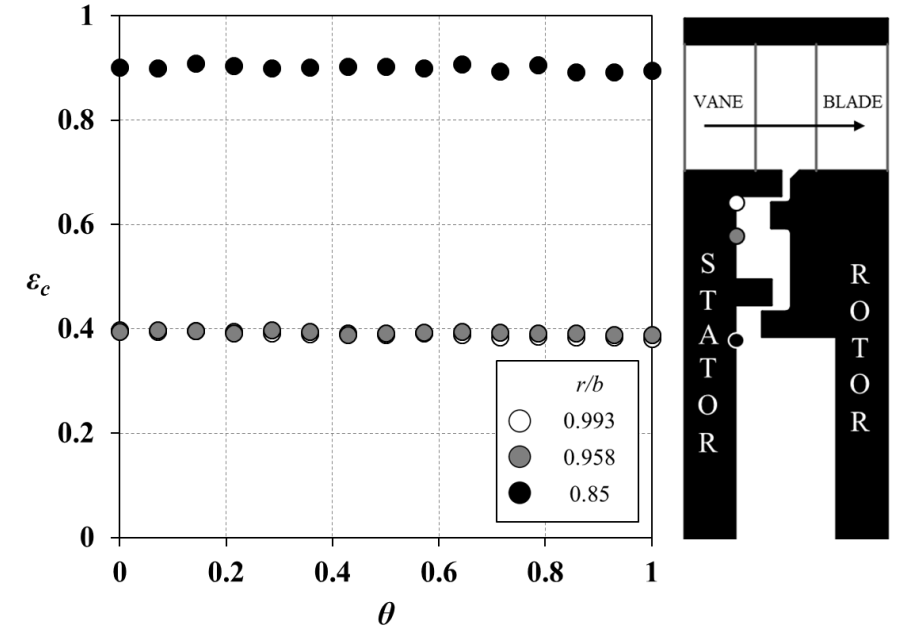

Figure 4.7: Circumferential variation of concentration effectiveness with non-dimensional vane pitch for the double radial-clearance seal in the upstream wheel-space and for three radial locations (Re_Φ = 7.2 × 10^5, C_F = 0.34 and Φ_0 = 0.012)

4.2.3 Variation of Sealing Effectiveness with Sealing Flow

Figures 4.8 and 4.9 show the variation of concentration effectiveness ε_c with non-dimensional sealing flow Φ_0 in the upstream wheel-space for both single and double radial-clearance seals at r/b = 0.958 and 0.85 respectively. For the case of the double seal r/b = 0.958 is located in in the outer wheel-space and r/b = 0.85 in the inner. In all cases ε_c increases with increasing $\Phi_{0,}$ as the sealing flow pressurises the wheel-space and reduces ingress through the rim-seals. The data collapse onto individual curves, which are independent of rotational Reynolds number, Re_Φ.

The data are fitted with the EI theoretical effectiveness curves (Eq. 2.14) using the maximum likelihood method described by Zhou *et al.* (2012). Good agreement between the theoretical model and the experimental measurements is observed in all cases. This is significant as it demonstrates that the simple orifice model of Owen (2010b) can qualitatively predict ingress in simplistic rigs with symmetrical blading, such as the one described by Sangan *et al.* (2012a), and more advanced rigs such as the 1.5-stage rig with turned blading. The estimated values of Φ_{min}, Φ_{min}' and Γ_c are shown in Table 4.3. Φ_{min}' is defined as the flow-rate required to achieve ε_c = 0.95. It is speculated that diffusion between the seeded sealing flow and the unseeded annulus prevents ε_c from reaching unity, despite the wheel-space being fully sealed; the result is an increasing deviation of the theoretical model from the experimental data for values of ε_c > 0.95. For this reason Φ_{min}' is preferred instead of Φ_{min} for evaluating rim-seal performance.

Parameter	Single Radial-Clearance Seal		Double Radial-Clearance Seal	
	Outer (r/b = 0.958)	***Inner (r/b = 0.85)***	***Outer (r/b = 0.958)***	***Inner (r/b = 0.85)***
Φ_{min}	0.0606	0.0632	0.0517	0.0220
Φ_{min}'	0.0367	0.0381	0.0383	0.0132
Γ_c	0.241	0.238	0.675	0.236
σ	0.00966	0.00772	0.0141	0.0118

Table 4.3: Theoretical fit parameters for single and double radial clearance seals in the upstream wheel-space

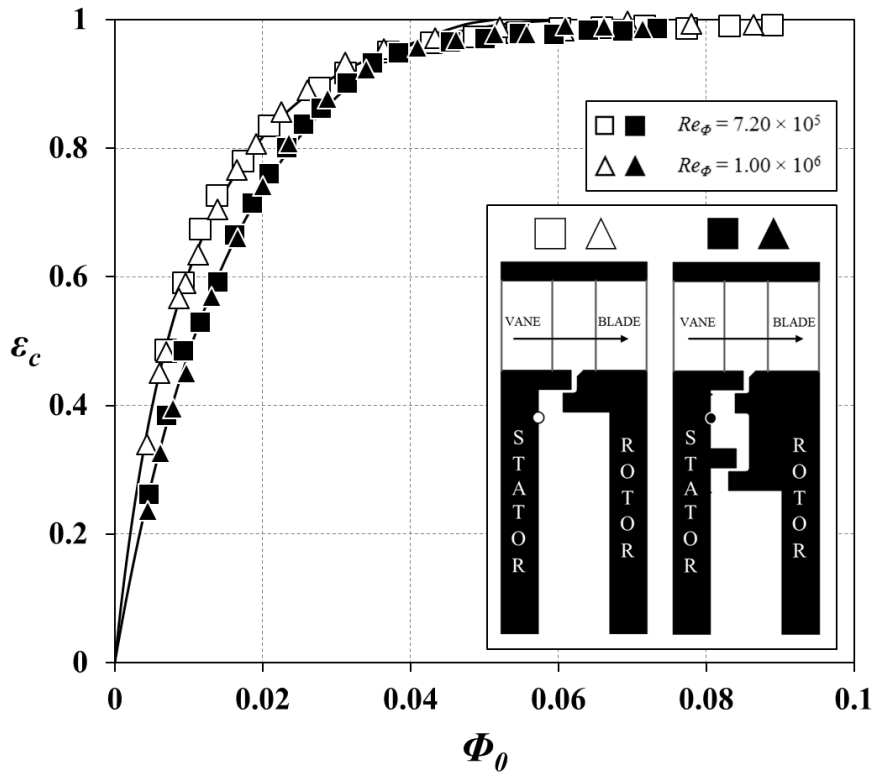

Figure 4.8: Variation of ε_c with Φ_0 for single (white symbols) and double (black symbols) radial-clearance seals at r/b = 0.958 in the upstream wheel-space (C_F = 0.34) (symbols denote data; solid lines are theoretical curves obtained from the orifice model)

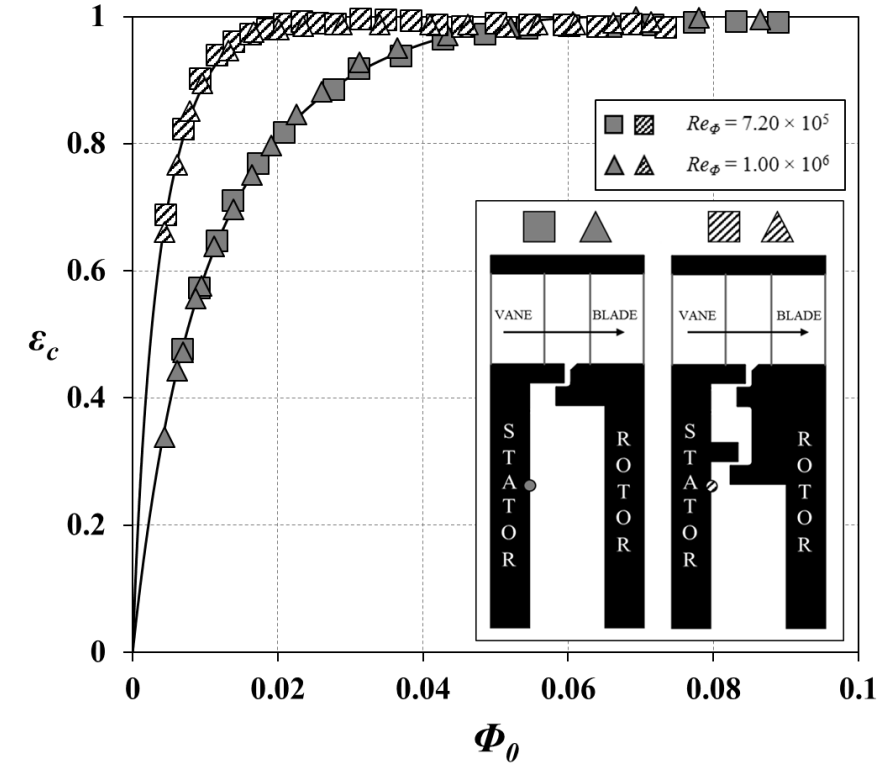

Figure 4.9: Variation of ε_c with Φ_0 for single (solid symbols) and double (hatched symbols) radial-clearance seal at r/b = 0.85 in the upstream wheel-space (C_F = 0.34) (symbols denote data; solid lines are theoretical curves obtained from the orifice model)

The results of Figures 4.8 and 4.9 are combined in Figure 4.10 to enable a comparison. The measurements corresponding to $Re_\Phi = 1.0 \times 10^6$ are omitted for clarity. First consider the data corresponding to the single radial-clearance seal. The effectiveness at $r/b = 0.958$ (white, solid symbols) and 0.85 (grey, solid symbols) are virtually identical. This is in agreement with measurements of the radial variation of ε_c in the wheels-space which showed that the effectiveness of the single radial-clearance seal is invariant with radius. Now consider the data corresponding to the double radial-clearance seal. In the outer wheel-space, at $r/b = 0.958$, the effectiveness of the double seal is identical to the one for the single seal. The small differences in the data are most probably due to slight alignment errors in the installation of the two seals. However, in the inner wheel-space, at $r/b = 0.85$, the effectiveness is significantly higher with the corresponding values of Φ_{min}' for the outer and inner wheel-spaces being 0.0383 and 0.0132 respectively. That is, the inner wheel-space requires approximately 34% of the sealing flow supplied to the outer wheel-space for 95% sealing to be achieved. Considering this, there is a clear benefit when double seals are used in engines as ingress is constrained within the outer wheel-space which is made of blading material capable of accommodating the high temperature of the ingested annulus gases.

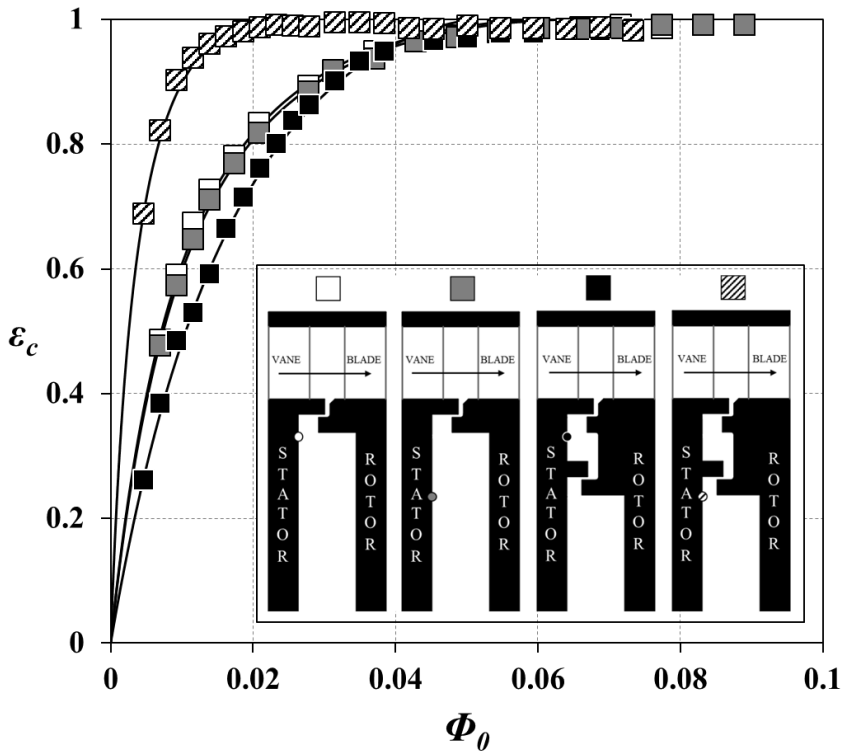

Figure 4.10: Comparison of the variation of ε_c with Φ_0 at $r/b = 0.958$ and 0.85 for the single (solid white and grey symbols) and double (hatched black and grey symbols) radial-clearance seals in the upstream wheel-space ($Re_\Phi = 7.2 \times 10^5$; $C_F = 0.34$) (symbols denote data; solid lines are theoretical curves obtained from the orifice model)

4.2.4 Wheel-Space Pressure and Swirl Measurements

Figure 4.11 illustrates the radial variation of swirl ratio β and static pressure coefficient C_p for the single radial-clearance seal in the upstream wheel-space. The tests were performed at $Re_\Phi = 7.2 \times 10^5$ and for several values of λ_T and hence Φ_0. The measurement points for the total pressure in the wheel-space (at $z/S = 0.25$) are also shown on the silhouette in the centre of the figure. In all cases ingress occurred with an annulus swirl ratio upstream of the blades, $\beta_{a,\,UPS} = 1.5$.

For $\lambda_T = 0$, there is no superposed flow and a core rotation $\beta = 0.4$ is observed for $r/b < 0.8$, in accordance with Daily *et al.* (1964). The swirl ratio at the larger radii increases radially outward under the influence of geometric features of the seal. Increasing the sealing flow causes a reduction in the core rotation as the wheel-space is pressurised.

Also shown on the right hand side of Figure 4.11 is the radial variation of C_p in the upstream wheel-space for the single radial-clearance seal. For a rotating inviscid core, the radial momentum equation reduces to a balance between the pressure force and the centripetal acceleration as shown in Eq. 4.1. Using the definitions of C_p and β (given by Eq. 3.7 and 3.8 respectively), Eq. 4.1 can be integrated to give

$$\frac{dp}{dr} = \rho \frac{V_{\Phi,\infty}^2}{r} \qquad \textbf{(Eq. 4.1)}$$

$$C_p = \frac{p - p_{ref}}{0.5\rho\Omega^2 b^2} = 2 \int_{x_{ref}}^{x} x\beta^2 dx \qquad \textbf{(Eq. 4.2)}$$

where p_{ref} is the pressure at $x = r/b = x_{ref}$; for the results presented here, $x_{ref} = 0.6$. The numerical integration was carried out using Simpson's rule, with values of β obtained from a least-squares cubic spline fitted to the experimental data. With the exception of measurements at $r/b > 0.941$, the results show very good agreement between the calculated and measured distributions of C_p. This shows that the radial distribution of the swirl ratio determines the radial distribution of pressure for the majority of the wheel-space and confirms the flow structure described in section 4.1.1. For $r/b < 0.9$, the pressure coefficient is seen to be invariant with radius and governed by λ_T.

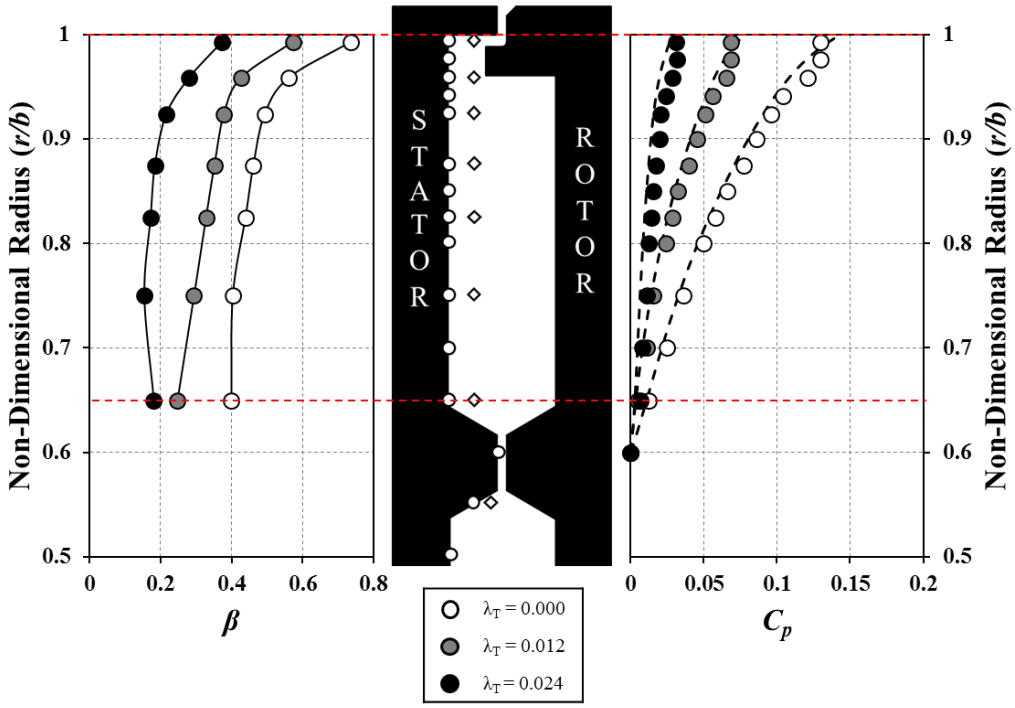

Figure 4.11: Effect of sealing flow rate on the distribution of swirl ratio and pressure coefficient in the upstream wheel-space for the single radial-clearance seal (symbols denote measured values; dash lines denote calculated distribution for C_p)

Figure 4.12 shows the radial variation of β and C_p for the double radial-clearance seal in the upstream wheel-space. The tests were performed under the same conditions as for the single radial-clearance seal and for all λ_T and hence Φ_0 cases tested, ingress occurred.

For the case of the double seal two regions exist: one being the inner wheel-space, between $0.65 \leq r/b \leq 0.875$, and the other the outer wheel-space, between $0.941 \leq r/b \leq 0.993$. Consider first the inner wheel-space in the case where $\lambda_T = 0$ and maximum ingress. The swirl ratio at $r/b < 0.8$ is $\beta = 0.4$, virtually identical to the results for the single seal. At the higher radii of the inner wheel-space the swirl ratio increases under the influence of the geometric features of the double seal. Once again, as the sealing flow increases and the pressure in the inner wheel-space rises, a reduction in the core rotation is observed. In the inner wheel-space a good agreement between measured and theoretical distributions of C_p is observed for all values of Φ_0 tested. This shows that the radial distribution of the swirl ratio determines the radial distribution of pressure in the inner wheel-space of the double radial-clearance seal; an observation which is in agreement with the flow structure portrayed in section 4.1.1.

In the outer wheel-space ($0.941 \leq r/b \leq 0.993$) the geometric features of the seal affected the distributions of swirl ratio and pressure. This is especially evident in the deterioration of the agreement between the theoretical and the measured distributions of C_p.

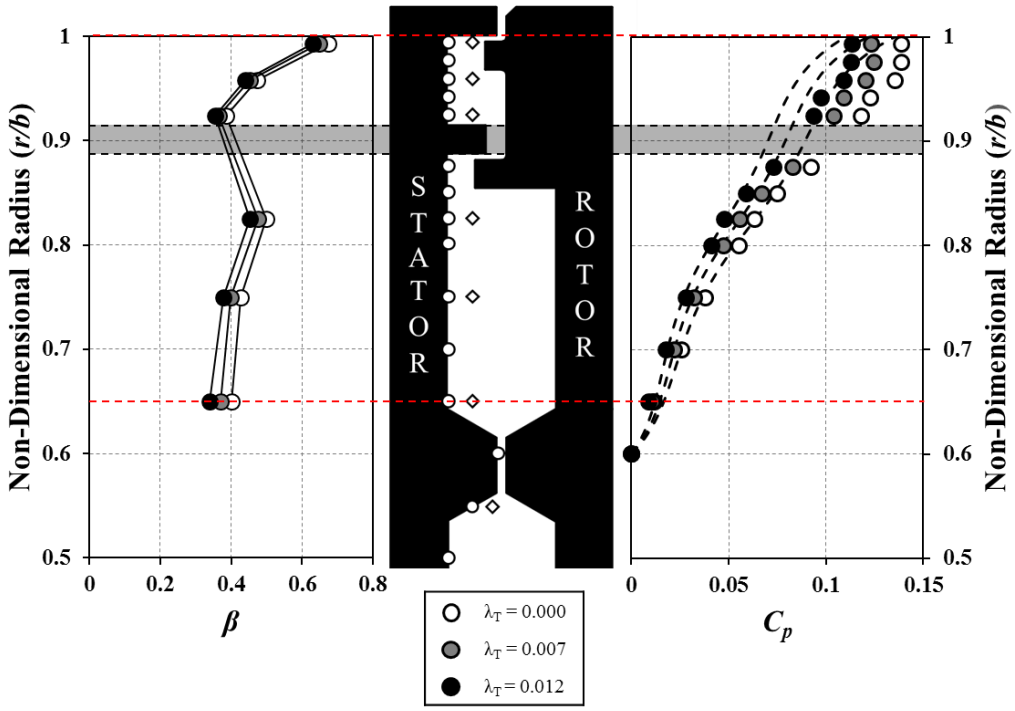

Figure 4.12: Effect of sealing flow rate on the distribution of swirl ratio and pressure coefficient in the upstream wheel-space for the double radial-clearance seal (symbols denote measured values; dash lines denote calculated distribution for C_p)

4.3 Ingress in the downstream wheel-space

This section presents experimental measurements of concentration effectiveness ε_c, swirl ratio β and pressure coefficient C_p in the downstream wheel-space. For these experiments the single and double radial-clearance seals described in Section 4.1.2 were used. The results reveal for the first time that the flow structure in the downstream wheel-space is a mirror-image of that in the upstream. In addition it is shown that the simple orifice model that was used to predict ingress in the *upstream wheel-space* can also be used to predict ingress in the *downstream wheel-space*.

4.3.1 Radial Distributions of Effectiveness

Figures 4.13 and 4.14 show the effect of the sealing flow rate on the radial distribution of effectiveness in the downstream wheel-space for the single and double radial-clearance seals respectively. The measurements were taken on the stator (circles) and in the rotating-core (diamond) at $z/S = 0.25$ using sampling probes. The experiments were conducted at $Re_\Phi = 7.2 \times 10^5$ and $C_F = 0.34$ with ingress occurring for all Φ_0 and hence λ_T values. The rapid increase in ε_c at the smaller radii in all cases is caused by the presence of the inlet seal where the sealing flow is introduced.

As it can be seen, the downstream distributions of both seals are qualitatively identical to the ones obtained in the upstream wheel-space; concentration increases as Φ_0 increases, $\varepsilon_{c,s} = \varepsilon_{c,\infty}$ and invariant with radius, and ε_c increases abruptly through the seals from an annulus $\varepsilon_c = 0$. This shows that the flow structure in the downstream wheel-space is qualitatively identical to that of the upstream wheel-space and in agreement with the flow-structure depicted in Section 1.1.1.

Figure 4.14 shows an increase in ε_c between the outer and inner wheel-spaces, similar to the one shown in Figure 4.5 for the upstream wheel-space. In the case of the upstream wheel-space this performance increase was due to the effect of the buffer cavity. The effect of the buffer cavity in the downstream wheel-space will be considered in further detail in Section 4.5.2.

The detailed measurements of concentration effectiveness in the downstream wheel-space discussed above provide, for the first time, strong experimental evidence of the similarity of the upstream and downstream flow structures and contribute to the extension of the current knowledge of ingress in gas turbine engines.

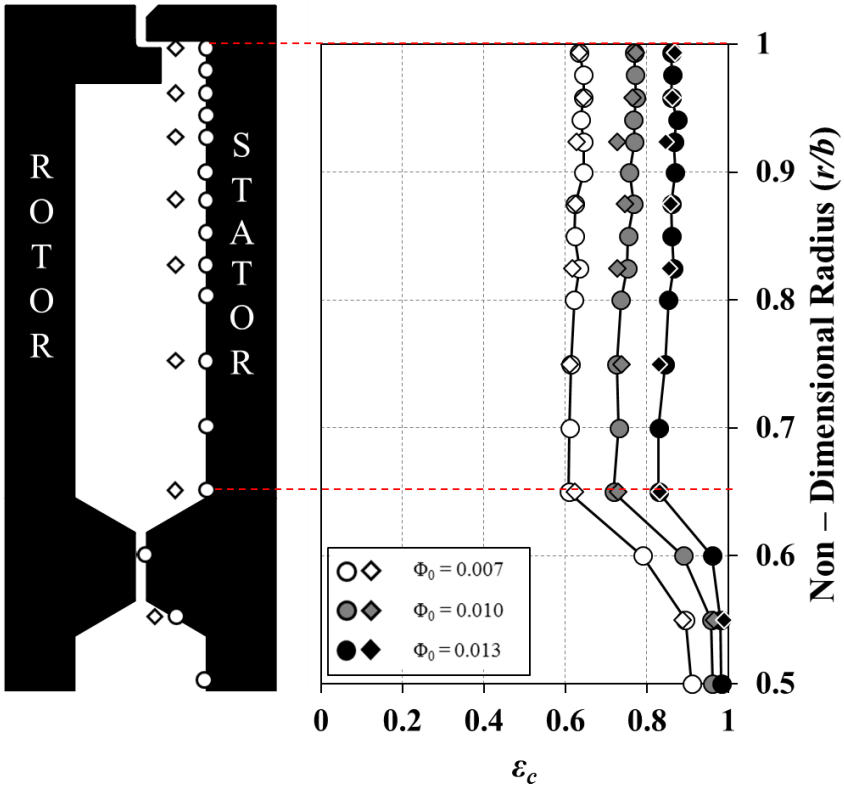

Figure 4.13: Effect of sealing flow rate on radial distribution of effectiveness for single radial-clearance seal in the downstream wheel-space ($Re_\Phi = 7.2 \times 10^5$, $C_F = 0.34$) (circles denote stator-wall measurements; diamonds denote rotating-core measurements)

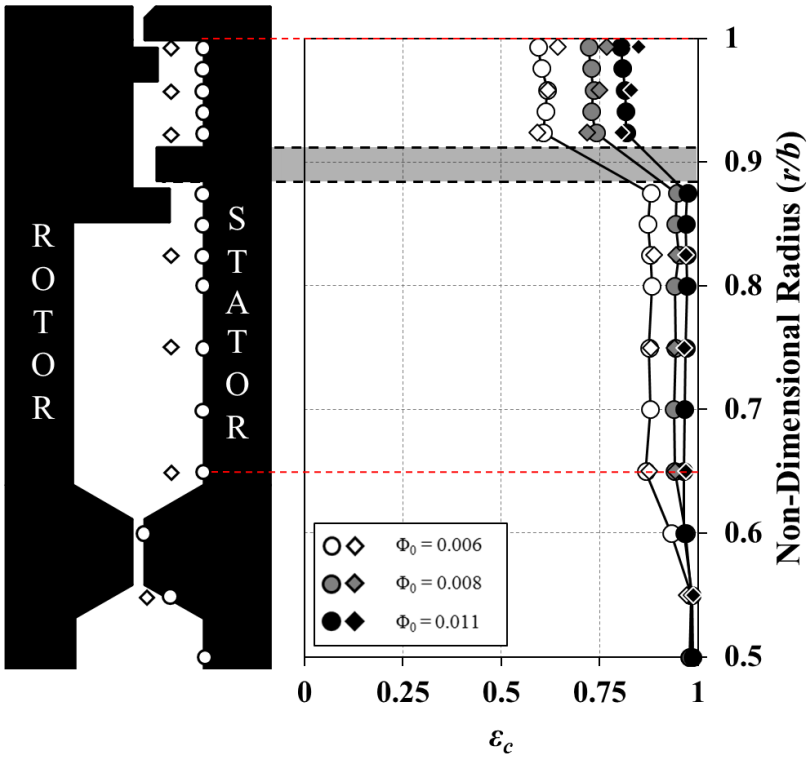

Figure 4.14: Effect of sealing flow rate on radial distribution of effectiveness for double radial-clearance seal in the downstream wheel-space (Re_Φ = 7.2 × 10^5, C_F = 0.34) (circles denote stator-wall measurements; diamonds denote rotating-core measurements)

4.3.2 Variation of Concentration Effectiveness with Sealing Flow

Figures 4.15 and 4.16 show the variation of concentration effectiveness ε_c with non-dimensional sealing flow Φ_0 in the downstream wheel-space for both single and double radial-clearance seals at r/b = 0.958 and 0.85 respectively. For the case of the double seal r/b = 0.958 is located in in the outer wheel-space and r/b = 0.85 in the inner. In all cases ε_c increases with increasing Φ_0, as the sealing flow pressurises the wheel-space and reduces ingress through the rim-seals. The data collapse onto individual curves, which are independent of rotational Reynolds number, Re_Φ.

The data are fitted with the EI theoretical effectiveness curves (Eq. 2.14) using the maximum likelihood method described by Zhou *et al.* (2012). Similarly to the upstream fits, good agreement between the theoretical model and the experimental measurements is observed in all cases. This is significant as it demonstrates that the simple orifice model of Owen (2010b) can qualitatively predict ingress not only to an upstream wheel-space where the annulus pressure field is dominated by the steady-state pressure asymmetry from the vanes, but also in the downstream wheel-space where an *unsteady* pressure variation from the rotor blades exists in the annulus. The estimated values of Φ_{min}, Φ_{min}' and Γ_c are shown in Table 4.4.

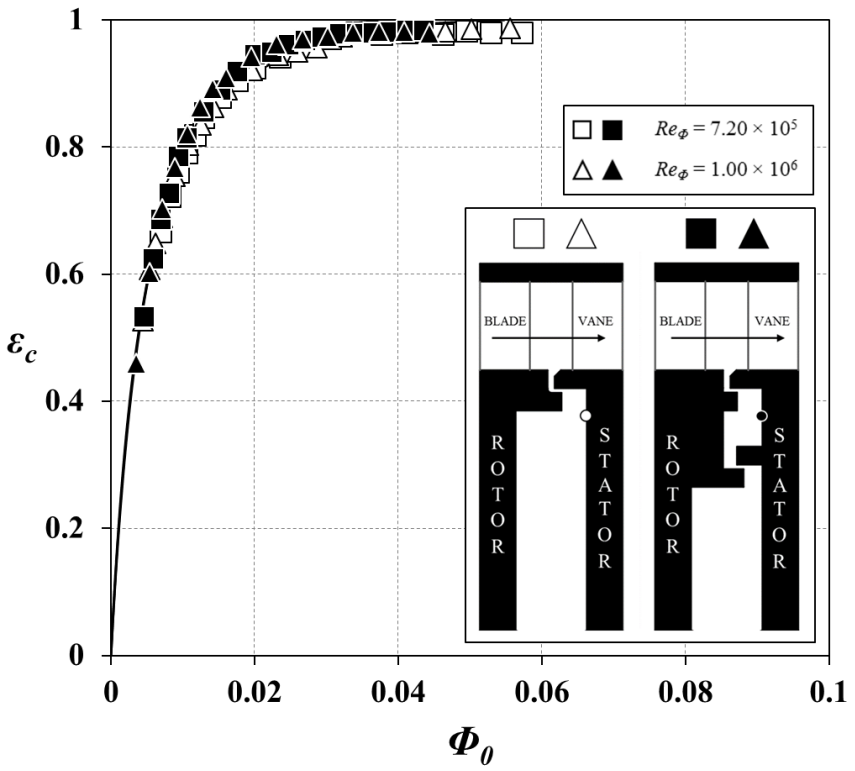

Figure 4.15: Variation of ε_c with Φ_0 for single (white symbols) and double (black symbols) radial-clearance seals at r/b = 0.958 in the downstream wheel-space (C_F = 0.34) (symbols denote data; solid lines are theoretical curves obtained from the orifice model)

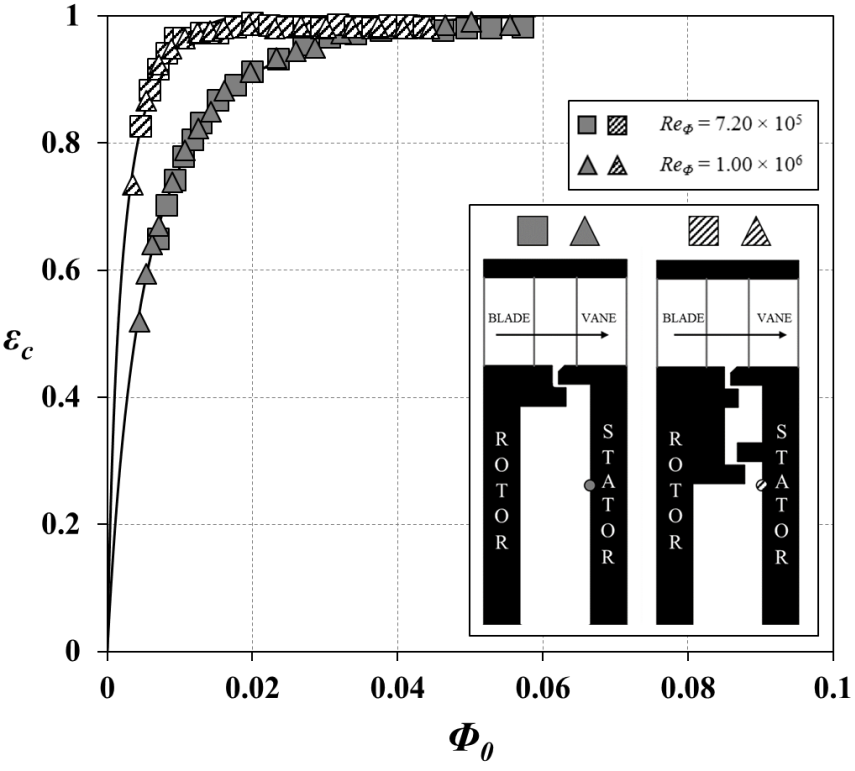

Figure 4.16: Variation of ε_c with Φ_0 for single (grey symbols) and double (hatched symbols) radial-clearance seals at r/b = 0.85 in the downstream wheel-space (C_F = 0.34) (symbols denote data; solid lines are theoretical curves obtained from the orifice model)

Parameter	Single Radial-Clearance Seal		Double Radial-Clearance Seal	
	Outer (r/b = 0.958)	*Inner (r/b = 0.85)*	*Outer (r/b = 0.958)*	*Inner (r/b = 0.85)*
Φ_{min}	0.0546	0.0588	0.0387	0.0192
Φ_{min}'	0.0258	0.0274	0.0217	0.00944
Γ_c	0.109	0.105	0.675	0.236
σ	0.0102	0.00916	0.0142	0.0153

Table 4.4: Theoretical fit parameters for single and double radial clearance seals in the downstream wheel-space

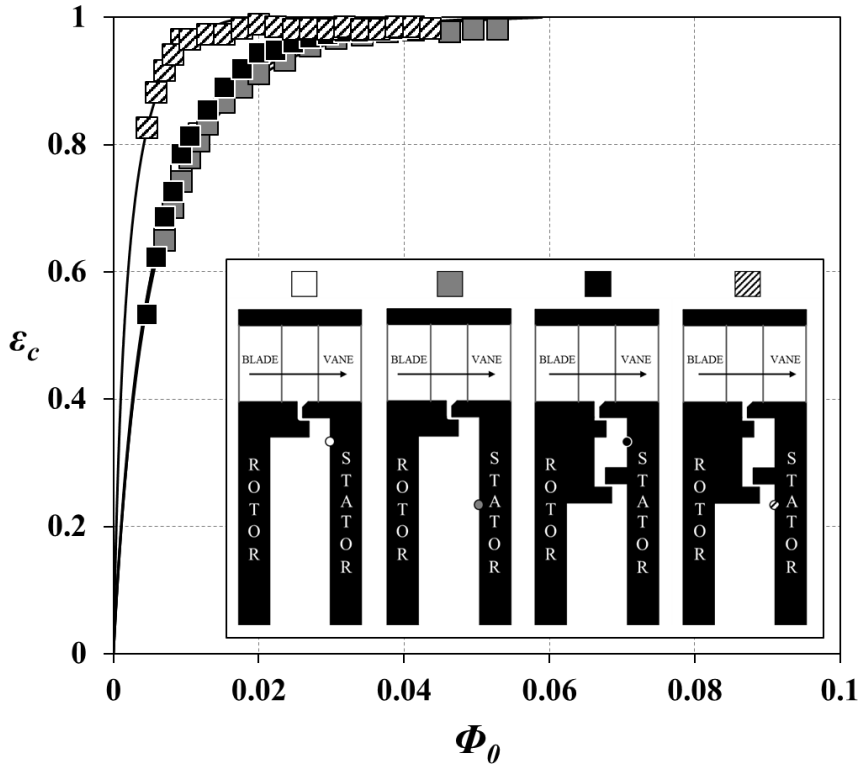

Figure 4.17: Comparison of the variation of ε_c with Φ_0 at r/b = 0.958 and 0.85 for the single (white and grey symbols) and double (black and hatched symbols) radial-clearance seals in the downstream wheel-space ($Re_\Phi = 7.2 \times 10^5$; C_F = 0.34) (symbols denote data; solid lines are theoretical curves obtained from the orifice model)

The results of Figures 1.15 and 1.16 are combined in Figure 4.17 to enable a comparison of the results. The measurements corresponding to $Re_\Phi = 1.0 \times 10^6$ are omitted for clarity.

First consider the data corresponding to the single seal. Similarly to the upstream wheel-space, the effectiveness at the two sampling radii in the downstream wheel-space (white and grey symbols) is virtually identical. Now consider the data corresponding to the double seal. In the outer wheel-space, at r/b = 0.958, the effectiveness of the double seal is identical to the

one of the single seal. However, in the inner wheel-space, at r/b = 0.85, the effectiveness of the double seal is significantly higher than that in the outer, at r/b = 0.958. A similar increase in ε_c was also observed in the case of the upstream measurements and was attributed to the effect of the buffer cavity. The effect of the buffer cavity in the downstream wheel-space will be considered in further detail in Section 4.5.2.

4.3.3 Wheel-Space Pressure and Swirl Measurements

Figures 4.18 and 4.19 illustrate the radial variation of swirl ratio, β and static pressure coefficient, C_p for the single and double radial-clearance seals respectively in the downstream wheel-space. The tests were performed at $Re_\Phi = 7.2 \times 10^5$ and for several values of λ_T and hence Φ_0. The measurement points for the total pressure in the wheel-space (at z/S = 0.25) are also shown on the silhouettes in the centre of the figures. In all cases ingress occurred with an annulus swirl ratio upstream of the blades, $\beta_{a,\,DWS} = 0.2$.

At $\lambda_T = 0$, no sealing flow is supplied to the wheel-space and the core rotation β = 0.4 at r/b < 0.8 for both seals. This was also the case for the measurements taken in the upstream wheel-space. The swirl ratio at the larger radii increases radially outward under the influence of the geometric features of the seal. Increasing the sealing flow causes a reduction in the core rotation as the wheel-space is pressurised.

Also shown on the right hand side of Figures 4.18 and 4.19 is the radial variation of C_p in the downstream wheel-space for the two seals. The symbols represent experimental data whereas the dashed lines represent calculated values of C_p, obtained using Eq. 4.2. Good agreement is observed between the calculated and measured distributions for the biggest part of wheels-space. This indicates that where theory and experiment agree the radial distribution of the swirl ratio determines the radial distribution of pressure. As it was the case for the upstream measurements, the agreement deteriorates at the higher radii for the case of the single seal and in the whole of the outer wheel-space of the double seal. This is because of the effect of the geometric features of the seals on the distributions of swirl ratio and pressure in these regions.

The results discussed in this section are in general qualitatively similar to the results discussed in Section 4.2.4 for the case of the upstream wheel-space. This provides additional experimental evidence that support the similarity of the upstream and downstream flow structures.

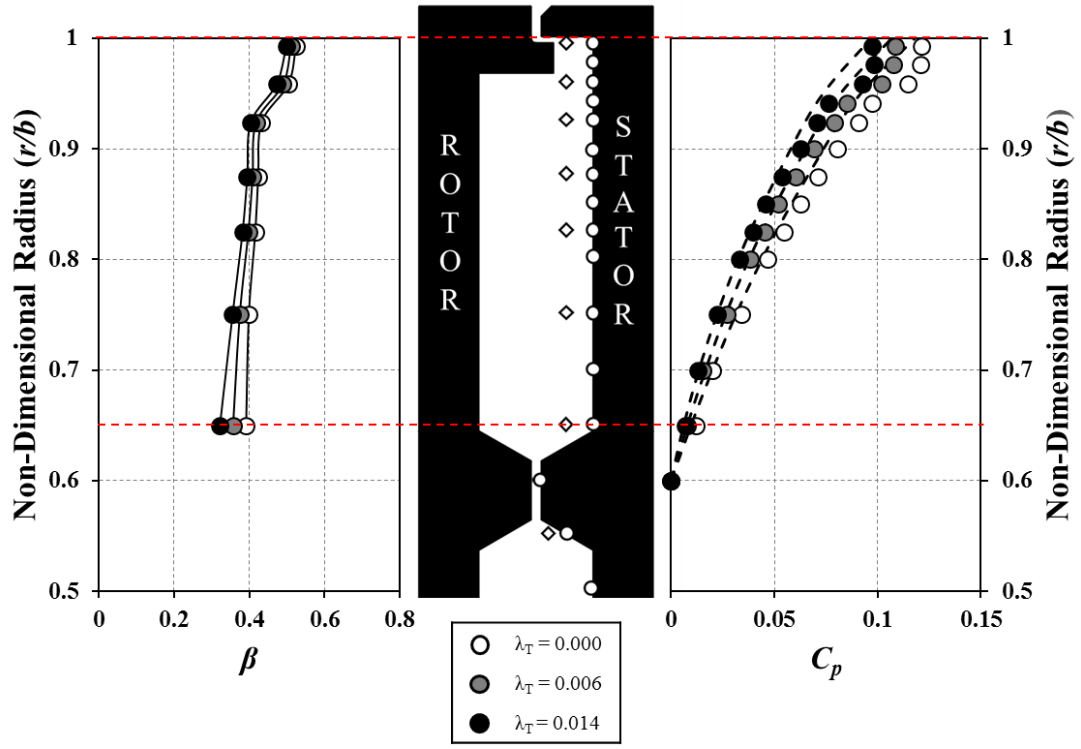

Figure 4.18: Effect of sealing flow rate on the distribution of swirl ratio and pressure coefficient in the downstream wheel-space for the single radial-clearance seal (symbols denote measured values; dash lines denote calculated distribution for C_p)

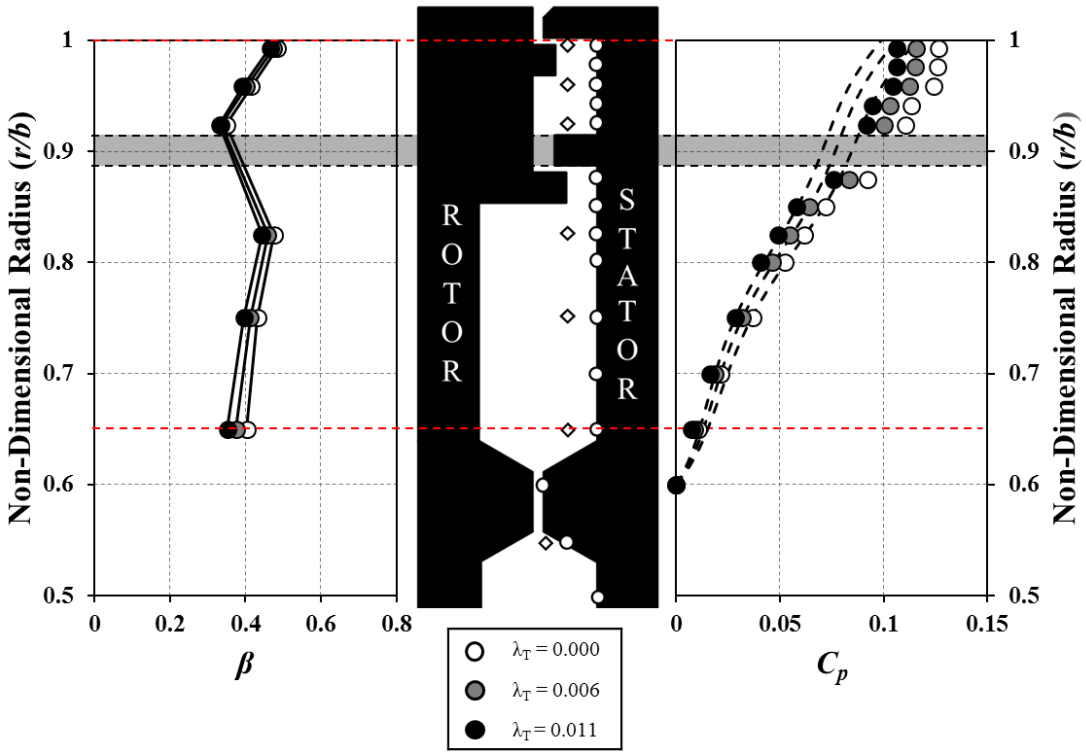

Figure 4.19: Effect of sealing flow rate on the distribution of swirl ratio and pressure coefficient in the downstream wheel-space for the double radial-clearance seal (symbols denote measured values; dash lines denote calculated distribution for C_p)

4.4 Upstream versus Downstream Ingress

In this section the magnitude of the concentration effectiveness in the upstream and downstream wheel-spaces is compared. The purpose of this is to highlight the distinct differences in the driver for ingress on either side of the rotating blades. The results indicate a weaker driver for ingress in the downstream wheel-space raising the possibility of rotationally induced (RI) ingress.

4.4.1 Radial Distribution of Effectiveness

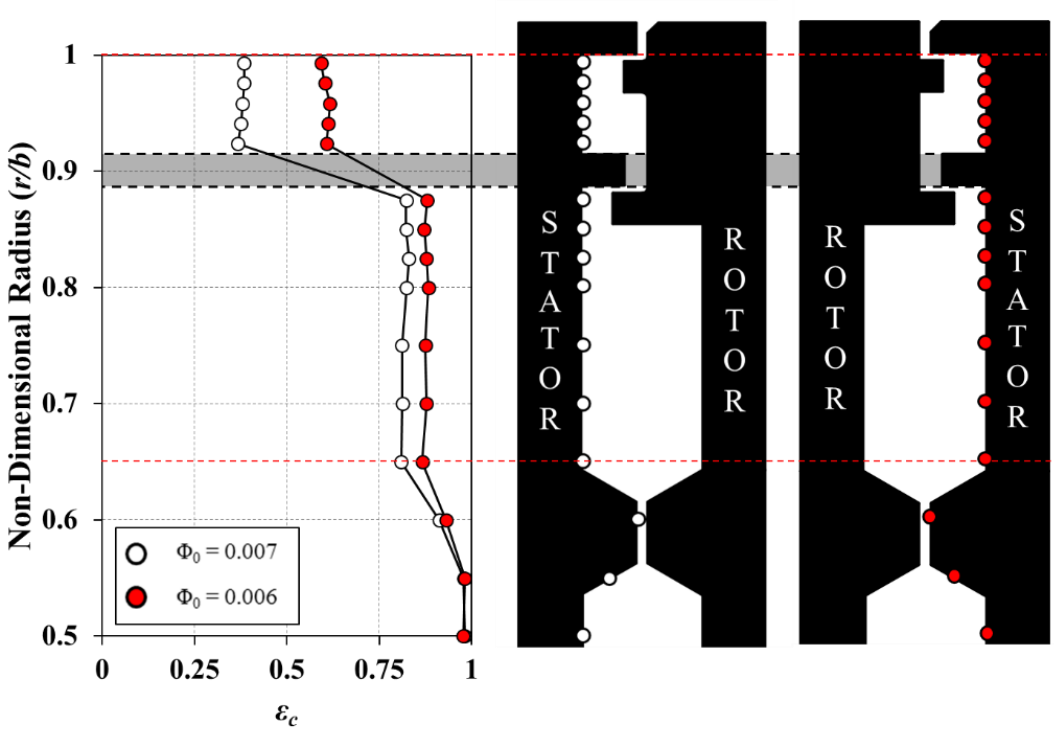

Figure 4.20: Comparison of the radial distribution of effectiveness in the upstream and downstream wheel-spaces for the double radial-clearance seal (Re_Φ = 7.2 × 10^5, C_F = 0.34)

Figure 4.20 shows a comparison of the radial distribution of effectiveness in the upstream (white circles) and in the downstream (red circles) wheel-spaces for the double radial-clearance seal. Both distributions were taken at a similar non-dimensional sealing flow rate, $\Phi_{0,UWS}$ = 0.007 and $\Phi_{0,DWS}$ = 0.006. As it can be seen, the effectiveness of the double radial-clearance seal in the upstream wheel-space is lower than that in the downstream wheel-space, suggesting a weaker driver for ingress in the latter. Despite quantitative differences, the two distributions are qualitatively similar. As discussed in sections 4.2.1 and 4.3.1 this provides evidence of the flow structure in the downstream wheel-space being a mirror-image of that in

the upstream. However in Section 4.1.1 it was discussed that a key difference between the upstream and downstream wheel-spaces is that in the case of the latter, the annulus flow has to cross an egress-fluid-barrier before being ingested into the wheel-space. The subsequent exchange of angular momentum and chemical species was expected to result in an increase in seal effectiveness in the downstream wheel-space which is consistent to the experimental measurements.

4.4.2 Variation of Concentration Effectiveness with Sealing Flow Rate

Figure 4.21 combines the double seal data shown in Figures 4.10 and 4.17 to enable a comparison of the variation of ε_c with Φ_0 at two radial locations, r/b = 0.958 and 0.85 in the upstream and downstream wheel-spaces for the double radial-clearance seal. The effectiveness in both the outer (r/b = 0.958) and inner (r/b = 0.85) wheel-spaces is always higher than that in the downstream wheel-space for the same Φ_0. This is in agreement with the radial distributions of effectiveness in Figure 4.20 and provides additional evidence for a weaker driver for ingress in the downstream wheel-space as a result of the effect of egress-fluid-barrier.

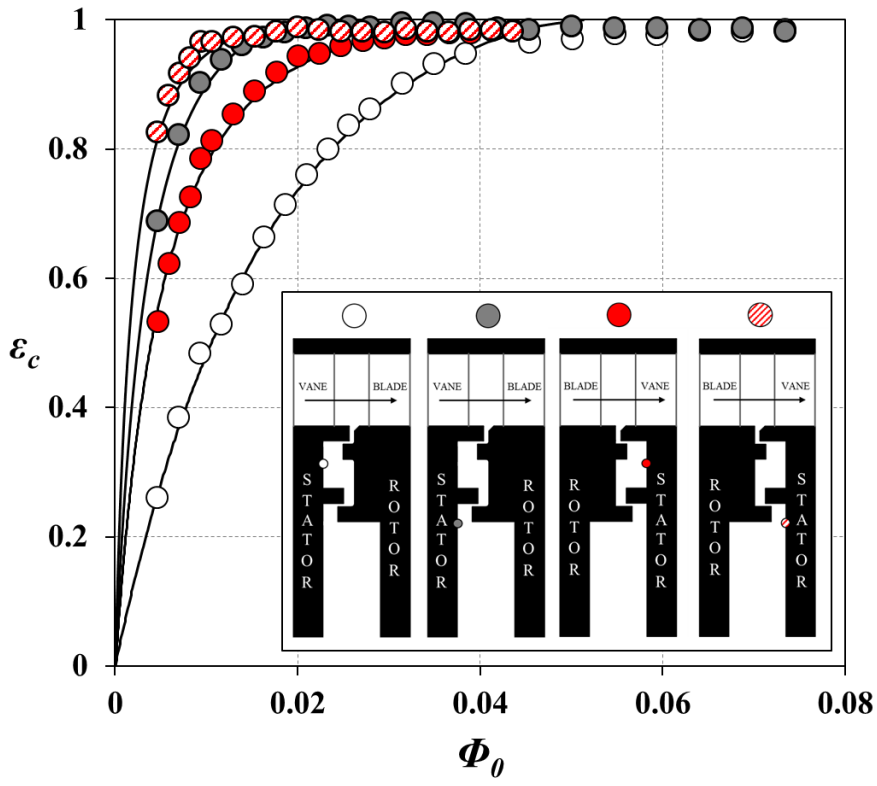

Figure 4.21: Comparison of the variation of ε_c with Φ_0 at r/b = 0.958 and 0.85 in the upstream (white and grey symbols) and in the downstream (red, solid and hatched symbols) wheel-spaces for the double radial-clearance seal ($Re_\Phi = 7.2 \times 10^5$, $C_F = 0.34$) (solid lines are theoretical curves obtained from the orifice model)

4.5 Driving Mechanism for Ingress in the Downstream Wheel-Space

In the previous section it was shown that for the same sealing flow rate, the effectiveness of a seal in the downstream wheel-space was greater than the effectiveness of the same seal in the upstream wheel-space. This indicated a weaker driver for ingress into the downstream wheel-space which was hypothesised to be as a result of the effect of the egress-fluid-barrier. However, the question remains: *what is the driving mechanism for ingress in the downstream wheel-space?*

To answer this question the variation of ε_c with Φ_0 for the double radial-clearance seal in the downstream wheel-space was measured in an experiment under rotationally induced (RI) ingress conditions. To achieve RI conditions the rotor and downstream stator were extracted from the outer casing and the rig was fitted with a bladeless rotor as shown in Figure 4.22. The results of these experiments are given in the following sections.

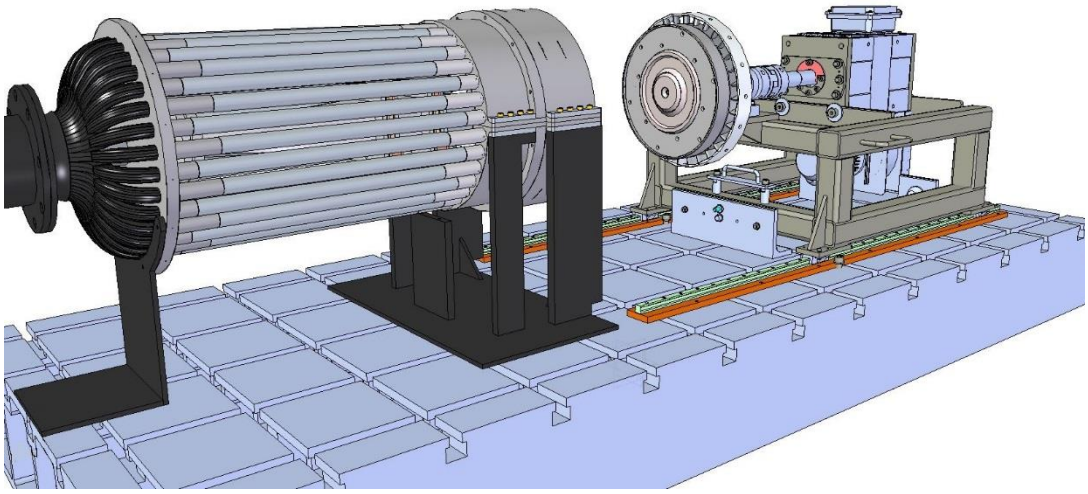

Figure 4.22: Rig configuration for rotationally-induced (RI) ingress experiments in the downstream wheel-space

4.5.1 Variation of Concentration Effectiveness with Sealing Flow

Figure 4.23 shows the variation of ε_c with Φ_0 for the double radial-clearance seal in the downstream wheel-space under (*i*) RI ingress conditions and (*ii*) conditions with blades and external flow at $C_F = 0.34$. The measurements were taken at $Re_\Phi = 7.2 \times 10^5$ and 1.0×10^6 at two locations: in the outer wheel-space at $r/b = 0.958$ in the inner wheel-space at $r/b = 0.85$. In all cases ε_c increases with Φ_0 with the results being independent of Re_Φ.

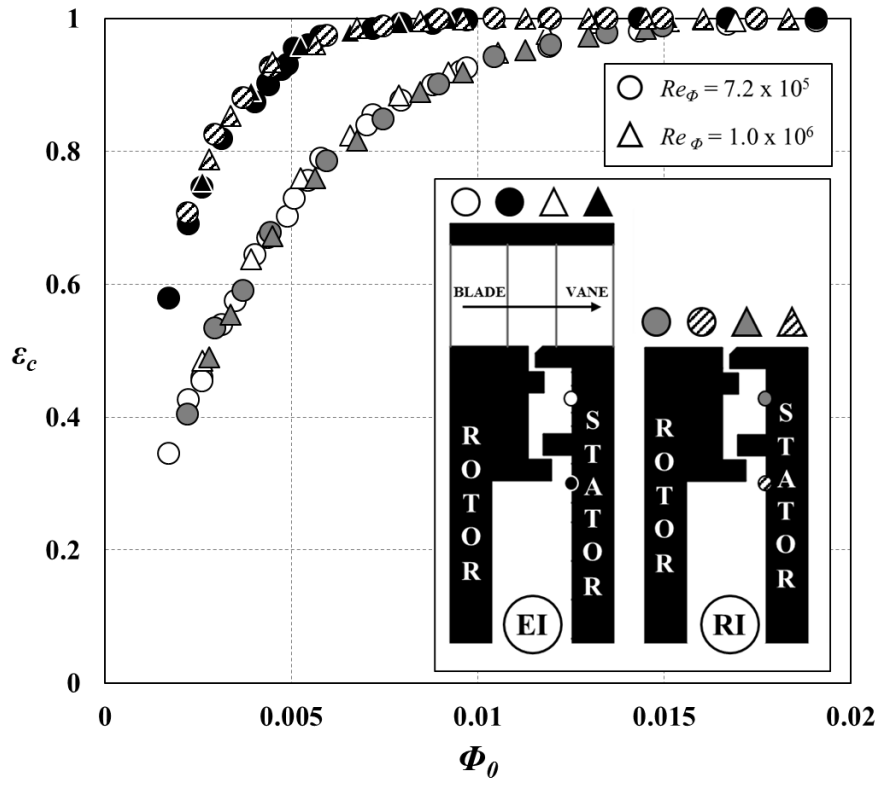

Figure 4.23: Variation of ε_c with Φ_0 for the double radial-clearance seal at r/b = 0.958 and 0.85 in the downstream wheel-space under EI (white and black symbols) and RI (grey and hatched symbols) conditions

The curves corresponding to the RI experiments collapse onto those corresponding to the external flow experiments indicating that ingress in the downstream wheel-space is RI dominated. This finding is somewhat surprising as the unsteady circumferential pressure variation in the annulus downstream of the rotor blades was expected to cause EI ingress. The external flow has to cross the egress-fluid-barrier (see Figure 4.24) before it is ingested in the downstream wheel-space. It is hypothesised that the exchange of angular momentum and concentration during this process attenuates the unsteady circumferential pressure variation in the annulus, resulting in RI being the dominant mechanism for ingress.

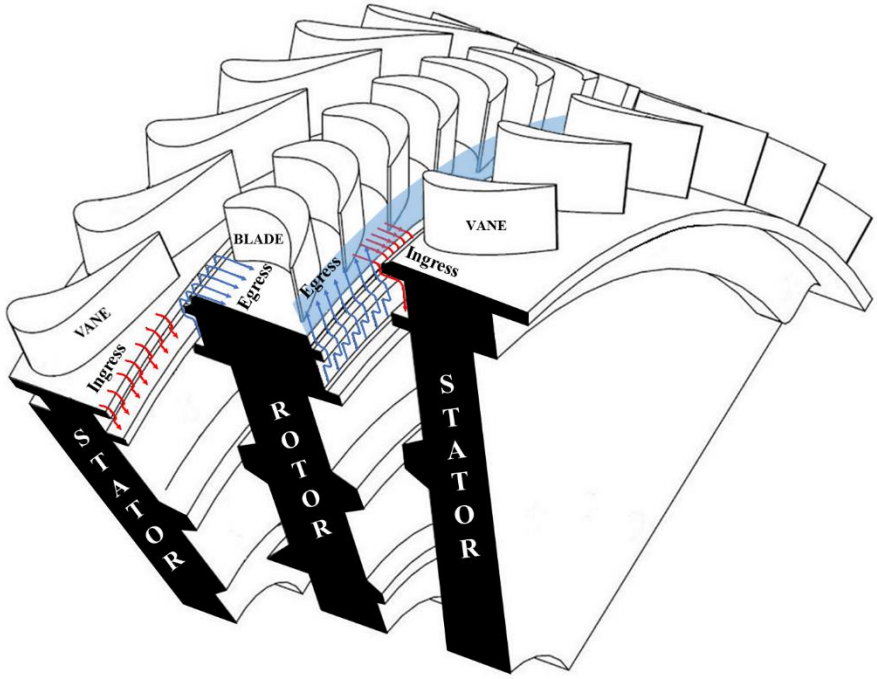

Figure 4.24: Differences between ingress and egress in the upstream and downstream wheel-space with an illustration of the egress-fluid-barrier in the downstream wheel-space

4.5.2 New Method of Analysis for Ingress through Double Radial-Clearance Seals

In the previous section it was shown that RI ingress occurs in the downstream wheel-space. If this is the case, then *why are there two different curves for the inner and the outer wheel-spaces of the double seal?* To answer this question a new method for analysing the concentration measurements is presented. The steps taken for the development of the new method and the results of its application to the measurements are provided below.

Figure 4.25 shows the flow of ingress through a double radial-clearance seal. Although in this figure the seal is fitted in the upstream wheel-space the following discussion also applies to the downstream wheel-space. In a typical experiment, sealing flow is supplied to the wheel-space at low radius with a concentration c_0 = 1%. The sealing flow rate is less than Φ_{min} and therefore ingress of annulus flow with an initial concentration of c_a = 0% occurs. As the annulus flow penetrates the outer seal it passes through a mixing region in which it mixes with the sealing flow. The flow then exits this mixing region into the outer wheel-space before entering a second mixing region as it penetrates through the inner seal and into the inner wheel-space. In other words, the annulus supplies the ingress flow into the outer wheel-space and the outer wheel-space supplies the ingress flow to the inner wheel-space. The concentration in the outer wheel-space $c_{s,out}$ will therefore be such that $c_a < c_{s,out} < c_{in.}$ and the concentration in the inner wheel-space $c_{s,out}$ will be such that $c_{s,out} < c_{s,in} < c_{0.}$

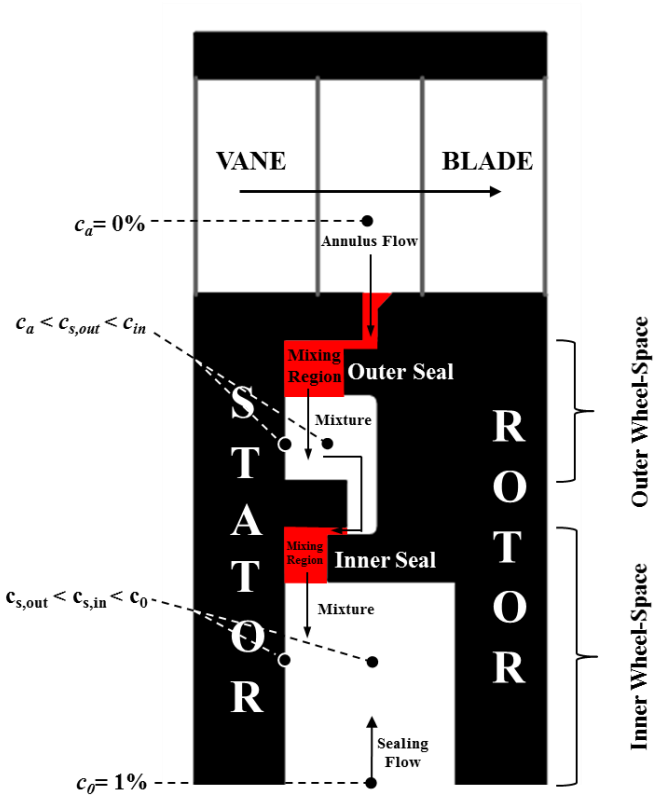

Figure 4.25: Ingress through double radial-clearance seals

Based on the above discussion a new definition for the concentration effectiveness in the inner wheel-space $\varepsilon_{c,in}^*$ was developed, given by

$$\varepsilon_{c,in}^* = \frac{c_{s,in} - c_{s,out}}{c_0 - c_{s,out}} \qquad \textbf{(Eq. 4.3)}$$

where the asterisk is used to distinguish between new and original definitions given by Eq. 2.18. The original definitions can still be used to evaluate the concentration effectiveness in the outer wheel-space $\varepsilon_{c,out}^*$ such that

$$\varepsilon_{c,out}^* = \frac{c_{s,out} - c_a}{c_0 - c_a} = \varepsilon_c \qquad \textbf{(Eq. 4.4)}$$

To reflect the changes in the definitions of ε_c new definitions of Φ_0 were also developed for the outer and inner wheel-spaces. The new definitions use the radial clearance, $s_{c,rad}$ as the controlling clearance for the seal as opposed to the axial clearance $s_{c,ax}$ used in the original definitions. The distinction between the outer and inner seals in the new definitions is made by using the corresponding radius of each seal b_{out} and b_{in} respectively.

The non-dimensional sealing flow parameter for the inner and outer seals $\Phi_{0,in}^*$ and $\Phi_{0,out}^*$ are given by

$$\boldsymbol{\Phi_{0,in}^* = \frac{\dot{m}_0}{2\pi s_{c,rad} b_{in}^2 \rho \Omega}} \qquad \textbf{(Eq. 4.5)}$$

$$\boldsymbol{\Phi_{0,out}^* = \frac{\dot{m}_0}{2\pi s_{c,rad} b_{out}^2 \rho \Omega}} \qquad \textbf{(Eq. 4.6)}$$

where $s_{c,rad}$ = 1.28 mm and the same for both seals and b_{in} = 168.5 mm and b_{out} = 190 mm.

The data shown in Figure 4.23 were re-analysed using the new definitions and are presented in Figure 4.26. The data corresponding to $Re_\Phi = 1.0 \times 10^6$ are omitted for clarity. As it can be seen, The use of the new definitions collapsed the curves corresponding to the inner and outer wheel-spaces collapsed onto a *single* curve. The effectiveness of the inner and outer seals is therefore equal for all sealing flow rates. This is now consistent with the *single* effectiveness curve expected for RI ingress.

The data are fitted with a single RI theoretical effectiveness curve (Eq. 2.11) using the maximum likelihood method described by Zhou *et al.* (2012). Good agreement between the theoretical model and the experimental measurements is observed. The estimated values of Φ_{min}^*, $\Phi_{min}^{*\prime}$ and Γ_c are shown in Table 4.5.

The concentration measurements for the double seal in the upstream wheel-space shown in Figure 4.10 were also re-analysed using the new definitions and presented in Figure 4.27. The results of Figure 4.26 were also added to enable a comparison between the upstream and downstream wheel-spaces. In the upstream wheel-space where EI ingress occurs, there are two distinct curves for the inner and outer wheel-spaces as opposed to a single curve in the downstream wheel-space where RI ingress occurs. The effectiveness in the outer wheel-space $\varepsilon_{c,in}$* is higher than the effectiveness in the inner wheel-space $\varepsilon_{c,out}$* and closer to the RI curve of the downstream wheel-space. This shows the effect of the buffer cavity to attenuate, but not completely eliminate, the circumferential variation of pressure in the ingested flow. In the downstream wheel-space where the egress-fluid-barrier completely attenuated the circumferential pressure variation, the buffer cavity has no effect on ingress and $\varepsilon_{c,in}$* = $\varepsilon_{c,out}$*.

The upstream data are fitted with the EI theoretical effectiveness curves (Eq. 2.14) using the maximum likelihood method described by Zhou *et al.* (2012). Good agreement between the theoretical model and the experimental measurements is observed. The estimated values of Φ_{min}^*, $\Phi_{min}^{*\prime}$ and Γ_c are shown in Table 4.5.

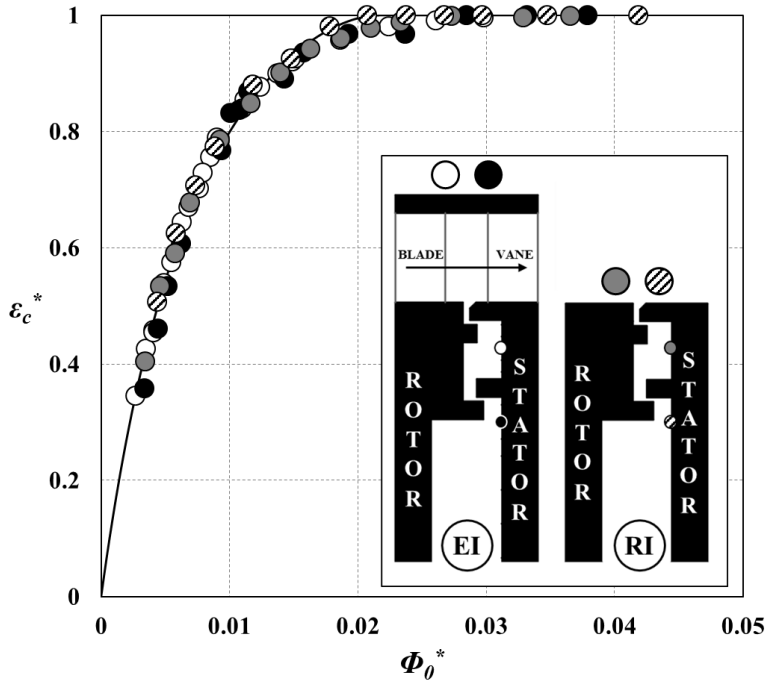

Figure 4.26: Variation of of ε_c^* with Φ_0^* for the double radial-clearance seal at r/b = 0.958 and 0.85 in the downstream wheel-space under EI (white and black symbols) and RI (grey and hatched symbols) conditions ($Re_\Phi = 7.2 \times 10^5$; for EI, C_F = 0.34) (solid lines are theoretical curves obtained from the orifice model)

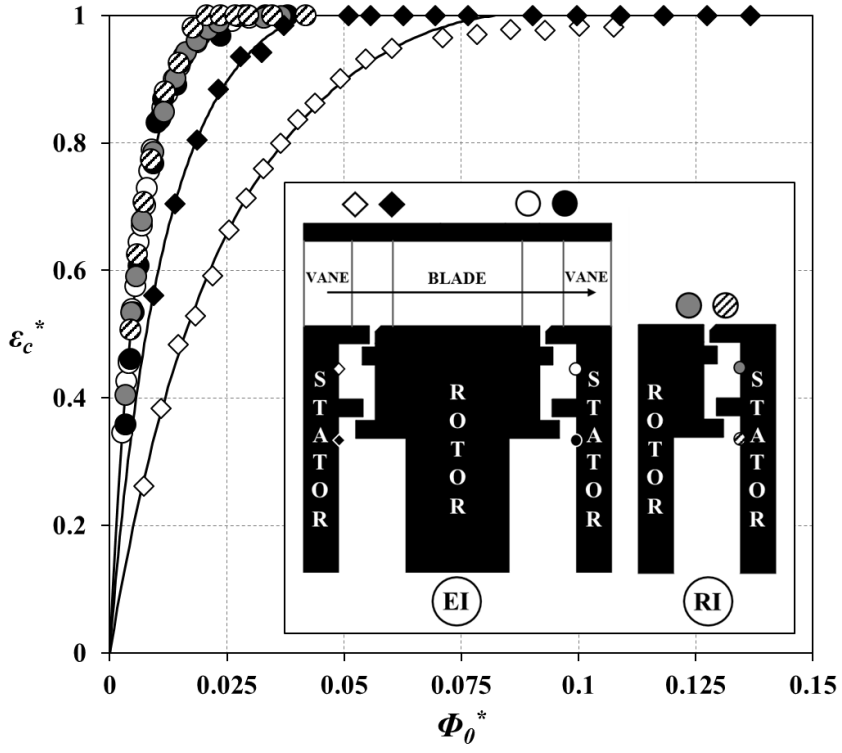

Figure 4.27: Variation ε_c^* with Φ_0^* for the double radial-clearance seal at r/b = 0.958 and 0.85 in the upstream and downstream wheel-spaces - white and black diamond and circles represent EI experiments in the upstream and downstream wheel-space respectively; grey and hatched circles represent RI experiments in the downstream wheel-space ($Re_\Phi = 7.2 \times 10^5$; for EI, C_F = 0.34) (solid lines are theoretical curves obtained from the orifice model)

Parameter	Upstream Wheel-Space		Downstream Wheel-Space	
	Outer (r/b = 0.958)	*Inner (r/b = 0.85)*	*Outer (r/b = 0.958)*	*Inner (r/b = 0.85)*
Φ_{min}^{*}	0.0832	0.0436	0.0217	
$\Phi_{min}^{*'}$	0.0608	0.0310	0.0160	
Γ_c	0.603	0.506	0.685	
σ	0.0139	0.00520	0.0171	

Table 4.5: Theoretical fit parameters for double radial clearance seal in the downstream wheel-space

4.5.3 Off-Design Concentration Measurements

Owing to the profoundness of the results presented in the previous two sections a series of experiments were conducted at off-design conditions involving annulus pressure measurements upstream and downstream of the rotor blades and concentration measurements in the two wheel-spaces. The aim of these experiments was to provide additional evidence to support RI ingress in the downstream wheel-space.

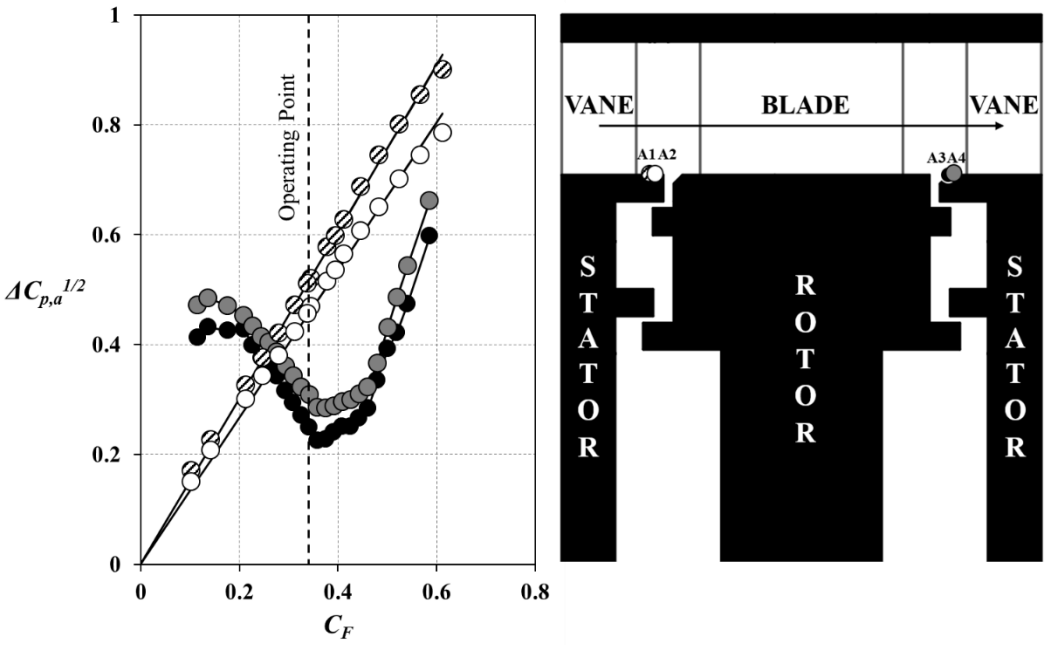

Figure 4.28: Variation of $\Delta C_{P,a}^{1/2}$ with flow coefficient C_F on the vane platform in the annulus upstream and downstream of the rotor blades ($Re_\Phi = 7.2 \times 10^5$, $\Phi_0 = 0$)

The circumferential variation of pressure in the annulus $C_{p,a}$ at various location on the hub and shroud upstream and downstream of the rotor blades is discussed in detail in Section 3.5.3. Figure 4.28 shows the variation $\Delta C_{p,a}^{1/2}$ with flow coefficient C_F in the annulus upstream and downstream of the rotor blades. The measurements were taken on the vane platform as indicated in the silhouette adjacent to the graph and in the absence of any sealing flow rate i.e. at $\Phi_0 = 0$. Upstream of the blades $\Delta C_{p,a}^{1/2}$increases linearly with C_F for all measurement locations. With reference to the orifice model discussed in Section 2.7 and as shown by Eq. 2.15 which is repeated below for convenience as Eq. 4.7, the amount of ingestion of mainstream flow in the upstream wheel-space and hence Φ_{min} are expected to increase as C_F increases.

$$\boldsymbol{\Phi_{min} = \frac{2}{3} C_{d,e} \Delta C_p^{1/2}} \qquad \textbf{(Eq. 4.7)}$$

where $C_{d,e}$ the discharge coefficient for egress. Unlike the upstream variation, downstream of the blades $\Delta C_{p,a}^{1/2}$ reaches a minimum at a flow coefficient close to the operating point, where the flow velocity triangles are aligned with the inlet angle of the downstream vane. Either side of this, the blockage increases as the flow impinges on the vane causing an increase in pressure. The effect of this pressure variation on ingress in the downstream wheel-space still remains unknown. Nevertheless, should there be an effect, it will be relatively small considering that the downstream $\Delta C_p^{1/2}$ is much smaller than that upstream at flow coefficients at and around the operating point.

Figures 4.28 and 4.29 show the variation of ε_c^* with Φ_0^* in the downstream and upstream wheel-spaces of the double radial-clearance seal respectively for three flow coefficients C_F = 0.3, 0.34 and 0.36. In Figure 4.29 the RI case where $C_F = 0$ was also included. An RI experiment in the upstream wheel-space could not be performed as the outer casing could not be removed.

First consider Figure 4.29 and the downstream wheel-space measurements. As it can be seen, the data corresponding to the measurements in the outer and inner wheel-space collapse onto a single curve, independent of C_F. This indicates that RI ingress in the downstream wheel-space does not only occur at the operating point where $C_F = 0.34$ but also for a range of sealing flow coefficients between $0.3 \leq C_F \leq 0.36$. Now consider the upstream wheel-space measurements shown in Figure 4.30. There is a consistent decrease in effectiveness in both the outer and inner seals as the flow coefficient increases. This is as a result of the increase of $\Delta C_{p,a}^{1/2}$ with C_F which, as previously discussed and showed by Eq. 4.7, results in a larger amount of ingress into the upstream wheel-space.

In summary, the results of Figures 4.27 and 4.28 show that in the upstream wheel-space where EI ingress occurs the effectiveness in the outer and inner wheel-spaces reduces as C_F increase and $\Delta C_{p,a}^{1/2}$ increases. In the downstream wheel-space where the egress-fluid-barrier is thought to have attenuated the unsteady pressure variation due to the blades, RI ingress occurs for a range of flow coefficients at and around the operating point between $0.3 \leq C_F \leq 0.36$. At this range, the circumferential variation on the downstream vane platform reaches a minimum and does not seem to be affecting ingress. At higher flow coefficients where the rig operates off-design, the circumferential pressure variation on the vane platform increases and so does the unsteady pressure variation due to the blades. Under these high C_F conditions combined (CI) ingress is expected to occur in the downstream wheel-space.

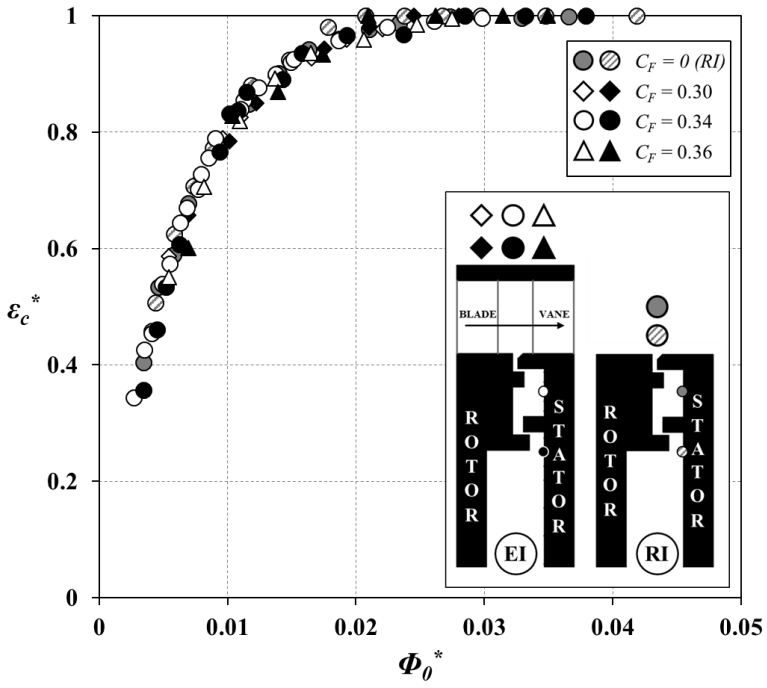

Figure 4.29: Effect of flow coefficient C_F on the variation of ε_c^* with Φ_0^* in the downstream outer (white and grey symbols) and inner (black and hatched symbols) wheel-spaces of the double radial-clearance seal ($Re_\Phi = 7.2 \times 10^5$)

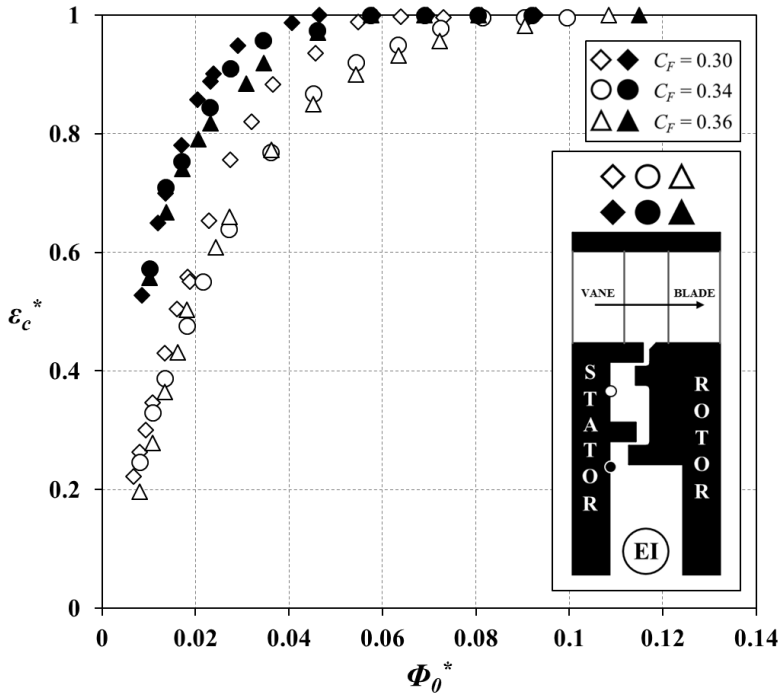

Figure 4.30: Effect of flow coefficient C_F on the variation of ε_c^* with Φ_0^* in the upstream outer (white symbols) and inner (black symbols) wheel-spaces of the double radial-clearance seal ($Re_\Phi = 7.2 \times 10^5$)

4.6 Summary

In this chapter measurements of concentration effectiveness ε_c, swirl ratio β and pressure coefficient C_p in the upstream and downstream wheel-spaces of the 1.5-stage rig were presented. These measurements were used to examine the flow structure in the two wheel-spaces.

The flow structure in the upstream and downstream wheel-spaces was expected to be qualitatively similar, featuring two separated boundary layers, one on the stator and one on the rotor disc, with a rotating core of inviscid fluid between the two. A significant difference between the flow structures in the two wheel-spaces is that in the downstream wheel-space the annulus flow has to cross a fluid-barrier of egress before being ingested into the wheel-space. The subsequent exchange of angular momentum between the ingress and egress flow was expected to cause: (*i*) a reduction in the unsteady non-axisymmetric distribution of pressure immediately outside the seal clearance and (*ii*) an increase in the level of CO_2 concentration of the ingested fluid. These effects would result in an improved effectiveness for the downstream seal. Attenuation of the pressure asymmetry in the flow near the seal clearance would tend to create combined (CI) ingress and, in the limit, rotationally-induced (RI) ingress.

Measurements of the radial distribution of ε_c were taken in both the upstream and downstream wheel-spaces for a single and double radial-clearance seals. In all cases the concentration effectiveness on the stator was almost equal to that in the rotating core. This showed that, as expected, the stator boundary layer is the source of flow to the rotating core. The stator and core distributions were shown to be broadly invariant with radius. This showed that near-complete mixing between ingress and egress had occurred in a region very close to the periphery of the wheel-space. The qualitative similarity of the upstream and downstream distributions showed, for the first time, that the flow structure in the downstream wheel-space is a "mirror-image" of the one in the upstream.

The radial distribution of β and C_p was also measured in the upstream and downstream wheel-spaces for the two radial seals. As it was the case for the concentration measurements the results in the two wheel-space were qualitatively similar. As expected, in the absence of sealing flow and at low radius, $\beta \approx 0.4$ for all cases. The distribution of the swirl ratio was shown to control the distribution of pressure in the wheel-space, reinforcing the expected flow structure in the two wheel-spaces.

Measurements of the variation of concentration effectiveness with sealing flow rate were taken in the upstream and downstream wheel-spaces at two rotational Reynolds number conditions ($Re_\Phi = 7.2 \times 10^5$ and 1.0×10^6) using both radial seals. In all cases the effectiveness of the two seals increased with sealing flow and was indented of rotational Reynolds Number. A theoretical orifice model was fitted to the experimental data showing good agreement between theory and experiment in all cases. This was a significant finding as it demonstrated that the simple orifice model can qualitatively predict ingress not only to an upstream wheel-space where the annulus pressure field is dominated by the steady-state pressure asymmetry from the vanes, but also in the downstream wheel-space where an *unsteady* pressure variation from the rotor blades exists in the annulus.

A comparison of the radial distribution of ε_c and variation of ε_c with sealing flow rate Φ_0 in the upstream and downstream wheel-spaces for the double radial-clearance seal was provided. A significant improvement in the performance of the double seal in the downstream wheel-space was observed. This indicated a weaker driver for ingress in the downstream wheel-space.

To identify the driving mechanism for ingress in the downstream wheel-space a rotationally-induced (RI) ingress experiment was conducted using the double seal. The curves corresponding to the RI test were found to collapse on the one corresponding to the externally-induced (EI) ingress test showing the RI ingress dominates in the downstream wheel-space.

A new method of analysis for the concentration measurements obtained using double seals was introduced. Re-analysing the downstream concentration measurements using the new method resulted in the collapse of, what was before two distinct curves for the inner and outer wheel-spaces, onto a single curve. This is consistent with RI ingress.

To further strengthen the argument for RI ingress in the downstream wheel-space the variation of ε_c with Φ_0 was measured for a range of flow coefficients between $0.3 < C_F < 0.36$. The resulting curves where all found to collapse on the RI curve showing that RI ingress dominates for a range of flow coefficients around the operating point. At higher C_F values where the unsteady pressure variation due to the blades increases CI ingress is expected to dominate the downstream wheel-space.

Chapter 5: Ingress through Industrial Rim-Seals

This chapter presents three parametric studies including eight Siemens proprietary seal geometries. The design of the seals were supplied by Siemens and adapted for testing in the 1.5-stage rig. The first study examined the effect of circumferentially-spaced radial slots of different widths on the performance of single radial-clearance seals. The second study investigated a potential increase in the performance of single angel-wing seals by the addition of secondary features, namely winglets, and a single radial-clearance seal at a lower radius. The last study explored the effect of a buffer cavity on the performance of angel-wing seals.

All of the aforementioned studies were conducted in the downstream wheel-space using CO_2 concentration and pressure measurements. The results presented in the following sections include radial distributions of effectiveness, swirl ratio and pressure in the wheel-space as well as variations of effectiveness with sealing flow rate.

Siemens is expected to use these results to validate their CFD simulations and to gain insight on the effect the various design features of the seals have on ingress. Using this information new, more effective geometries can be designed.

5.1 Background

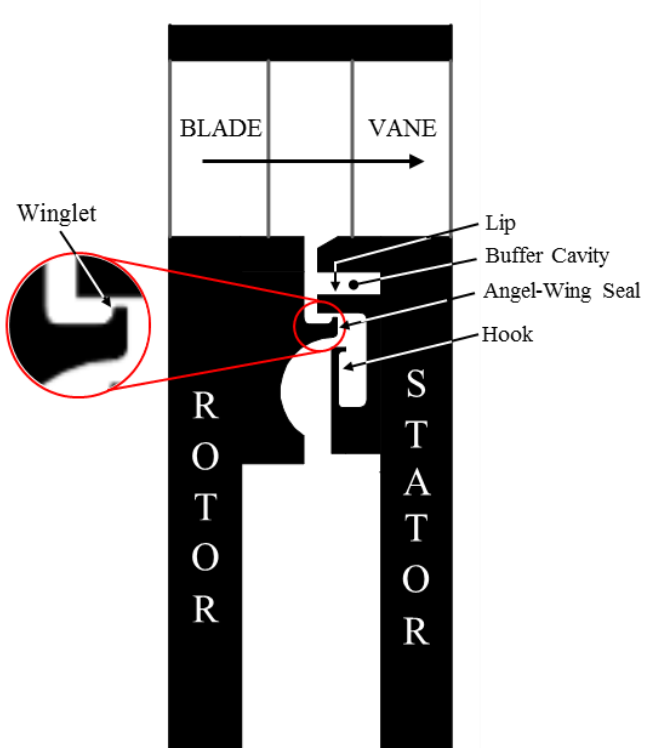

Figure 5.1: Compound rim-seal geometry

Industrial rim-seal designs vary from simple geometries such as single and double radial-clearance seals to more complex designs such as angel-wing seals (see Section 1.3.1). Each of these seals helps to minimise ingress into the wheel-space in a way unique to the geometrical features of the seal. To take advantage of the benefits of the various geometries, compound designs are considered by Siemens such as the one shown in Figure 5.1. This seal features a buffer cavity at high radius, a single-winglet angel-wing seal and a stator side hook. The seals described in the following sections include many of these features.

5.2 Parametric Study 1: Slotted Seals

This study investigates the effect of different sizes of circumferentially-spaced radial slots on the effectiveness of radial clearance seals in the downstream wheel-space. The slots simulate platform gaps between the turbine rotor blades in engines. The experiments described in the following sections were conducted at the operating point where $C_F = 0.34$.

5.2.1 Seal Geometries

In gas turbine engines, thermal expansion considerations require a small gap between the platforms of two adjacent blades as shown in Figure 5.2. The rim-seal is manufactured integrated with the blades and therefore the platform gap also creates a gap in the seal. To investigate the effect of this gap on ingress, two slotted seal configurations were manufactured with the slots simulating the inter-blade gaps.

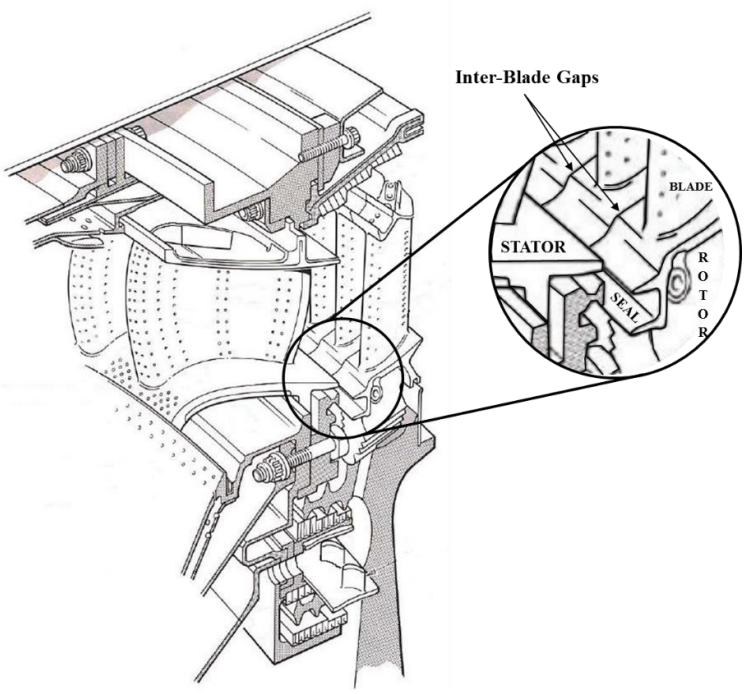

Figure 5.2: Typical high pressure gas turbine stage (adapted from Rolls-Royce (1996))

The geometry of the **s**lotted **s**eal variant **1** (**SS1**) and variant **2** (**SS2**) are shown in Figures 5.3 and 5.4 respectively. The static dimensions of these seals are provided in Table 5.1. Both seals were bolted to the underside of the rotor shroud, forming seal lips positioned at a smaller radius than the stator shroud. The lips featured 48 (one per blade) circumferentially-spaced radial slots with a pitch of 1.67º for the case of SS1 and 0.14º for the case of SS2. Both seal geometries have the same radial clearance formed between the rotor-side lip and the stator shroud, $s_{c,rad}$ = 1 mm. The axial clearance $s_{c,ax}$, and the wheel-space axial distance, S are also the same for both seal geometries and equal to 2 mm and 20 mm respectively. It should be noted that the external flow is from left to right.

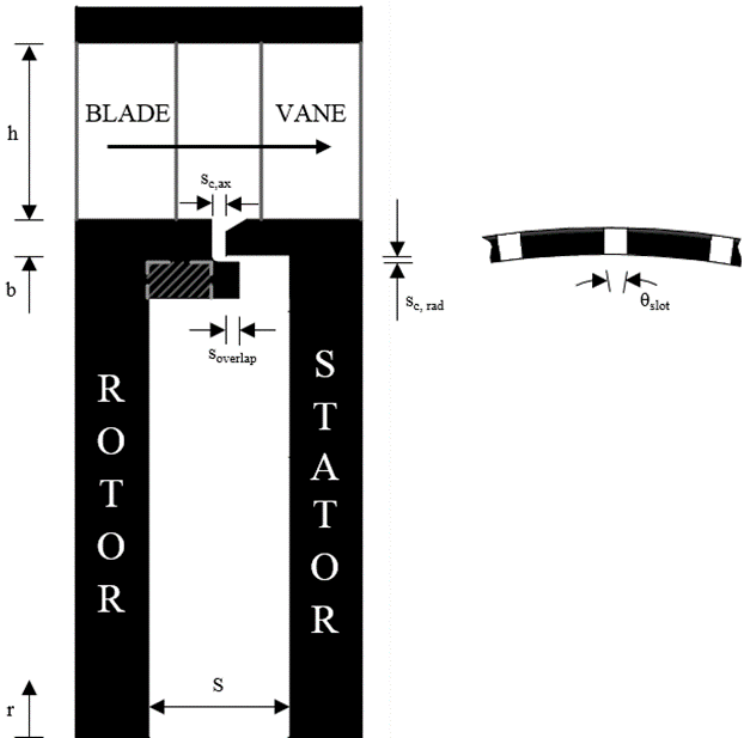

Figure 5.3: Geometry of slotted-seal variant 1 (SS1)

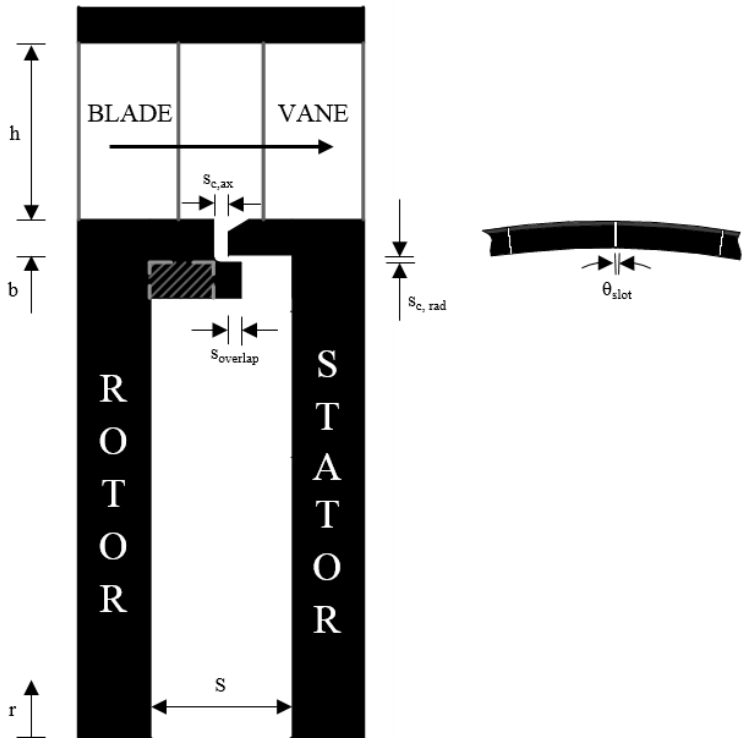

Figure 5.4: Geometry of slotted seal variant 2 (SS2)

Dimensional Parameter	Dimensions (mm)	
	SS1	SS 2
h	25	
b	190	
S	20	
$s_{c,ax}$	2	
$s_{c,rad}$	1	
$s_{overlap}$	1.86	
θ_{slot}	1.67°	0.14°

Table 5.1: Dimensions of SS1 and SS2

5.2.2 Radial Distribution of Effectiveness

Figures 5.5 and 5.6 show the radial distribution of concentration effectiveness ε_c for seal SS1 and SS2 respectively. The measurements were taken on the stator (circles) and in the rotating core (diamonds) at $z/S = 0.25$ using sampling probes. The experiments were conducted at $Re_\Phi = 7.2 \times 10^5$and for three different Φ_0 and hence λ_T values. In all cases ingress occurred. For both seals, ε_c on the stator and in the core increases as Φ_0 increases and the sealing flow raises the pressure in the wheel-space relative to the annulus. For $r/b \geq 0.65$ the distributions are invariant with radius showing that the flow structure described in Section 4.1.1 exists in

this part of the wheel-space. The rapid increase in ε_c at the smaller radii in all cases, is caused by the presence of the inlet seal where the sealing flow is introduced.

The concentration in the core is seen to be equal to that on the stator at all radial locations with the exception of the measurements taken at the higher radii where the concentration of the core is higher. The ingress will enter the wheel-space on the stator side (with low ε_c) and the egress will exit the wheel-space on the rotor side (with high ε_c) under the influence of the *pumping-effect* of the rotor disc. The core sampling probes at the higher radii are located in a region affected by the high concentration of the pumped fluid exiting the wheel-space. The sample drawn by these probes will therefore have a high concentration consistent with the measurements.

Figure 5.7 shows a comparison of the radial distribution of ε_c on the stator for SS1 (blue circles) and SS2 (green circles) for the same Φ_0. For all radial locations the effectiveness of SS2 is higher than that of SS1. This shows that the effectiveness of the seal deteriorates with the increase in the width of the slots.

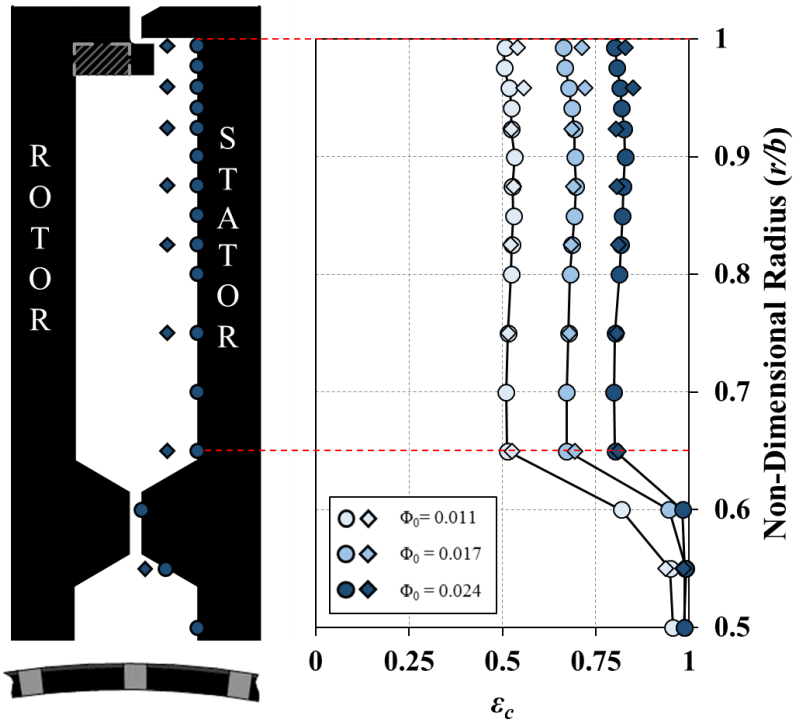

Figure 5.5: Effect of sealing flow rate on radial distribution of effectiveness for SS1 (Re_Φ = 7.2 × 10^5, C_F = 0.34) (circles denote stator measurements; diamonds denote rotating-core measurements)

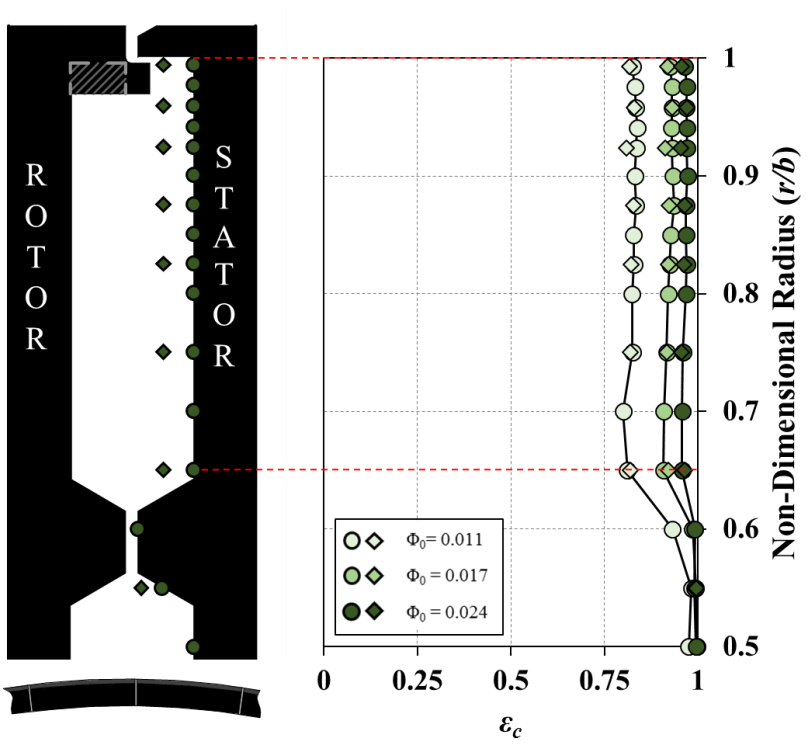

Figure 5.6: Effect of sealing flow rate on radial distribution of effectiveness for SS2 (Re_Φ = 7.2 × 10^5, C_F = 0.34) (circles denote stator measurements; diamonds denote rotating-core measurements)

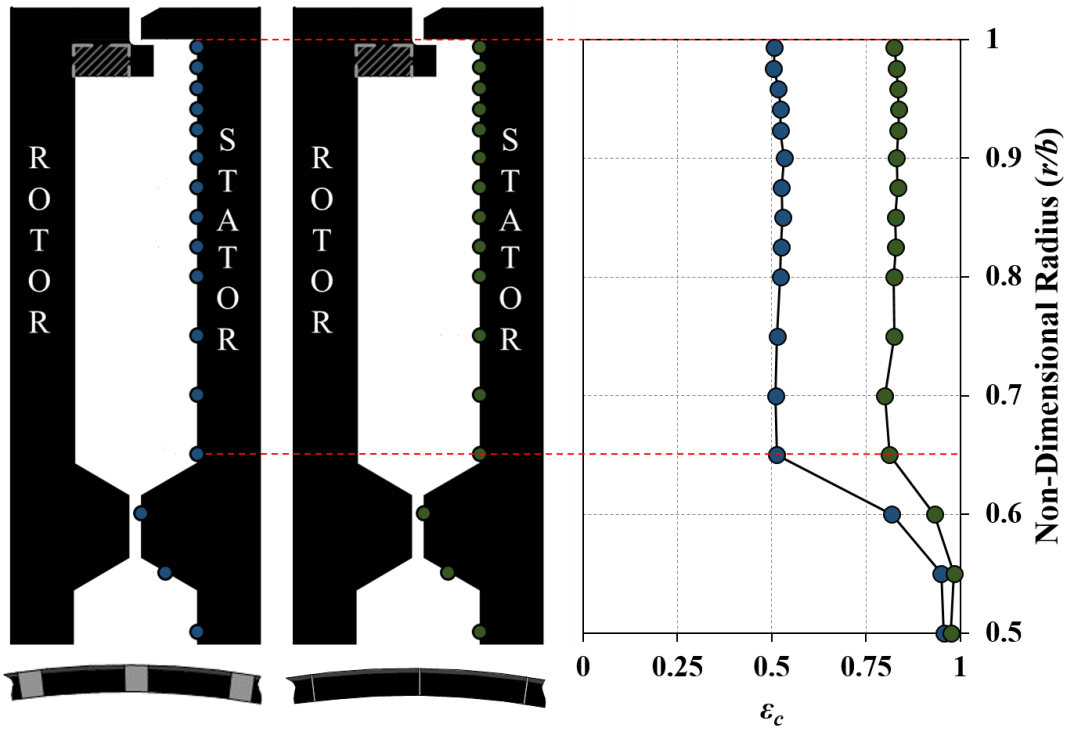

Figure 5.7: Comparison of the radial distribution of effectiveness of SS1 and SS2 (Re_Φ = 7.2 × 10^5, C_F = 0.34, Φ_0 = 0.011)

5.2.3 Variation of Concentration Effectiveness with Sealing Flow

Figures 5.8 and 5.9 show the variation of concentration effectiveness ε_c with non-dimensional sealing flow rate Φ_0 for SS1 and SS2 respectively. The measurements were taken at two radial locations r/b = 0.958 (dark symbols) and 0.85 (light symbols) and for two rotational Reynolds numbers Re_Φ = 7.2 × 10^5 and 1.0 × 10^6. In all cases ε_c increases with Φ_0, as the sealing flow pressurises the wheel-space and reduces ingestion through the rim-seals. The data for each seal collapse onto single curves which are independent of sampling location and Re_Φ. This is in agreement with the radial distributions of ε_c discussed in the previous section.

The RI theoretical effectiveness curves (Eq. 2.11) were fitted to the experimental data indicating good agreement between theory and experiment in all cases. The estimated values of Φ_{min} and Γ_c and their 95% confidence intervals along with the values of Φ_{min}', and standard deviation σ between the data and the fitted curves are tabulated in Table 5.2.

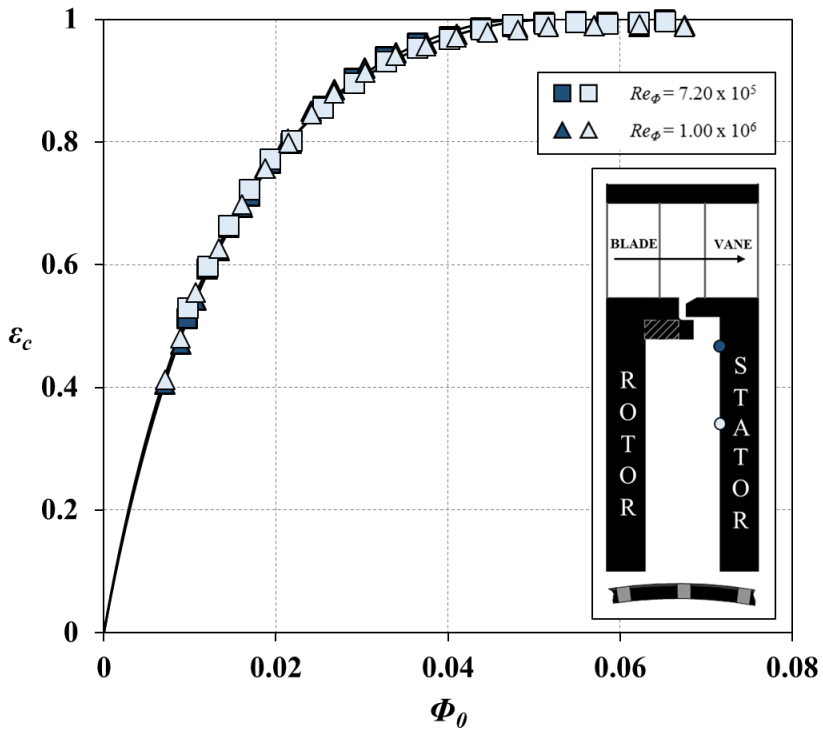

Figure 5.8: Variation of ε_c with Φ_0 for SS1 at r/b = 0.958 (dark blue symbols) and r/b = 0.85 (light blue symbols) (C_F = 0.34) (symbols denote data; solid lines are theoretical curves obtained from the orifice model)

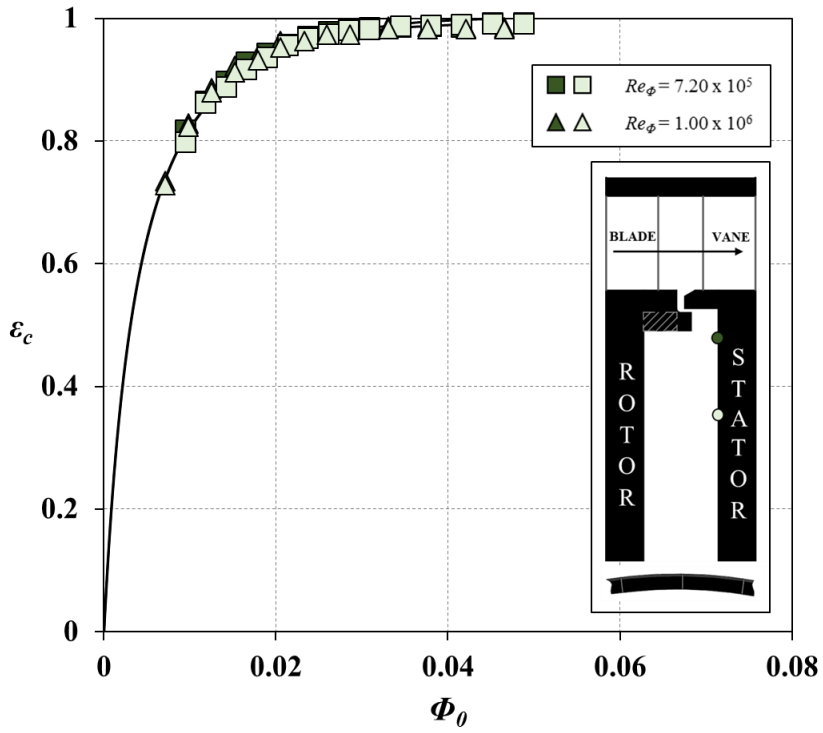

Figure 5.9: Variation of ε_c with Φ_0 for SS2 at r/b = 0.958 (dark green symbols) and r/b = 0.85 (light green symbols) (C_F = 0.34) (symbols denote data; solid lines are theoretical curves obtained from the orifice model)

Parameter	SS1		SS2	
	r/b			
	0.958	***0.85***	***0.958***	***0.85***
Φ_{min}	0.0475	0.0507	0.0413	0.0457
Φ_{min}'	0.0351	0.0362	0.0201	0.0214
Γ_c	0.638	0.522	0.119	0.106
σ	0.00759	0.00685	0.00817	0.00824

Table 5.2: Theoretical fit parameters for SS1 and SS2 seals

The results of Figures 5.8 and 5.9 are combined in Figure 5.10 to enable a comparison of the effectiveness of SS1 and SS2. The measurements corresponding to $Re_\Phi = 1.0 \times 10^6$ are omitted for clarity. The effectiveness of SS2 is higher than the one of SS1 for all values of Φ_0. As consequence of the wider slots in SS2, a smaller level of pressurisation is achieved for the same amount of sealing flow rate and hence a lower effectiveness.

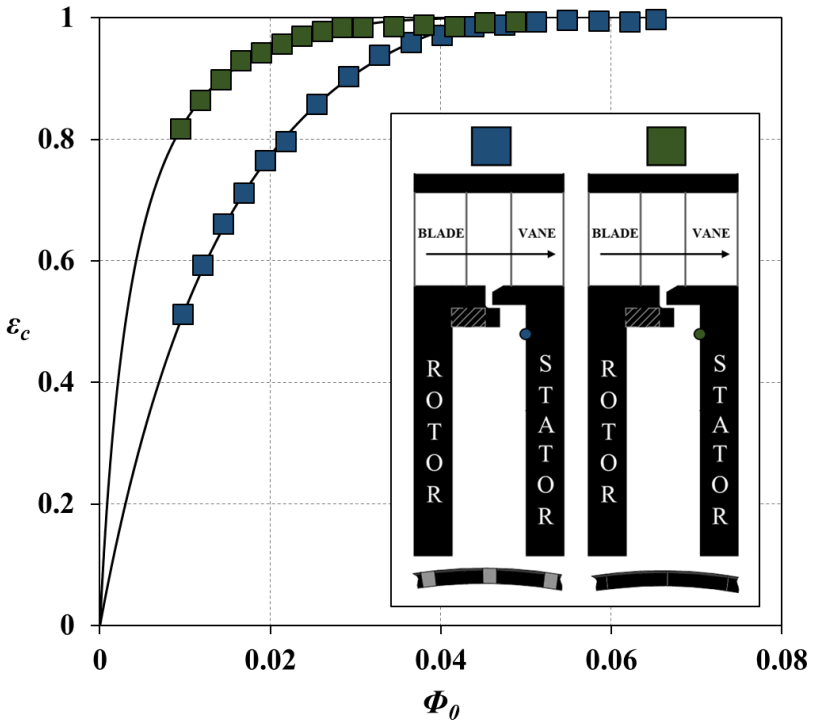

Figure 5.10: Comparison of the variation of ε_c with Φ_0 at r/b = 0.958 for SS1 (blue squares) and SS2 (green squares) (Re_Φ = 7.2 × 10^5; C_F = 0.34) (symbols denote data; solid lines are theoretical curves obtained from the orifice model)

5.2.4 Wheel-Space Pressure and Swirl Measurements

Figures 5.11 and 5.12 illustrate the variation of swirl ratio and static pressure coefficient in the wheel-space with non-dimensional radius for SS1 and SS2 respectively. The measurements were taken at Re_Φ = 7.2 × 10^5 for several values of λ_T and hence Φ_0. The measurement points for the total pressure in the wheel-space (at z/S = 0.25) are shown as diamond symbols on the silhouettes in the centre of the figures. In all cases ingress occurred with an annulus swirl ratio downstream of the blades, $\beta_{a,\,DWS}$ = 0.2.

For λ_T = 0, there is no superposed flow and the core rotation β = 0.4 at r/b < 0.8 for both seals. The swirl ratio at the larger radii outside of the core region increases radially under the influence of the ingested flow. Increasing the sealing flow causes a reduction in the core rotation as the wheel-space is pressurised. The level of swirl at the periphery of the wheel-space is also reduced as the increased sealant flow decreased ingestion from the annulus.

Also shown in Figures 5.11 and 5.12 is the radial variation of the pressure coefficient C_p in the wheel-space for the two seals. For all sealing flow rates and up to r/b = 0.958, C_p increases radially due to the existance of a radial pressure gradient which is a result of the swirling motion of the core. As the sealing flow increases the rotation of the core and hence the radial

pressure gradient are reduced resulting in lower C_p values. Theoretical distributions of C_p, calculated using Eq. 4.2 are also plotted on the same graphs indicating good agreement between experiment and theory. This shows that the radial distribution of static pressure is controlled by the swirl ratio. For $r/b \geq 0.958$ the distribution of C_p is invariant with radius indicating that the region of the wheel-space at these high radii is not under the influence of the rotating core but under the influence of ingress and the features of the seal.

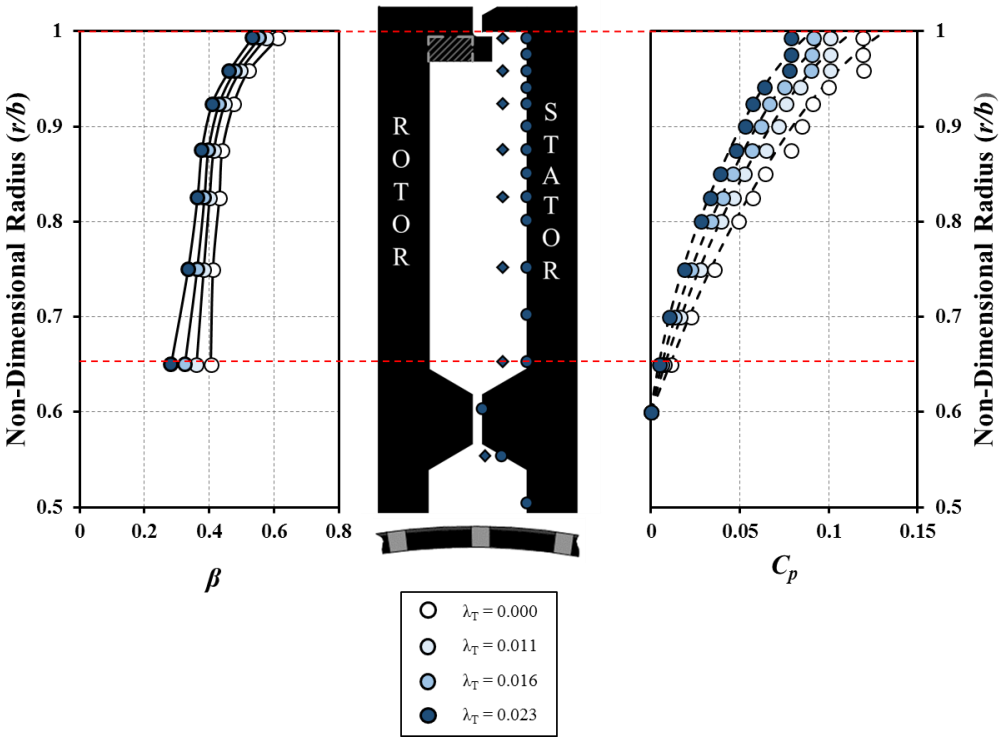

Figure 5.11: Effect of sealing flow rate on the distribution of swirl ratio and pressure for SS1 (symbols denote measured values; dash lines denote calculated distribution for C_p)

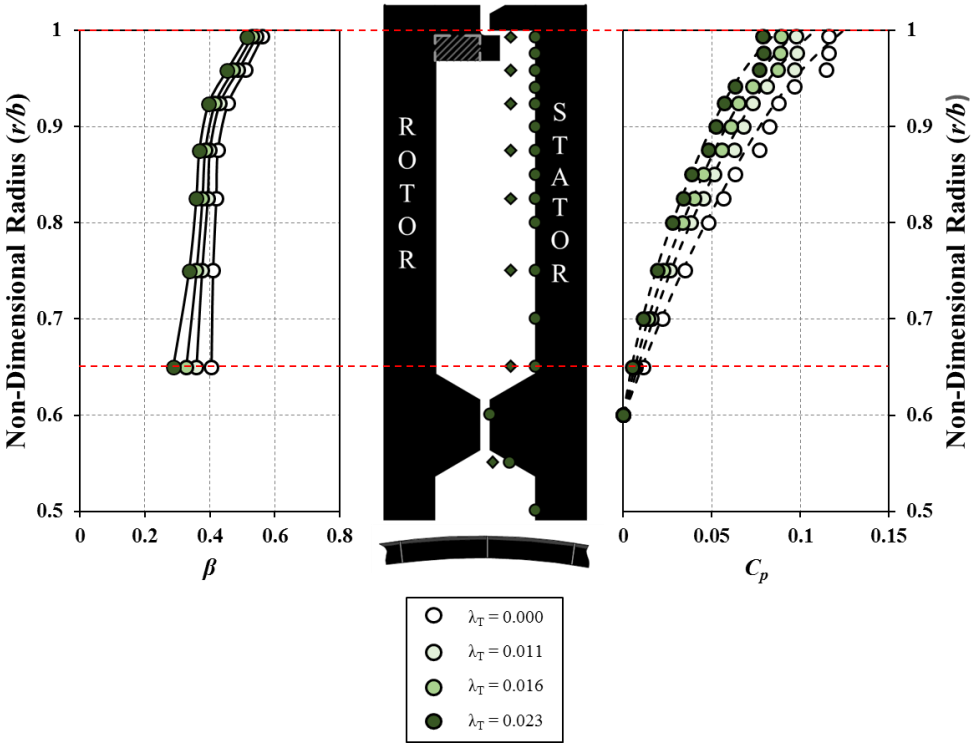

Figure 5.12: Effect of sealing flow rate on the distribution of swirl ratio and pressure for SS2 (symbols denote measured values; dash lines denote calculated distribution for C_p)

5.3 Parametric Study 2: Angel-Wing Seals

This study investigates a potential increase in the performance of angel-wing seals by the addition of secondary features, namely winglets, and a single radial-clearance seal at a lower radius. The experiments described in the following sections were conducted at the operating point where $C_F = 0.34$.

5.3.1 Seal Geometries

The geometry and static dimensions of the **a**ngle **w**ing (**AW1),** double winglet angel-wing (**AW2**) and compound angel-wing (**AW3**) seals are shown in Figure 5.13 (a) to (c) and Table 5.3. AW1 features a simple angel-wing seal and is considered as the baseline geometry. AW2 is the same seal as AW1 with an additional winglet. AW3 is a compound seal consisting of an inner and an outer seal. The outer seal is the same as AW1, the inner seal is a single radial-clearance seal. All seals feature the same axial clearance $s_{c,ax} = 2$ mm, radial clearance, $s_{c,rad} = 0.7$ mm and axial overlap $s_{,overlap} = 2.8$ mm. The seal-clearance ratio, $G_c = s_{c,ax} / b = 0.0105$ is also consistent between all geometries.

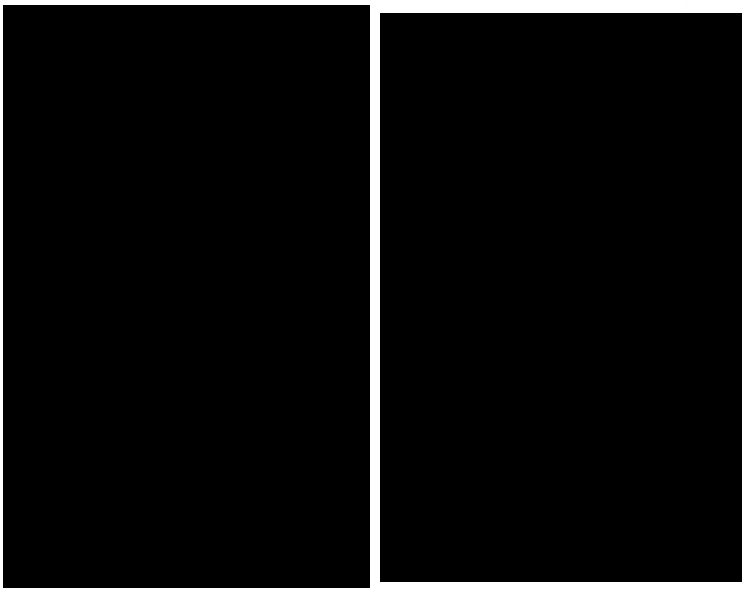

(a) (b)

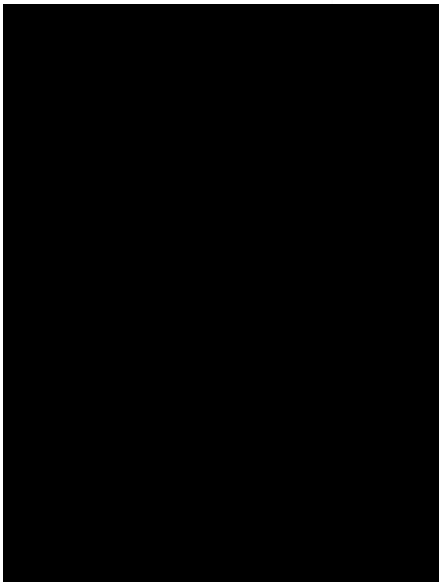

(c)

Figure 5.13: Geometries of: (a) angel-wing (AW1), (b) double winglet angel-wing (AW2) and (c) compound angel-wing (AW3) seals

Dimensional Parameter	Dimensions (mm)		
	AW1	AW2	AW3
h		25	
b		190	
S		20	
$s_{c,ax}$		2	
$s_{c,rad}$		0.7	
$s_{overlap}$		2.8	

Table 5.3: Dimensions of AW1, AW2 and AW3 seals

5.3.2 Radial Distribution of Effectiveness

Figures 5.14 to 5.16 show the radial distribution of ε_c for AW1, AW2 and AW3 respectively. The measurements were taken on the stator (circles) and in the rotating core (diamonds) for three different Φ_0 values. For all three seals, ε_c on the stator is equal to that in the core and increases as Φ_0 increases and the sealing flow raises the pressure in the wheel-space relative to the annulus. The increase in ε_c at the smaller radii in all cases, is caused by the presence of the inlet seal where the sealing flow is introduced.

For seals AW1 and AW2 the distribution of ε_c is invariant with radius for $r/b > 0.65$ and for all sealant flow rates suggesting that near-complete mixing has occurred in a region very close to the periphery of the wheel-space.

For seal AW3 a concentration gradient exists for $r/b > 0.948$ where ε_c decreases as the non-dimensional radius increases. This is indicative of a mixing region where the ingested annulus flow mixes with the sealing flow. Outside of this mixing region, ε_c is invariant with radius and the flow structure described in Sections 2.4 and 4.1.1 exists.

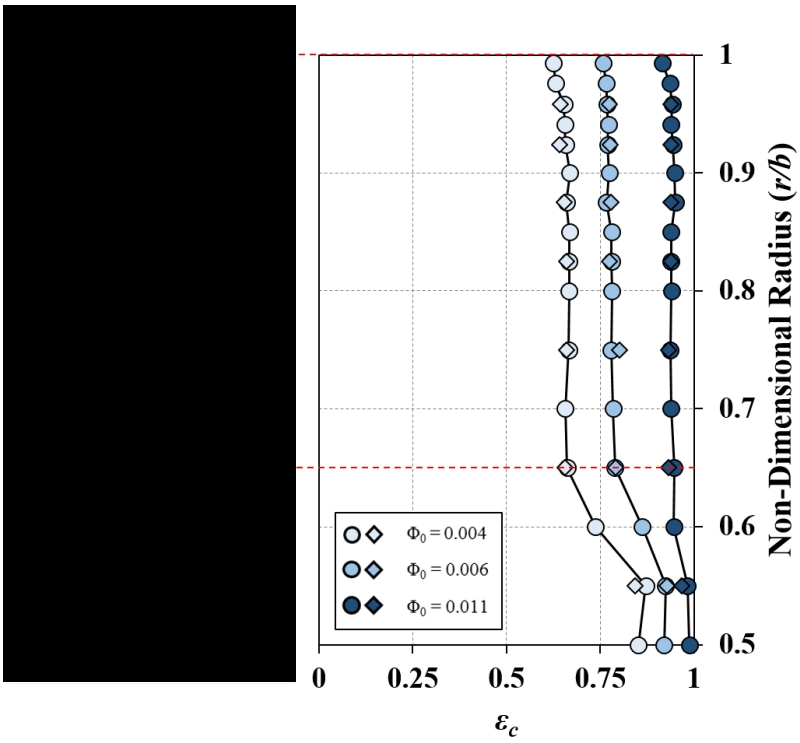

Figure 5.14: Effect of sealing flow rate on radial distribution of effectiveness for AW1 seal ($Re_\Phi = 7.2 \times 10^5$, $C_F = 0.34$) (circles denote stator-wall measurements; diamonds denote rotating-core measurements)

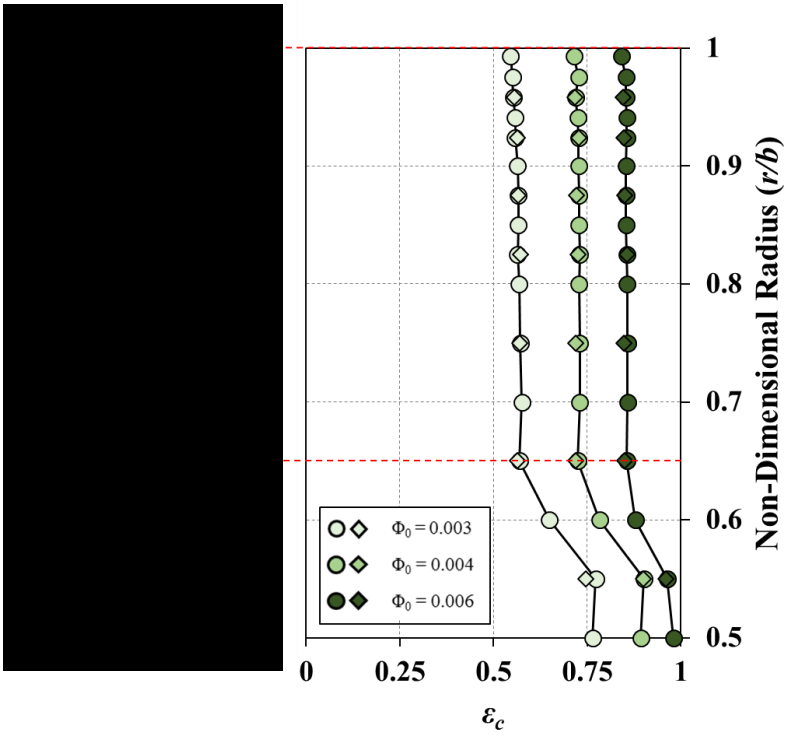

Figure 5.15: Effect of sealing flow rate on radial distribution of effectiveness for AW2 seal (Re_Φ = 7.2 × 10^5, C_F = 0.34) (circles denote stator-wall measurements; diamonds denote rotating-core measurements)

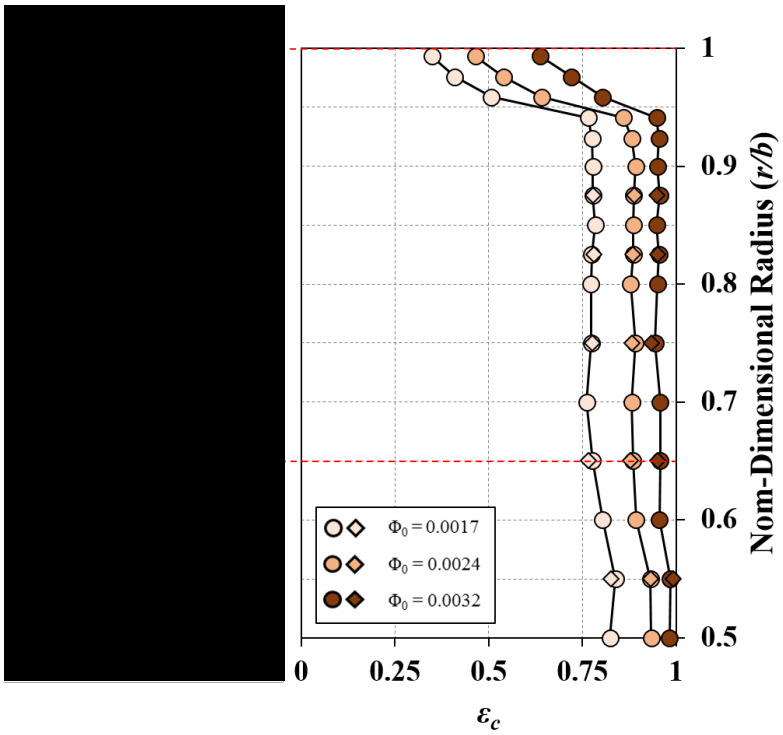

Figure 5.16: Effect of sealing flow rate on radial distribution of effectiveness for AW3 seal (Re_Φ = 7.2 × 10^5, C_F = 0.34) (circles denote stator-wall measurements; diamonds denote rotating-core measurements)

5.3.3 Variation of Concentration Effectiveness with Sealing Flow

Figures 5.17 to 5.19 show the variation of ε_c with Φ_0 for seals AW1, AW2 and AW3 respectively. The measurements were taken at two radial locations, *r/b = 0.958* (dark symbols) and *0.85* (light symbols) and at two rotational Reynolds numbers $Re_\Phi = 7.2 \times 10^5$ and 1.0×10^6. In all cases ε_c increases with increasing Φ_0, as the sealing flow pressurises the wheel-space and reduces ingestion through the rim-seal. The data are shown to be independent of Re_Φ.

For the case of AW1 and AW2 seals, the variation of ε_c with Φ_0 at both sampling locations is similar. In contrast, the concentration of AW3 at *r/b* = 0.85 is higher than that at *r/b* = 0.958.This shows that ingress was predominantly constrained within the region between the outer angel-wing seal and the inner radial-clearance seal. If such a seal was to be fitted in an engine, ingress of hot mainstream flow would be confined in a region of temperature resistant blading material leaving the vulnerable inner wheel-space protected.

Also shown in Figures 5.17 to 5.19 are the RI theoretical effectiveness curves that were fitted to the experimental data. Good agreement between theory and experiment was observed in all cases. The estimated values of Φ_{min} and Γ_c and their 95% confidence intervals along with the values of Φ_{min}', and standard deviation σ between the data and the fitted curves are given in Table 5.4.

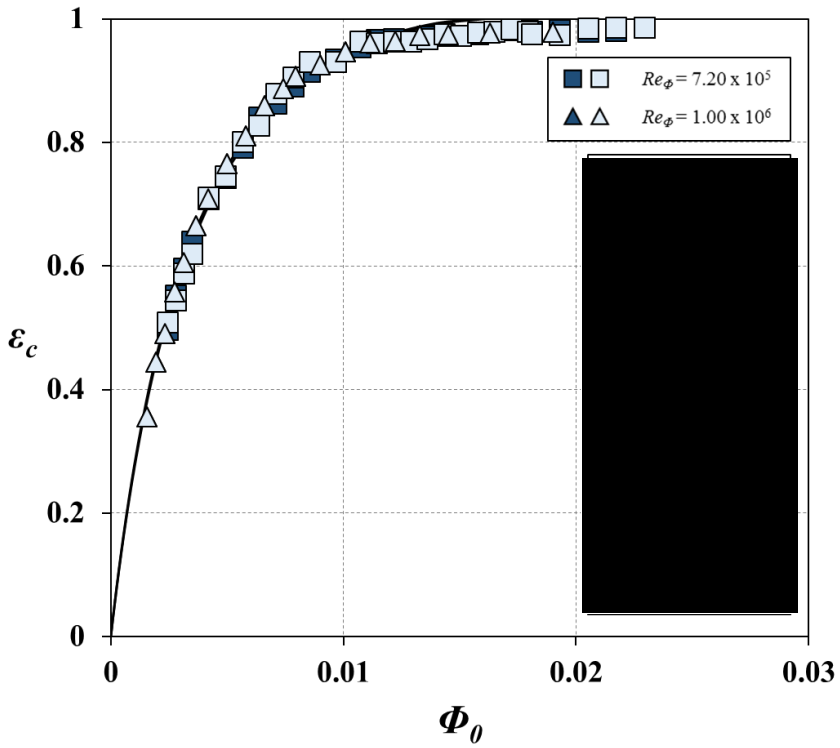

Figure 5.17: Variation of ε_c with Φ_0 for AW1 seal at *r/b* = 0.958 (dark blue symbols) and *r/b* = 0.85 (light blue symbols) (C_F = 0.34) (symbols denote data; solid lines are theoretical curves obtained from the orifice model)

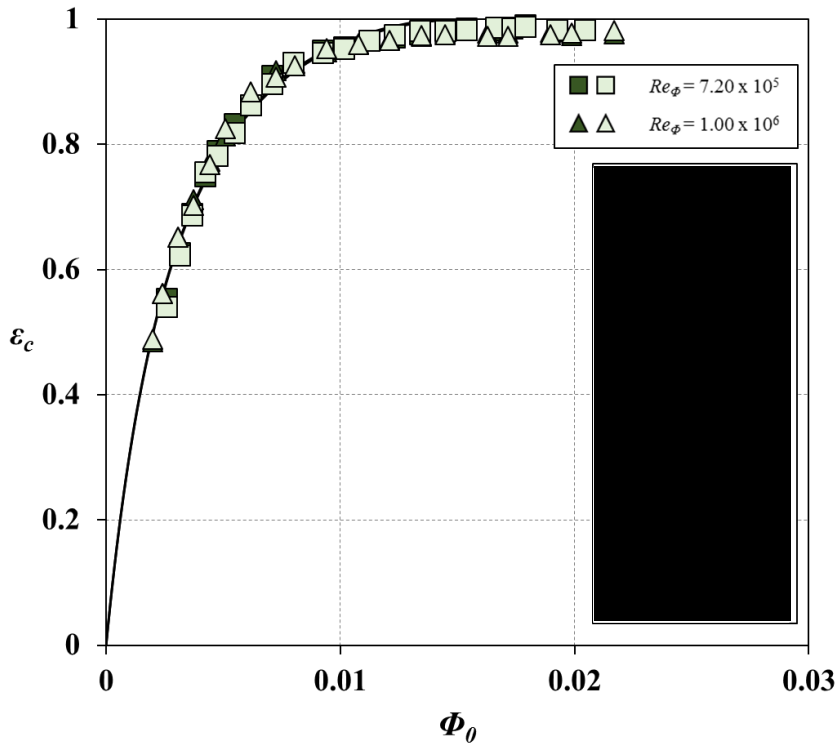

Figure 5.18: Variation of ε_c with Φ_0 for AW2 seal at r/b = 0.958 (dark green symbols) and r/b = 0.85 (light green symbols) (C_F = 0.34) (symbols denote data; solid lines are theoretical curves obtained from the orifice model)

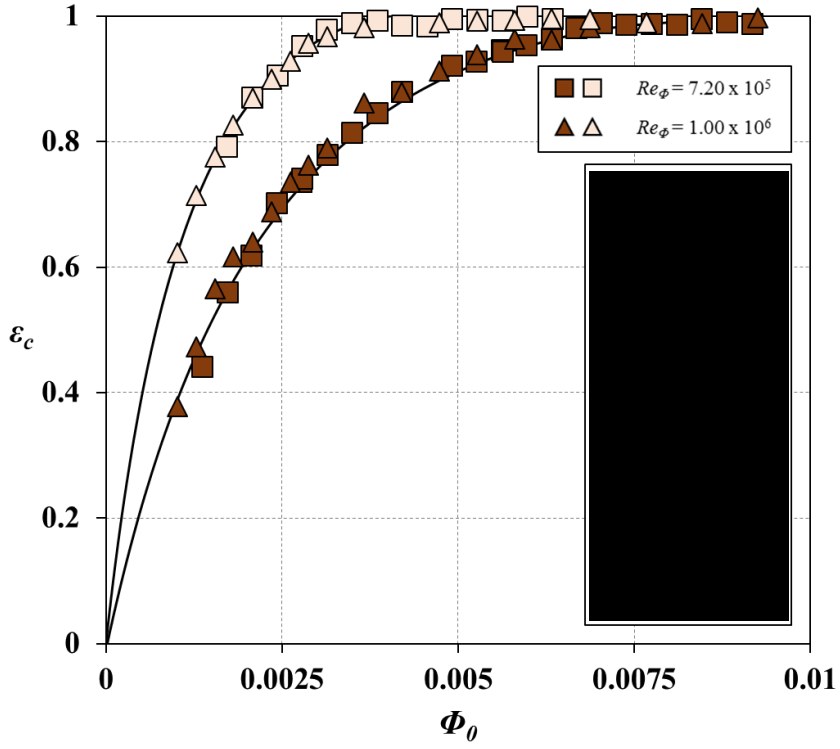

Figure 5.19: Variation of ε_c with Φ_0 for AW3 at r/b = 0.958 (dark brown symbols) and r/b = 0.85 (light brown symbols) (C_F = 0.34) (symbols denote data; solid lines are theoretical curves obtained from the orifice model)

Parameter	AW1		AW2		AW3	
	r/b					
	0.958	***0.85***	***0.958***	***0.85***	***0.958***	***0.85***
Φ_{min}	0.0161	0.0158	0.0144	0.0149	0.00803	0.254
Φ_{min}'	0.0105	0.0103	0.00938	0.00954	0.00565	0.00286
Γ_c	0.338	0.335	0.321	0.305	0.450	0.00126
σ	0.0149	0.0177	0.0169	0.0181	0.0144	0.0532

Table 5.4: Theoretical fit parameters for AW1, AW2 and AW3

The results of Figures 5.17, 5.18 and 5.19 are combined in Figure 5.20 to enable a comparison of the performance of AW1, AW2 and AW3. The measurements corresponding to $Re_\Phi = 1.0 \times 10^6$ are omitted for clarity. The curve corresponding to the measurements taken at $r/b = 0.85$ for AW3 is also added to the figure for completeness. In the following discussion the geometry of AW1 will be considered as the baseline geometry.

First consider the measurements corresponding to seals AW1 and AW2. For all Φ_0 values, the effectiveness of AW2 (green symbols) is slightly higher than the one of AW1 (blue symbols). This shows that adding a second winglet to the baseline geometry has a marginally positive effect on the performance of the seal.

Now consider the measurements for the compound seal, AW3. The effectiveness of AW3 at the outer location is significantly higher than that of AW1 and AW2 seals. At this point it is worth noting that, as shown by the radial distributions of ε_c (Figure 5.16), the outer sampling location in the case of AW3 is in a mixing region where a radial gradient of concentration exists. For this reason the measurements taken at this radial location are only indicative of the local change of ε_c with Φ_0 and should not be used for performance comparisons. The measurements taken at the inner sampling location were used instead. At this location the effectiveness of AW3 is also significantly higher than that of AW1 and AW2 seals. This is due to an additional pressure drop across the inner radial-clearance seal featured in AW3.

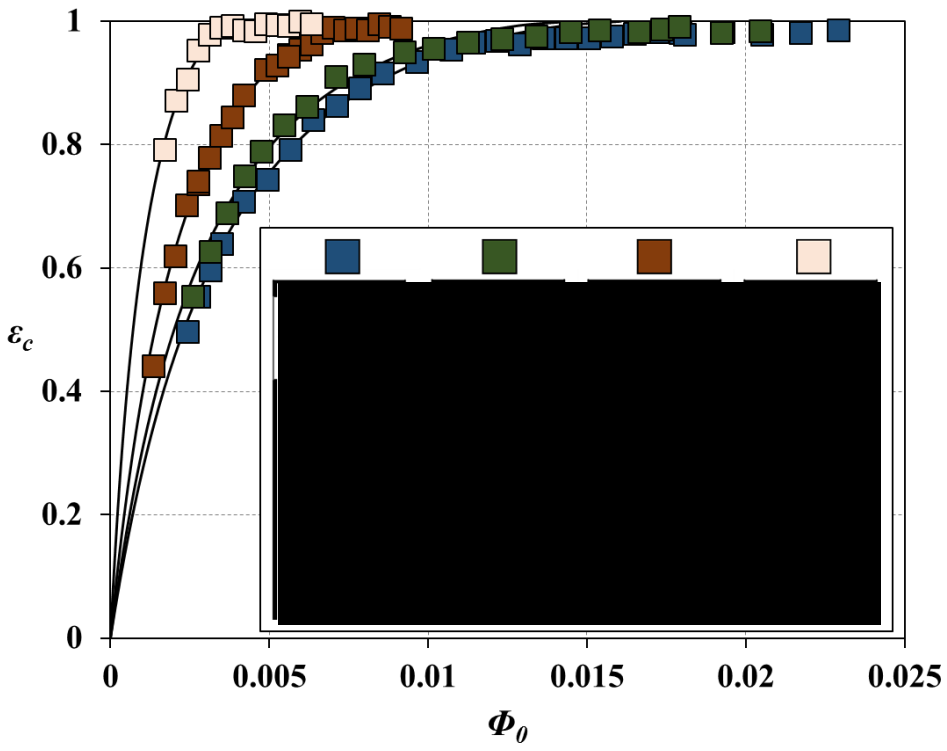

Figure 5.20: Comparison of the variation of ε_c with Φ_0 for AW1 (blue symbols), AW2 (green symbols) and AW3 (dark and light brown symbols) seals (Re_Φ = 7.2 × 10^5; C_F = 0.34) (symbols denote data; solid lines are theoretical curves obtained from the orifice model)

5.3.4 Wheel-Space Pressure and Swirl Measurements

Figures 5.21 to 5.23 illustrate the variation of β and C_p in the wheel-space with non-dimensional radius for AW1, AW2 and AW3 respectively. The measurements were taken at Re_Φ = 7.2 × 10^5 for several values of λ_T and hence Φ_0. The measurement points for the total pressure in the wheel-space (at z/S = 0.25) are shown as diamond symbols on the silhouettes in the centre of the figures. In all cases ingress occurred with an annulus swirl ratio downstream of the blades, $\beta_{a,\,DWS}$ = 0.2.

For λ_T = 0, there is no superposed flow and the core rotation $\beta \approx 0.44$ at $r/b < 0.875$ for all three seals. This shows that the flow structure described in Sections 2.4 and 4.1.1 exists in this region. The swirl ratio at the larger radii increases radially under the influence of the ingested flow and the geometric features of the seals. Increasing the sealing flow caused a reduction in the core rotation as the wheel-space is pressurised.

Also shown in Figures 5.21 to 5.23 is the radial variation of the pressure coefficient, C_p in the wheel-space for the three seals. For all sealing flow rates and up to r/b = 0.958, C_p increased radially under the influence of the swirling motion of the core. As the sealing flow increases the rotation of the core and hence the radial pressure gradient are reduced resulting

in lower C_p values. Also plotted on the same graphs are the theoretical distributions of C_p, based on the experimental measurements of the swirl ratio and calculated using Eq. 4.2. Good agreement between experiment and theory is observed. This shows that the radial distribution of static pressure is controlled by the swirl ratio. For $r/b \geq 0.958$ the distribution of C_p is invariant with radius and the agreement between the theoretical and experimental distributions deteriorates. This region of the wheel-space is under the influence of ingress and the geometric features of the seals.

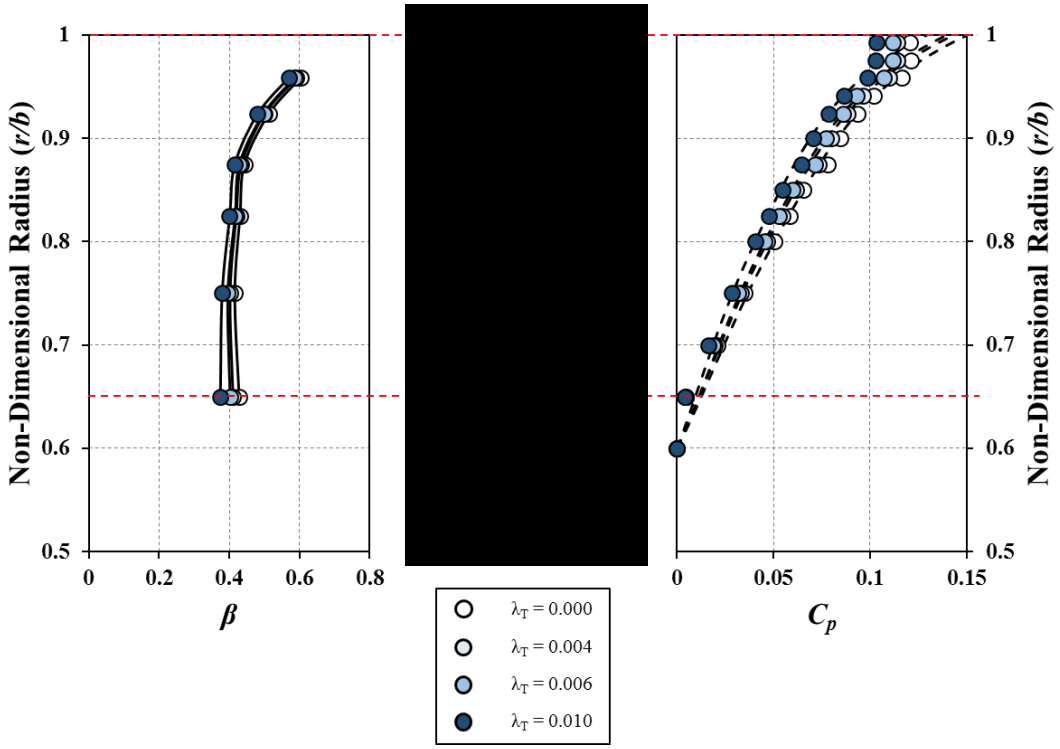

Figure 5.21: Effect of sealing flow rate on the distribution of swirl ratio and pressure for AW1 (symbols denote measured values; dash lines denote calculated distribution for C_p)

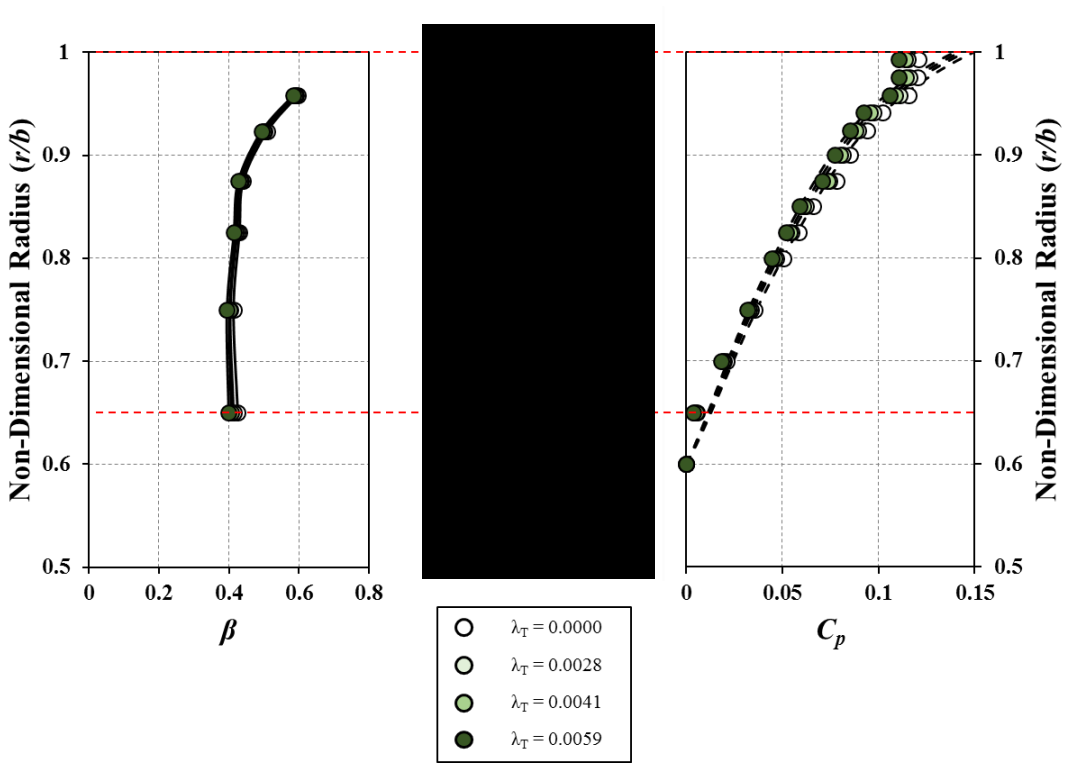

Figure 5.22: Effect of sealing flow rate on the distribution of swirl ratio and pressure for AW2 (symbols denote measured values; dash lines denote calculated distribution for C_p)

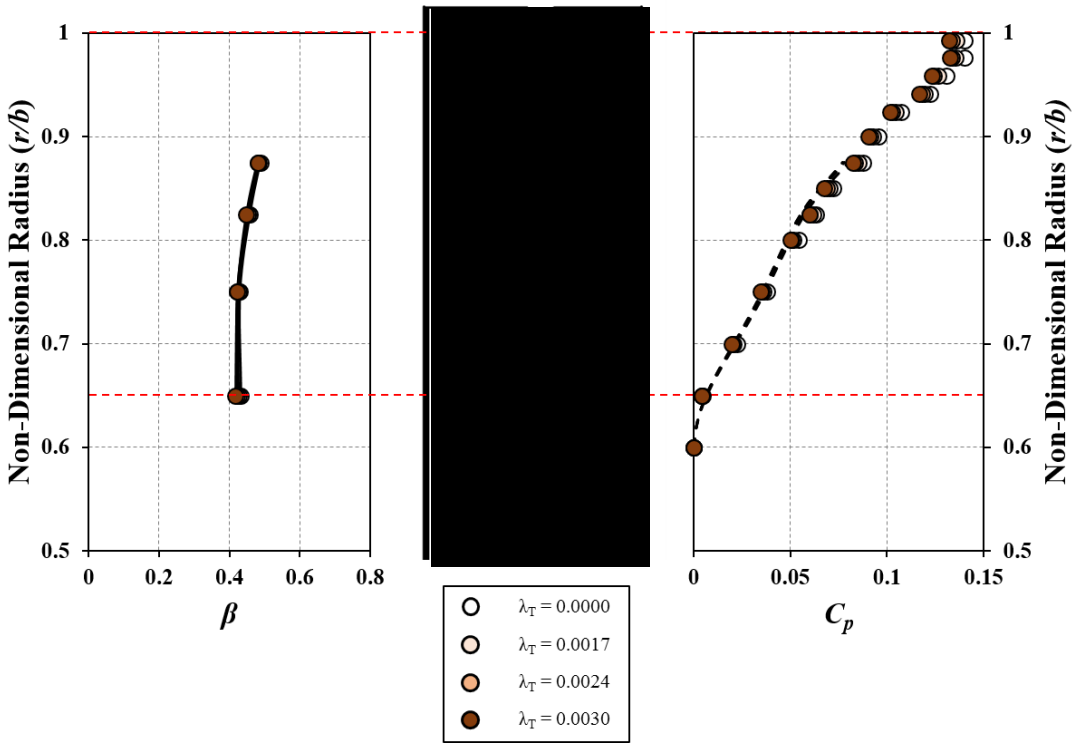

Figure 5.23: Effect of sealing flow rate on the distribution of swirl ratio and pressure for AW3 (symbols denote measured values; dash lines denote calculated distribution for C_p)

5.4 Parametric Study 3: Angel-Wing Seals with Buffer Cavity

This study investigated the effect of a buffer cavity on the performance of angel-wing seals. The experiments described in the following sections were conducted at the operating point where $C_F = 0.34$.

5.4.1 Seal Geometries

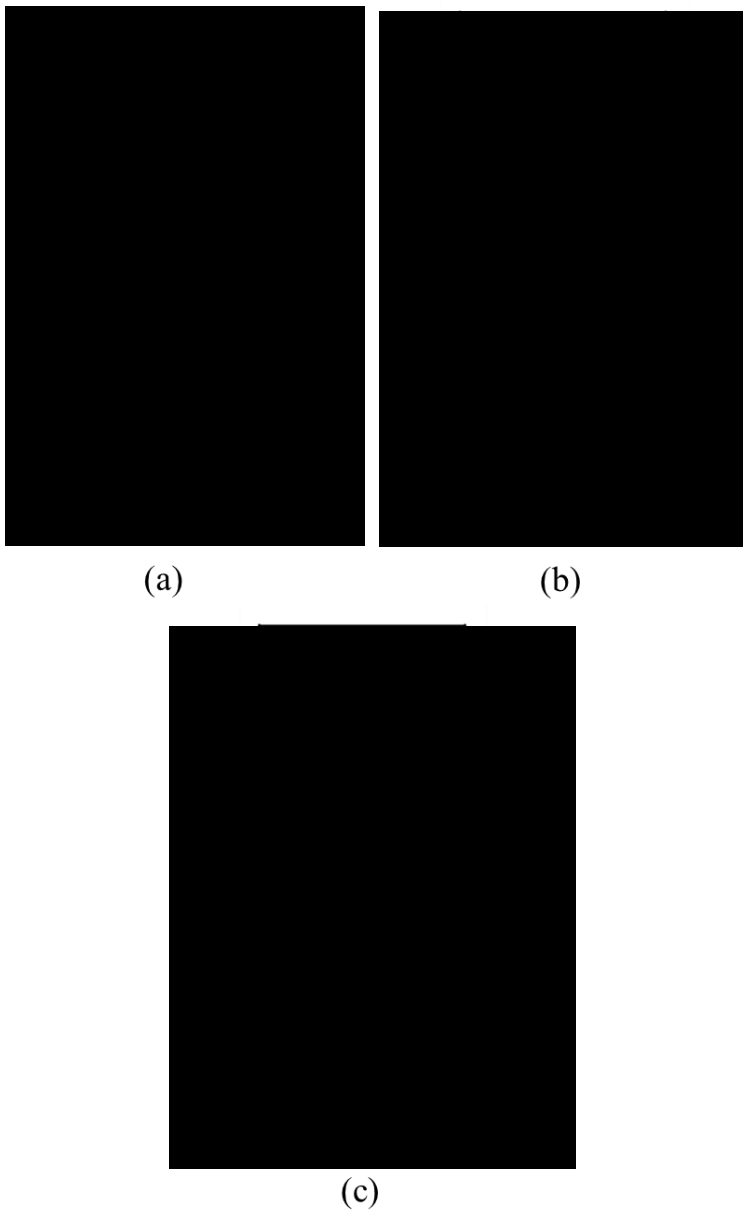

Figure 5.24: Geometries of: (a) angel-wing with buffer cavity (AWBC1), (b) angel-wing without buffer cavity (AWBC2) and (c) compound angel-wing with buffer cavity (AWBC3) seals

The geometry and static dimensions of the three angel-wing seals used in this parametric study are shown in Figure 5.24 and Table 5.5. **AWBC1** is considered as the baseline geometry and features an **a**ngel-**w**ing seal with a **b**uffer **c**avity at higher radius. **AWBC2** is the same as AWBC1 but without the buffer cavity. **AWBC3** is a compound seal consisting of seal AWBC1 and a stator-side hook. All seal geometries feature the same axial clearance $s_{c,ax}$ = 2 mm, the radial clearance, $s_{c,rad}$ = 0.7 mm and axial overlap $s_{,overlap}$ = 2.8 mm. The seal-clearance ratio, $G_c = s_{c,ax} / b$ = 0.0105 is also consistent for all seal geometries.

Dimensional Parameter	Dimensions (mm)		
	AWBC1	AWBC2	AWBC3
h		25	
b		190	
S		20	
$s_{c,ax}$		2	
$s_{c,rad}$		0.7	
$s_{overlap}$		2.8	
$s_{c,rad,hook}$	-	-	1.5
h_{buffer}	3.3	-	3.3

Table 5.5: Dimensions of AWBC1, AWBC2 and AWBC3 seals

5.4.2 Radial Distribution of Effectiveness

Figures 5.25 to 5.27 show the radial distribution of concentration effectiveness, ε_c in the downstream wheel-space for AWBC1, AWBC2 and AWBC3 respectively. The measurements were taken on the stator (circles) and in the rotating core (diamonds) for three different Φ_0 values. In all cases ingress occurred. For all three seals, ε_c on the stator is equal to that in the core and increases as Φ_0 increases and the sealing flow raises the pressure in the wheel-space relative to the annulus. The increase in ε_c at the smaller radii is caused by the presence of the inlet seal where the sealing flow is introduced.

Consider first the case of AWBC1 and AWBC2. For $0.65 \leq r/b \leq 0.941$, ε_c is invariant with radius for all sealant flow rates suggesting that near-complete mixing has occurred in a region very close to the periphery of the wheel-space. At $r/b = 0.9$ a sudden decrease in effectiveness can be seen for both seals. It is thought that in that region, the relatively large radius featured on the rotor-side part of the seal promotes recirculation of high concentration flow from the rotor boundary layer to the stator boundary layer as illustrated in Figure 5.28. The positive effect of this is not sensed right in the corner of the inner stator-side lip where the sampling tap at $r/b = 0.9$ is located.

For $r/b > 0.941$ a steep concentration gradient exists for all Φ_0 values with ε_c decreasing as the non-dimensional radius increases. This indicates a mixing region where the ingested annulus flow mixes with the sealing flow. The concentration of the outer most sampling point at r/b = 0.993, is very small in comparison to the measurements taken deeper in the wheel-space. This indicates that the region immediately inboard of the wheel-space shroud is highly affected by the ingested annulus flow which has a concentration $c_\alpha = 0$.

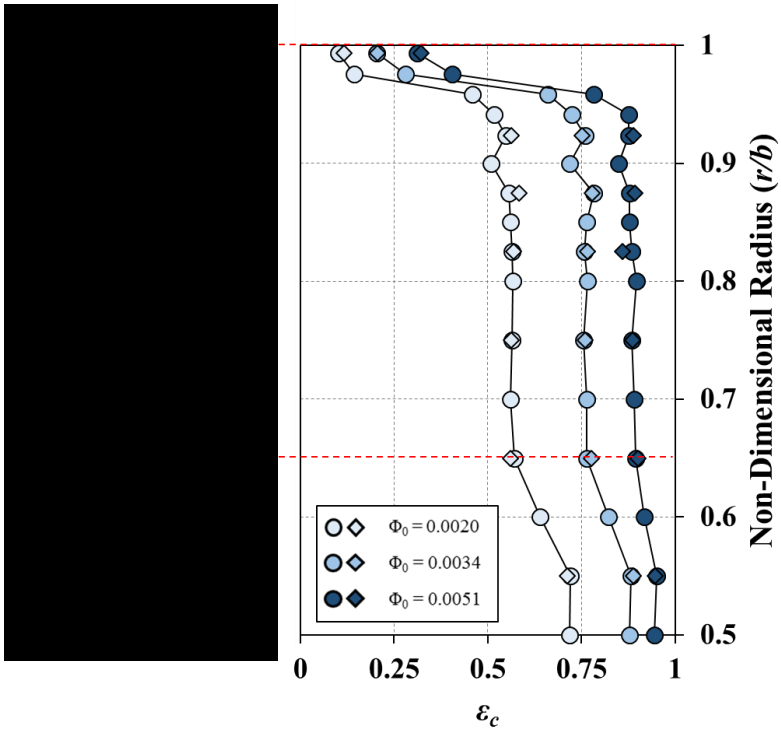

Figure 5.25: Effect of sealing flow rate on radial distribution of effectiveness for AWBC1 ($Re_\Phi = 7.2 \times 10^5$, $C_F = 0.34$) (circles denote stator-wall measurements; diamonds denote rotating-core measurements)

Now consider the case of AWBC3. Three distinct regions can be seen in the distributions of ε_c. The first region is between $0.993 \geq r/b \geq 0.976$ and is referred to as the outer wheel-space. In the outer wheel-space a steep concentration gradient exists for all Φ_0 values, with ε_c decreasing as the non-dimensional radius increases. This indicates a mixing region where the ingested annulus flow mixes with the sealing flow. In addition, the effectiveness in the outer wheel-space is very small compared to the effectiveness at the lower radii indicating that this region is strongly affected by the ingested flow. The second region is between $0.958 \geq r/b \geq 0.9$ and is referred to as the intermediate wheel-space. The concentration in the intermediate wheel-space is broadly invariant with radius and higher than the one in the outer wheel-space. As it can be seen the most significant increase in ε_c occurs across the angel-wing, from r/b =

0.976 to 0.958. This shows the importance of the angel-wing as a design feature for rim-seals. The third region is between $0.875 \leq r/b \leq 0.65$ and is referred to as the inner wheel-space. In the inner wheel-space ε_c is broadly invariant with radius and higher than that in the intermediate wheel-space for all Φ_0 values. The flow structure described in Sections 2.4 and 4.1.1 is also expected to be found in this region.

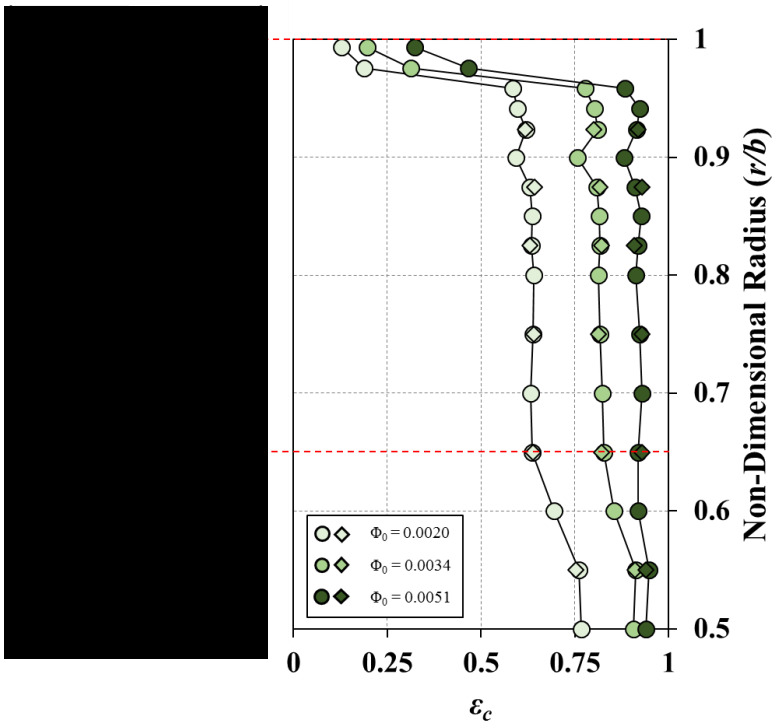

Figure 5.26: Effect of sealing flow rate on radial distribution of effectiveness for AWBC2 ($Re_\Phi = 7.2 \times 10^5$, $C_F = 0.34$) (circles denote stator-wall measurements; diamonds denote rotating-core measurements)

Figure 5.29 shows a comparison of the radial distributions of effectiveness on the stator wall between AWBC1 (blue symbols), AWBC2 (green symbols) and AWBC3 (brown symbols) for the same non-dimensional sealing flow rate, Φ_0. The silhouettes of the three seals have also been added underneath the figure indicating the radial locations at which the measurements were taken. The geometry of AWBC1 will be considered as the baseline geometry in the following discussion.

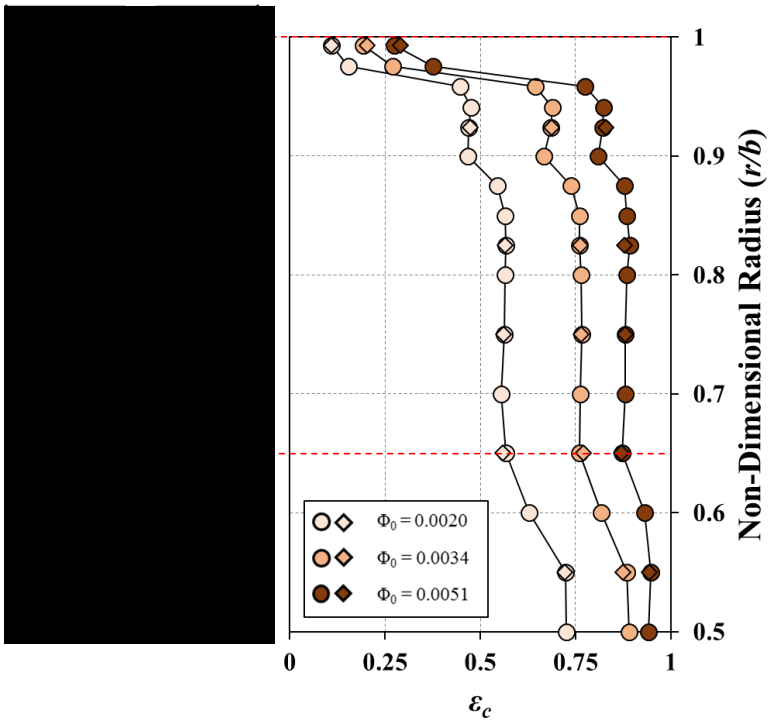

Figure 5.27: Effect of sealing flow rate on radial distribution of effectiveness for AWBC3 (Re_Φ = 7.2 × 10^5, C_F = 0.34) (circles denote stator-wall measurements; diamonds denote rotating-core measurements)

Consider first the distributions corresponding to seals AWBC1 and AWBC2. For 0.85 < *r/b* < 0.958 the effectiveness of AWBC2 is higher than that of AWBC1. This shows that the addition of the buffer cavity to AWBC1 had a negative impact on the performance of the seal. With reference to Section 4.5 rotationally induced (RI) ingress occurs in the downstream wheel-space with no circumferential pressure variation to be attenuated in the cavity. Therefore what was initially designed as a *buffer cavity* is more like an *expansion cavity* requiring a higher amount of sealing flow for the same level of wheel-space pressurisation to be achieved. Due to this the performance of the seal deteriorates.

Now consider the distributions corresponding to seals AWBC1 and AWBC3. The two distributions are similar apart from the locations affected by the stator side hook (0.875 ≤ *r/b* ≤ 0.958). At these locations the effectiveness of AWBC3 is lower than that of AWBC1. This suggests that the addition of the stator-side hook to the baseline geometry has acted as a barrier that prevented the high concentration re-circulating flow form the rotor boundary layer to reach across to the stator boundary layer as shown in Figure 5.28 (c).

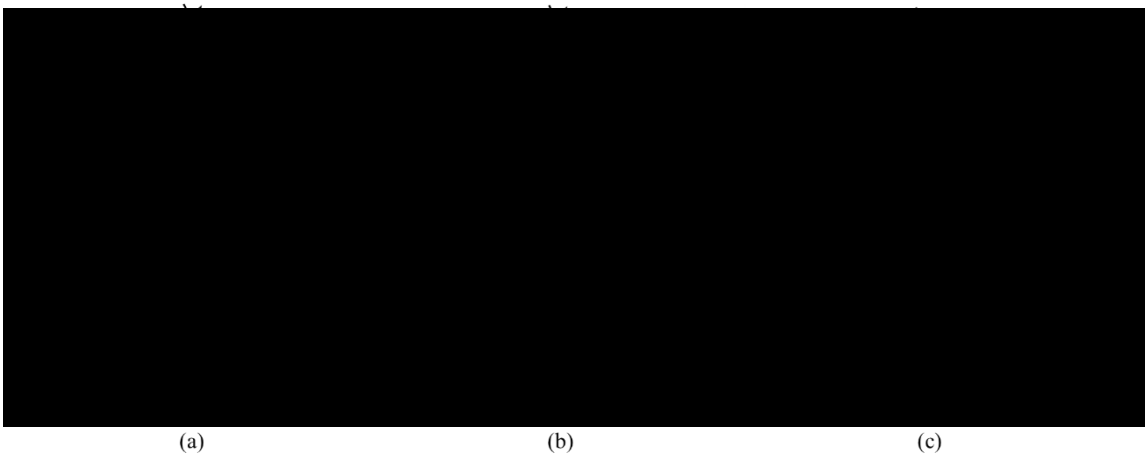

Figure 5.28: Simplified illustrations of suggested flow of ingress and egress through (a) AWBC1 (b) AWBC2 and (c) AWBC3 seals including concentration sampling locations on the stator

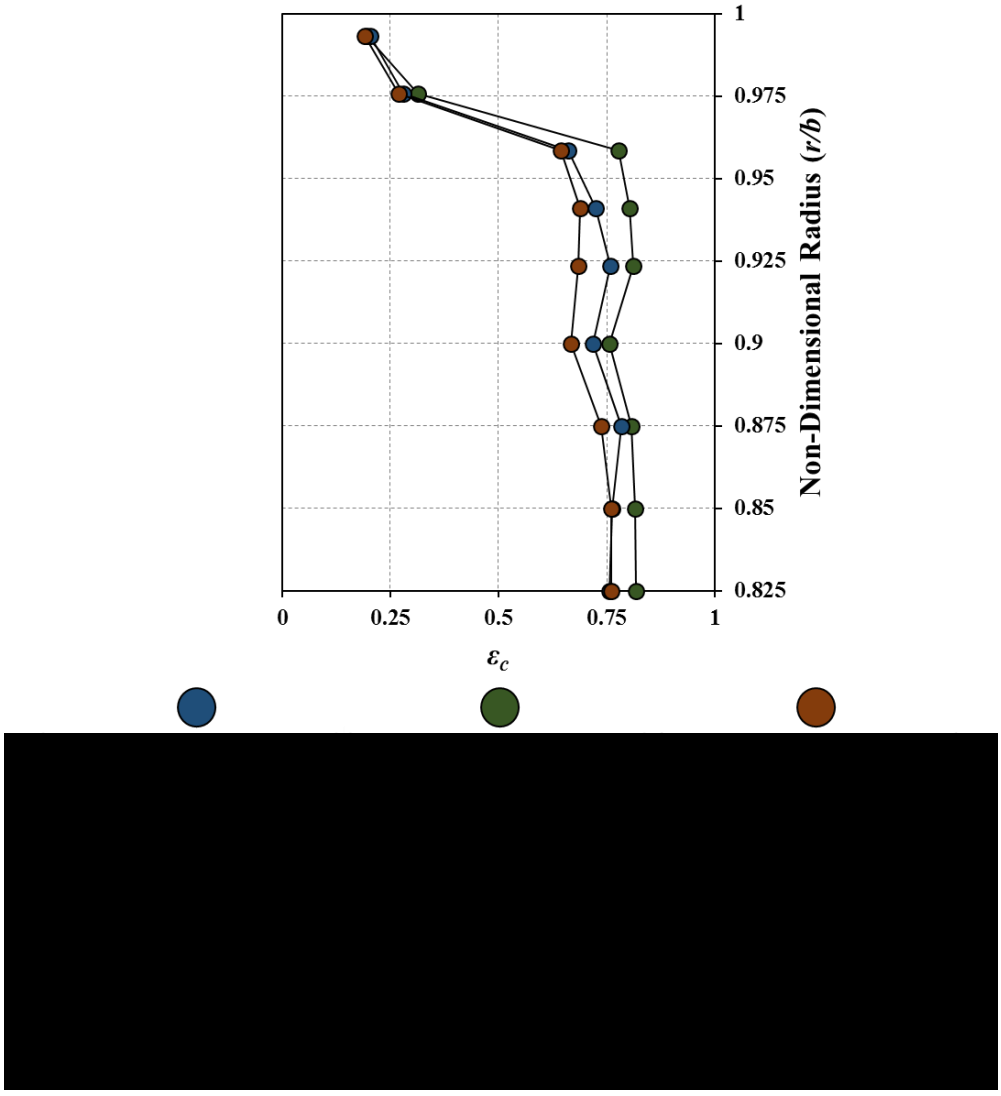

Figure 5.29: Comparison of the radial distribution of effectiveness of AWBC1, AWBC2 and AWBC3 (Re_Φ = 7.2 × 10^5, C_F = 0.34, Φ_0 = 0.0034)

5.4.3 Variation of Concentration Effectiveness with Sealing Flow Rate

Figure 5.30 to 5.32 show the variation of concentration effectiveness, ε_c with non-dimensional sealing flow rate Φ_0 for AWBC1, AWBC2 and AWBC3 respectively. The measurements were taken at two radial locations, $r/b = 0.958$ (dark symbols) and 0.85 (light symbols) and at two rotational Reynolds number conditions $Re_\Phi = 7.20 \times 10^5$ and 1.00×10^6. In all cases ε_c increases with increasing Φ_0, as the sealing flow pressurises the wheel-space and reduces ingestion through the rim-seals. The data collapse onto individual curves which are independent of Re_Φ.

Also shown in Figures 5.30 to 5.32 are the RI theoretical effectiveness curves that were fitted to the experimental data. Good agreement between theory and experiment is observed in all cases. The estimated values of Φ_{min} and Γ_c and their 95% confidence intervals along with the values of Φ_{min}', and standard deviation σ between the data and the fitted curves are tabulated in Table 5.6.

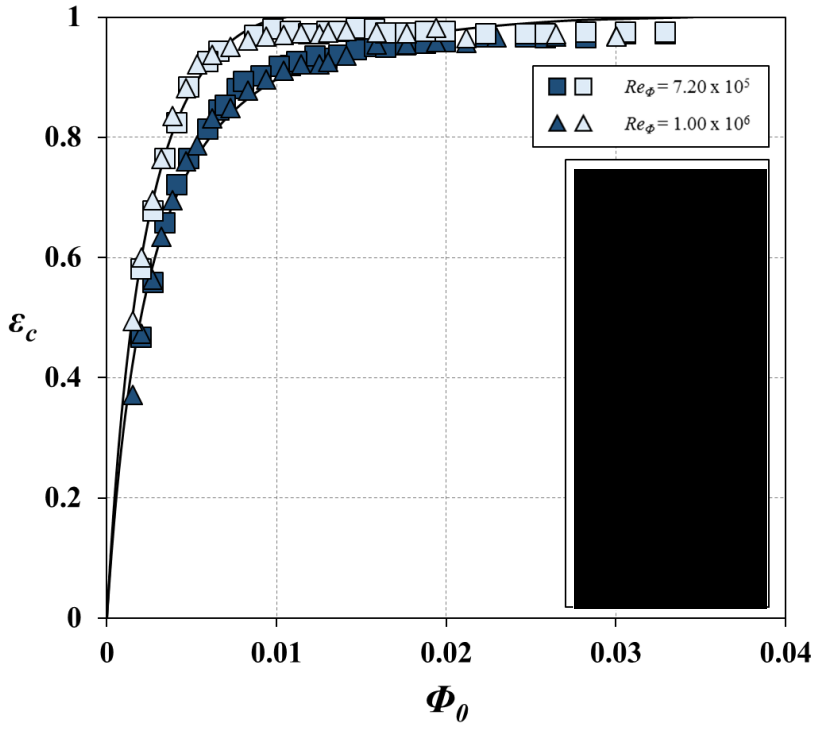

Figure 5.30: Variation of ε_c with Φ_0 for AWBC1 at r/b = 0.958 (dark blue symbols) and r/b = 0.85 (light blue symbols) (C_F = 0.34) (symbols denote data; solid lines are theoretical curves obtained from the orifice model)

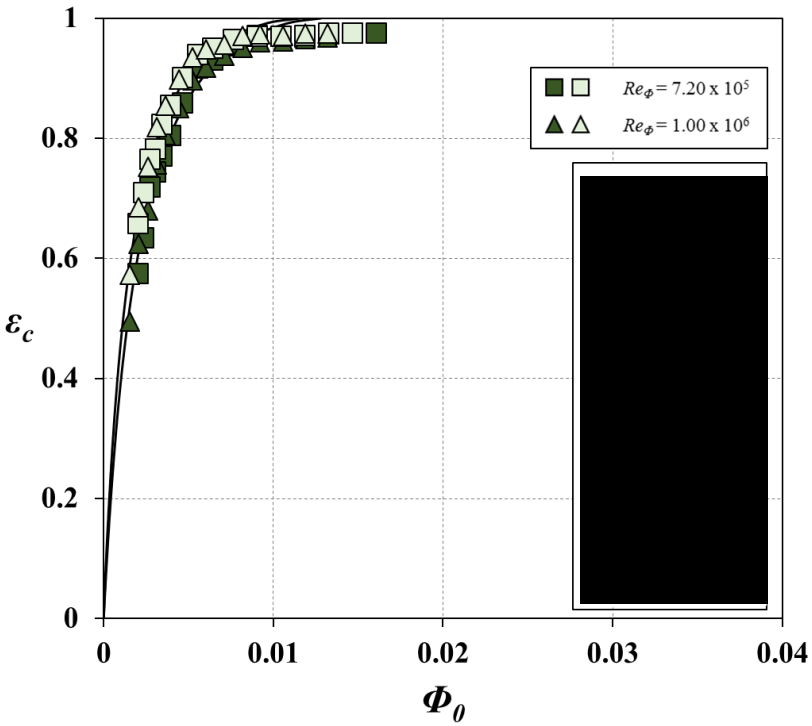

Figure 5.31: Variation of ε_c with Φ_0 for AWBC2 at r/b = 0.958 (dark green symbols) and r/b = 0.85 (light green symbols) (C_F = 0.34) (symbols denote data; solid lines are theoretical curves obtained from the orifice model)

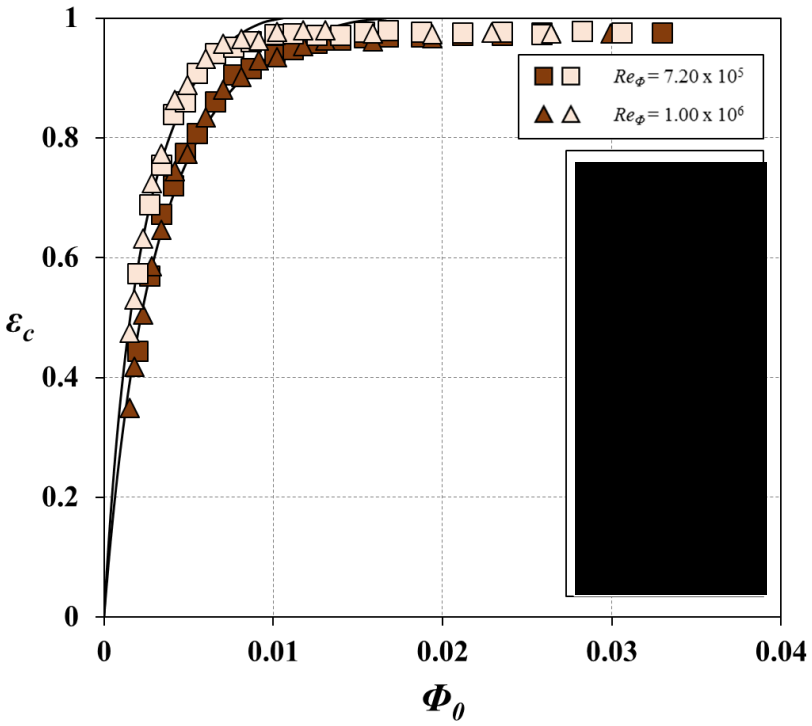

Figure 5.32: Variation of ε_c with Φ_0 for AWBC3 at r/b = 0.958 (dark brown symbols) and r/b = 0.85 (light brown symbols) (C_F = 0.34) (symbols denote data; solid lines are theoretical curves obtained from the orifice model)

Parameter	AWBC1		AWBC2		AWBC3	
	r/b					
	0.958	***0.85***	***0.958***	***0.85***	***0.958***	***0.85***
Φ_{min}	0.0348	0.0106	0.0129	0.0115	0.0167	0.0106
Φ_{min}'	0.0149	0.00690	0.00763	0.00653	0.0105	0.00698
Γ_c	0.0857	0.328	0.224	0.187	0.287	0.344
σ	0.0204	0.0227	0.0195	0.0170	0.0227	0.0214

Table 5.6: Theoretical fit parameters for AWBC1, AWBC2 and AWBC3

The measurements of Figures 5.30 and 5.31 are combined in Figure 5.33 to enable a performance comparison between AWBC1 (the baseline geometry) and AWBC2. The measurements corresponding to $Re_\Phi = 1.0 \times 10^6$ are omitted for clarity. At both the inner and outer sampling locations the effectiveness of AWBC2 is equal and virtually the same as the effectiveness of AWBC1 at the inner sampling locations. A significantly lower effectiveness can be seen for AWBC1 at the outer sampling location. This is consistent with the measurements of the radial distributing of ε_c in the wheel-space providing additional evidence of the negative impact of the buffer cavity in the performance of angel-wing seals.

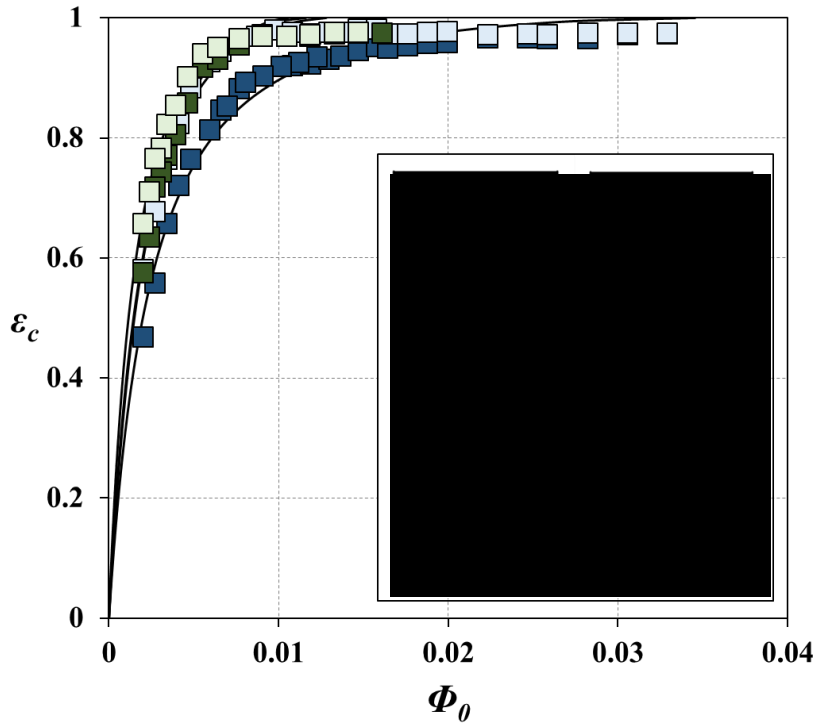

Figure 5.33: Comparison of the variation of ε_c with Φ_0 for AWBC1 (blue symbols), AWBC2 (green symbols) ($Re_\Phi = 7.2 \times 10^5$; $C_F = 0.34$) (symbols denote data; solid lines are theoretical curves obtained from the orifice model)

Figure 5.34 combines the measurements shown in Figures 5.31 and 5.32 to enable a performance comparison between AWBC1 and AWBC3. The effectiveness of the seals is virtually the same at r/b = 0.85 whereas at r/b = 0.958, AWBC3 demonstrates a slightly higher effectiveness. This shows that at these two radial locations there is no effect of the stator-side hook on the performance of the seals. However, as shown by the radial distributions of ε_c in the wheel-space (Figure 5.29), the stator-side hook resulted in a lower effectiveness in the region between the hook and the stator surface. Considering this, there is no clear benefit for incorporating such a feature in the design of compound angel-wing seals.

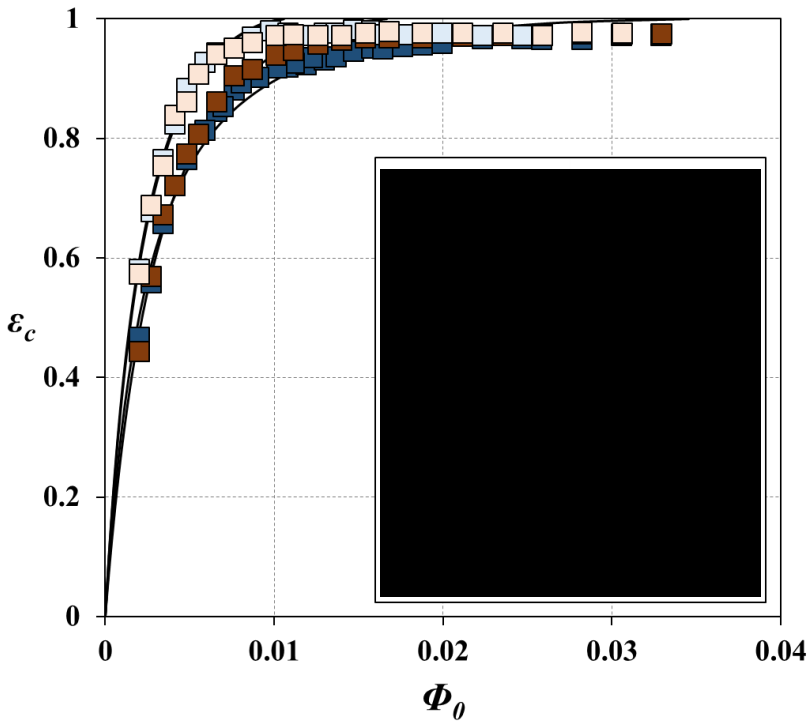

Figure 5.34: Comparison of the variation of ε_c with Φ_0 for AWBC1 (blue symbols), AWBC3 (brown symbols) (Re_Φ = 7.2 × 10^5; C_F = 0.34) (symbols denote data; solid lines are theoretical curves obtained from the orifice model)

5.4.4 Wheel-Space Pressure and Swirl Measurements

Figures 5.35 to 5.37 illustrate the variation of β and C_p in the wheel-space with non-dimensional radius for seals AWBC1, AWBC2 and AWBC3 respectively. The measurements were taken at $Re_\Phi = 7.2 \times 10^5$ for several values of λ_T and hence Φ_0. The measurement points for the total pressure in the wheel-space (at $z/S = 0.25$) are shown as diamond symbols on the silhouettes in the middle of the figures. In all cases ingress occurred with an annulus swirl ratio downstream of the blades, $\beta_{a,\,DWS} = 0.2$.

For $\lambda_T = 0$, there is no superposed flow and the core rotation $\beta \approx 0.44$ at $r/b < 0.875$ for all three seal geometries. The swirl ratio at the larger radii increases radially under the influence of the geometric features of the seals. This shows that the flow structure described in Sections 2.4 and 4.1.1 exists in this region. The swirl ratio at the larger radii increases radially under the influence of the geometric features of the seals. Increasing the sealing flow causes a reduction in the core rotation as the wheel-space is pressurised.

Also shown in Figures 5.35 to 5.37 is the radial variation of C_p in the wheel-space for the three rim-seal geometries mentioned above. Theoretical distributions of C_p, based on the experimental measurements of the swirl ratio and calculated using Eq. 4.2 are also plotted on the same graphs. In all cases as the sealing flow increases the radial pressure gradient is reduced resulting in lower C_p values. This shows that the radial distribution of static pressure in the downstream wheel-space is controlled by the swirl ratio.

A sudden decrease in the swirl ratio can be seen at the upper most sampling location where $r/b = 0.993$ for all three seals. With reference to Figures 5.30, 5.31 and 5.32 this sudden decrease in the swirl ratio is attributed to the strong effect of the ingested flow in the region immediately inboard of the wheel-space shroud. Increasing the sealing flow causes a reduction in the core rotation as the wheel-space is pressurised.

Looking at the radial variation of C_p in the wheel-space (right hand side plots in Figures 5.35 and 5.36), three regions (see Figure 5.38) with distinct pressure gradients can be identified. The first region is between $0.65 \leq r/b \leq 0.875$ and is referred to as the inner wheel-space. In the inner wheel-space there is a positive radial gradient of C_p, indicating that this region is dominated by the rotating core. In this region there is very good agreement between the thoeretical and experimental distributions of C_p, showing that the distribution of the swirl ratio controlls the distribution of pressure in this part of the wheel-space. The second region is between $0.9 \leq r/b \leq 0.958$ and is referred to as the intermediate wheel-space. Here, a radial pressure increase can be seen with a shallower gradient than the one of the inner wheel-space. This indicates that the flow in the intermidiate wheel-space rotates faster than the core in the inner wheel-space. Good agreement between the thoeretical and experimental distributions of

C_p can also be seen in this region.The third region is for $r/b > 0.958$ and is referred to as the outer wheel-space. Here, the pressure remains almost constant with radius inidcating flow with very little or no swirling motion. As mentioned before, this region is dominated by the ingested annulus flow which enters the outer wheel-space with a very small swirl ratio, $\beta_{a,\,DWS} = 0.2$. As a result, the agreement between the theoretical and measured distributions of C_p in this region has deteriorated. Despite that, the calculated distributions of C_p still capture the general trend of pressure distribution at this high wheel-space radii.

Now consider the radial distribution of pressure for AWBC3 on the right hand side of Figure 5.37). Three regions with distinct pressure gradients can be seen, similar to the ones discussed above for seals AWBC1 and AWBC2. As opposed to seals AWBC1 and AWBC2, in the case of AWBC3 these three regions were also noticable in the measurements of the radial variation of ε_c in the wheel-space (see Section 5.4.3). In the inner wheel-space, between $0.65 \leq r/b \leq 0.875$, there is dominated a rotating core which results in a radial pressure gradient and hence an increase of C_p as the radius increases. As expected there is very good agreement between the thoeretical and experimental distributions of C_p in this region and therefore the distribution of the swirl ratio controlls the distribution of pressure in this part of the wheel-space. The intermediate wheel-space, between $0.9 \leq r/b \leq 0.958$, there is a higher non-dimensional pressure than in the inner wheel-space that is broadly invariant with radius indicating flow with very little or no swirling motion. This is consistent with the effect of the stator-side hook (first discussed in Section 5.4.3) to act as a barrier that prevents the high concentration re-circulating fluid from the rotor boundary layer to reach across to the stator boundary layer. In this region, the thoeretical and experimental distributions of C_p do not agree. In the outer wheel-space, at $r/b > 0.958$, the pressure is also constant with radius but higher than that of the intermediate wheel-space. Similarly to the case of the other two seal, this region is dominated by the ingested annulus flow which enters the outer wheel-space with a very low swirl ratio, $\beta_{a,\,DWS} = 0.2$. As a result there is poor agreement between the theoretical and measured distributions of C_p in this region.

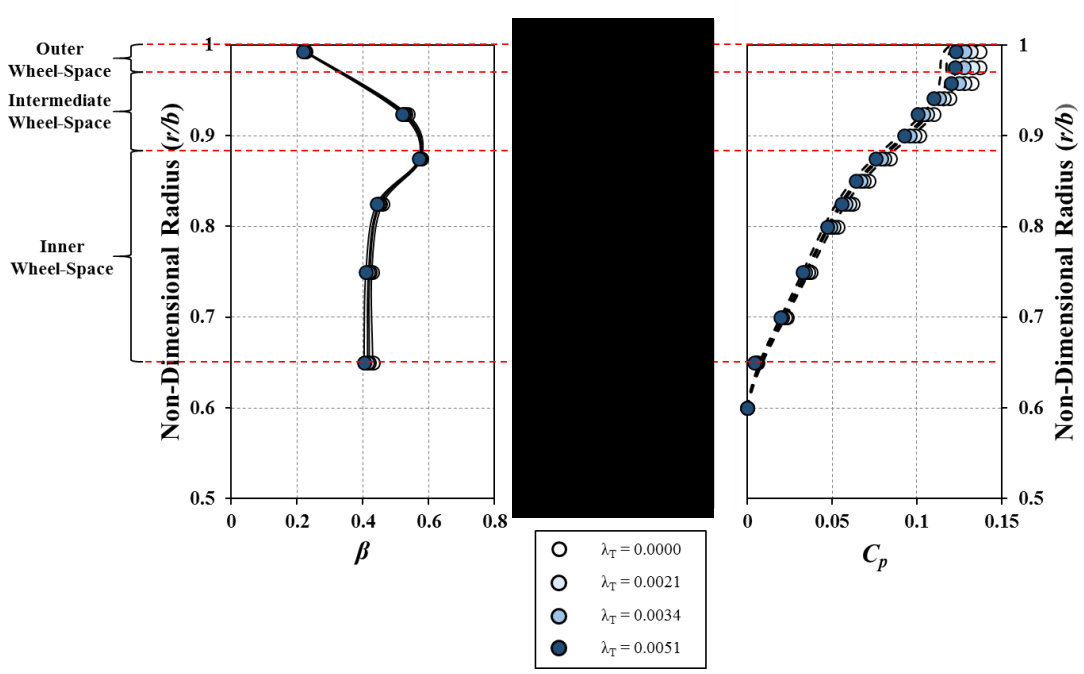

Figure 5.35: Effect of sealing flow rate on the distribution of swirl ratio and pressure for AWBC1 (symbols denote measured values; dash lines denote calculated distribution for C_p)

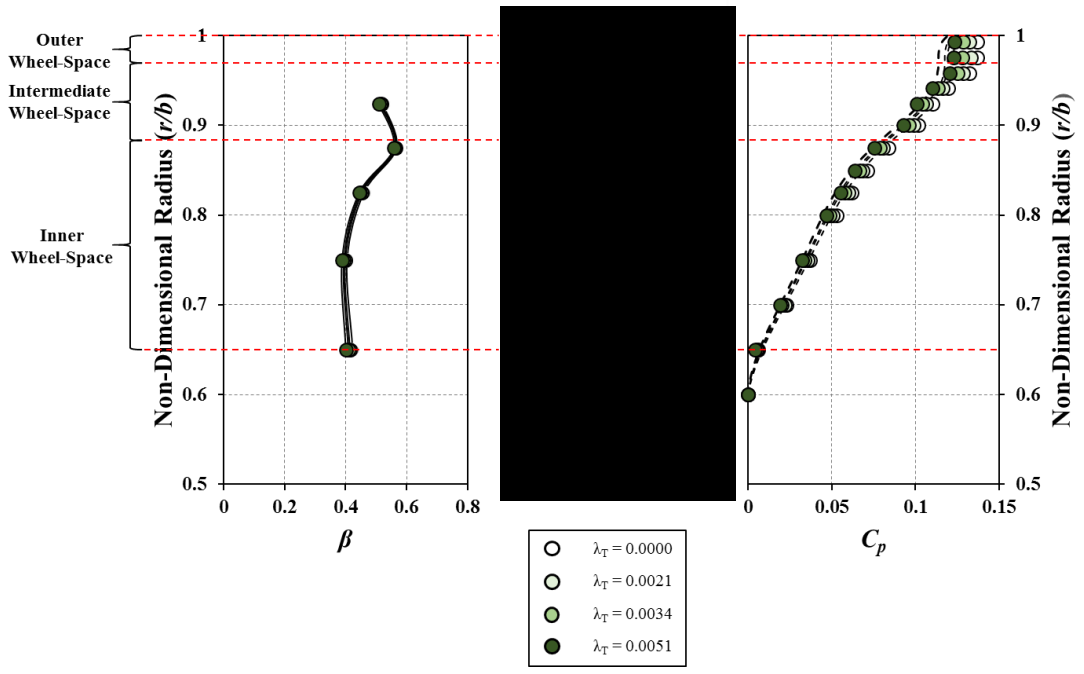

Figure 5.36: Effect of sealing flow rate on the distribution of swirl ratio and pressure for AWBC2 (symbols denote measured values; dash lines denote calculated distribution for C_p)

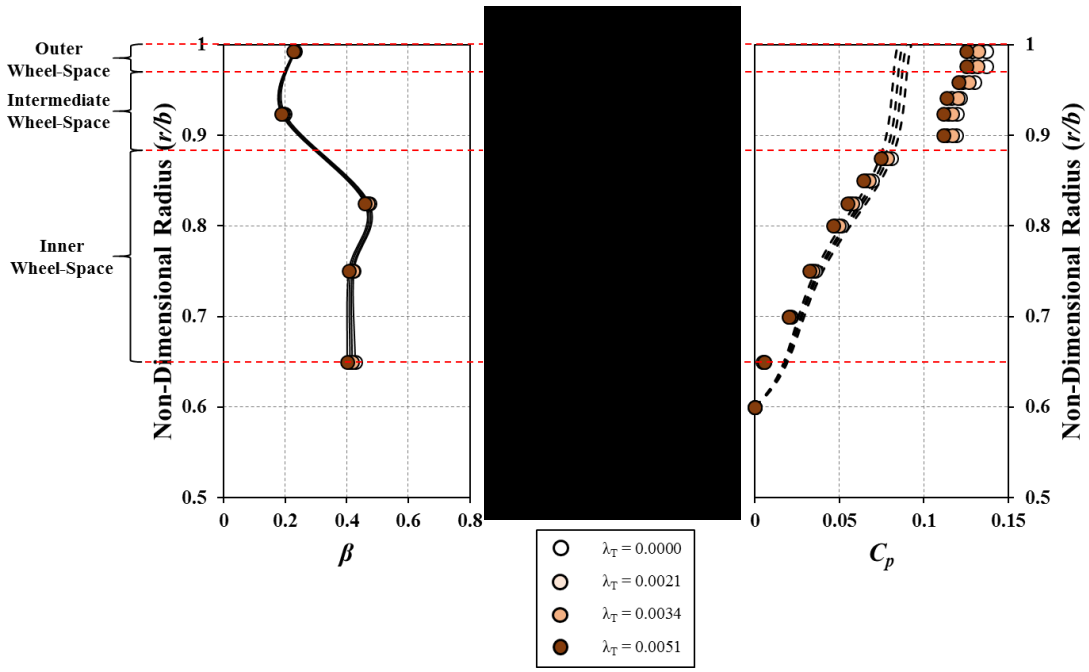

Figure 5.37: Effect of sealing flow rate on the distribution of swirl ratio and pressure for AWBC3 (symbols denote measured values; dash lines denote calculated distribution for C_p)

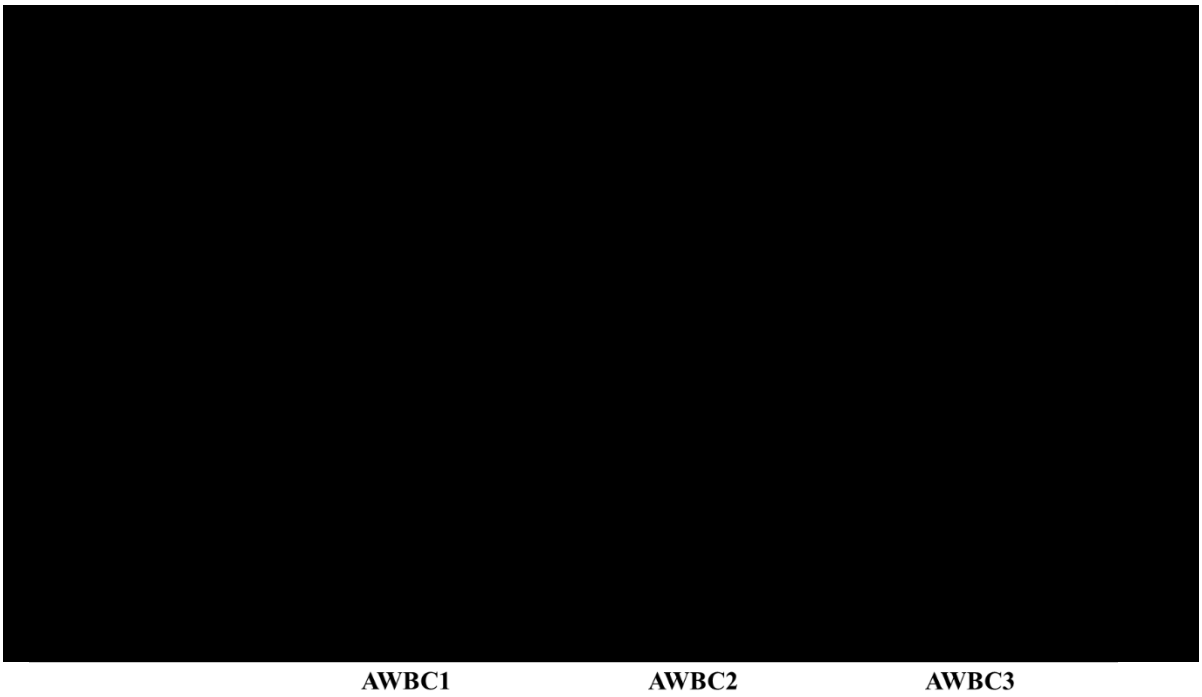

Figure 5.38: The three flow regions created as ingress penetrates through seals AWBC1, 2 and 3

5.5 Seal Effectiveness Rankings

Figure 5.39 shows a performance ranking of the six Siemens proprietary seals that were tested in parametric studies two and three. The seals are presented in an increasing order of performance from left to right, based on Φ_{min}'.

Considering the performance of the seals at r/b = 0.85 (green bars) it can be seen that AW3 was the smallest Φ_{min}' (most effective seal) and AW1 the largest (least effective seal). At r/b = 0.85 (grey bars) the most effective seal is also AW3 and the least effective seal is AWBC1.

Comparing the Φ_{min}' of AW3 with the one corresponding to the baseline geometry in parametric study 2, AW1, the clear benefit of using a compound angel-wing/radial-clearance seal as opposed to just an angel wing-seal can be seen; for an effectiveness of 95% at r/b = 0.85, AW3 requires around 30% of the sealing flow required for AW1 and at r/b = 0.958 around 50%. Comparing the Φ_{min}' at r/b = 0.958 of AWBC1 with the one corresponding to AWBC2, the negative effect of the buffer cavity on the performance of angel-wing seals can be seen; AWBC1 requires almost double the amount of sealing flow required in the case of AWBC2 for ε_c = 95%.

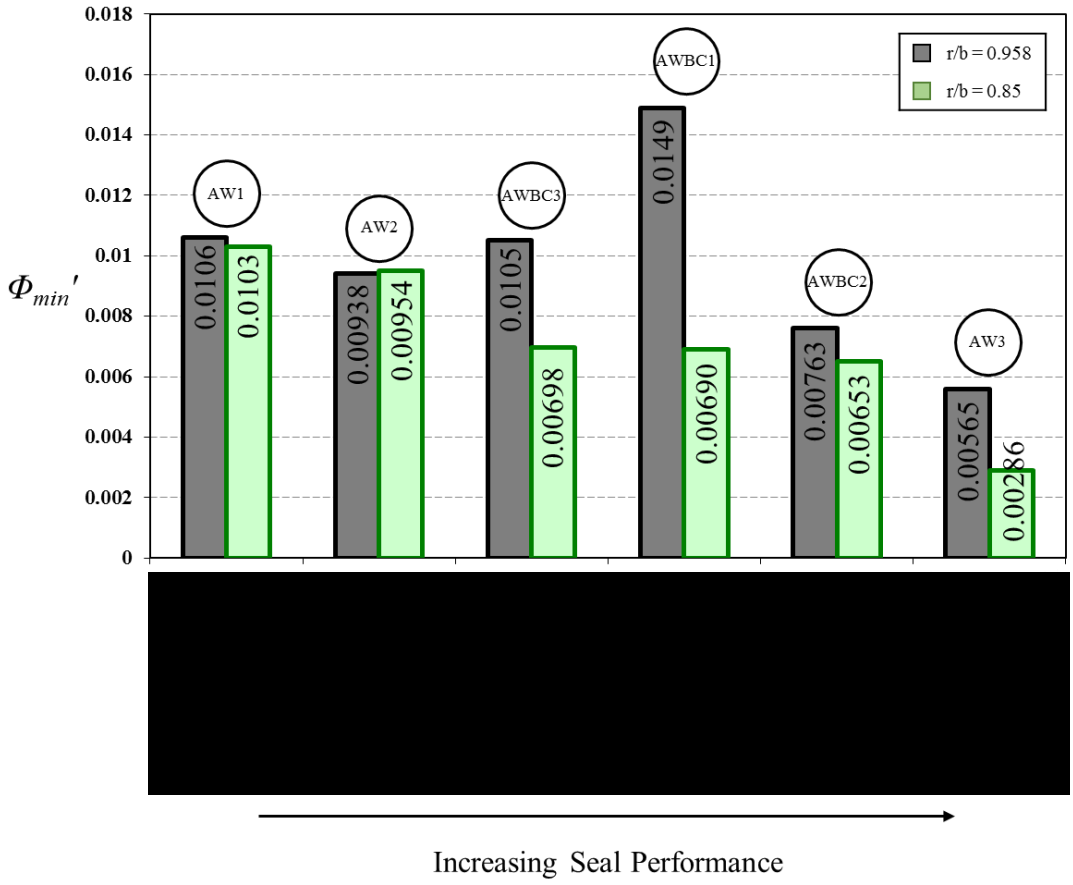

Figure 5.39: Performance ranking shown in order of magnitude of Φ_{min}' for the Siemens Proprietary Seals. The ranking is based on seal performance at r/b = 0.85

5.6 Summary

Three parametric studies including eight Siemens proprietary seals were presented in this chapter.

The first study involved two single radial-clearance seals, SS1 and SS2, each featuring 48 radial slots through their seal-lip. The slot width of SS1 was larger than the one of SS2. The experimental results of this study showed that the effectiveness of SS2 was lower than that of SS1. This was due to the wider slots featured in SS2.

The second study involved an angel-wing seal (baseline geometry), AW1, a double winglet angel-wing seal, AW2, and a compound angel-wing/radial-clearance seal, AW3. The experiments conducted for the purpose of this study showed that the addition of a second winglet to the baseline geometry had only a marginal effect on the performance of the seal whereas the addition of the radial-clearance seal at lower radius resulted in a significant increase in performance.

The third study investigated the performance of angel-wing seals with and without a buffer cavity. Three seal geometries were used in this study: AWBC1, an angel-wing seal with a buffer cavity (baseline geometry); AWBC2, an angel-wing seal without a buffer cavity; AWBC3, an angel-wing seal with a buffer cavity and a stator-side hook. In this study it was shown that the addition of a buffer cavity to angel-wing seals resulted in a decrease in their performance. As far as the addition of the stator side hook to the baseline geometry is concerned, both the radial distributions of effectiveness and the variation of effectiveness with sealing flow rate showed no tangible benefit on the performance of the seal when this additional feature is introduced.

In all cases, the flow structure in the region lower than the seal features was found to be in agreement with the one discussed in Sections 2.4 and 4.1.1. At the higher radii in the wheel-space this flow structure is altered by the strong effect of ingress and the geometric features of the seals in this region. The RI orifice model was shown to be capable of accurately capturing the variation of concertation effectiveness with sealing flow rate for all eight seals, despite their complex geometries.

Lastly, a performance ranking was provided showing that the most effective seal was the compound seal AW3. Comparing the performance of this seal with AW1 it was shown that, for an effectiveness of 95%, the compound seal required 30% and 50% less sealing flow rate than a simple angel-wing seal at r/b = 0.958 and 0.85 respectively.

Chapter 6: Conclusions

6.1 The 1.5-Stage Gas Turbine Test Facility

Following the completion of a successful three-year (2008 – 2011) research collaboration between the University of Bath and Siemens, a new collaboration was formed in 2013. The aim of the new collaboration was to expand the research of ingress through company proprietary rim-seals in a downstream wheel-space of a test facility featuring engine representative blade and vane geometries. To achieve this, a new 1.5-stage turbine test facility was designed and built.

The facility features two stator discs with a rotor disc in between the two, forming an upstream and a downstream cavity or wheel-space. The vanes of both stators were manufactured integrated to 180° split rings to form blings mounted at the periphery of the stator discs. The split design of the blings provides testing flexibility to the new facility as it allows virtually any rim-seal geometry, axially- or radially-assembled, generic or proprietary, to be installed and tested. The rotor disc is manufactured as a blisc, with the blades integrated to the disc. This rotor design ensures integrity of the highly stressed disc under all operating points. Both stators feature 32 vanes with the rotor featuring 48 turned blades. A dynamometer is used to absorb the power generated by the stage.

Experiments were performed at rotor disc speeds of 3000 and 4000 rpm, corresponding to rotational Reynolds numbers $Re_\Phi = 7.2 \times 10^5$ and 1.0×10^6 respectively. Mainstream flow was supplied to the annulus of the turbine at a range of flow rates allowing the rig to operate on and off design. An operating flow coefficient $C_F = 0.34$ was chosen for the experiments resulting in a maximum axial Reynolds Number $Re_w = 3.4 \times 10^5$. The vane exit Mach number at the higher operating conditions was $M = 0.37$.

Sealing flow was supplied to both the upstream and the downstream wheel-spaces, providing a wide range of non-dimensional sealing flow parameter numbers Φ_0. The sealing flow was fed to the wheel-spaces via specially made feed systems.

Measurements of static and total pressure and CO_2 concentration were made at various locations inside the upstream and downstream wheel-spaces and in the annulus. Pressure was measured using four Scani-Valves. CO_2 concentration was measured using a dual-channel, Signal Group gas analyser.

The test facility offers flexibility and expediency in terms of data collection over a wide range of sealing flow rates. This enables an efficient method of ranking and quantifying the performance of a wide range of generic and engine-specific seals that are developed in industry

using CFD simulations. The experiments are thus used to inform design criteria that can be scaled to engine operating conditions through the use of theoretical models and CFD.

6.2 Ingress through Generic Seals in the Upstream and Downstream Wheel-Spaces

The phenomenon of ingress in the upstream and downstream wheel-spaces of the new 1.5-stage rig was investigated using single and double radial-clearance seals. The experiments conducted involved measurements of concentration effectiveness, pressure and swirl in both wheel-spaces.

Measurements of the radial distribution of concentration effectiveness ε_c were taken in both the upstream and downstream wheel-spaces for both seals. In all cases, the stator ε_c was virtually equal to that in the rotating core. This showed for the first time that the stator boundary layer is the source of flow to the rotating core. The stator and core distributions were also found to be broadly invariant with radius. This showed that near-complete mixing between ingress and egress had occurred in a region very close to the periphery of the wheel-space. The qualitative similarity of the upstream and downstream distributions provided unprecedented experimental evidence of the flow structure in the downstream wheel-space being a "mirror-image" of that in the upstream.

Further evidence of the expected flow structure are provided by measurements of the radial variation of static pressure C_p and swirl ratio β in the two wheel-spaces. For both seals and for the case where no sealing flow was supplied to the wheel-spaces the swirl ratio of the core was shown to be $\beta = 0.4$. The radial distribution of the swirl ratio was found to control the radial distribution of pressure.

Measurements of the variation of concentration effectiveness with sealing flow rate were taken in the upstream and downstream wheel-spaces at two rotational Reynolds numbers ($Re_\Phi = 7.2 \times 10^5$ and 1.0×10^6) using both radial seals. In all cases the effectiveness of the two seals increased with sealing flow and was independent of rotational Reynolds number for a common flow coefficient in the annulus. A theoretical orifice model was fitted to the experimental data showing good agreement between theory and experiment in all cases. This was a significant finding as it demonstrated that the simple orifice model can qualitatively predict ingress not only to an upstream wheel-space where the annulus pressure field is dominated by the steady-state pressure asymmetry from the vanes, but also in the downstream wheel-space where an *unsteady* pressure variation from the rotor blades exists in the annulus.

A comparison of the radial distribution of ε_c and variation of ε_c with Φ_0 in both wheel-spaces for the double radial-clearance seal showed a significant improvement in the

performance of the seal in the downstream wheel-space This indicated a weaker driver for ingress in the downstream wheel-space.

To identify the driving mechanism for ingress in the downstream wheel-space a rotationally-induced (RI) ingress experiment was conducted using the double seal. The measurements were found to collapse to those corresponding to the externally-induced (EI) ingress test with flow through the annulus. This suggests that RI ingress dominates in the downstream wheel-space.

To further strengthen the argument for RI ingress in the downstream wheel-space the variation of ε_c with Φ_0 was measured for a range of flow coefficients between $0.3 < C_F < 0.36$. The results showed that RI ingress dominates for a range of flow coefficients around the operating point.

Based on the experimental measurements, qualitative illustrations of the flow structure in the upstream and the downstream wheel-space are provided and discussed. The flow structure in both wheel-spaces is identical consisting of two separated boundary layers, one on the stator and one on the rotor surface with a core of inviscid fluid rotating in between them. Radially inwards movement of fluid is constrained within the stator boundary layer and radially outwards movement of fluid within the rotor boundary layer. Complete mixing of the ingested mainstream flow from the annulus with the sealing flow provided to the wheel-space occurs in a region very close to the seal clearance and no further mixing occurs in the stator boundary layer. Flow to the rotor boundary layer is supplied by the stator boundary layer via the rotating core. In the rotating core there are no axial gradients of the tangential and axial components of velocity and the radial component of velocity is zero. The only difference between the flow structure in the upstream and downstream wheel-space is that in the case of the latter the mainstream flow has to pass through an axi-symmetric egress fluid-barrier before being ingested into the wheel-space. The subsequent exchange of angular momentum between the two streams is expected to attenuate any pressure asymmetries and result in a weaker driver for ingress. This hypothesis is consistent with the experimental findings.

6.3 Ingress through Industrial Rim-Seals

Three parametric studies including eight Siemens proprietary rim-seal geometries were performed in the downstream wheel-space of the 1.5-stage rig. The first study examined the effect of circumferentially-spaced radial slots of different widths on the performance of single radial-clearance seals. The second study investigated a potential increase in the performance of single angel-wing seals by the addition of secondary features, namely winglets, and a single radial-clearance seal at a lower radius. The last study explored the effect of a buffer cavity on

the performance of angel-wing seals. The experiments were conducted at C_F = 0.34 and involved measurements of concertation effectiveness, pressure and swirl ratio at two radial locations and two Re_Φ conditions ($Re_\Phi = 7.2 \times 10^6$ and 1.0×10^6).

The first study involved two single radial-clearance seals each featuring 48 radial slots through their seal-lip. These slots simulated small gaps between adjacent blades in turbines. The results of this study showed that the effectiveness of the seal deteriorates with the width of the slots. The flow structure in the wheel-space was found to be unaffected by the presence of the slots.

The second study investigated the effect of the addition of a second winglet and an inner radial-clearance seal on the performance of a simple angel-wing seal. Angel-wing seals are common features of modern gas turbine engines and therefore are of great interest to the engine designers. The results of this study showed that the addition of a second winglet to the simple angel-wing seal resulted in a marginal improvement in performance of the seal, whereas the addition of an inner radial-clearance seal resulted in a significant improvement.

The third study investigated the performance of angel wing-seals with and without a buffer cavity. The results of this study showed that the buffer had a negative impact on the performance of angel-win seals in the downstream wheel-space.

In all cases, the flow structure in the region lower than the seal features was found to be in agreement with the one discussed in Section 2.4 and 4.1.1. At the higher radii in the wheel-space this flow structure is altered by the strong effect of ingress and the geometric features of the seals in this region. The RI orifice model was shown to be capable of accurately capturing the variation of concertation effectiveness with sealing flow rate for all eight seals, despite their complex geometries.

A performance ranking was provided showing that the most effective seal was the compound angel-wing/radial-clearance seal. For an effectiveness of 95%, the compound seal required 30% and 50% less sealing flow rate than a simple angel-wing seal at r/b = 0.958 and 0.85 respectively.

6.4 Future Work

This thesis discusses experiments conducted since the commissioning of the 1.5-stage rig. Many questions still remain unanswered regarding ingress in both wheel-spaces. These questions are listed below and experiments are either currently on-going or planned to take place in the near future. The author of this thesis will be the lead researcher for many of these experiments, acting as a post-doctoral research associate.

Effect of vane position and vane-blade interactions

Externally-induced ingress in the upstream wheel-space is as a result of a circumferential pressure asymmetry in the annulus. The pressure asymmetry attenuates with axial distance from the vane trailing edge. Therefore, ingress is expected to decrease as the vanes are positioned further upstream of the edge of the seal-clearance. Altering the position of the vanes relative to the seal-clearance also alters the vane-blade spacing and therefore the way the vane wake and the blade bow wave interact. This interaction is also expected to have an effect on ingress but whether this would be positive or negative still remains unknown.

The effect of the vane position and vane-blade interactions will be investigated by making measurements of CO_2 concentration using various configurations of the upstream stage featuring a bladeless rotor and/or a new set of blings, with the vanes being closer to the edge of the platform. Unsteady pressure measurements in the annulus will also be required if the effect of these changes on ingress is to be completely understood.

Ingress at off-design conditions

In many occasions a gas turbine engine is required to operate at off-design conditions. Scobie *et al.* (2013) have investigated the effect of operating off-design on ingress in a single stage rig with symmetrical blades. However, their experiments were conducted in a test rig with symmetrical blades and only an upstream wheel-space. Therefore two questions remain: *does the effect of operating at off-design conditions on ingress change when engine realistic blade profiles are featured?* and *what is the effect of operating at off-design conditions in the downstream wheel-space?* These questions can be answered by conducting measurements of CO_2 concertation, pressure and swirl in both wheel-spaces of the 1.5-stage rig.

Re-ingestion

Re-ingestion is the phenomenon where egressed sealing (purge) flow, emerging from the upstream wheel-space, travels along the blade platform and is re-ingested into the downstream stage wheel-space. Re-ingestion is expected to have a positive effect on the effectiveness of rim-seals in the downstream wheel-space. Quantifying this effect will result in a more accurate prediction of the sealing flow rate required to prevent ingress in the downstream wheel-space which in turn can result in further improvements of engine-efficiency.

Effect of twisted blades on driver for ingress in the downstream wheel-space

The measurements presented in Chapter 4 showed that RI ingress occurs in the downstream wheel-space of the 1.5-stage rig. This was attributed to the effect of the egress-fluid-barrier which attenuates the unsteady circumferential pressure variation created by the rotating blades.

In an engine *3-dimensional, turned and twisted blades* are featured whereas in the rig *2-dimensional, turned-only blades* are featured. The effect of this blade design difference between engine and test rig on the magnitude of the unsteady circumferential pressure variation and on the egress-fluid-barrier, still remains unknown. Consequently, RI ingress in the downstream wheel-space of an engine remains just as a possibility.

To investigate this possibility even further, a new blade-vane set with twisted profiles will be manufactured and installed in the 1.5-stage rig. The magnitude of the unsteady circumferential pressure variation downstream of the blades will be measured on the rotor platform using a slip-ring system. Concentration measurements in the downstream wheel-space will be made for a generic seal geometry and will be compared with the results of an RI test. If the results of the EI and RI tests are the same then RI ingress is also expected to occur in the downstream wheel-space of an engine. Experimental investigation of the effect of the egress-fluid-barrier on the circumferential pressure asymmetry requires visual methods (e.g. PLIF[5], Volumetric velocimetry[6]) and significant modifications to the rig. For this reason a CFD study would be more appropriate.

Effect of Mach number on ingress

A collaboration between the University of Bath and the Department of Energy Technology at KTH Stockholm is in progress. Here the fundamentals of the complicated fluid dynamics associated with turbine internal cooling established at Bath is to be tested at engine representative Mach numbers. The aim of this collaboration is to demonstrate that the fluid dynamic understanding determined from theoretical and experimental modelling could be scaled to the elevated conditions capable at KTH. This would give Siemens greater confidence in the techniques currently employed in extrapolating to the real engine environment. In order to achieve this the KTH rig geometry will be replicated in the Bath facility where wheel-space measurements of ingress will be made with the required detail and resolution. Concurrent experiments at KTH at different conditions will allow the scaling of the orifice model equations to be tested.

[5] PLIF is an optical technique which uses a camera to track light emissions from fluorescing carbon dioxide species within a laser light sheet.

[6] Volumetric velocimetry is a 3D version of classical particle image velocimetry which comprises the use of three cameras to track tracers introduced in a flow illuminated by a laser cone

Effect of sealing flow supply location

The effect of introducing sealant flow at alternative locations in the rig will be achieved by modifying the entry location to each wheel-space. Provision for this was accounted for in the original design of the rig although new stator-side cover-plates will have to be manufactured to facilitate new entry holes. The effect of swirling the sealant flow in the direction of rotor disc rotation will also be investigated. By using the additional N_2O analyser the effect of this new sealant flow entry location can be studied in conjunction with the existing setup by seeding with a second gas.

References

Balasubramanian, J., Michael, M., Roy, R.P., Kim, Y.W. and Moon, H.K., 2016, "Experiments on Front-and-Aft-Disk Cavity Ingestion in a Sunscale 1.5-Stage Axial Trubine", *ASME Paper No. GT2016-56214*.

Barringer, M., Coward, A., Clark, K., Thole, K.A., Schmitz, J., Wagner, J., Alvin, M.A., Burke, P. and Dennis, R., 2014, "Development of a Steady Aero Thermal Rsaerch Turbine (START) for Studying Secondary Flow Leakages and Airfoil Heat Transfer", *ASME Paper No. GT2014-25570*.

Batchelor, G.K., 1951, "Note on a Class of Solutions of the Navier-Stokes Equations Representing Steady Rotationally-Symmetric Flow", *The Quarterly Journal of Mechanics and Applied Mathematics*, 4(1), 29-41.

Bayley, F.J. and Owen, J.M., 1970, "The Fluid Dynamics of a Shrouded Disk System With a Radial Outflow of Coolant", *Journal of Engineering for Power*, 92(3), 335-341.

Beard, P.F., Chew, J.W., Gao, F. and Chana, K.S., 2016, "Unsteady Flow Phenomena in Turbine Rim Seals", *ASME Paper No. GT2016-56110*.

Bohn, D., Rudzinski, B., Surken, N. and Gartner, W., 2000, "Experimental and Numerical Investigation of the Influence of Rotor Blades on Hot Gas Ingestion Into the Upstream Cavity of an Axial Turbine Stage", *ASME Paper No. 2000-GT-0284*.

Bohn, D. and Wolff, M., 2003, "Improved Formulation to Determine Minimum Sealing Flow – Cw, min – for Different Sealing Configurations", *ASME Paper N0. GT2003-38465*.

Bohn, D.E., Decker, A., Ma, H. and Wolff, M., 2003, "Influence of Sealing Air Mass Flow on the Velocity Distribution in and Inside the Rim Seal of the Upstream Cavity of a 1.5-Stage Turbine", *ASME Paper No. GT2003-38459*.

Chew, J.W., Green, T. and Turner, A.B., 1994, "Rim Seling of Rotor - Stator Wheelspaces in the Presence of External Flow", *ASME Paper No. 94-GT-126*.

Childs, P.R.N., 2011. *Rotating Flow.* Oxford: Butterworth-Heinemann.

Cho, G., Sangan, C.M., Michael Owen, J. and Lock, G.D., 2015, "Effect of Ingress on Turbine Disks", *Journal of Engineering for Gas Turbines and Power,* 138(4), 042502-042502.

Cumpsty, N., 2003. *Jet Propulsion: A Simple Guide to the Aerodynamic and Thermodynamic Design and Performance of Jet Engines.* 2 ed. Cambridge: Cambridge University Press.

Daily, J.W., Ernst, W.D. and Asbedian, V.V., 1964. *Enclosed Rotating Discs With Superposed Throughflow: Mean Steady and Periodoc Unsteady Characteristics of Induced Flow.*

Daily, J.W. and Nece, R.E., 1960, "Chamber Dimension Effects on Induced Flow and Frictional Resistance of Enclosed Rotating Discs.", *Journal of Basic Engineering,* 82(1), 217-232.

Gentilhomme, O., Chew, J.W., Hills, N.J. and Turner, A.B., 2003, "Measurement and Analysis of Ingestion Through a Turbine Rim Seal", *Journal of Turbomachinery,* 125(3), 505-512.

Graber, D.J., Daniels, W.A. and Johnson, B.V., 1987. *Disc Pumping Test.* Air Force Wright Aeronautical Laboratories, (Report No. AFWAL-TR-87-2050).

Gregory, N., Stuart, J.T. and Walker, W.S., 1955, "On the Stability of Three-Dimensional Boundary Layers with Application to the Flow Due to a Rotating Disk", *Philosophical Transactions of the Royal Society of London. Series A, Mathematical and Physical Sciences,* 248(943), 155-199.

Hills, N.J., Chew, J.W. and Turner, A.B., 2002, "Computational and Mathematical Modeling of Turbine Rim Seal Ingestion", *Journal of Turbomachinery,* 124(2), 306-315.

Jakoby, R., Zierer, T., Lindblad, K., Larsson, J., deVito, L., Bohn, D.E., Funcke, J. and Decker, A., 2004, "Numerical Simulation of the Unsteady Flow Field in an Axial Gas Turbine Rim Seal Configuration", *ASME paper No. GT2004-53829*.

Mear, L.I., Owen, J.M. and Lock, G.D., 2015, "Theoretical Model to Determine Effect of Ingress on Turbine Disks", *Journal of Engineering for Gas Turbines and Power,* 138(3), 032502-032502.

Meher-Homji, C.B., 2000, "The Historical Evolution of Turbomachinery", *Proceedings of the 29th Turbomachinery Symposium*, 281-321.

Owen, J.M., 2010a, "Prediction of Ingestion Through Turbine Rim Seals—Part I: Rotationally Induced Ingress", *Journal of Turbomachinery,* 133(3), 031005-031005.

Owen, J.M., 2010b, "Prediction of Ingestion Through Turbine Rim Seals—Part II: Externally Induced and Combined Ingress", *Journal of Turbomachinery,* 133(3), 031006-031006.

Owen, J.M. and Rogers, R.H., 1989. *Flow and Heat Transfer in Rotating-Disc Systems.* Taunton, Somerset, England: Research Studies Press Ltd.

Palafox, P., Ding, Z., Bailey, J., Vanduser, T., Kirtley, K., Moore, K. and Chupp, R., 2013, "A new 1.5-Stage Turbine Wheelspace Hot Gas Ingestion Rig (HGIR) - Part I: Experimental Test Vehicle, Measurement Capability and Baseline Results", *ASME Paper No. GT2013-96020.*

Phadke, U.P. and Owen, J.M., 1988, "Aerodynamic Aspects of the Sealing of Gas-Turbine Rotor-Stator Systems: Part 3: The Effect of Nonaxisymmetric External Flow on Seal Performance", *International Journal of Heat and Fluid Flow,* 9(2), 113-117.

Rolls-Royce, 1996. *The jet engine.* 5th ed. Derby: Rolls - Royce Plc.

Roy, R.P., Paolillo, R.E., Feng, J. and Narzary, D., 2005, "Experiment on Gas Ingestion Through Axial-Flow Turbine Rim Seals", *Journal of Engineering for Gas Turbines and Power,* 127(3), 573-582.

Sangan, C.M., Pountney, O.J., Scobie, J.A., Wilson, M., Owen, J.M. and Lock, G.D., 2013, "Experimental Measurements of Ingestion Through Turbine Rim Seals-Part 3: Single and Double Seals", *Journal of Turbomachinery,* 135(5), 051011.

Sangan, C.M., Scobie, J.A., Michael Owen, J., Lock, G.D., Tham, K.M. and Laurello, V.P., 2014, "Performance of a Finned Turbine Rim Seal", *Journal of Turbomachinery,* 136(11), 111008-111008.

Sangan, C.M., Zhou, K.Y., Owen, J.M., Pountney, O.J., Wilson, M. and Lock, G.D., 2012a, "Experimental Measurements of Ingestion Through Turbine Rim Seals. Part 1: Externally-Induced Ingress", *Journal of Turbomachinery,* 135(2), 021012.

Sangan, C.M., Zhou, K.Y., Owen, J.M., Pountney, O.J., Wilson, M. and Lock, G.D., 2012b, "Experimental Measurements of Ingestion Through Turbine Rim Seals. Part 2: Rotationally-Induced Ingress", *Journal of Turbomachinery,* 135(2), 021013.

Savov, S.S., Atkins, N.R. and Uchida, S., 2016, "Comparison of Single and Double Lip Rim Seal Geometry", *ASME paper No. GT2016-56317.*

Scobie, J.A., Sangan, C.M., Michael Owen, J. and Lock, G.D., 2016, "Review of Ingress in Gas Turbines", *Journal of Engineering for Gas Turbines and Power,* 138(12), 120801-120801.

Scobie, J.A., Sangan, C.M., Teuber, R., Pountney, O., Owen, J.M., Wilson, M. and Lock, G., 2013, "Experimental Measurements of Ingestion Through Turbine Rim Seals. Part 4: Off-Design Conditions", *ASME Paper No. GT2013-94147.*

Scobie, J.A., Teuber, R., Sheng Li, Y., Sangan, C.M., Wilson, M. and Lock, G.D., 2015, "Design of an Improved Turbine Rim-Seal", *Journal of Engineering for Gas Turbines and Power,* 138(2), 022503-022503.

Stewartson, K., 1953, "On the Flow Between Two Rotating Coaxial Disks", *Mathematical Proceedings of the Cambridge Philosophical Society*, 49(02), 333-341.

Wang, C.-Z., Mathiyalagan, S.P., Johnson, B.V., Glahn, J.A. and Cloud, D.F., 2013, "Rim Seal Ingestion in a Turbine Stage From 360 Degree Time-Dependent Numerical Simulations", *Journal of Turbomachinery*, 136(3), 031007-031007.

Zhou, D.W., Roy, R.P., Wang, C.Z. and Glahn, J.A., 2010, "Main Gas Ingestion in a Turbine Stage for Three Rim Cavity Configurations", *Journal of Turbomachinery*, 133(3), 031023.

Zhou, K., Wood, S.N. and Owen, J.M., 2012, "Statistical and Theoretical Models of Ingestion Through Turbine Rim Seals", *Journal of Turbomachinery*, 135(2), 021014.